Flow Structure Characterization and Performance Evaluation of Pin Fins Produced using Cold Spray

Philippe Dupuis
B.A.Sc., Mechanical Engineering, University of Ottawa, 2012

Thesis submitted to the Faculty of Graduate and Postdoctoral Studies
in partial fulfillment of the requirements for the degree of

Doctorate in Philosophy
in Mechanical Engineering

Department of Mechanical Engineering
University of Ottawa
Ottawa, Ontario, Canada
November 2016

ABSTRACT

Energy efficiency has become a growing concern in a world driven by a fossil fuel economy. Recuperated micro-gas-turbine systems offer the possibility of high efficiency power generation for low output power systems. To this end, increasing the performance while decreasing the cost, the weight and the volume of heat exchangers such as recuperators has become a critical research focus. Recent work done by Brayton Energy Canada (BEC) has renewed interest in Wire Mesh Heat Exchangers (WMHE) by introducing a new production method that uses cells of stacked wire mesh sheets that have a thick external shell deposited by cold spray. Fins are then machined in this external shell, creating a heat exchanger.

Net shaped pin fins were successfully deposited using Cold Gas Dynamic Spraying (CGDS or simply cold spray) as an additive manufacturing technique to replace the plate fin arrays currently used. This new development is envisioned to save costs while providing higher heat transfer efficiency than traditional fin arrays. Increasing the performance of such fin arrays would yield higher heat exchanger efficiencies and increase the total efficiency of the gas turbine system.

The present thesis provides a description of the research performed, as well as the results thereof, with regards to the performance of pin fin arrays produced using cold spray. A review of the relevant literature is performed to establish the motivation of this study and to describe the relevant work that has been performed by other authors in this respect. **The research objectives are to evaluate the thermal and hydrodynamic performance of these fin arrays and relate those to the flow structures arising from fluid motion between these extended surfaces**. Furthermore, the proposed approach and the experimental equipment that will be used are described in this work. The research objectives were successfully met, with the results obtained from this work presented in the form of peer-reviewed publications.

PREFACE

This thesis is presented as a peer-reviewed paper based work. As such, a statement regarding the contributions the co-authors from the various papers is presented to highlight and justify my individual contribution to this collaborative work.

I have co-authored (second author) the paper "Net Shape Fins for Compact Heat Exchanger Produced by Cold Spray", presented in chapter 5 (pages 72 to 83) with Mr. Yannick Cormier, Dr. Bertrand Jodoin and Mr. Antoine Corbeil. As for my contribution to this work, I was responsible for the design, construction and validation of the custom performance test fixture described in this work, in collaboration with Yannick Cormier, after a thorough literature review of the relevant techniques used for such performance testing. I have also produced samples for this work, as well as conducted the hydrodynamic and heat transfer tests required for the performance evaluation of the fin arrays manufactured. I have contributed directly to the production of the written document, from the initial drafting to the submission and review process, including the interpretation of the performance data results that the experimental testing has generated. Mr. Cormier ensured the production of the figures for this article, as well as performing the typesetting. He has also produced several samples included in this work, and participated in their hydrodynamic and thermal performance testing. Dr. Jodoin, my thesis supervisor, guided me on the required tests to be performed. He also provided insights and reviewed the manuscript to ensure its quality prior to submission. The fourth author, Antoine Corbeil, is the president of Brayton Energy Canada, industrial sponsor for this work. He also helped direct the investigations towards the commercial concerns and set out several technical-engineering requirements for his company. I also used the spray equipment at his facility to produce the samples used in this work.

I have co-authored (first author) the second paper entitled "Performance evaluation of near-net pyramidal shaped fin arrays manufactured by cold spray" presented in chapter 6 (pages 85 to 94), with Mr. Yannick Cormier, Mr. Aslan Farjam, Dr. Bertrand Jodoin and Mr. Antoine Corbeil. I have contributed directly to this work by manufacturing the cold sprayed plain rectangular (straight cut) fin arrays for this work and by conducting their hydrodynamic and thermal performance testing. I also performed the post-processing grinding operations for the samples included in this work. I have contributed directly to the production of the written document, from the initial drafting to the submission and review process, including the interpretation of the performance data results that the experimental testing has generated. Mr. Cormier has performed the surface preparation and produced the cold sprayed samples included in this work, and participated in their hydrodynamic and thermal performance testing. Mr. Farjam, the third author, has performed the measurements of the fin dimensions reported in this work. Dr. Jodoin, my thesis supervisor, guided me on the required tests to be performed. He also provided insights and reviewed the manuscript to ensure its quality prior to submission. The fifth author, Mr. Corbeil, is the president of Brayton Energy Canada, industrial sponsor for this work. He also helped direct the investigations towards the commercial concerns and set out several technical-engineering requirements for his company. I also used the spray equipment at his facility to produce the samples used in this work.

I have co-authored (first author) the third paper entitled "Performance of Cold Sprayed Near-net Pyramidal Shaped Arrays under Forced Convection" presented in chapter 6 (pages 95 to 109), with Mr. Yannick Cormier, Dr. Bertrand Jodoin and Mr. Antoine Corbeil. I have contributed directly to this work by manufacturing the cold sprayed fin arrays for this work and by conducting their hydrodynamic and thermal performance testing. I also performed the post-processing grinding operations for the samples included in this work. I have contributed directly to the production of the written document, from the initial drafting to the submission and review process, including the interpretation of the performance data results that the experimental testing has generated. Mr. Cormier, listed as the second author, has performed the substrate surface preparation and produced the Nusselt number correlations from the data I have generated. Dr. Jodoin, my thesis supervisor, guided me on the required tests to be performed. He also provided insights and reviewed the manuscript to ensure its quality prior to submission. The fourth author, Mr. Corbeil, is the president of Brayton Energy Canada, industrial sponsor for this work. He also helped direct the investigations towards the commercial concerns and set out several technical-engineering requirements for his company. I also used the spray equipment at his facility to produce the samples used in this work. I am the first author of the paper since all the co-authors agreed that I have been the one to contribute the most to the technical/engineering content of the paper.

I have co-authored (first author) the fourth paper entitled “Flow Structure Identification and Analysis in Fin Arrays Produced by Cold Spray Additive Manufacturing” presented in chapter 7 (pages 112 to 124). I have contributed directly to this work by producing the sample that was tested. Also, I performed the design and construction of the custom fixture used for the µPIV manipulations. I have also performed the acquisition and post-processing of the µPIV data, and I developed the numerical model used in this work. I have produced the written document (production of the figures, tables, typesetting, submission and review process) as well as elaborated the draft document itself through the interpretation of the data results that the experimental testing has generated. Mr. Cormier, listed as second author, participated in discussions on this subject, provided useful insights and reviewed the manuscript prior to submission. Dr. Marianne Fenech, the third author, provided training and counsel regarding the µPIV analysis and reviewed the manuscript prior to submission. Dr. Jodoin, my thesis supervisor, guided me on the required tests to be performed. He also provided insights and reviewed the manuscript to ensure its quality prior to submission. Mr. Corbeil, the fourth author, is the president of Brayton Energy Canada, industrial sponsor for this work. He also helped direct the investigations towards the commercial concerns and set out several technical-engineering requirements for his company. I am the first author of the paper since all the co-authors agreed that I have been the one to contribute the most to the technical/engineering content of the paper.

I have co-authored (first author) the fifth paper entitled “Heat Transfer and Flow Structure Characterization for Pin Fins Produced by Cold Spray as an Additive Manufacturing Process” presented in chapter 8 (pages 126 to 137). I have contributed directly to this work by producing every sample tested. Also, I conducted all thermal and hydrodynamic tests, as well as performed the design and construction of the custom fixture used for the µPIV manipulations. I have also performed the acquisition and post-processing of the µPIV data. Mr. Cormier, listed as second author, participated in discussions on this subject, provided useful insights and reviewed the manuscript prior to submission. Dr. Marianne Fenech, the third author, provided training and counsel regarding the µPIV analysis and reviewed the manuscript prior to submission. Dr. Jodoin, my thesis supervisor, guided me on the required tests to be performed. He also provided insights and reviewed the manuscript to ensure its quality prior to submission. I am the first author of the paper since all the co-authors agreed that I have been the one to contribute the most to the technical/engineering content of the paper.

ACKNOWLEDGEMENTS

I would first like to thank my thesis supervisor, Professor Bertrand Jodoin for his mentorship, support and guidance over the course of my studies, both as an undergraduate and a graduate student. Professor Jodoin is an exemplary teacher, supervisor and researcher who strives for greatness in everything he undertakes and who leads others by example to also achieve their potential. Thank you for the valuable discussions and your investment in my personal growth!

I would also take this opportunity to thank Yannick Cormier for all the valuable discussions we had, about every subject imaginable. Your knowledge and your help were greatly appreciated, and you have always known how to be a true friend, an exemplary colleague and even a mentor to me. Your perseverance and your dedication to the ideals of science are an inspiration to us all, myself in particular. I look forward to working with you again, and I will always remember the past seven years with gratitude for all that you have done for me.

Acknowledgements are also due to the project's industrial partner, Brayton Energy Canada, and its staff for their support and guidance regarding the commercial side of this endeavour. I would also like to acknowledge the contribution of the support staff of the Department of Mechanical Engineering, especially those at the machine shop, for the help they provided.

I thank the Ontario Graduate Scholarship (OGS), the Natural Sciences and Engineering Research Council (NSERC) and the Mitacs program for their financial support.

I would finally like to thank my wife, Caroline, and my parents, Marc and Louise for their support, patience and love. Without all of you, I would not be where I am today, and as such, I am forever grateful.

This work is dedicated to my daughter Zoé,
I hope one day you will share my passion
for knowledge and science, and that
you may stand tall on my shoulders,
and see further than I could ever have imagined.

♪ But there’s no sense
crying over every mistake,
You just keep on trying
‘til you run out of cake,
And the science gets done,
And you make a neat gun
For the people who are
Still Alive ♪

TABLE OF CONTENTS

LIST OF FIGURES

LIST OF SYMBOLS

Nomenclature

Δ	Difference
ε	Effectiveness
η	Efficiency
η_{fan}	Fan efficiency
η_o	Overall fin efficiency
θ	Pyramid angle [°]
λ	Wavelength [m]
λ_r	Reduction in effectiveness
μ	Dynamic viscosity [Pa s]
ρ	Fluid density [kg/m^3]
τ	Relaxation time [s]
A	Area [m^2]
A_{flow}	Flow area [m^2]
A_k	Cross-section area for conduction [m^2]
B	Fin base length [m]
C	Proportionality constant
C_{min}	Minimal thermal capacitance [J/K]
C_p	Specific heat capacity [J/(kg·K)]
C_r	Thermal capacitance ratio
D	Fin diameter [m]
D_{10}	Size limit for 10% of particles
D_{50}	Size limit for 50% of particles
D_{90}	Size limit for 90% of particles
d_h	Hydraulic diameter [m]
e	Pumping power [kW]
f	Friction factor
FD	Fin density [fin per meter]
H	Fin Height [m]
h	Convective heat transfer coefficient [W/m^{2}K]
I	Turbulence intensity
I_1	Bessel function of first order
I_2	Bessel function of second order
J	Colburn factor
K	Turbulence kinetic energy [m^2/s^2]
k	Curve fitting coefficient for pressure drops
k_{fl}	Thermal conductivity of the fluid [W/m K]
k_m	Thermal conductivity of the fin material [W/m K]
L	Length [m]
L_{HX}	Heat exchanger length [m]
m	Fin heat transfer parameter [m^{-1}]
$\dot{m}$	Mass flow rate [kg/s]
N_f	Number of fins

NTU	Number of transfer units
Nu	Nusselt number
P	Pressure [Pa]
P_{flow}	Flow frontal perimeter [m]
Pr	Prandtl number
q	Heat transfer rate [W]
R	Thermal resistance [K/W]
Re_D	Reynolds number based on the feature diameter
Re_{Dh}	Reynolds number based on the hydraulic diameter
S	Fin spacing [m]
Stk	Stokes number
T	Temperature [K]
t	Fin top length [m]
U	Thermal conductance per unit area [W/m^{2}K]
u	Axial velocity [m/s]
$\bar{u}$	Mean axial velocity [m/s]
UA	Thermal conductance [W/K]
V	Volume [m^3]
$\dot{V}_f$	Volumetric flow rate [m^3/s]
W	Width [m]
x	Curve fitting exponent
y	Curve fitting exponent
y^+	Dimensionless wall distance

Subscripts

∞	Free stream conditions
b	Base area
bare	Bare plate
c	cold
cond	Conduction
conv	Convection
eq	Equivalent
f	Fin
fl	Fluid
H	Heat transfer
h	Hot
i	Inlet
lm	Log-mean
L	Length
M	Momentum transfer
max	Maximum
o	Outlet
p	Particle
t	Total
us	Unfinned surface
v	Volume
w	Wall

Superscripts

′	Root-mean-square
‘	Length derivative
“	Area derivative
·	Time derivative

CHAPTER 1 INTRODUCTION

1.1 Background

Significant social and economic pressures are being felt over the world to reduce the environmental impact and the global dependence on fossil fuels. While “green” and environment friendly approaches such as wind and solar power are gaining momentum, the higher cost associated with these alternative methods still deter most countries when it comes to power generation. Because of this, cleaner and more efficient ways to burn fuel are a main focus when it comes to hydrocarbon based power generation.

Distributed power generation offers a novel approach to reduce power losses, as electricity has to be carried over shorter distances to the end users, thus reducing losses in power lines. This method also has the advantage of protecting the grid against widespread electrical failure, as generators are substantially smaller than typical power plants and accordingly they individually serve a smaller population [1, 2]. For this purpose, compact and high efficiency power generation methods must be developed for distributed power generation to be successful. Micro-turbines are an example of a viable candidate for the development of a high efficiency distributed power generation system.

Micro-turbines are small scale, single stage and single shaft gas turbines generators. Commercial models currently available can produce from 25 kW to 250 kW and provide the combined advantages of low emissions, high reliability and decent efficiency in a compact generator [3]. A schematic diagram of a basic gas turbine generator is shown in the following figure.

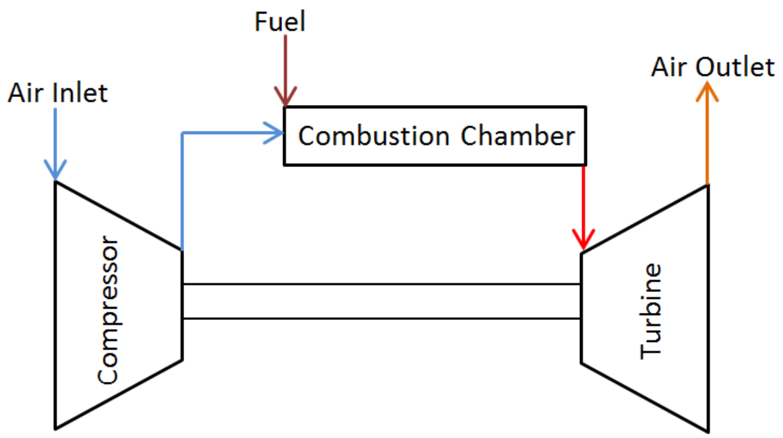

Figure 1: Simple, Open System Gas Turbine Diagram

The simplest micro-turbine designs often have thermal efficiencies below 20%, compared to diesel and gasoline engines which typically operate between 30-35% thermal efficiencies over the same power production range [4]. The real advantage of micro-turbines becomes obvious when a heat exchanger (also called a recuperator) is added to the system (see Figure 2). The waste energy from the exhaust gases of the turbine can be used to pre-heat the inlet gases before the combustion chamber, increasing the thermal efficiency of the system well over 50% [4]. This increase in performance can be understood by noting that less fuel needs to be burned to obtain the same combustion temperature, due to the re-use of the outlet gas' thermal energy. Furthermore, the waste heat could also be used for plant processes requiring heating, local hot water production or for air conditioning purposes. In this case, net efficiencies on the order of 80% are attainable by such systems, called combined heat and power systems [3].

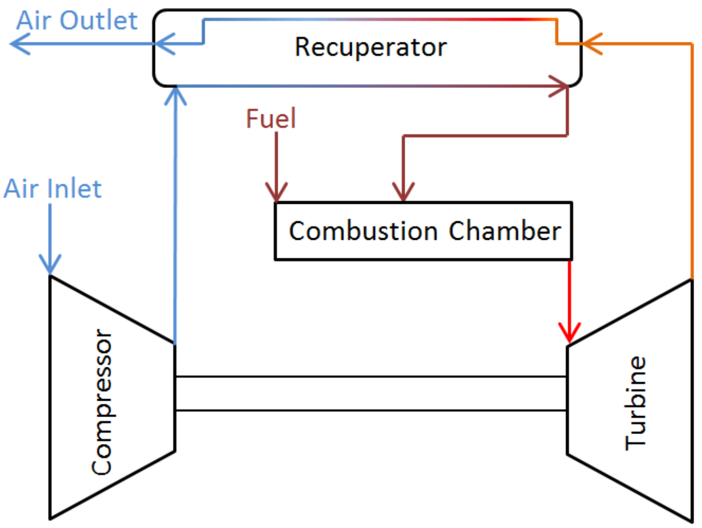

Figure 2: Single Shaft, Open System Recuperated Gas Turbine Diagram

Recuperators play a vital role to a successful micro-turbine design, and often represent from 20-25% of the cost and 20-35% of the volume of a micro-turbine package [4]. Typically, unit cost and volume are closely tied together, as material costs are one of the main contributors to the total package cost. Decreasing package volume could also reduce other operating costs, such as capital costs associated with land ownership or rental. Furthermore, increasing recuperator efficiency by 5 to 10% can improve the overall thermal efficiency of the gas turbine system by the same amount [4]. Currently, state-of-the-art recuperators operate from 75% to 85% efficiencies.

A new design of compact heat exchangers, referred to as a Wire Mesh Heat Exchanger (WMHE), was developed as a solution for common high efficiency compact heat exchanger problems. The concept of using a metallic wire mesh as a conductive material inside a cellular metal sandwich structure was first investigated in the late 1980s [5, 6]. The first configuration developed using this concept was the folded wire mesh geometry, shown in Figure 3. The folded wire mesh geometry is produced by successively folding wire mesh textiles and brazing thin sheets to these folds to create a pressure barrier. The disadvantage of this technique is that there is a limited quantity of heat that can be transferred to the brazed plate due to the small contact area per fold combined with the maximum number of times the wire mesh can be folded per unit length. This limitation, in addition to the large cost associated with this technique, calls for a production method which can reduce both cost and volume while maintaining high heat transfer properties.

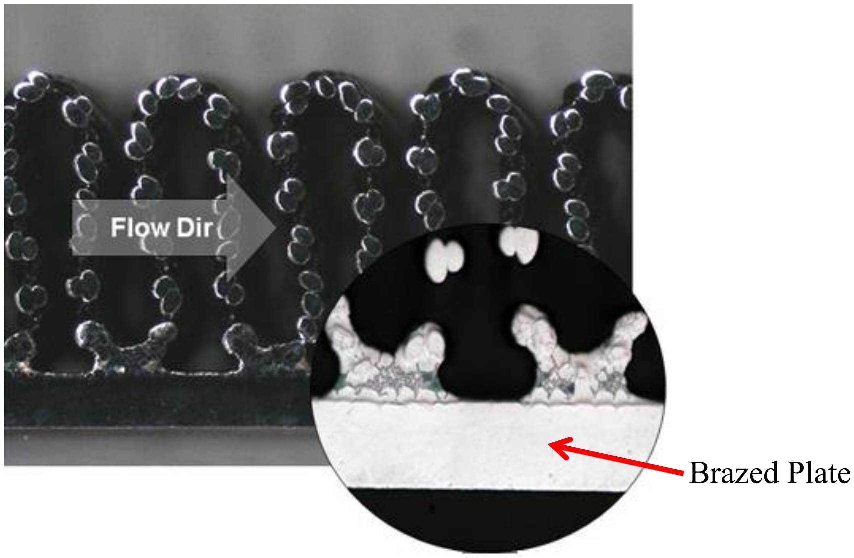

Figure 3: Folded Wire Mesh Heat Exchanger Configuration [7]

To this end, Brayton Energy Canada (BEC) has patented a new method for producing WMHE. The innovation in this approach is that instead of folding the wire mesh onto itself, sheets are stacked and then cut perpendicular to the stacking direction, yielding thin wafers of wire mesh textiles. These wafers are then sealed by brazing a metallic sheet to its external surfaces. Finally, fins are machined into this sheet to make the other heat transfer extended surface. These steps are illustrated in Figure 4. The heat exchange occurs between the fluid going through the mesh and the fluid flowing in the machined fin array.

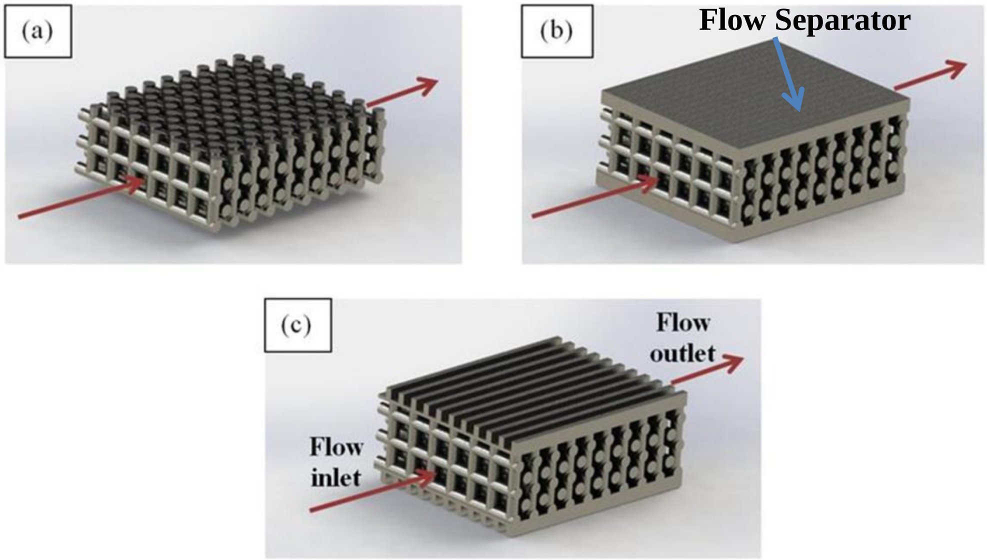

Figure 4: Successive Steps in the Production of BEC's WMHE Unit Cell

This process yields heat exchanger unit cells which can then be stacked, attached to manifolds and sealed to form full heat exchangers. The size and number of cells used in a full heat exchanger unit is tailored to the application specifications.

This new design for producing WMHE does offer some areas for improvement. Currently, the cost associated with brazing a metal sheet to the wire mesh is very high and labour intensive. To replace this process, research has been done where a thick and dense metallic coating is deposited using thermal or kinetic spray processes, as demonstrated in the work of Assad et al. [8], to replace the brazed sheet as a flow separator. Once this coating has been applied, fins are machined on the outer surface to produce fins with simple geometries as the second stage heat transfer enhancing extended surface. This process is limited to producing plain continuous rectangular fins which typically have a low heat transfer capacity, which is further reduced by problems such as axial conduction [9].

It is envisioned that using a mask to shield the substrate from cold spray deposition, one could produce near-net shape pin fin arrays with superior thermal and hydrodynamic performance. This solution could solve several of the issues presented previously regarding the performance of plain continuous rectangular fin arrays, namely by reducing axial conduction due to the interrupted nature of the pin fins, increasing the fin array's local convective heat transfer coefficient by increasing the amount of fluid mixing and reducing the production costs by the removal of the labour intensive and costly post-processing machining steps, as well as the brazing step.

1.2 Motivation of Research and General Objectives

This study was motivated by the possibility offered by Cold Gas Dynamic Spraying (CGDS or simply cold spray) to create near-net shape pin fin arrays. As detailed previously, pin fin arrays have the potential to increase the efficiency of heat exchangers, while reducing production costs due to the removal of post-processing steps. The production and optimization of pin fin arrays thus becomes a critical research priority to increase heat exchanger efficiencies. The focus of the proposed study would be the description and study of various parameters affecting the thermal and hydrodynamic performance of these fin arrays. This will allow design engineers to select the proper parameters to obtain maximal heat transfer efficiency depending on the application constraints on volume, pressure loss, production costs, etc. To achieve this objective, the following specific studies are mandated:

a) Determine the effect of varying the pyramid's base angle, the fin density and the fin height on the thermal and hydrodynamic performance of the fin array at intermediate Reynolds numbers (250 – 3000), relevant to the commercial applications.
b) Determine the effect of using different type of pin fin geometries and arrangements on the flow structures and the performance of the array, while demonstrating the superior performance of pins fins when compared to plain rectangular (continuous) fins.

c) Visualize the flow structures at varying Reynolds numbers to identify regions of increased fluid turbulence and to observe the recirculation structures believed to exist in the pin fin's wake.

d) Measure the different turbulence quantities in the regions of interest and correlate these metrics to the thermal and hydrodynamic performance of the fin arrays

1.3 Thesis Outline

The content of this thesis has been organized into nine chapters. The first chapter offers an introduction to the subject covered in this work, with the relevant background information presented. The motivation of research and the general objectives of this work are also briefly presented, along with a brief outline.

The second chapter provides a detailed review of the relevant literature pertinent to the research performed. This includes a thorough review of different heat exchangers types and geometries as well as describing the recent advances in the development of new fin geometries and investigations regarding the performance of fin arrays. Furthermore, the methods used for the assessment of the performance of heat exchangers are discussed. A brief overview of thermal and kinetic spray techniques as well as of additive manufacturing is presented. Finally, several methods of flow structure characterization are reviewed, with a section regarding the characterization of flow in fin arrays and around pyramidal structures.

The third chapter details the general and the specific objectives of the proposed thesis, namely the evaluation of the performance of pyramidal pin fin arrays and the characterization of the flow structures encountered in this type of fin array.

The fourth chapter details the experimental equipment and procedures used to achieve the aforementioned objectives. The masked CGDS technique used to produce the pyramidal fins is described, as well as the equipment used to evaluate the geometry of these arrays. Furthermore, a description of the thermal and hydrodynamic performance test apparatus is made. Finally, the flow visualization technique and the equipment employed for this type of research is described.

The fifth, sixth, seventh and eighth chapters detailed the results obtained as a fruit of this endeavour. The results are presented as five separate peer-reviewed papers, with each article addressing a part of the specific objectives detailed in chapter three. A brief introduction for each paper describes the work contained therein.

Finally, chapter nine summarizes the major conclusions and contributions of this work, as well as presenting the author’s suggestions for future work regarding the topic of pin fin production using cold spray as an additive manufacturing technique.

CHAPTER 2 REVIEW OF RELEVANT LITERATURE

In this chapter, a review of the relevant work done in fields related to the topics covered in this thesis is completed. The first segment of this chapter is dedicated to the basic function and types of heat exchangers, as well as covering the features that make BEC's WMHE design unique. The problems and opportunities that arise from these differences are also discussed. The second section of this literature review focuses on the recent advances in the characterization of various geometries of fin arrays. The following section will detail the theoretical work that has been published with regards to the performance of compact heat exchangers and fin arrays, namely the heat transfer and hydrodynamic properties of these features. The fourth part of this chapter consists of a review of the basic principles behind thermal and kinetic spray processes, with a focus on the cold spray process since it is the production method employed for the samples used in this study, followed by a brief introduction to additive manufacturing. Finally, several flow visualization techniques will be discussed.

2.1 Heat Exchangers

2.1.1 Types of Configuration

Heat exchangers come in a variety of shapes, sizes and configurations. There are three main types of configurations, sorted in order of increasing effectiveness: parallel flow, cross-flow and counter-flow. For heat exchangers, regardless of their configuration, the effectiveness (ε) is defined as the ratio of energy transferred to the maximal amount of energy that can be transferred between the two working fluids, which is represented schematically in Figure 5. An effectiveness computed to a value of one implies that there is no thermal resistance between the two fluids and that perfect heat transfer is achieved between them.

$$\varepsilon = \frac{q}{q_{max}} = \frac{(T_i - T_o)_{\max h,c}}{(T_{h,i} - T_{c,i})} \qquad \text{(Eq 1)}$$

In Eq 1, $(T_i - T_o)_{max\ h,c}$ represents the maximal value of temperature difference either within the hot side or within the cold side while $(T_{h,i} - T_{c,i})$ represents the temperature difference between the inlet of the hot fluid and inlet of the cold fluid, respectively. This definition can be used regardless of the heat exchanger configuration.

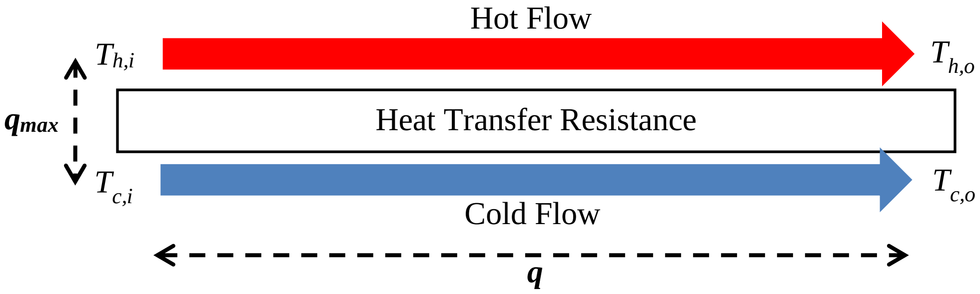

Figure 5: Efficiency Definition for Two Fluid Flow Heat Exchanger

Parallel flow heat exchangers allow the highest temperature gradient between the hot and cold fluids at the inlet but suffer from a lower efficiency than the other heat exchanger configurations. This limit is due to the small temperature difference maintained after the second half of the heat exchanger's length, as it can be seen in Figure 6. Another limitation arises from the fact that the maximal temperature attained by the cold fluid for an infinite length heat exchanger is the exit temperature of the hot fluid.

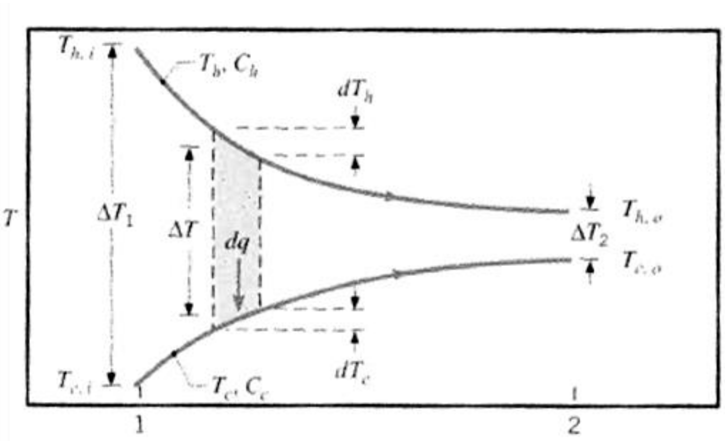

Figure 6: Temperature Distribution as a Function of Position for a Parallel Flow Heat Exchanger [10]

The counter-flow heat exchanger does not suffer from the same drawbacks as the parallel flow heat exchanger. This configuration can reach the highest efficiencies of all three configurations when optimally designed [10]. One of its main advantages is that the cold fluid outlet temperature may surpass the hot fluid's outlet temperature. The thermal gradient for this configuration is less steep than for the other configurations, but it is almost constant along the heat exchanger's length, as shown in Figure 7.

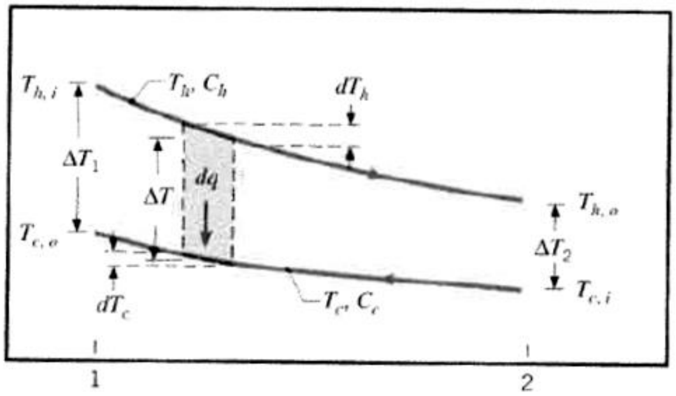

Figure 7: Temperature Distribution as a Function of Position for a Counter-Flow Heat Exchanger [10]

The third type of heat exchanger is the cross-flow heat exchanger. The term cross-flow comes from the fact that the two fluids flow perpendicularly to each other. This configuration is very common in heat exchangers with cellular designs because its effectiveness is typically higher than a parallel flow heat exchanger while maintaining a smaller envelope and a less complex manifold design than the counter-flow configuration.

Depending on the heat exchanger's configuration, different relations are used to determine the effectiveness (ε) as a function of the number of transfer units (*NTU*) and the fluids' thermal capacity ratio (C_r, defined as the smaller thermal capacitance of the two fluid, divided by the larger thermal capacitance of the two fluids). The results of analytical work are shown in the following table, adapted from "Fundamentals of Heat and Mass Transfer" [10]. The equations in this table demonstrate that regardless of the pair of *NTU* and C_r chosen, the counter-flow configuration will always have the highest effectiveness, as shown in Figure 8. More details regarding the calculation of the number of transfer units and of their significance in quantifying heat transfer are provided in chapter 2.3.1.

Table 1: Effectiveness Relation with NTU and C_r for Various Heat Exchanger Configurations

Configuration	**Equation**	**Equation number**
Parallel flow	$\varepsilon = \dfrac{1 - \exp[-NTU \cdot (1 + C_r)]}{1 + C_r}$	(Eq 2)
Single Pass Cross-Flow, Fluids Unmixed	$\varepsilon = 1 - \exp\left[\dfrac{1}{C_r} \cdot NTU^{0.22} \cdot \{exp[-C_r \cdot NTU^{0.78}] - 1\}\right]$	(Eq 3)
Counter-Flow	$\varepsilon = \dfrac{1 - \exp[-NTU \cdot (1 + C_r)]}{1 - C_r \cdot \exp[-NTU \cdot (1 + C_r)]}$	(Eq 4)

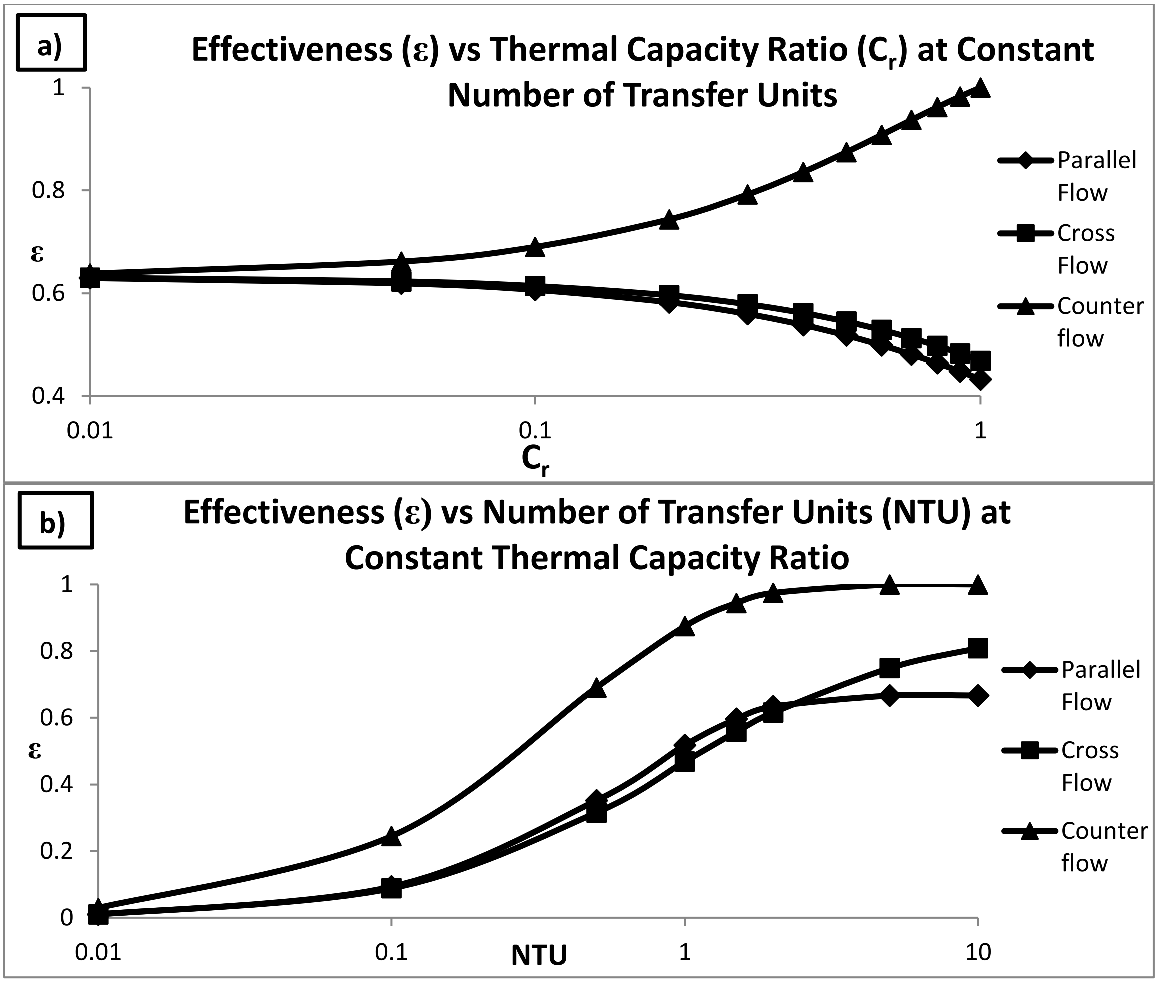

Figure 8: Effectiveness as Functions of (a) the Thermal Capacity Ratio; (b) of the Number of Transfer Units

2.1.2 State-of-the-Art Heat Exchangers

Shell and tube heat exchangers are some of the most common geometries used in industrial applications due to their low complexity [9]. Figure 9 shows a typical configuration for a shell and tube heat exchanger. In this counter-flow design, a fluid flows through the shell side without mixing with the fluid that flows in the tubes. Heat is transferred from the shell-side fluid to the tube-side fluid or vice-versa through convection to the tube walls. To increase the amount of heat transferred, baffles are installed on the shell side to increase the amount of turbulence and the dwell time of the fluid, while minimizing the amount of low flow volume sections. The turbulence in turn increases the convective heat transfer of the shell-side fluid to the tube walls. Typically, there is no heat transfer enhancing features on the inside of the tubes, limiting the efficiency of this process. The efficiency of such exchangers is proportional to the length of the exchanger, meaning that very large heat exchangers must be used to attain high efficiencies [11]. Furthermore, axial conduction along the length of the tubes can reduce the efficiency of these heat exchangers by 5 to 10% [9].

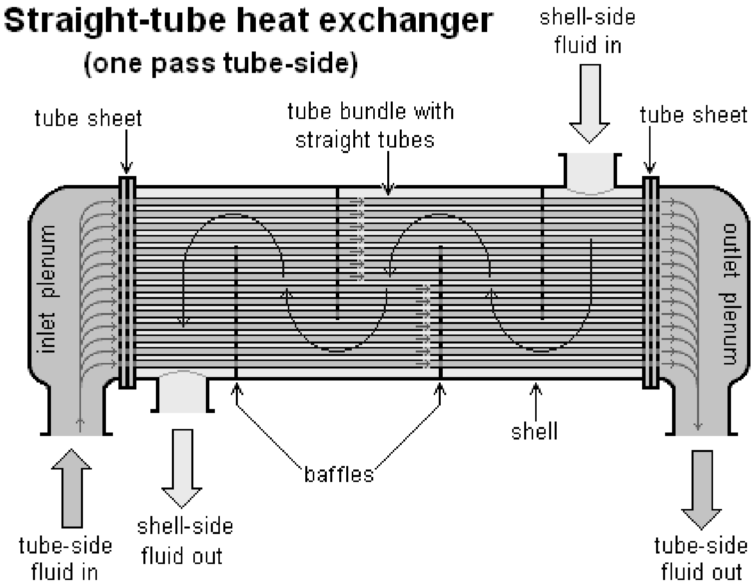

Figure 9: Typical Shell and Tube Heat Exchanger Diagram (Modified from [7])

Other types of heat exchangers remedy this limitation with the use of heat transfer enhancing media for both the hot and cold fluid sides of the heat exchanger. Examples of these would be packed bed geometries or stacked plate heat exchangers (Figure 10 (a) and (b)). Both types of heat exchangers share a similar design, where stages of heat transfer enhancing media are sandwiched between parting plates to form cells, which are then stacked and joined to form heat exchanger units (Figure 10 (c)). The structure is maintained together usually either by sintering, brazing or welding [12]. The main advantage of this type of design is the very high efficiency levels that can be attained by these geometries [12]. Using convection enhancing features on both sides of the heat exchanger allows heat transfer efficiencies of up to 85% to be reached [12]. The main problems with this type of design are that the joints are prone to failure, which can cause fluid leakage, as well as the significant manufacturing costs associated to the brazing or welding operations. Furthermore, a significant efficiency loss is encountered when using this type of fins and is attributed to axial conduction due to the continuous nature of the heat transfer enhancing features [12].

An innovative design of compact heat exchangers using wire mesh as the heat transfer extended surface was developed as a solution for common high efficiency compact heat exchanger problems. This type of heat exchanger is commonly referred to as Wire Mesh Heat Exchangers (WMHE). The concept of using a metallic wire mesh as a conductive material inside a cellular metal sandwich structure was first patented in 1989 [5, 6].

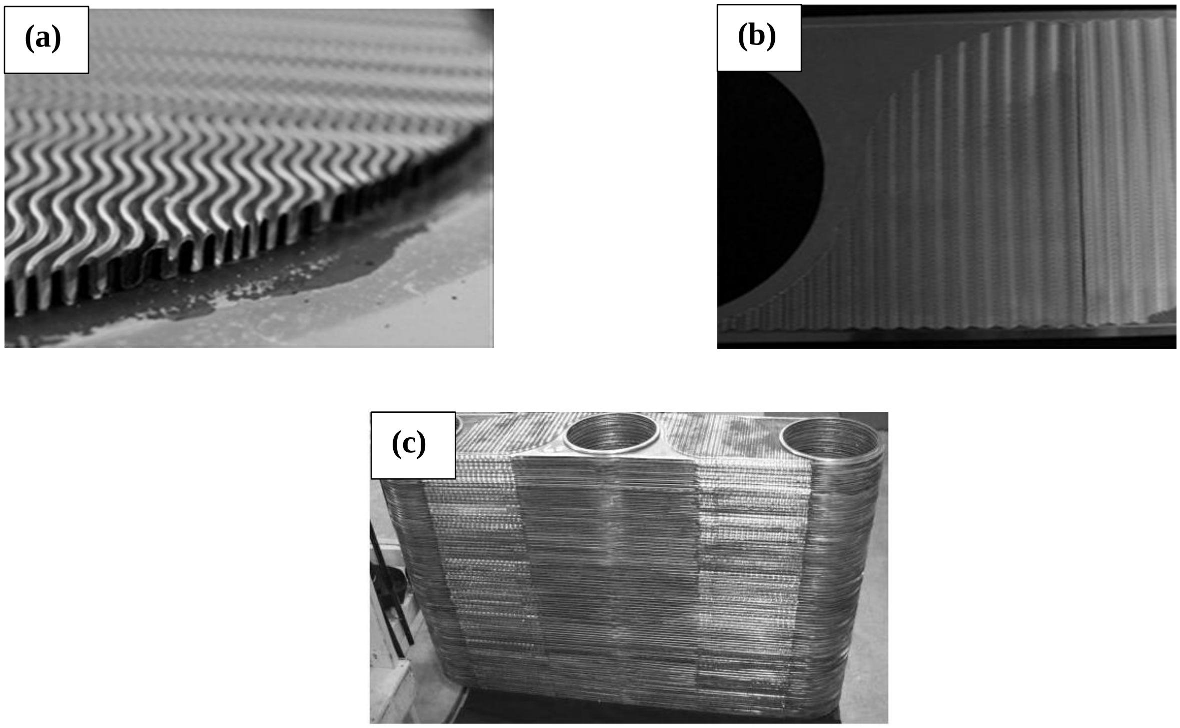

Figure 10: (a) Packed Bed Core; (b) Stacked Plate Core; (c) Heat Exchanger Casing [7]

The first configuration developed using this structure was the folded WMHE, shown in Figure 11. The folded wire mesh geometry is produced by folding wire mesh textiles on themselves and brazing metallic sheets to the tips of the folds to create a parting plate which prevents the hot and the cold fluid from mixing. The disadvantage of this technique lies with the fact that only a limited quantity heat transfer area between the mesh textile and the brazed plate can be created due to the small contact area per fold combined with the maximum number of times the wire mesh can be folded per unit length. This limitation, in addition to the large cost associated with brazing, makes this type of heat exchanger uncommon in industrial applications.

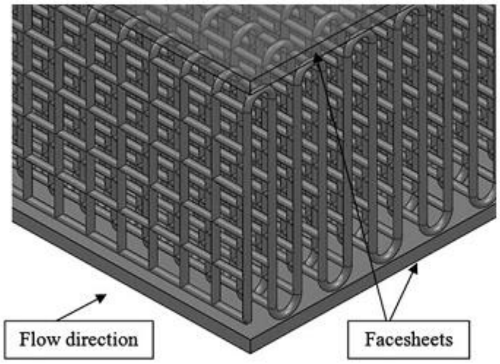

Figure 11: WMHE with folded wire screen and brazed metallic sheets [8]

Other interesting and promising types of heat exchangers were developed using a similar principle as WMHE but with different types of internal heat transfer medium, such as metal foam heat exchangers encased in a metallic skin deposited using wire-arc or plasma spray, as investigated by Salimi Jazi et al. and Azarmi et al. [13, 14]. In this case, thermal spray processes are used to seal commercially available nickel foam bricks with Inconel 625 to create fully enclosed heat exchangers. No heat transfer enhancing features are used on the outer surface of the heat exchangers.

2.1.3 BEC’s WMHE Design

The design brought forward by BEC consists of unit cells stacked in parallel with each other to form a heat exchanger core. Two manifolds deliver the hot and cold fluids to the entrance of the unit cells, while two more manifolds handle the discharge of hot and cold fluids to the unit cells, respectively. A cell has two extended surfaces types to increase the amount of heat transferred. The finned surface is called external side, while the wire mesh surface is usually called internal side, due to its appearance when looking at a single unit cell (see Figure 12). The two extended surfaces are separated by a parting plate, which ensures that the hot and cold fluids cannot come into contact or mix with each other. The inlet and outlet manifold configuration creates a heat exchanger in a counter flow configuration.

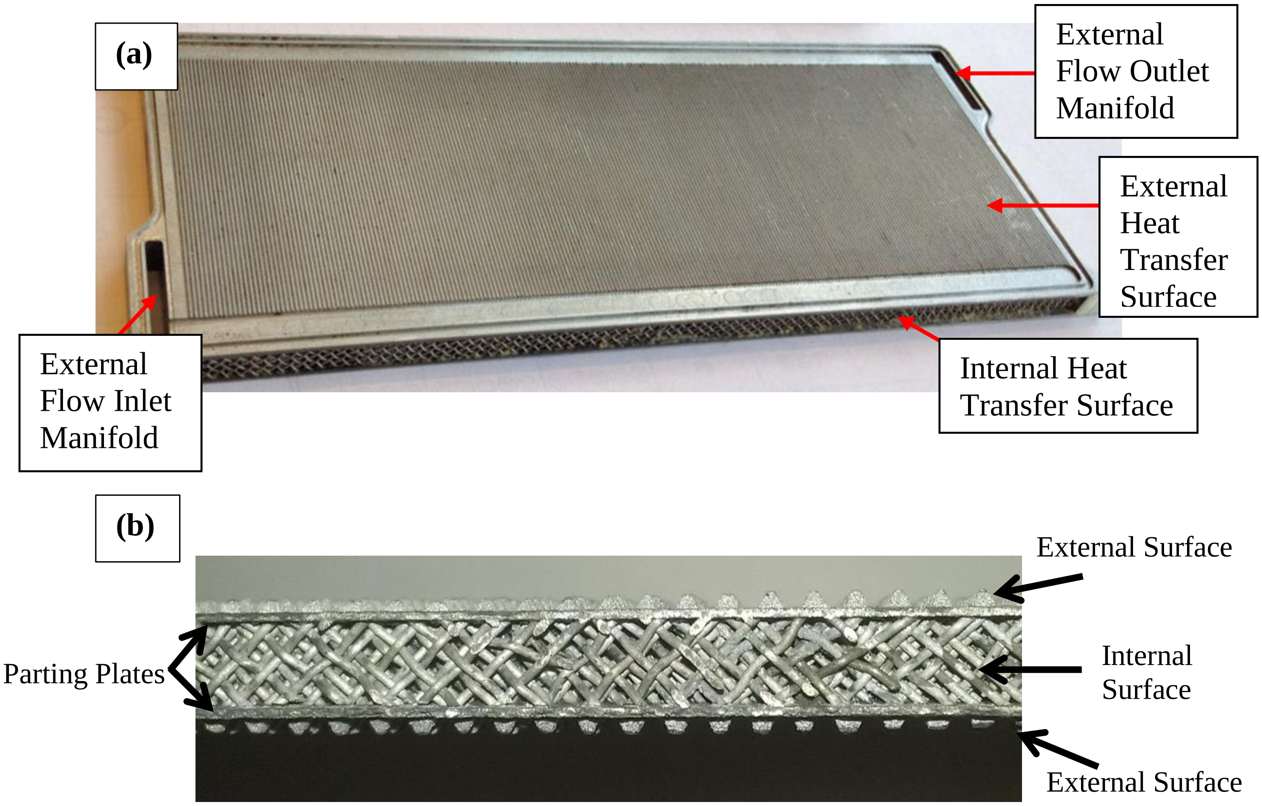

Figure 12: BEC's WMHE Designs: (a) Plate Fin Internal Surface; (b) Pin Fin External Surface

These cells are then stacked and sealed to form heat exchanger units. The size and amount of cells used in a heat exchanger unit is tailored to the application specifications.

2.2 Advances in the Study of Fin Arrays

The first authors to publish an extensive study on the use of fin extended surfaces in compact heat exchangers were Kays and London, in a study which described and characterized over 100 types and configurations of extended surface for use in compact heat exchangers [9]. This landmark publication is now considered a basis to the study of compact heat exchangers and contains design data and correlation curves for the thermal and hydrodynamic performance of many types of plate fin and pin fin arrays. In their work, Kays and London also developed the ε–NTU method and the first method for quantifying the gains of using finned surfaces by computing the j-factor (a complex non-dimensional number used to measure the heat transfer efficiency, calculated by dividing the Nusselt number by the Reynolds number and the cubic root of the Prandtl number) on a volumetric basis to obtain a volume goodness factor.

Pin fin research was spearheaded by Žukauskas when he published his work on the heat transfer and hydrodynamic properties of banks of tubes [15]. His study of banks of tubes, which is analogous to circular cross-section pin fin arrays, yielded what is now the basis of the explanation of the mechanism behind the performance gain of pin fins when compared to plain rectangular continuous fins. Indeed, Žukauskas proposed that the flow structures of a fluid flowing in a bank of tubes could be separated in three regimes. A laminar regime can be identified from very low Reynolds numbers (with the tube diameter used as the characteristic length: Re_D) to approximately 1000, where the flow is dominantly laminar and attached to the tube surface, with large scale recirculation regions behind the heat transfer features. The sub-critical regime starts at $Re_D = 500$ and extend to $Re_D = 200\ 000$, with the flow structure being largely laminar but becoming increasingly turbulent, especially in the fin's wake due to flow detachment from the fin surface. A small overlap between the regimes is found between Reynolds numbers of 500 and 1000, where the flow is in a transitional state. The exact point of this transition depends on the tube array geometry. The critical regime would extend from $Re_D = 200\ 000$ until the limits of the studied Reynolds numbers and would be characterized by a completely turbulent flow.

Many other researchers have devoted time and resources comparing different fin geometries and cross-sections in order to determine which type of fin is the most efficient and also to quantify this gain in efficiency [16-31]. One approach was to use simulation to determine the properties both of plate fin and pin fin heat exchangers [16, 17]. Comparisons were made using different efficiency criterions which lead to the same conclusion that pin fins have a better overall heat transfer surface efficiency when compared to plain rectangular continuous fins. The flow structures were also extensively studied numerically to understand the mechanism of this gain, which is attributed to the increased turbulence and the periodic disruption of the boundary layer caused by the discontinuous features of pin fin arrays. Experimental validation of the numerical comparisons between the various pin fin geometries such as square, circular, ellipsoid and drop shaped, for example, was also performed more recently by Yang et al. [18]. Due to their increased performance, pin fins have replaced traditional continuous fin shapes such as rectangular or wavy fins in critical applications due to their higher heat transfer rate [9, 10]. The increased heat transfer attained by pin fins is often partially offset by higher pressure losses through the fin array, but yields a better overall performance than their continuous counterparts [15, 16, 18-20]. Sahiti et al. [16, 19, 20] have demonstrated that pin fins offer the best performance for a given pumping power and heat exchanger volume compared to other fin array configurations.

Various pin fin array parameters have been investigated over the past thirty years. The relative height parameter (H/D, where H is the fin height and D is the pin fin diameter) of circular pin fins was one of the first parameters to be detailed by Brigham and Van Fossen [21, 22]. Their study revealed that for cylindrical staggered fins, longer pin fins (H/D > 4) tend to transfer more heat than shorter ones. Sparrow et al. [23, 24] and Metzger et al. [25] have also extensively studied the heat transfer characteristics of cylindrical pin fins in the inline and staggered configurations. A major conclusion from these studies is that the pin fin surface convective heat transfer coefficient was approximately 100% larger than that of the end wall. Different pin fin geometries have been investigated by Li et al. and Chen et al. [26, 27]. It was determined that the heat transfer of drop shaped and ellipse shaped pin fins is increased when comparing to similar circular cross-section pin fins. Furthermore, both types of fins also present less pressure loss than their circular counterparts. Although their performance is superior, this ellipse and drop shaped fin geometries are rarely used due to the increased production costs. Grannis and Sparrow [28] have developed correlations for the friction factor of fluid flow through diamond shaped pin fin arrays. Square base pin fins have also received some attention by You and Chang [29], who used numerical simulations to study the performance of inline square base pin fins in a rectangular channel and have provided correlations for the Nusselt number this type of geometry at different fin densities. Șara [30] has also studied several geometric parameters of staggered rectangular base pin fins such as fin spacing and shroud clearance and provided correlations for these parameters. Jeng and Tzeng [31] have also experimentally confirmed correlations found in the literature regarding the inter-fin pitches of square pin fins in both inline and staggered configurations. It was found that the performance of some configurations of square base pin fins can exceed that of similar size cylindrical cross-section pin fins under the same flow conditions.

2.3 Heat Transfer Performance Characterization

When it comes to compact heat exchangers, several factors are considered to be important, such as the heat transfer and hydrodynamic properties, as well as its cost and envelope volume. The heat transfer and hydrodynamic properties of heat exchangers were extensively researched, with results of the relevant works summarized in this chapter. For this purpose, heat transfer relations for the prediction of heat exchanger efficiency will be discussed first, followed by the equations used to calculate the efficiency decrement caused by axial conduction. Afterwards, the equations describing the thermal performance of fins and their pressure loss will be detailed. Finally, the different efficiency indices proposed in the literature will be discussed.

2.3.1 Heat Exchanger Properties with the ϵ-NTU Method

Several methods can be used to determine the performance of a heat exchanger, such as the ϵ-NTU method, the finite difference method and the log-mean temperature difference approach. The log-mean temperature difference approach is the simplest of the three methods, but consequently its applications are much more constrained by the simplifying hypotheses used. The log-mean temperature difference method requires that the inlet and outlet temperatures of both fluids be known prior to the analysis. The finite difference method is the approach that yields results closest to reality, but this accuracy comes at the price of increased computational power requirements. This method also becomes much more complex when estimating losses due to axial conduction is a concern. A two-dimensional model must be constructed, which again greatly increases the computational requirements. The alternative is the ϵ-NTU method which yields moderately accurate results with a simpler calculation procedure. It has the advantages of being relatively simple to model, while requiring a modest quantity of calculations to be performed. Another advantage is that simple approximations for the axial conduction losses can be used, and a finite element method can be applied in conjunction to this approach to increase the accuracy of this method. Additionally, for certain configurations of heat exchangers, not enough data is known on the fluid inlet and outlet conditions to use the log mean temperature difference approach. The ϵ-NTU method is less constrained in this way, as an iterative process can be used to circumvent this difficulty. By first guessing the efficiency and performing the calculations to obtain a new efficiency, one can use the result of the calculations as the next guess, until the results converge.

The ϵ-NTU method is based on the idea that, for any heat exchanger, the heat exchanger effectiveness ϵ is solely a function of NTU, C_r and the heat exchanger's configuration where C_r is the ratio of heat capacity rates of the two fluids and NTU is the number of transfer units. As previously stated, the equation linking the effectiveness of a counter-flow heat exchanger and the number of transfer units is:

$$\varepsilon = \frac{1 - \exp[-NTU \cdot (1 + C_r)]}{1 - C_r \cdot \exp[-NTU \cdot (1 + C_r)]} \qquad \text{(Eq 5)}$$

The number of transfer units can be found from the following equation:

$$NTU = \frac{UA}{C_{min}} \qquad \text{(Eq 6)}$$

where U is the thermal conductance term of the heat exchanger, A is the associated heat transfer area and C_{min} is the minimal value for the heat capacity of the fluids. To illustrate the two fluid heat exchanger's function and determine the thermal conductance, a thermal circuit diagram such as the one in Figure 13 is built.

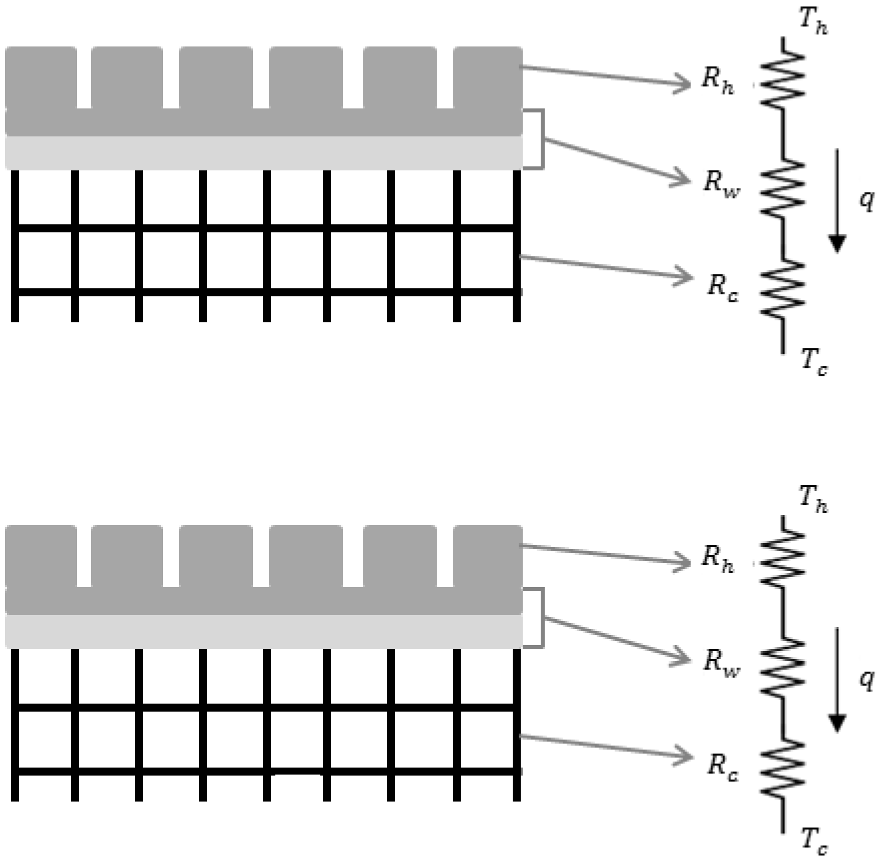

Figure 13: Thermal Circuit Diagram for a Two Fluid Heat Exchanger Unit Cell

As shown in the previous figure, to diminish the temperature potential T_h -T_c, a heat flux per unit area q'' flows from T_h to T_c by the way of the finned outer extended surface and the meshed internal extended surface, represented here by the thermal resistances R_h and R_c, and the plate that separates both, R_w. With this diagram, one can construct the basic heat transfer equations for this case:

$$q = UA \cdot (T_h - T_c) \qquad \text{(Eq 7)}$$

With the parameter *UA* calculated with the following relation:

$$UA = (R_h + R_w + R_c)^{-1} \qquad \text{(Eq 8)}$$

The thermal resistance to convective heat transfer (in this case R_h and R_c) can easily be calculated knowing the convective heat transfer coefficient:

$$R_{conv} = \frac{1}{\eta_o \cdot h \cdot A} \qquad \text{(Eq 9)}$$

where h is the convective heat transfer coefficient, η_o is the efficiency of the heat transfer surface and A is the associated heat transfer surface area. In the same manner, the conductive resistance (R_w) term can be calculated with the following relation:

$$R_{cond} = \frac{L}{k_m \cdot A} \qquad \text{(Eq 10)}$$

where L is the length of the conduction path, k_m is the conductivity of the material and A is the cross-sectional area associated with this resistance. Substituting equations 9 and 10 into equation 8 yields:

$$UA = \left[\left(\frac{1}{\eta_o \cdot h \cdot A}\right)_h + \left(\frac{L}{k \cdot A}\right)_w + \left(\frac{1}{\eta_o \cdot h \cdot A}\right)_c\right]^{-1} \qquad \text{(Eq 11)}$$

The heat transfer area, extended surface efficiency and conductive length are all solely functions of the heat exchanger's geometry, while the thermal conductivity is a material property. These properties can be evaluated if the heat exchanger's design properties are known. The convective coefficient, however, is dictated by the fluid mechanics of the heat transfer extended surfaces. Finding the convective coefficient for a metallic mesh extended surface is a fairly complex analytical procedure that will not be covered in this work, but the author refers to work done by A. Corbeil [3] for further reading, details and derivations of the final formulas. Conversely, the convective coefficient for a fin array is usually found experimentally or numerically and is usually given in a non-dimensional form such as a function of Nusselt number, which itself is a function of Reynolds number. When the convective coefficient is determined, U can be calculated and a NTU value can be obtained.

It is now evident that to increase a heat exchanger's effectiveness, one must strive to increase the number of transfer units. To this end, the thermal conductance UA must be increased as much as possible, which can be achieved in one of three ways for the convective heat transfer contribution: by increasing the amount of available heat transfer area, by increasing the fin array efficiency or by increasing the convective coefficient through disruption of the fluid's boundary layers such as creating recirculation zones and turbulences in the flow. The determination and augmentation of this convective coefficient for the pin fin side of this equation is the focus of this work and will lead to the increase of the total performance of the heat exchanger.

2.3.2 Finned Surface Heat Transfer Performance

Fins arrays are used to increase convective heat transfer between a surface and a fluid. Since building these fins require an additional effort, assessing the performance of the fin array versus an unfinned surface helps determine the gain that could be obtained from building such an array.

Studying a typical fin array's thermal resistance circuit delivers insight on how its performance is calculated. The following figure shows this diagram, and the simplified model proposed by Incropera [10].

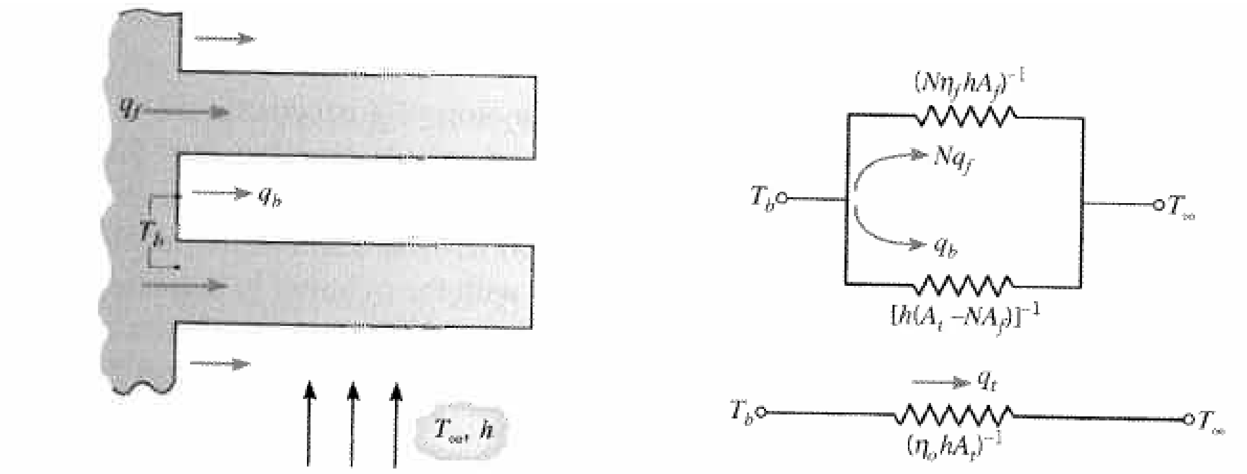

Figure 14: Thermal Resistance Diagram [10]

This simplified resistance model accounts for the different convection paths, as well as the fin efficiency parameter and allows the creation of a relation between the finned surface's efficiency and its thermal resistance. The associated thermal resistance, in turn, is indicative of the fin array's performance. The thermal resistance can be calculated using the following equation:

$$R_f = \frac{1}{\eta_o \cdot h \cdot A_t} \qquad \text{(Eq 12)}$$

In this equation, the parameter A_t designates the total finned and unfinned surface of the heat transfer surface, while the η_o parameter represents the total surface's efficiency and h represents the convective coefficient.

To assess a finned surface's properties against another surface, one only has to compare their thermal resistance values. A lower thermal resistance value indicates a surface will transfer more heat per unit area and is preferable when dealing with fins. Ideally, a negligible thermal resistance is optimal, but this rarely can be obtained. Finally, knowing the thermal resistance of the finned surface allows one to compute the heat flux associated with a temperature difference between the fluid and the base of the finned surface.

The convective coefficient can also be obtained using empirical relations relating the Nusselt number (*Nu*) and the Reynolds number. To determine the convective coefficient for a given Nusselt number, the following equation is used:

$$h = \frac{Nu \cdot k_{fl}}{d_h} \qquad \text{(Eq 13)}$$

where k_{fl} is the fluid's thermal conductivity and d_h is the hydraulic diameter of the flow passage. The Nusselt number is usually given in an equation of the form [10]:

$$Nu = C \cdot Re^{x} \cdot Pr^{y} \qquad \text{(Eq 14)}$$

where C is a proportionality constant, while x and y are curve fitting exponents.

2.3.3 Axial Conduction in a Heat Exchanger

Axial conduction is the result of a temperature gradient existing in the longitudinal direction of the wall or continuous fin of the heat exchanger from the hot section towards the cold section. This negatively affects the performance of the heat exchanger because it diminishes the temperature difference between the two flows, effectively reducing the heat transfer potential. This effect is magnified when the resistance to conduction is low along the wall length, as it is the case for plain rectangular fins. A schematic diagram of this effect is presented in Figure 15.

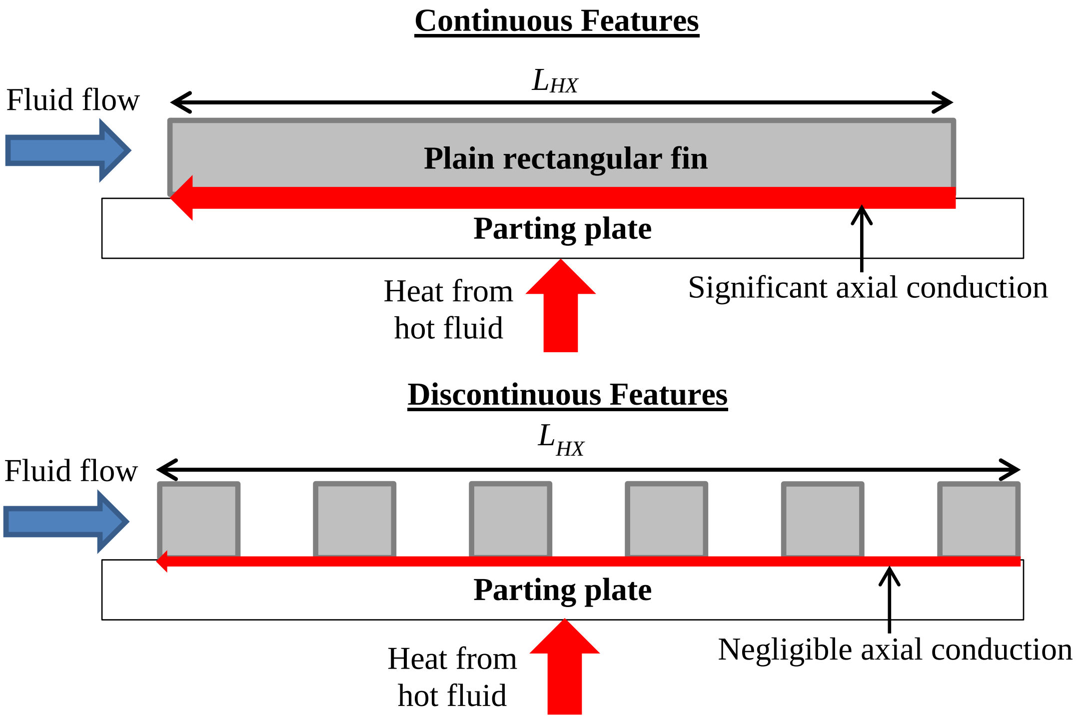

Figure 15: Schematic Diagram of Axial Conduction for Continuous and Discontinuous Features

Kays and London suggest approximating the relative reduction of effectiveness (λ) of continuous features with the following equation [9]:

$$\frac{\delta\varepsilon}{\varepsilon} \approx \lambda_r = \frac{k_m \cdot A_k}{L_{HX} \cdot C_{min}} \qquad \text{(Eq 15)}$$

where $\delta\varepsilon$ is the differential loss of effectiveness, ε is the actual effectiveness of the heat exchanger, k_m is the thermal conductivity of the fin material, A_k is the cross-sectional area of the heat transfer extended surfaces, L_{HX} is the length of the heat transfer enhancing features and C_{min} is the lowest thermal capacitance between the two working fluids. This equation demonstrates that for compact heat exchangers using plain rectangular fins or similar continuous features, axial conduction is a significant problem, more so than in shell and tube exchangers, for example. Indeed, the ratio of conduction area (A_k) to the heat exchanger length (L_{HX}) is much larger for compact heat exchangers than for traditional heat exchangers, due to the fact that the design objective for compact heat exchangers is to increase the conduction area as much as possible while minimizing the length of the heat exchanger as much as possible.

Discontinuous fins do not have this disadvantage, however, due to the fact that there is a negligible temperature gradient between the leading and trailing edges of one fin due to the short length of the fins in the streamwise direction. This decrement in efficiency can also be encountered due to the thermal gradient that exists in the parting plate used to separate the hot and the cold fluid.

2.3.4 Pressure Losses in Heat Exchangers

The pressure losses most commonly encountered in a heat exchanger can be categorized under three different types: constriction pressure losses, heat transfer medium pressure losses and expansion pressure gains. This is illustrated in Figure 16 for a plate fin heat exchanger. The change in pressure between 1 and 2 are named inlet pressure losses (ΔP_i), which are due to the flow constrictions when entering the heat transfer medium (in this case a plate fin array). This is followed by a linear decrease in pressure with distance ΔP_f between points 2 and 3 which is attributable to the skin friction which viscously dissipates the flow's energy in the boundary layers attached to the fin walls. Finally, a pressure gain due to the flow expansion between points 3-4 are expressed as the outlet pressure gain (*ΔP_o*). The inlet and outlet pressure changes are not the focus of this work, as proper designs for headers minimize the negative effects of these changes in pressure.

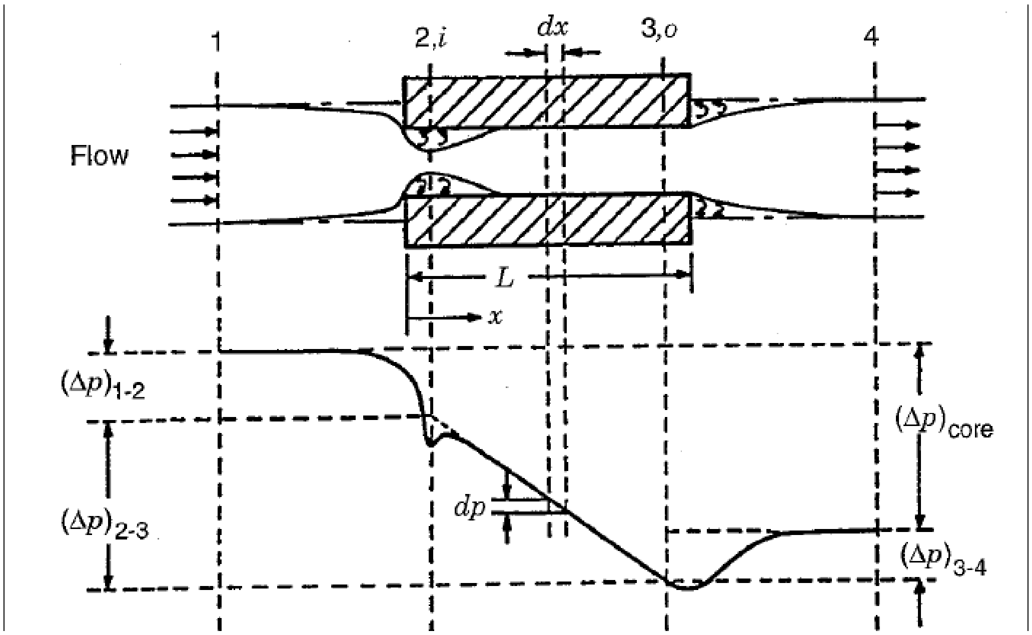

Figure 16: Pressure Losses in a Heat Exchanger [3]

The pressure loss encountered in a fluid flowing through a longitudinally continuous surface such as plain rectangular fins is calculated using the Darcy friction factor (*f*) definition [9]:

$$\Delta P_f = f \cdot \frac{L_{HX}}{d_h} \cdot \frac{\rho \bar{u}^2}{2} \qquad \text{(Eq 16)}$$

where ρ is the fluid's density and $\bar{u}$ is the mean stream velocity. This relation is slightly modified to accommodate non-continuous surfaces, such as pin fin arrays [9]:

$$\Delta P_f = f \cdot L_{HX} \cdot FD_L \cdot \frac{\rho \bar{u}^2}{2} \qquad \text{(Eq 17)}$$

The parameter $\frac{L_{HX}}{d_h}$ is replaced by $L_{HX} \cdot FD_L$, which is equal to the number of fin columns the flow has to cross from the entrance of the heat transfer surface to its exit.

For this type of heat exchangers, the contraction and expansion of the flow at the entrance and exit of the fin array can be calculated with:

$$\Delta P_{i,o} = k \cdot \frac{\rho \bar{u}^2}{2} \tag{Eq 18}$$

The k factor is determined experimentally for different contraction and expansion cases, but can vary from fractions to hundreds, depending on the severity of flow impediment.

For most cases of experimental work, the term ΔP is usually measured using pressure transducers and is usually not computed.

2.3.5 Efficiency Index

As demonstrated previously, the assessment of the performance of a heat exchanger is a tedious task. Comparing the performance of different types and geometries of heat exchangers, however, becomes even more difficult due to the range of different criteria used to determine this. To ensure the most efficient surface is used in a given application, one must select a performance criterion which adequately describes both the thermal and hydrodynamic performance of the heat exchanger. For this purpose, several authors have proposed efficiency indices or performance evaluation criteria for the determination of efficiency.

One of the first methods proposed for assessing and comparing the performance of heat exchangers was proposed by Colburn [32]. His approach was to directly compare the Colburn *J*-factor for heat transfer to the Colburn *J*-factor for fluid friction in the following manner:

$$\frac{J_H}{J_M} = \frac{\frac{Nu}{Re\,Pr^{1/3}}}{\frac{f}{2}} \qquad \text{(Eq 19)}$$

Plotting this factor as a function of the Reynolds number or the flow rate would yield curves that could be compared to one another. Picking the curve with the highest j-factor ratio at a given flow rate would allow one to select the most efficient surface under the testing conditions. This comparison would represent the heat exchanger with the least required frontal area for a given heat transfer and pressure loss and is considered an area goodness factor. Colburn's approach was modified by London and Ferguson [33] to make this criterion a volume goodness factor, which instead selects the heat exchanger that takes up the least amount of volume for a given heat transfer and pressure loss. This was achieved by plotting the convective coefficient (h) of the extended surface as a function of the required pump power (e), normalized by the heat exchanger's entire wetted area, from the heat exchanger's J_H and J_M factors. This method was more appropriate to the comparison of compact heat exchangers as the volume was taken into account instead of the exchanger's frontal area, but tended to overestimate the gains of using a heat exchanger with a higher *h/e* curve [16].

Several efficiency factors have also been proposed in recent years which assess the performance of a given heat exchanger extended surface using the Nusselt number and the friction factor, following the reasoning of London and Ferguson. Early propositions included using an effectiveness parameter based on comparing Nusselt number of heat transfer surfaces divided by the Nusselt number of a comparable size unfinned channel at a given flow rate [21, 30]. This criterion, however, only takes into account the thermal performance of a heat transfer surface and not its hydrodynamic performance. Other authors have proposed variations of this parameter by dividing it by the friction factor ratio of the fin to a bare plate [34]:

$$\frac{\frac{Nu}{Nu_{bare}}}{\frac{f}{f_{bare}}} \qquad \text{(Eq 20)}$$

This criterion has the advantage of comparing both components of heat exchanger performance. This index has a tendency to overestimate the contribution of friction losses, meaning that plain channels are typically considered more efficient than finned surfaces when using this parameter for design. It has thus been proposed to moderate the contribution of the friction factor by applying a 1/3 exponent to this parameter. This was justified by noting that the important parameter for a heat exchanger is actually the thermal performance over the required pumping power. This parameter is plotted as a function of Reynolds number, so consequently both contributions (thermal performance and pumping power) should have a similar dependence on Reynolds number. Since the Nusselt number is approximately proportional with *Re* and the pumping power is approximately proportional to the friction factor and the cube of *Re*, then logically the following parameters could be used [12, 35]:

$$\frac{\frac{Nu}{Nu_{bare}}}{\left(\frac{f}{f_{bare}}\right)^{1/3}} \ or \ \frac{Nu}{f^{1/3}} \qquad \text{(Eq 21)}$$

These methods do not take into account variations in driving temperature differences that arise from the use of various configurations of heat exchangers, however. Using the *J*-factor, the Nusselt number or the convective coefficient also presents difficulties for comparing with the literature as the values obtained are sample geometry dependent and the values published cannot be adapted without knowing the intimate details of the calculation procedure of the source.

To remedy this shortcoming, Soland et al. have proposed an efficiency indicator which is based on the driving temperature difference as a function of the required power input to drive the fluid

[36]. This was achieved practically by comparing the number of transfer units (*NTU*) to the pumping power (e), normalized by the total heat exchanger volume (V). The advantage of this method is the ease of computation and its independence with testing conditions. Indeed, these data are independent of the heat exchanger geometry, which allows other authors to directly compare their results to the curves produced in the literature without knowing the exact details of geometry of the test sample in question.

Recently, Sahiti et al. have proposed an efficiency indicator which better predicts the effectiveness increase attainable when changing heat exchanger parameters by using more dimensional parameters for the determination of the pumping power and the thermal performance [16]. The thermal conductance is plotted against the required pumping power and are both normalized by the total heat exchanger volume in the following manner:

$$UA_v = \frac{1}{R_{eq} \cdot V} = \frac{h \cdot A_t \cdot \eta_o}{V} \qquad \text{(Eq 22)}$$

$$e_v = \frac{\dot{V}_f \cdot \Delta P_f}{\eta \cdot V} \qquad \text{(Eq 23)}$$

In the previous relation, e_v is the pumping power per unit volume, $\dot{V}_f$ is the volumetric flow rate of the fluid, η is the fan efficiency while V is the volume of the heat exchanger. This method is found to predict the performance more accurately than the previously proposed methods, which tend to over predict performances of pin fin heat exchangers [16]. Furthermore, the data presentation allows one to perform the comparisons without requiring the details of the geometry and of the calculations of the surface to compare with, which is typical of approaches that compare non-dimensional numbers such as the *J*-factor or the Nusselt number.

2.4 Thermal Spray Techniques

Thermal spray techniques are coating processes that differ from other coating techniques such as directed vapour deposition or electrochemical plating as they are non-atomistic processes. Instead of being deposited on the substrate material on a molecular level, the deposition is done using relatively large clusters of molecules that consist of solid, micron sized powders, which are usually heated to a molten or semi-molten state and projected onto a substrate's surface at varying speeds depending on the process used. Figure 17 shows a tree of the most commonly used thermal spray techniques.

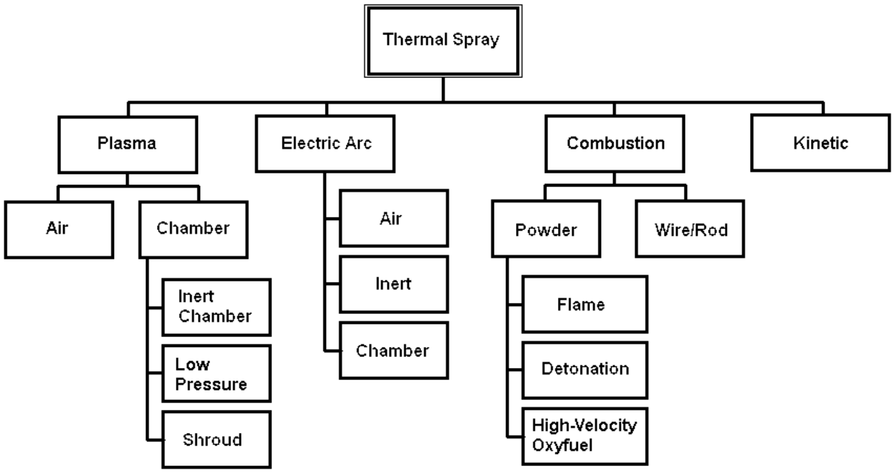

Figure 17: Thermal Spray Processes (Adapted from [37])

Kinetic spray processes such as CGDS rely on the transfer of momentum from a high pressure inert gas (usually helium or nitrogen) to relatively cold particles, which are deposited onto a substrate's surface. The high-pressure driving gas is heated and subsequently accelerated to supersonic speeds using a converging-diverging (DeLaval) nozzle, where its kinetic energy is imparted to the particles by drag effects [38, 39]. A schematic of the cold spray process is shown in Figure 18, where the main components of a cold spray system are illustrated.

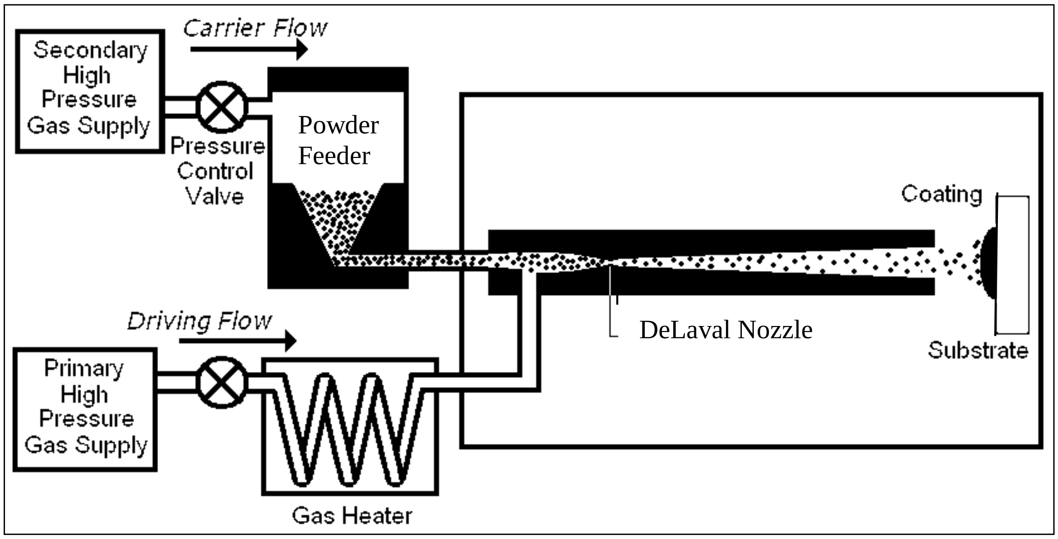

Figure 18: Schematic of Cold Spray Process

Upon colliding with the substrate, the particle's kinetic energy is converted to plastic deformation of the particles and substrate, which induces adhesion. In the cold spray process, this impact between the particles and the substrate occurs at relatively low temperatures, which is typically less than half the material's melting temperature in Kelvin. In cold spray, the particle's mechanical deformation is attributed to the adiabatic shear instabilities created during the impact, which causes the material to viscously flow outwards from the center of the particle [40]. For this process, metallurgical bonding to the substrate is attributed to localized high pressure waves breaking oxide layers and promoting intimate contact between the particle and the substrate [41], while for other thermal spray processes the adhesion is sustained by the solidification of the melted particles on the substrate's surface.

2.5 Additive Manufacturing

2.5.1 Three-dimensional Printing

Additive manufacturing and 3D printing are subjects which have attracted a massive amount of interest over the past decade. This interest was sparked by the potential cost savings and the reduced environmental impact that near net shape production of parts could provide, due to the minimized amount of wasted material, when compared to more traditional material removal shaping methods [42]. Furthermore, certain features can be manufactured with additive manufacturing which are hard, even impossible, to make with traditional methods such as machining or casting [42].

The additive manufacturing processes that have obtained the most success recently consist of using a robotic control to move a nozzle which deposits layers of molten polymers, which are successively deposited to build a part up, layer by layer [43]. The robotic control is guided by a computer generated 3D model, which is converted to a layer by layer map of where deposition should occur. The buildup speed is limited by the output capacity of the nozzle, with particles being typically in the range of 50 to 100 microns in diameter, creating layers with similar thicknesses [43]. The parts built in this manner have limited structural strength but usually have good integrity with adequate spatial resolution [43]. If the tolerances are very strict, it is possible to over deposit and use a post-processing step such as machining. The main drawback of such technique is the low build rate of the parts, with larger parts requiring unrealistic timeframes for build-up [42, 43]. For small parts or very small batches of larger parts, this option can be very convenient and economically interesting [42, 43].

This type of technique can also be used to produce parts made of other types of materials, such as metals (which carries the name fused deposition modeling), where the consolidation of the part is obtained by heat treatments such as sintering but are still in their infancy stage [43]. Other techniques such as selective laser melting or direct laser sintering can be used to create metallic parts using additive manufacturing are also being developed, but are not yet widespread industrially.

2.5.2 Additive Manufacturing in Thermal Spray

Additive manufacturing in thermal spray is a topic that has received very little attention previously, but which is a growing interest in the scientific community. Conventionally, thermal spray techniques have been used to deposit coatings instead of building net shape or near-net shape features. The first group to study this subject was led by Prinz and Weiss, who used a stackable and disposable mask sheets to selectively block the deposition from a plasma spray torch [44, 45]. This method, however, has certain disadvantages, including poor spatial resolution, part warpage due to thermal stresses and poor mechanical strength for a metallic part.

In the last years, investigations have been conducted regarding the possibility of using CGDS to produce net-shape deposits, with the first studies concentrating on the use of masked deposition [46]. These investigations focused on building electrodes for solar cells, where the electrode consists of a continuous copper deposit. The deposits in question have a pyramidal section, which was explained as being due to the large carrier gas flow recirculation zones found near the edges of the mask due to the lack of clearance between the mask and the part that requires coating, as depicted in Figure 19. This leads to preferential deposition near the center of the mask opening, with little deposition near the mask edges. The limitations of this technique are that there is a risk of embedding the substrate into the mask and that the height limit of the deposit is tied to the thickness of the mask.

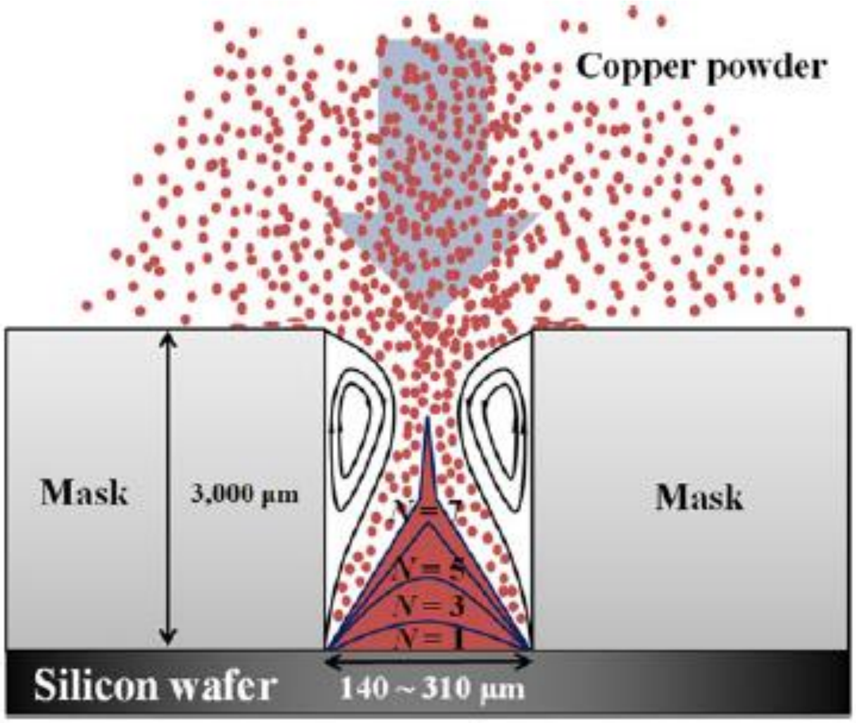

Figure 19: Schematic of the Deposition Process for CGDS with a mask [46]

2.6 Flow Structure Visualization

2.6.1 Flow Visualization Techniques

Flow visualization techniques can be separated into three groups based on the approach for data collection and the type of data collected:

i. Surface flow visualization techniques
ii. Optical methods
iii. Tracer particle methods

The first type of flow visualization techniques focuses on flow structures near walls or other solid surfaces. One example of this uses coloured oils applied to the surface of an object in a wind tunnel. The oil reacts to the shear stress in the boundary layer of air at the solid surface and forms a pattern from which flow information can be deduced.

The second approach relies on differences in the optical properties between regions in a fluid to determine the flow structure. The optical properties observed can either be based on refraction differences, such as those arising from high temperature gas stream in a room temperature environment, or based on evaluating the color of a stream in which dye has been injected. The differences in refractive index can be visualized using Schlieren photography or using a shadowgraph while the dye concentration methods typically use laser-induced fluorescence or light attenuation techniques.

The third method of flow visualization relies on the principle of tracking the displacement of tracer particles in the flow to determine the streamlines of the fluid or the pathline of the particles in the stream. To this end, particles such as smoke or fluorescent plastic pellets can be injected in the fluid stream at varying concentrations. Several different flow structure evaluation algorithms have been developed depending on the concentration of particles in the fluid under study.

Regardless of particle concentration, the necessary equipment for using tracer particle methods is of the same nature, with this equipment illustrated in Figure 20. Photographs are taken with a very short time interval between each and pairs of pictures are analyzed together. Charge-Coupled Device (CCD) cameras are usually used to capture and convert the images to digital files which are sent to a computer. For this procedure to occur successfully, an illumination source is triggered simultaneously with the camera's shutter opening using a synchronizer. This synchronizer acts as an external trigger source for the camera and the illumination source. The illumination source, depending on the actual tracking particle method used, is usually a laser, conditioned to obtain a thin sheet of light to illuminate solely the zone of interest. The data generated by the light received by the CCD camera is then analyzed using cross-correlation signal processing algorithms. For the proposed work, the Particle Image Velocimetry (PIV) method is most appropriate, as the particle concentration is high enough to allow one to obtain the whole flow field with one sequence of images, while it is low enough to ensure that the properties and behaviour is not affected by the particle density [47]. With this goal in mind, small tracer particles are chosen with a density very similar to that of the fluid being analyzed as to minimize disturbances stemming from the seeding particles.

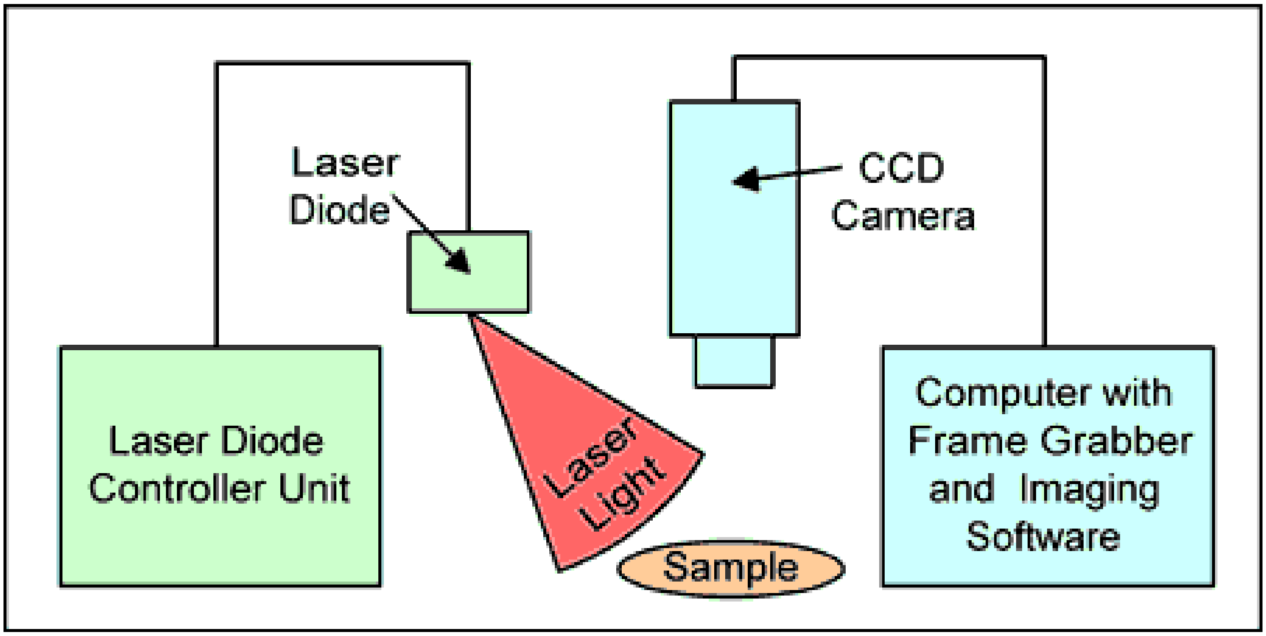

Figure 20: Typical Tracer Particle Technique Apparatus [48]

The PIV data post-processing method relies on the identification of groups of particles and tracking the movement of these groups, as opposed to particle tracking algorithms which only follow the displacement of single particles. The PIV algorithm separates the camera's field of view into smaller interrogation windows, in which the particle groups' displacement is measured. The size of the interrogation window must be selected to be at least twice as large as the maximum expected displacement [47]. Once the displacement of the particle groups has been determined, a velocity vector is generated for this window. The resolution, or maximal amount of information that can be obtained using this technique, is thus inversely proportional to the interrogation window size.

Larger windows allow for easier resolution of the algorithm since the particle displacements will be small compared to the window size, but the large size of the window limits the amount of velocity vectors that can be determined using this method [47]. It is thus critical to choose the appropriate correlation window size.

Two methods for estimating the displacement of the particles exists for PIV analysis: auto-correlation and cross-correlation. The first method consists of taking a single picture with a long exposure time and two short illuminations during the acquisition. This yields a single frame, where the same particle groups appear twice, in different positions, in the frame. The auto-correlation algorithm matches particle group positions within this single frame to determine the amount of motion that occurred between the illuminations, which in turn can be converted to a velocity field. The cross-correlation algorithm, in contrast, uses a camera capable of performing two short exposition times in quick succession to capture two different frames, one for each illumination event. The algorithm then determines particle movement from the identification of the motion between one frame and the next, with a known time interval between the capture of both frames. This requires the use of complex equipment, such as a high end camera and a synchronizer, to ensure that the illumination pulses coincide with the exposure time of the camera. The first method requires a much simpler camera setup, but is less accurate than the cross-correlation method due to the difficulty in correctly identifying individual particle groups [47].

Due to the nature of the equipment used, non-stereoscopic PIV processes are considered two-dimensional analyses. Indeed, the very small depth-of-focus of the camera and the thin nature of the laser illumination limit the gathering of information to a plane [47]. This implies that PIV analysis is much more suited to applications which have a very small amount of displacement perpendicular to the analysis plane, as if there is much movement in that direction, the software will not be able to find matching particle groups between camera frames and the analysis will fail [47]. For flow fields which have a negligible vertical component of velocity, it is possible to obtain a depth-composite velocity profile by using the horizontal plane for analysis and by moving the position of the focus of the laser optics and the camera's focus along the vertical axis.

When micron size flow features are to be observed, μPIV must be used instead of traditional PIV [49, 50]. To obtain the spatial precision required, the camera must be equipped with optics to enhance its resolution. This is usually accomplished by outfitting a very sensitive camera with microscope lenses tailored to the acquisition of small intensity fluorescence signals [49]. Due to the sensitivity of the apparatus, care must be taken to ensure that none of the laser's primary signal is sent to the exposure plate, which is accomplished by the use of a dichroic filter, which allows light at the primary wavelength to pass through in one direction (towards the sample) and light from the fluorescent particles at the secondary wavelength back (towards the camera). This technique also differs from traditional PIV in its treatment of the illumination. Since the microscope lens has a sufficient depth-of-focus to obtain results with the desired precision, there is no need for complex optics to condition the light coming from the laser to a light sheet [49, 50]. Instead, a full volume illumination is used and the depth of the measurement plane is solely dictated by the camera optics [49]. Micro-PIV has the same limitation as regular PIV does with respect to the planar nature of the results. Once again, it is possible to obtain a depth-composed profile by moving the focus along the vertical axis to obtain many planes along the depth. This method, however, does not take into account the depth-wise velocity component.

The Stokes number (Stk) is used to determine how closely the particles follow the fluid's trajectory. It is defined as the ratio of the characteristic time of the particle's movement to the characteristic time of the fluid's movement [47]:

$$Stk = \frac{\tau u_\infty}{d_h} \quad \text{(Eq 24)}$$

where u_∞ is the mean fluid free flow velocity, d_h is the hydraulic diameter and τ is the relaxation time of the particle (the time constant of the exponential decay of fluid momentum due to drag effects), which is calculated with:

$$\tau = \frac{\rho_p d_p^2}{18\mu} \quad \text{(Eq 25)}$$

In this equation, ρ_p is the particle's density, d_p is the particle's diameter and μ is the fluid's dynamic viscosity. The Stokes number must be verified after the proper particle size has been selected for the desired resolution to insure that they appropriately follow the fluid's motion. The criterion for having tracing accuracy errors smaller than 1% is to have a Stokes number less than 0.1 [47].

2.6.2 Flow Visualization in Heat Exchangers

To properly understand the performance behaviour of heat exchangers, the flow structures that are present must be understood. Indeed, in forced convection applications, the turbulence levels and the local fluid velocity around heat transfer enhancing features determine the local convective heat transfer coefficient and play a significant part in determining the hydrodynamic losses. For this reason, visualizing the flow structures in heat exchangers has been a growing concern in recent years.

Flow structure visualization using PIV has been performed by several authors with the goal of characterizing heat transfer [51-56]. Wen et al. [51] focused on the determination of the effect of the flow structures found in the headers upstream of a plate fin heat exchanger and the consequences of maldistribution of fluid on the performance of such fin arrays. Jones et al. [52] used µPIV measurements to examine the flow maldistribution in microchannel heat sinks, which allowed experimentally determining that maldistribution increases drastically as the Reynolds number is increased, thus decreasing the thermal performance of the heat exchanger. Uzol et al. studied both the performance and the flow structures arising from circular and elliptical pin fin arrays and found that the elliptical shaped fins transferred less heat at a much lower aerodynamic cost, which yields a better overall efficiency than their circular cross-section pin fins [53]. This was attributed to the early flow separation from the circular pin fin's surface, which creates a large low velocity wake behind the fin, which could be identified and characterized using PIV [54]. Furthermore, the higher levels of turbulent kinetic energy measured in the circular fin's wake helped explain the increased thermal performance of this type of geometry when compared to ellipses [54].

2.6.3 Flow around Pyramidal Structures

Although the literature regarding sub-millimeter scale structures is lacking, flow patterns around large scale structures have been studied extensively due to their application in pollution control in cityscapes. The flow structures around pyramidal shaped structures have been investigated by Martinuzzi et al., who found very complex three dimensional flow geometries for scaled down (approximately 1 meter high) pyramids [55-57]. From these studies, several horseshoe and hairpin vortical structures were identified, leading to a broad low pressure zone behind the pyramidal structure, as illustrated in Figure 21. These flow features induce a significant amount of fluid mixing, stretching as far as three times the base length downstream of the pyramid.

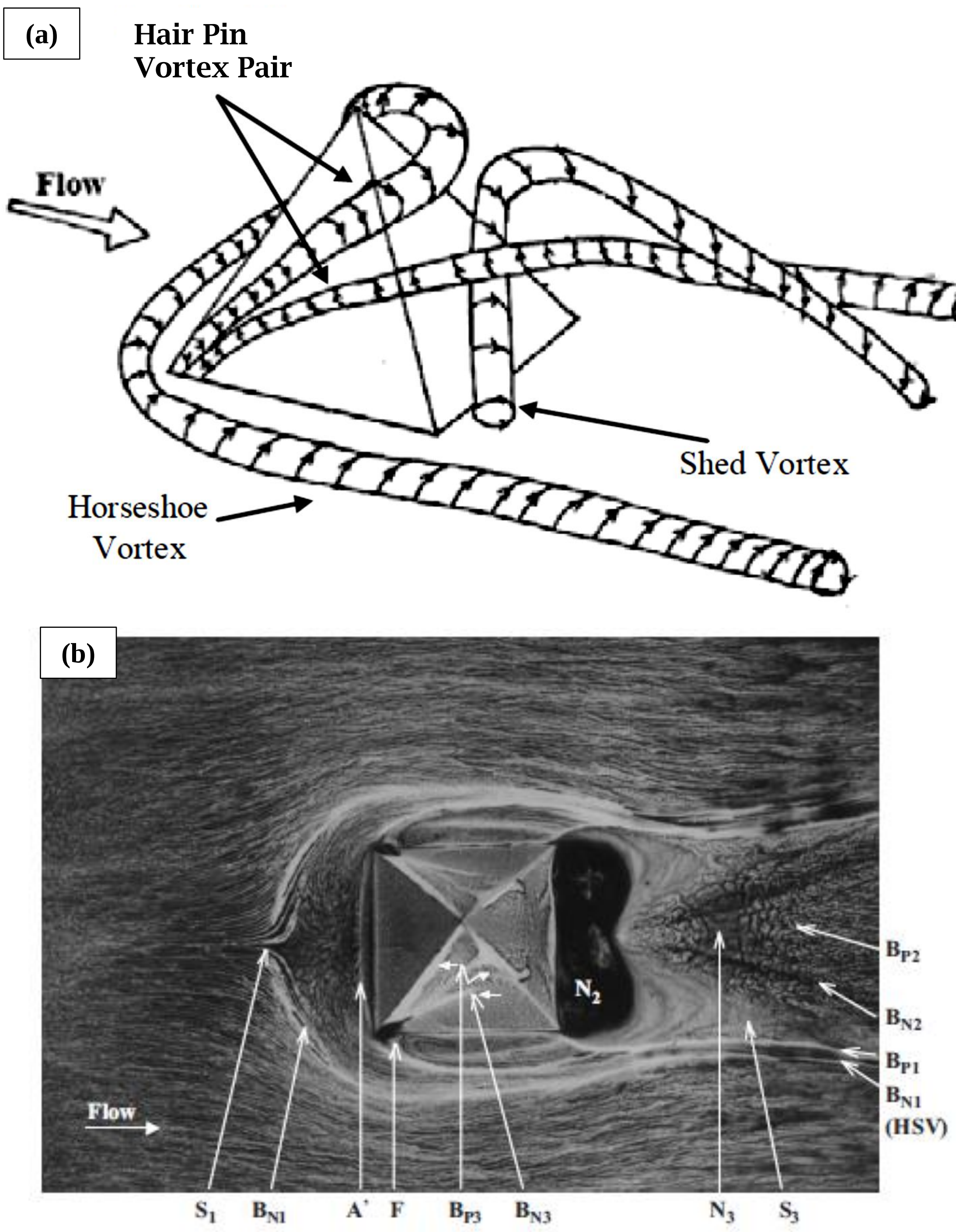

Figure 21: Flow Structures Around Pyramids Indicating the Various Types of Flow Structures Encountered: (a) Schematized (Adapted from [56]); (b) From Flow Visualization [56]

CHAPTER 3 RESEARCH OBJECTIVES

3.1 General Objectives

As stated previously, the general objective of this work is to increase compact heat exchanger efficiencies by using net-shaped pin fins produced using cold spray. To allow designers to properly select the size, geometry and configurations while maximizing the performance of the fin array under the given design conditions, certain specific objectives are proposed:

a) Determine the effect of varying the pyramid's base angle, the fin density and the fin height on the thermal and hydrodynamic performance of the fin array at low Reynolds numbers (250 – 3000).

b) Determine the effect of using different type of pin fin geometries and arrangements on the flow structures and the performance of the array, while demonstrating the superior performance of pins fins when compared to plain rectangular (continuous) fins.

c) Visualize the flow structures at varying Reynolds numbers to identify regions of increased fluid turbulence and to observe the recirculation structures believed to exist in the pin fin's wake.

d) Measure the different turbulence quantities in the regions of interest and tentatively correlate these metrics to the thermal and hydrodynamic performance of the fin arrays.

These objectives can be split into two categories of specific objectives: those related to the evaluation of the performance of the various fin arrays and those related to the observation of the flow structures of the pin fins arrays described in this work. The following sections will detail these specific objectives and the work plan that was developed to attain these goals.

3.2 Evaluation of the Performance of Pin Fins Produced using Cold Spray

The general objective is to obtain performance data for several parameters, namely the thermal conductance and the pressure loss through the fin array. Furthermore, demonstrating the superior performance of the near-net shape pin fin arrays produced by cold spray to that of several geometries of plain rectangular fins is performed, to prove the commercial viability of using this technology industrially.

The first parameter studied was the dependence of the thermal and hydrodynamic performance to the flow condition which was determined by testing the fin array at different Reynolds numbers. For the type of wire mesh heat exchangers described previously, the Reynolds numbers are usually low (500 to 2000) due to the cellular nature of the heat exchanger. Consequently, the study was focused on determining the performance at Reynolds numbers varying between 250 and 3000. This range of Reynolds number covers the application range with some margin on either side.

The next parameters that were studied are basic geometric parameters such as the fin height, fin base angle and the fin density. Varying the fin height and the fin base angle is achieved by modifying the production procedure, namely by increasing the number of spray passes. The fin height was varied between 1.0 mm and 2.5 mm, which was once again chosen to reflect what is currently required by the application. The fin base angle parameter was varied between the minimal angle obtained with the as-sprayed fin geometry and the maximal angle obtained by depositing fin material to a height greater than required, and subsequently removing the excess material by grinding the top of the fin to the desired height. Finally, the fin density can be varied by changing the mask used with the CGDS process. This parameter was varied according to the type of commercially available wire mesh masks obtainable.

The last geometric parameters that was studied is the effect of changing the cross-section of the fins produced and their configuration, namely by producing square-base pyramid, diamond-base pyramid and cone shaped fins in the inline or staggered configuration. This is motivated by the fact that different types of cross-sections cause different levels of flow disturbances (and potentially different flow structures), which could significantly affect the thermal and hydrodynamic performance of the fin array even though the other geometric parameters are kept identical. Furthermore, using fin arrays in an in-line or in a staggered configuration could also change the performance of the fin array, and has been investigated to allow proper selection of the fin array production procedure. The combination of fin shape and configuration was also selected as a function of the commercial availability of the different mask geometries.

3.3 Observation of Flow Structures of Pin Fin Arrays

The observation of the flow structures in pin fin arrays is a fundamental necessity because the disruptions of the boundary layers on the fin walls and the flow structure in the fin’s wake is the principal mechanism for the increased performance of this type of extended surface. This is especially true when comparing with plate fin arrays, for which the performance increase with respect to an unfinned surface is attributed to the greatly increased heat transfer area. Indeed, plain rectangular fin arrays have a comparable average convective heat transfer coefficient to an unfinned surface.

To properly understand the performance gain mechanism of pin fins such as those described in this work, one must visualize the movement of the fluid to understand where the critical heat transfer and pressure loss driving zones are located. This could allow, in turn, for the design of fin arrays which maximize the effect or the size of these zones and further increase the performance of this type of fin array.

Furthermore, the high convective coefficients that are usually measured for pin fin arrays could potentially be explained and correlated to the different turbulence quantities usually measured for heat exchangers, namely the turbulence intensity and the turbulent kinetic energy. Understanding how the performance varies with the turbulence metrics in various flow regions could allow for better optimization of the pin fin array performance and thus increase the heat transfer efficiency of this type of fin array.

CHAPTER 4 RESEARCH APPROACH

4.1 Fin Production using the Masked CGDS Deposition Technique

The CGDS system that was used for the exploratory work is a commercially available Plasma Giken PCS-1000, available through BEC. This machine was used to perform early trials and to validate the production procedure and parameters for the industrial partner. An SST-EP series CGDS system from Centerline was used for the in-depth research work due to its availability at the University of Ottawa Cold Spray Laboratory, and the lower operation costs of this smaller apparatus. The Plasma Giken system is optimized for large scale production, and thus is not as suitable as the smaller scale SST-EP system for a research endeavour. Using the latter system allow the minimization of cost and operation time of the Plasma Giken system. Both systems were used with nitrogen gas to reduce production costs of the fin arrays, when compared to production costs with helium gas as the propellant.

Figure 22 shows the Centerline EP cold spray apparatus, complete with the essential components: the spray enclosure, the powder feeder, the control cabinet, the robot controller, the air filter and

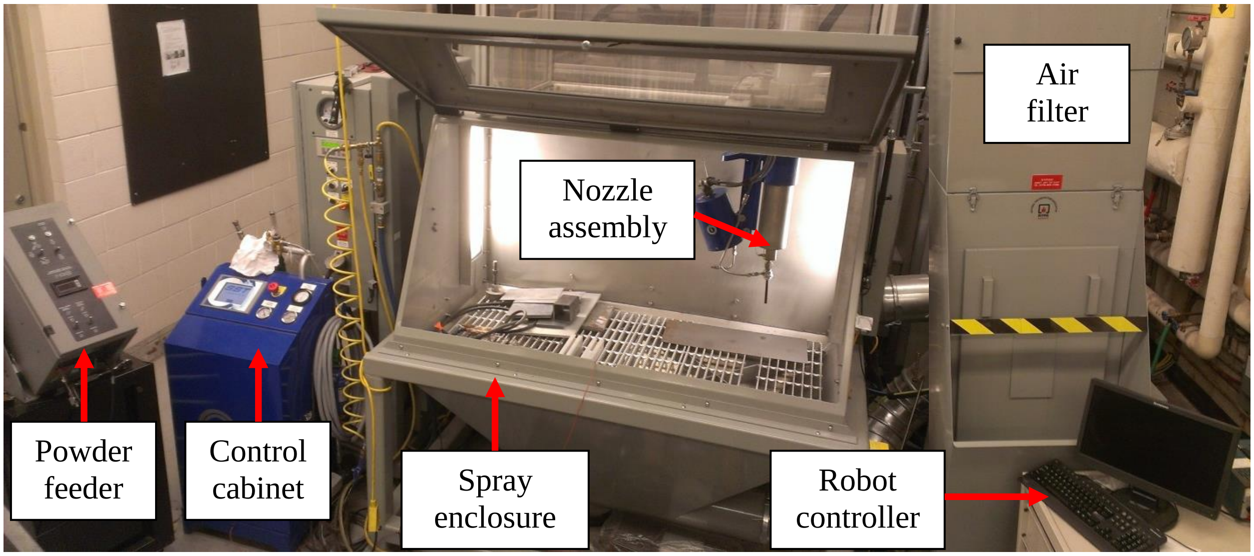

Figure 22: SST-EP Cold Spray Apparatus

the nozzle assembly. The spray enclosure and air filter ensure that the powders used for cold spray depositions are contained and properly filtered out of the atmospheric air, while the control cabinet is used to power on and off the system and to input the desired temperature and pressure. A computer is used to control the robot on which the gun is mounted to create spray patterns. Finally, a Thermach powder feeder is used to feed particles to the nozzle of the SST-EP system. This powder feeder uses pressurized nitrogen to force a measured amount of powder from the canister to the cold spray nozzle. Powder flow rates are controlled by means of a rotating wheel with holes along the rim. A hammer mechanism is used to ensure the holes are completely filled and that when the holes align with the flow valve, all the powder flows out into the nozzle feed line. Varying the speed of rotation or the number and size of the holes in the feeder wheel allows one to control the powder feed rate.

Figure 23 illustrates the technique used to create square based pyramidal fin arrays using commercially available plain woven, steel wire mesh (McMaster-Carr, Aurora, OH, USA) to mask the substrate from cold spray deposition. This configuration creates a pyramidal fin array with peaks aligning with the holes of the screened area and little or no deposition underneath the wires.

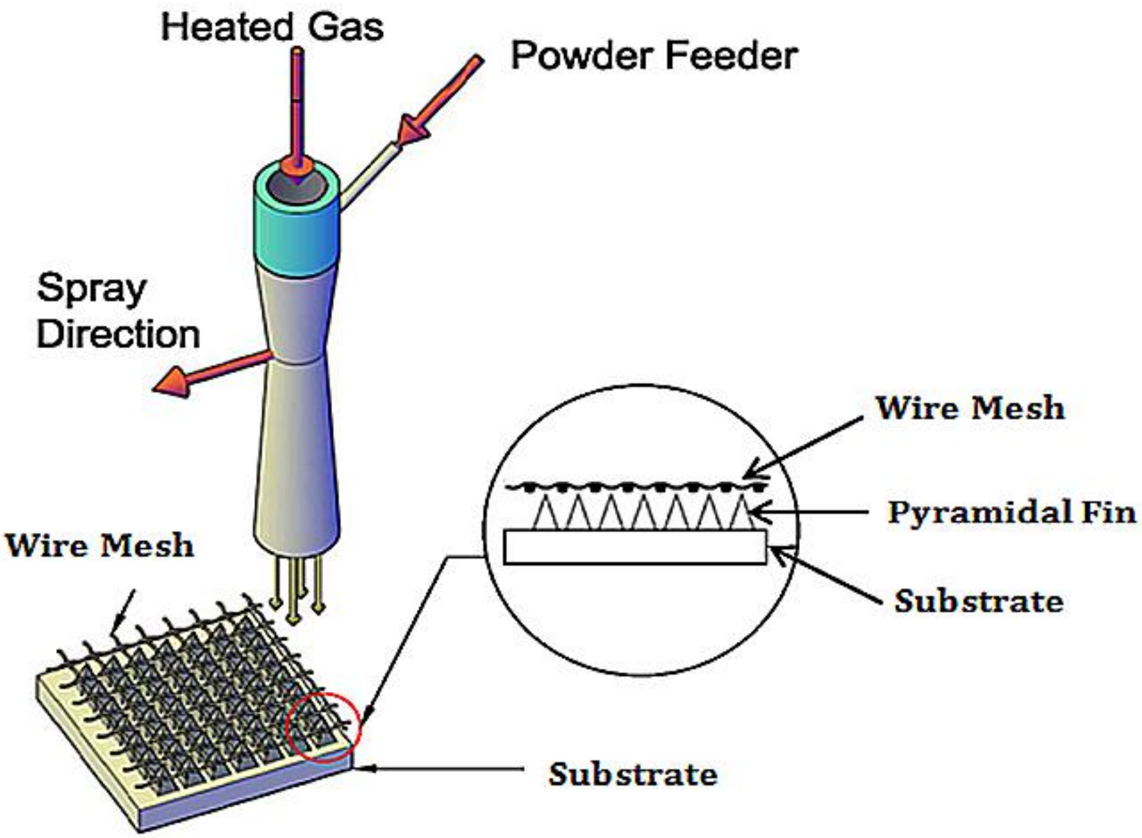

Figure 23: Schematic of the Masking Technique with Resulting Pyramidal Fin Array

The main factor that determines if adhesion occurs with the CGDS process is the particle's normal impact velocity with respect to the substrate. Thus, since the CGDS flow near the edges of the mask holes is affected by wall (viscous) effects, particles present in the CGDS flow in the vicinity of the mask wires are slowed down. As such, the particles tend to build up a coating preferentially on the substrate underneath the center of the mask holes. This creates a zone near the center of the holes where build-up is more pronounced than on the sides. This preferential build-up leads to the creation of an angle between the top and the base, thus forming a tapered section structure. When this angle becomes sharp enough, particles do not have a sufficient normal impact velocity and adhesion stops, with subsequent particles simply bouncing off the feature. The working principles of the CGDS process make it an ideal candidate for the proposed masking technique used to produce pin fins. Using other thermal spray techniques such as Plasma Spraying and High Velocity Oxy Fuel (HVOF) would cause issues where the mesh would either melt or be clogged by the molten particles in the very high temperature gas stream. Furthermore, mask distortion and softening could become problematic production issues that are completely avoided when using cold spray.

The feedstock powder used is aluminum (99.8% Al), purchased from Centerline (Windsor) Ltd. (Windsor, Ontario, Canada), and distributed commercially under the name SST-A5001. The powder size range is characterized by a size distribution where 10% of the particles are smaller than 13.29 microns (D_{10} value), 50% of the particles are smaller than 25.35 microns (D_{50} value) and 90% of the particles are smaller than 49.58 microns (D_{90} value), as measured by a Microtrac (Montgomeryville, Pennsylvania, USA) S3500 laser diffraction analysis apparatus. Figure 24a presents an image of the powder taken by a Scanning Electron Microscopy (SEM) EVO-MA 10 (Zeiss, Oberkochen, Germany). It presents an elongated, non-spherical geometry. The grain structure is shown in Figure 24b, as etched with Keller’s reagent. The grains have an equiaxial shape in the center of the particle, while the exterior is composed mostly of elongated grains. This type of powder was used due to its low cost and the high sprayability of aluminum, combined with its high thermal performance. Furthermore, the project’s industrial partner was interested in the performance properties of aluminum fin arrays produced by cold spray.

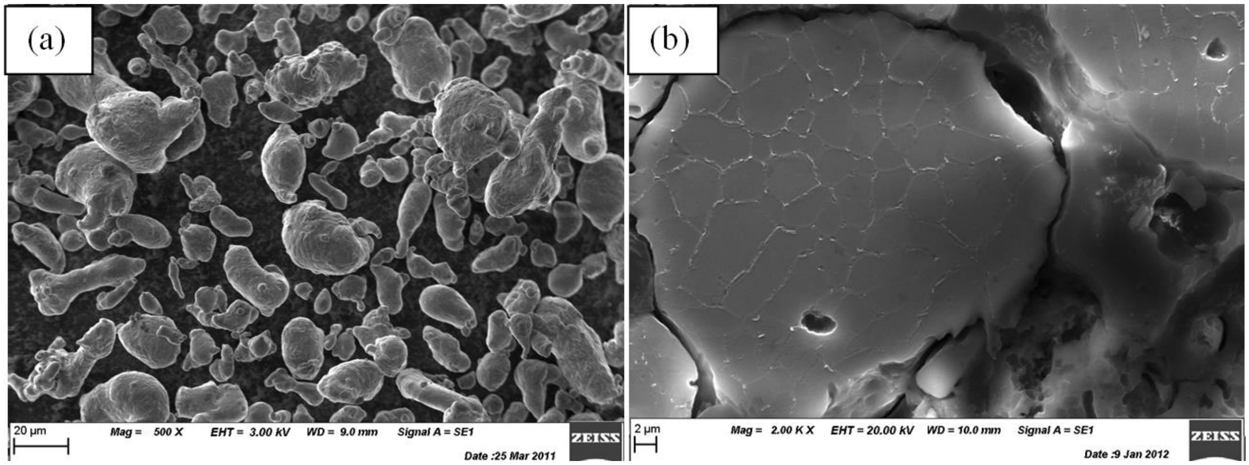

Figure 24: SEM Micrographs of SST-A5001 Feedstock Powder (a) As-Received; (b) Etched Cross-Section

Fins were cold sprayed on aluminum substrates (Al6061 T6) with standard dimensions of 5.1 cm by 5.1 cm. The cold spray trials detailed in this work are done on extruded aluminum substrates instead of thermal sprayed coatings on the WMHE to demonstrate viability. As only the thermal and hydrodynamic performance of the fins are of interest, it was felt to be necessary to isolate the fin system from the rest of the WMHE system to reliably report the performance of the fin array independently from issues that may arise in the production of the WMHE which could skew the results. The substrates were cleaned and degreased using acetone after being cut to size. No further coupon preparation steps such as grit-blasting or heat treatments were performed. To determine the effect of changing the fin base angle for a constant height, samples are cold sprayed to a height larger than the target height and then ground down to the target height with using a conventional sanding belt with 320 grit sandpaper and water as coolant. This process yields fins with a trapezoidal prism shape, as illustrated in Figure 25. No other type of post-treatment of the sprayed samples was performed.

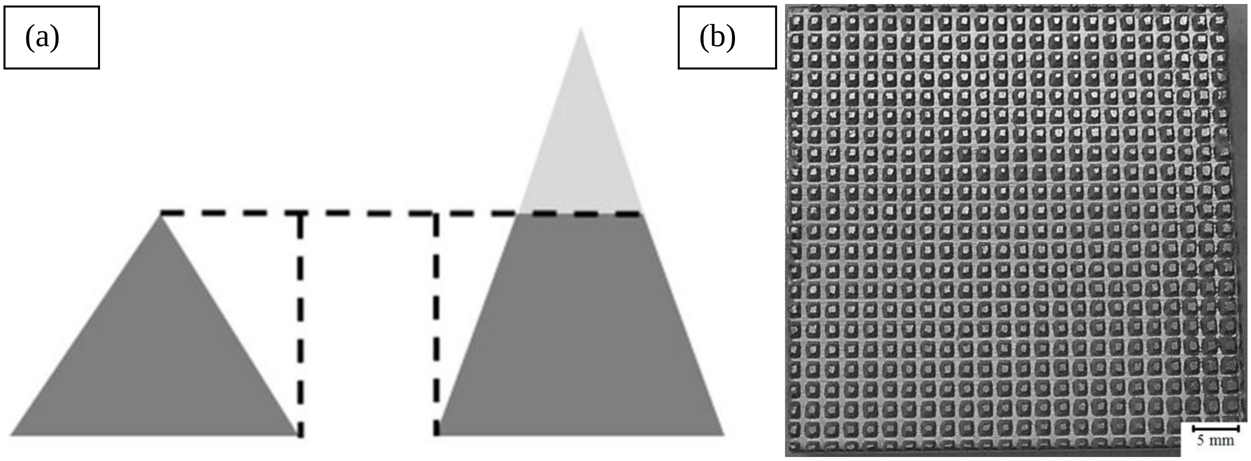

Figure 25: (a) Comparison between As-Sprayed and Ground Fin Geometry; (b) Ground Fin Sample

4.2 Fin Array Characterization

Fin array samples were measured using a depth of field microscope VHX-2000 which was acquired from Keyence (Mississauga, Ontario, Canada) which allows building three dimensional images of the given samples. This non-destructive method will be used to characterize the base dimensions and the height of the samples to be tested, while standard metallographic procedures were used to obtain cross-sections of the sprayed samples. All the micrograph image analyses were performed using Clemex Vision Lite (Clemex Technologies Inc., Longueuil, Qc, Canada) image analysis software.

4.3 Heat Transfer Efficiency Determination

4.3.1 Performance Test Apparatus

The performance of the various fin arrays produced was assessed using a heat transfer and pressure drop test apparatus designed at the University of Ottawa. A schematic of this test fixture is shown in Figure 26.

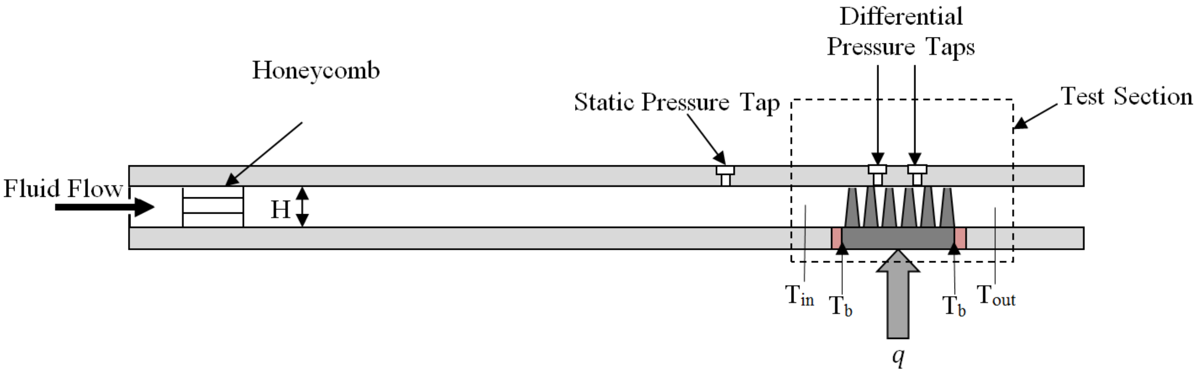

Figure 26: Thermal and Hydrodynamic Test Fixture

The main components of this apparatus are the test section, the heating pad, the air supply and the data acquisition system. The air is supplied by a compressed air line, properly filtered and dehumidified to obtain room temperature, dry air, free from oil contamination. The air inlet flow rate is controlled by a needle valve and is measured with a flow meter. This air is smoothly expanded into a horizontal rectangular channel with a diffuser and a honeycomb flow straightener. The honeycomb flow straightener consists of a series of 10 mm diameter, 25 mm long flexible tubes placed side by side to ensure there are low levels of turbulence in the inlet air. The rectangular channel's top and bottom plates (76.2 mm wide by 457.2 mm long by 19.1 mm thick) are made of acrylic, and they are spaced apart using a rectangular rubber gasket, which is compressed to ensure there is no clearance between the fins and the shroud surface. These gaskets also ensure that the joint is leak-proof. A length of 457 mm of unobstructed flow ensures that the fluid is thermally and hydrodynamically fully developed before reaching the test section for the given range of hydraulic diameters and Reynolds numbers [10].

The test sample is subjected to a constant heat flux provided by a strip heater. A conducting block is used to ensure that heat is evenly distributed onto the substrate's surface. A set of differential pressure measurement taps is located 12.7 mm upstream (high pressure side) and downstream (low pressure side) from the middle of the test section. Two thermocouples are located 6.0 mm before and after the test section at mid-height to record the fluid's local average temperature. Four thermocouples are attached to the fin array's base, with two on the side facing the incoming flow, and two on the side facing the exiting flow. On each face, one thermocouple is located on the centerline, while the other thermocouple is located 6 mm from the wall. All the thermocouples used are T-type, butt-bonded, thin gauge (32 gauge) thermocouples. Radiative heat transfer losses are neglected since they would account for less than 0.5% of the total heat input for similar test surfaces at test temperatures less than 75 °C [58, 59].

4.3.2 Data Analysis Method

To analyze the raw data obtained and compare it in suitable manner, flow conditions are expressed using the Reynolds number. This study provides non-dimensional numbers with a characteristic length based on the hydraulic diameter for the comparison of different fin arrays.

The Reynolds number based on the hydraulic diameter is given by:

$$Re_{Dh} = \frac{\rho u d_h}{\mu} = \frac{\dot{m} \cdot d_h}{W \cdot FD \cdot A_{flow} \cdot \mu} \qquad \text{(Eq 27)}$$

where $\dot{m}$ is the mass flow rate, d_h is the hydraulic diameter of the fin array, W is the sample width, FD is the fin density, μ is the fluid's dynamic viscosity and A_{flow} is the total face area the fluid can flow into. For the works related to pyramidal fins, the characteristic length was chosen to be the hydraulic diameter, as the fin array geometry promotes structures typical of internal flows. Indeed, due to the small size of the passages, the boundary layer growth and coalescence in this type of fin array is more akin to that of internal flows than to external flows. The variables d_h and A_{flow} are given by:

$$d_h = \frac{4 \cdot A_{flow}}{P_{flow}} = \frac{2 \cdot A_{flow}}{\frac{H}{\cos(\theta)} + S + H \cdot \tan(\theta)} \quad \text{(Eq 28)}$$

$$A_{flow} = (S + H \cdot \tan(\theta)) \cdot H \quad \text{(Eq 29)}$$

where P_{flow} is the flow channel's perimeter, θ is the fin angle, S is fin spacing from edge to edge and H is the fin height.

Figure 27 shows a thermal circuit of the fin array, with the reduction of the thermal resistances of the fins and the unfinned surface designated respectively by R_f and R_{us} to an equivalent resistance R_{eq}.

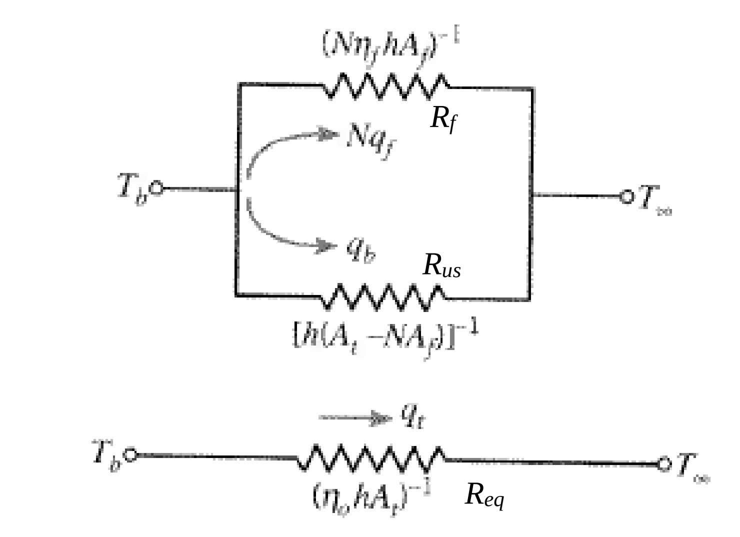

Figure 27: Thermal Resistance Circuit of Fin Arrays (Adapted from [10])

The thermal conductance parameter UA can be calculated as:

$$UA = \frac{1}{R_{eq}} = h \cdot A_t \cdot \eta_o \quad \text{(Eq 30)}$$

where h is the convective heat transfer coefficient, η_o is the overall surface efficiency and A_{tot} is the total heat transfer area for pyramidal fins, given by:

$$A_t = A_f + A_{us} = N_f \left(\frac{B^2}{\tan(\theta)\cos(\theta)} - \frac{t^2}{2\sin(\theta)} \right) + (WL - N_f B^2) \qquad \text{(Eq 31)}$$

In the previous equation, N_f is the number of fins in the array, B is the fin's length at its base, L is the sample's length, A_f denotes the total fin heat transfer area, A_{us} represents the unfinned base's exposed area while t is the fin's top length, given by:

$$t = B - 2Htan(\theta) \qquad \text{(Eq 32)}$$

The overall efficiency is calculated using the following equation:

$$\eta_o = 1 - \frac{A_f}{A_t}(1 - \eta_f) \qquad \text{(Eq 33)}$$

where η_f is the individual fin efficiency, defined as the heat transferred by the fin over the maximum possible heat that can be transferred, which is numerically equal to:

$$\eta_f = \frac{2}{mH} \frac{I_2(2mH)}{I_1(2mH)} \qquad \text{(Eq 34)}$$

with:

$$m = \sqrt{\frac{4h}{k_m D}} \qquad \text{(Eq 35)}$$

In the previous equations adapted from Incropera's work [10], I_1 and I_2 denote the first and second order Bessel functions, respectively, while k_m is the thermal conductivity of the fin's metal.

The individual fin efficiency equation for triangular pin fins are used for the sprayed pyramidal pin fins in this work since it is the shape with the most similar geometry. The only difference between the two is the shape of the base, since the equation is for a circular base while the manufactured fins have a square base. Therefore, D in the previous equation is replaced by the fin length at the base (B).

The fin array's convective heat transfer coefficient and Nusselt number are calculated with the following relations:

$$h = \frac{q}{\Delta T_{lm} A_t \eta_o} \quad \text{(Eq 36)}$$

$$Nu = \frac{h \cdot d_h}{k_{fl}} \quad \text{(Eq 37)}$$

In these equations, q is the heating rate, ΔT_{lm} is the log-mean temperature difference between the fluid and the fin array and k_{fl} is the fluid's thermal conductivity. The log-mean temperature difference is calculated with:

$$\Delta T_{lm} = \frac{\Delta T_1 - \Delta T_2}{\ln(\frac{\Delta T_1}{\Delta T_2})} \quad \text{(Eq 38)}$$

where $\Delta T_1$and ΔT_2 are the temperature difference between the fin surface and the flow at the inlet and outlet respectively. The total heat input rate to the system is calculated using:

$$q = \dot{m} \cdot (T_o - T_i) \cdot Cp \quad \text{(Eq 39)}$$

where $(T_o - T_i)$ is the fluid temperature difference between the entry and the exit of the test section, Cp is the fluid's thermal capacitance.

Based on the literature review performed, the efficiency indicator proposed in Sahiti's work [16] was selected. The required pumping power input was calculated according to Sahiti's definition [16]:

$$\mathrm{e} = \frac{\dot{V}_f \cdot \Delta P_f}{\eta_{fan}} \qquad \text{(Eq 40)}$$

In the previous relation, e is the pumping power, $\dot{V}_f$ is the volumetric flow rate of the fluid while η_{fan} is the fan efficiency. A fan efficiency of 0.8 was chosen as a reasonable value to perform these calculations [16]. The pumping power is divided either by the fin array base (A_b) to yield the pumping power per unit area or by the volume (V) of the fin array to obtain the pumping power per unit volume.

4.4 Particle Image Velocimetry Flow Characterization

4.4.1 µPIV Apparatus and Equipment

The system that was used to determine the flow structures, to measure the flow velocity and to determine the turbulence quantities for this work is a commercial µPIV Flowmaster3 apparatus available at the University of Ottawa. It was purchased from LaVision and includes the necessary hardware and software to perform a PIV analysis on the micron scale. The principle of operation is the same that is described in chapter 2.5. Figure 28 shows the Flowmaster3 apparatus and its components.

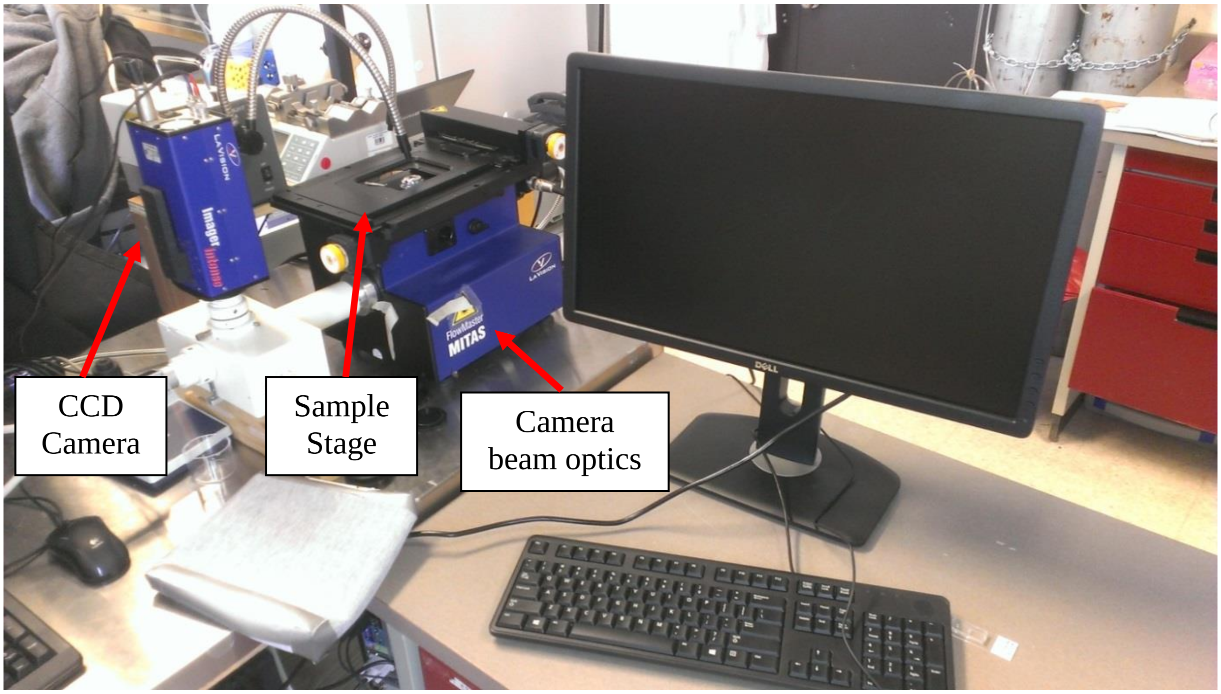

Figure 28: Flowmaster 3 µPIV Apparatus

The pin fin array sample was mounted in an aluminum sample holder equipped with a transparent polycarbonate viewing window. A centrifugal pump was used to pump the fluorescent polyester particle doped water through the system. A precision flow meter equipped with a needle valve was used to adjust the flow rates to obtain Reynolds numbers varying between 500 and 2000. Schematics of the apparatus are shown in Figure 29 and Figure 30.

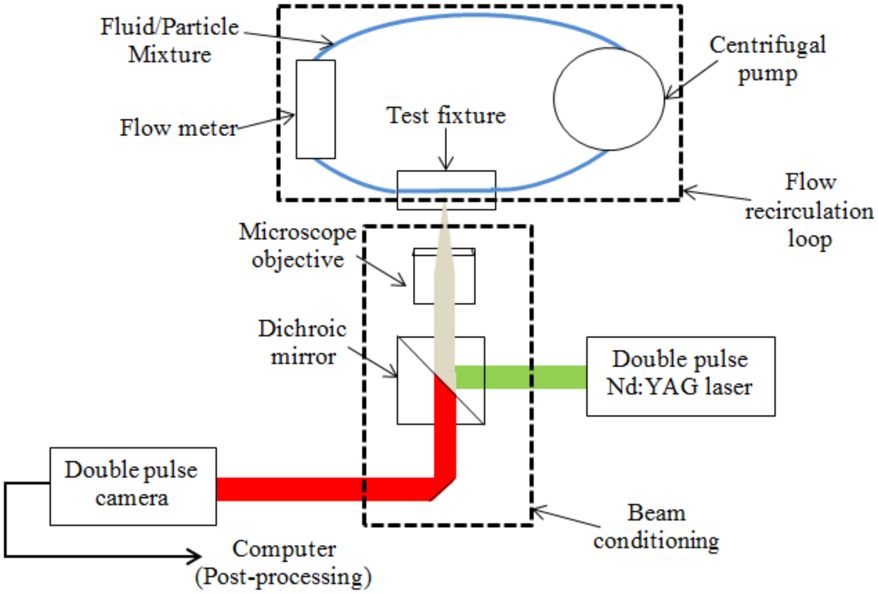

Figure 29: Schematic of μPIV Setup

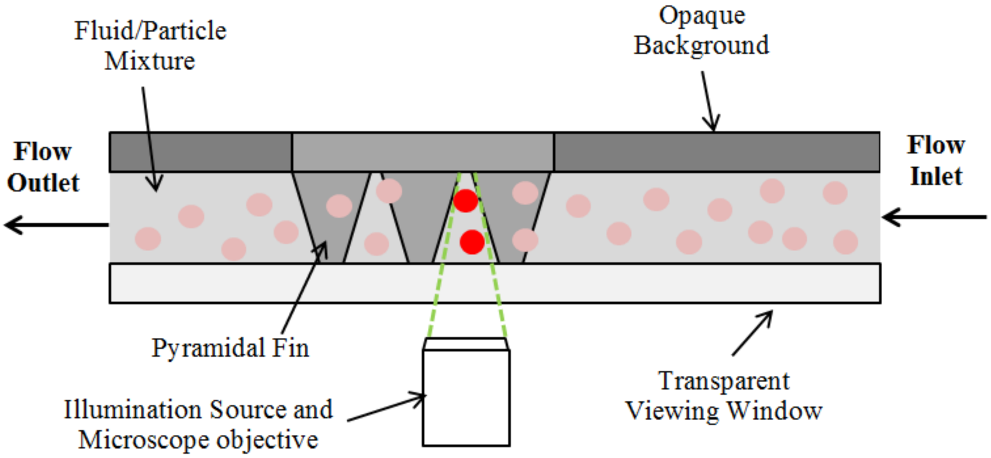

Figure 30: Schematic of μPIV Test Fixture

The camera used to record the visual information is a double pulsed CCD camera equipped with a microscope to condition the incoming light. It has a 5 Hz frame rate with a minimal time interval of 0.5 μs between two successive exposures. The camera offers a resolution of 1376x1040 pixels with an exposure plate of 8.9x6.7 mm and was used in conjunction with a microscope long working distance objective lens with 5x magnification. This yielded a pixel width of 1.31 μm and a depth of field of 28 μm.

The laser source used for sample illumination is a double pulsed Nd:YAG laser used in conjunction with a dichroic filter, which only allows green light (λ = 532 nm) towards the sample and the red light (λ = 650 nm) that is emitted by the fluorescent tracer particles back to the camera. The laser pulses are collinear and produce a full volume illumination in the test section, with the depth of focus being solely a function of the microscope optics, which were described previously. The laser pulse delay between successive exposures was adjusted to maintain particle displacements of five to ten pixels for the bulk of the fluid in each measurement zone, as the local fluid velocity distribution varied significantly at a given Reynolds number.

The tracer particles used are Fluoro-Max red particles (Fisher, Waltham, MA, USA) with a particle diameter of 0.8 μm. These polystyrene particles have a density of 1.05 g/cm^3 and a refractive index of 1.59 for 589 nm wavelength light at 298 K. This particle size, used in conjunction with the aforementioned lens, yielded a depth of correlation of 27 μm [47, 48]. The maximal Stokes number (at the largest flow rate tested for the fin array with the smallest hydraulic diameter) was calculated to be 0.01, much smaller than the 0.1 limit for particle tracer errors of 1%.

Water was used as the particle carrier liquid as the particles closely match the density and refractive index of the fluid to produce accurate results. Tests were performed at flow rates of 60 to 150 mL/min, which corresponds to Reynolds numbers relevant to the application (between 500 and 2000), which was used to characterize the flow conditions to ensure that the flow structures visualized are the same as those obtained in equivalent flow conditions for air. To reduce the amount of fluid that needs to go through the system at a time, samples with three flow channels wide were produced with the same length as the performance sample, to determine the length for full development of the fluid flow.

To reduce the amount of measurement artefacts originating from signals reflected from the fin array sample's surface, the fins and sample base were painted with a layer of black ink (less than 5 µm thick, measured from a painted fin's cross-section), which absorbs the reflected intensity.

4.4.2 µPIV Image Post-processing

The raw image pairs in a set were first averaged to obtain a picture of the background intensity, as well as the remaining amount of the sample's reflected light. The averaged picture was then subtracted from the raw images, yielding images that contained only the position of particles, with most of the measurement artefacts removed. These images were then post-processed using Flowmaster's standard PIV cross-correlation algorithm, using a two-step process in which the interrogation window size is reduced from 64x64 pixels to 32x32 pixels, both with 0% overlap. Spurious vectors were then removed using the software's built-in vector filter function, where vectors with more than three standard deviations of difference to their neighbours were removed. This created image sets with low amounts of measurement artefacts, suitable for analysis. The image sets were then processed to create maps of average velocity, turbulence intensity and turbulence kinetic energy with the software's built-in functions.

4.4.3 Data Reduction

The different quantities measured by the µPIV analysis are presented in this section. The Reynolds number was calculated according to definition given previously in chapter 4.3.2. The turbulence intensity (I) of the flow was computed as:

$$I = \frac{u'}{\bar{u}} \qquad \text{(Eq 41)}$$

where *u'* denotes the Root-Mean-Square (RMS) value of the velocity fluctuations in time and $\bar{u}$ represents the mean velocity.

The Turbulence Kinetic Energy (TKE) of the fluid is evaluated using Flowmaster 7's built-in function, evaluated as:

$$K = \frac{1}{2}\left(\overline{u_1'}^2 + \overline{u_2'}^2\right) \qquad \text{(Eq 42)}$$

where K is turbulence kinetic energy, $\overline{u_1'}$ is the value of the axial velocity fluctuations and $\overline{u_2'}$ is the value of the transverse velocity fluctuations. This informal definition of the turbulent kinetic energy is attributable to the 2D nature of the μPIV measurements, where the software neglects the contribution of the fluctuations of the 3rd velocity component ($\overline{u_3'}$). This definition is used as the variations in properties in the third axis cannot be measured or adequately approximated.

4.5 CFD Simulation

A computational model was developed to complement the experimental studies described in chapter seven. This model was constructed using a commercial computational fluid dynamics (CFD) software: Gambit was used to create the domain geometry and mesh, while Fluent was used to solve the mass, momentum and energy equations in a coupled semi-implicit scheme (SIMPLE) for steady-state, incompressible fluid flow. The Reynolds Averaged Navier-Stokes (RANS) equations approach was used to model the turbulent behavior of the flow, using the realizable k-ε turbulence equations for three different mass flow rates (0.00136, 0.00272 and 0.00550 kg/s), which correspond to Reynolds numbers of 500, 1000 and 2000. Although the Reynolds numbers involved potentially lie in the sub-critical regime, the use of a turbulence model (instead of a purely laminar model) is warranted due to the complexity of the expected flow structures and the non-negligible contribution of turbulence, as demonstrated in the literature [60, 61]. Furthermore, as it will be shown in Chapter 7, the turbulence intensity levels obtained with the simulation cannot be neglected, especially near the surface of the heat transfer enhancing features. Fluent's standard wall functions were selected, as the mesh is sufficiently fine ($y^+ = 0.31$) to appropriately resolve the near-wall features of the flow. Gravity and radiative heat transfer were neglected.

The three-dimensional solution domain is separated in a solid zone (pin fins) and a fluid zone (flow), with the fluid zone meshed with unstructured tetrahedral mesh and the solid zone meshed with hexahedral element dominated mesh. The solid zone mesh point density was set at 20 points per edge, while the fluid zone was set to 50 mesh points per edge. A schematic of the computational domain is shown in Figure 31 and the boundary conditions applied to the different surfaces are summarized in Table 2**.**

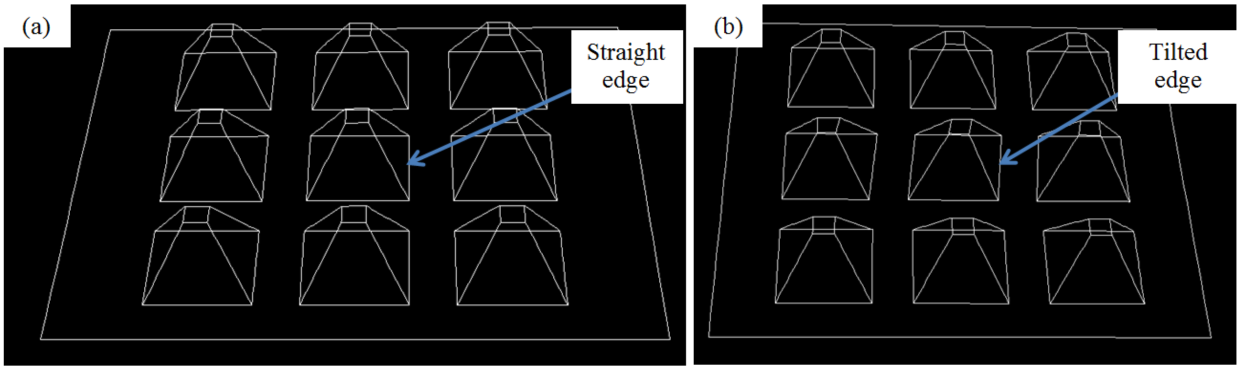

Figure 31: Computational Domain: (a) for the Regular (Straight Pyramidal Fin) Model; (b) for the Modified (Tilted Pyramidal Fin) Model

A cross-section of the computational domain is shown in Figure 32, with the white edges representing the edges of the fluid mesh elements and the red edges belonging to the edges of the solid mesh elements.

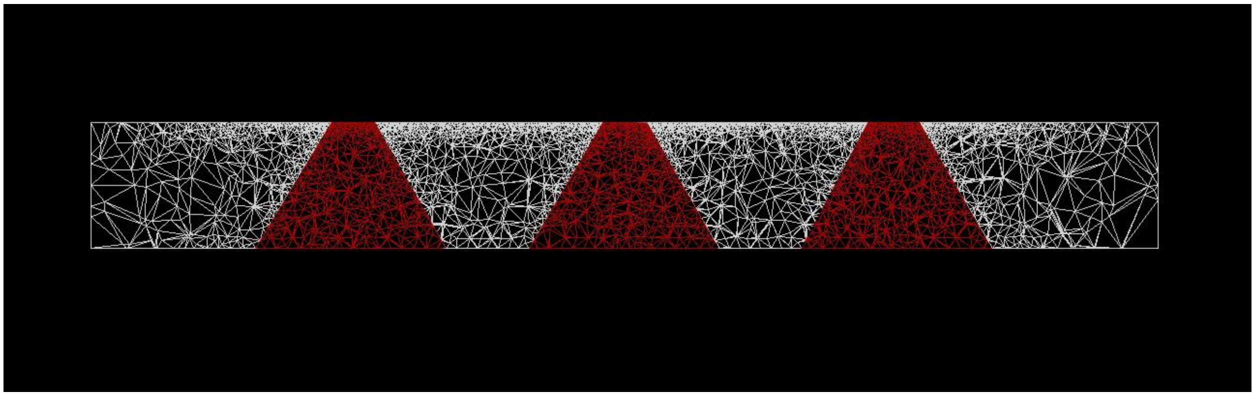

Figure 32: Cross-section of the Computational Domain with red edges representing the edges of the solid mesh elements and the white edges representing the fluid mesh elements

To model the heat transfer, a constant wall surface temperature of 360 K and a fluid inlet temperature of 300 K were selected to reflect typical temperature differences observed in the thermal performance experiments. For the purpose of simplicity, the fin surface walls were treated as smooth conductive surfaces in the solid zone, while the bounding walls were considered to be smooth, adiabatic surfaces.

Table 2: Surface Boundary Conditions for Fluent Model

Surfaces	Boundary condition	Comment/ Values
Inlet	Mass Flow Inlet	Flow normal to surface, turbulence intensity specified at 5% with hydraulic diameter of 1.019 mm, flow rate dependant on target Reynolds number, fluid temperature of 300 K
Outlet	Outflow	No outlet specifications
Top, Sides	Wall	Adiabatic, no-slip
Flow Channel Floor, Pyramid Floor	Wall	Constant surface temperature (T = 360 K), no slip
Pyramid Side Surfaces	Wall	Conductive, no-slip

The model has the same width as the μPIV experimental samples, but has a reduced length, to save computation time. This reduction in domain length can be achieved as it was observed experimentally that the large scale recirculation structures do not vary significantly as the number of rows increases. The dimensions used for the pyramids and passage width reflect the average measured dimensions of the specimens used for the μPIV study which are presented in Chapter 7. Figure 31 (b) shows a second computational domain that was used for modeling, with the main difference being that the middle row of the fin array has transverse flow passages at an 85° angle with the axial flow passages (instead of being purely perpendicular), following observations which are detailed in Chapter 7. A grid independency test was performed and it was determined that 597,275 cells yielded satisfactory results while not being too expensive on computational time. Calculations were conducted until the absolute residuals of the heat, mass and momentum were evaluated to be less than 10^{-6}, at which point the solution was considered to have reached convergence. Temperature and pressure were also monitored at the outlet to ensure that their value had reached a steady value that did not change with further iterations.

CHAPTER 5 PROOF OF CONCEPT AND EARLY CHARACTERIZATION OF PIN FINS ARRAYS PRODUCED BY CGDS

The article presented in this chapter presents the early work performed regarding the production of pin fin arrays with CGDS. The manufacturability of such arrays is explored with the use of stainless steel and aluminum feedstock powders, using a Plasma Giken CGDS system. Different sizes of wire mesh masks were investigated and trials were performed to determine the stand-off distance required between the CGDS nozzle and the mask, as well as the distance required between the mask and the substrate for the production of near-net shape fin arrays with clean passages and well defined fins. Furthermore, this article details the elaboration of an in-house test fixture for the determination of the hydrodynamic and thermal performance of heat transfer surfaces. The results obtained with this apparatus for an unfinned surface were compared to data previously reported in the literature by Kays and London [9] and were found to agree closely, which validated the use of this fixture for further tests on pin fin arrays.

Several tests were also performed regarding the production of net shape plain rectangular fin arrays with the CGDS process. These tests were not included in the article due to the mitigated success of the production of such fin arrays. As such, efforts were concentrated on improving the manufacturability and performance of the near-net shape pin fin arrays from then on.

This peer-reviewed article was reproduced with the permission of the copyright owner, ASM International.

JTTEE5 22:1210–1221
DOI: 10.1007/s11666-013-9968-x
1059-9630/$19.00 © ASM International

Peer Reviewed

Net Shape Fins for Compact Heat Exchanger Produced by Cold Spray

Yannick Cormier, Philippe Dupuis, Bertrand Jodoin, and Antoine Corbeil

(Submitted April 29, 2013; in revised form June 25, 2013)

This work explores the manufacturability of pyramidal fin arrays produced using the cold spray process. Near-net shaped pyramidal fin arrays of various sizes and fin densities were manufactured using masks made of commercially available steel wire mesh. The feedstock powders used to produce the fins are characterized using scanning electron microscopy. Obstruction of the masks was investigated. The standoff distances between the substrate, mesh, and nozzle were empirically determined. Fin array characterization was performed using digital microscopy. The fin arrays' heat transfer performance was assessed experimentally for a range of Reynolds number relevant to the application sought. The fins produced using the cold spray process outperform traditional straight (rectangular) fins at the same fin density and it is hypothesized that this is due to increased fluid mixing and turbulence.

Keywords cold spray, compact heat exchanger, heat transfer, net shape forming, pyramidal fin array

1. Introduction

Distributed power generation (DPG) offers a novel approach to reduce power losses, as electricity is carried over shorter distances to the end users, thus decreasing power line losses. It also presents the advantage of protecting the grid against widespread electrical failure, as generators individually serve a smaller population (Ref 1, 2). Micro-turbines (MT) are instrumental in the development of a high efficiency DPG system. MTs are small scale, single stage, and single shaft gas turbine generators. They provide the combined advantages of low emissions, high reliability, and good efficiency in a compact package (Ref 3). The major drawback is the associated wasted heat. Increasing the viability of DPG is directly linked with the development of higher efficiency MTs that generate between 25 and 500 kW. The simplest MT designs often have efficiencies below 20%, a lower value than diesel, and gasoline engines which typically operate between 30 and 35% thermal efficiencies over the same power production range (Ref 4). However, MTs equipped with a recuperator preheating the inlet gas using the heat recovered from the hot exhaust gases have the potential to theoretically attain 50% thermal efficiency (Ref 4). This waste heat could also be used for plant processes requiring heating or hot water production. In these cases, efficiencies in the order of 80% are attainable by such systems, referred to as combined heat-power (CHP) systems (Ref 3).

Recuperators play a vital role to a successful MT design, and often represent 20-25% of the cost and 20-35% of the volume of a MT package (Ref 4). Typically, unit cost and volume are closely tied together, as material cost is one of the main contributors to the total cost. Increasing recuperator efficiency by 5-10% can improve the overall thermal efficiency of the system by the same amount (Ref 4). Currently, recuperators operate at efficiencies ranging from 75 to 85%. These recuperators usually use shell and tube or packed bed geometries, however they experience problems such as leakage, high pressure losses, axial conduction losses, and high manufacturing cost (Ref 5, 6).

A design of compact heat exchangers, referred to as a wire mesh heat exchanger (WMHE), was developed as a solution for common challenges faced by high efficiency compact heat exchanger. WMHE are based on the concept of using a metallic wire mesh as a conductive material inside a cellular metal sandwich structure, first investigated in the late 1980s (Ref 7, 8). The first configuration developed using this concept was the folded wire mesh geometry, shown in Fig. 1. This geometry is produced by successively folding wire mesh textiles and brazing thin metallic sheets to these folds to create a flow barrier. The disadvantage of this technique is that the contact area per fold between the mesh the brazed plates is small, combined with the maximum number of times the wire mesh can be folded per unit length, thus limiting the heat that can be transferred (Ref 9). This limitation, in addition to the large cost associated with the manufacturing technique, calls for an improved production method which can reduce both cost and volume while maintaining high heat transfer properties.

This article is from a presentation at the 2013 International Thermal Spray Conference, held May 13-15, 2013, in Busan, South Korea, and has been expanded from the original presentation.

Yannick Cormier, Philippe Dupuis, and **Bertrand Jodoin,** Department of Mechanical Engineering, University of Ottawa, Ottawa, ON Canada; and **Antoine Corbeil**, Brayton Energy Canada, Aylmer, QC Canada. Contact e-mail: yannick.cormier@uottawa.ca.

Nomenclature

ΔT_1	Inlet temperature difference (K)
ΔT_2	Outlet temperature difference (K)
ΔT_{lm}	Log-mean temperature difference (K)
η_{f}	Individual fin efficiency
η_{o}	Overall fin efficiency
θ	Spray angle (°)
μ	Dynamic viscosity (Pa s)
ρ	Fluid density (kg/m^3)
A_{f}	Fin heat transfer area (m^2)
A_{flow}	Net flow area (m^2)
A_{tot}	Total heat transfer area (m^2)
A_{u}	Unfinned heat transfer area (m^2)
B	Base fin length (m)
Cp	Fluid specific heat capacity (kJ/(kg K))
D	Base diameter (m)
d_{h}	Hydraulic diameter (m)
FD	Fin density (fin/m)
H	Channel height (m)
h	Convective heat transfer coefficient (W/(m^2 K))
I_1	Bessel function of order one
I_2	Bessel function of order two
j	Colburn factor
k_{f}	Fluid thermal conductivity (W/(m K))
k_{m}	Fin material thermal conductivity (W/(m K))
L	Sample length (m)
$\dot{m}$	Mass flow rate (kg/s)
m	Fin heat transfer parameter (m^{-1})
Nu_{D}	Nusselt number based on hydraulic diameter
N_{f}	Number of fins
P_{flow}	Flow perimeter (m)
Pr	Prandtl Number
q	Heat flux (W/m^2)
Re_{D}	Reynolds number based on hydraulic diameter
R_{eq}	Equivalent thermal resistance (K/W)
S	Space between fin edges (m)
T_{in}	Inlet fluid temperature (K)
T_{out}	Outlet fluid temperature (K)
UA	Thermal conductance (W/K)
V	Fluid velocity (m/s)
W	Channel width (m)

To this end, a new method for producing WMHE has recently been developed. The innovation of this approach resides in the fact that the wire mesh textile is stacked and cut, then sealed with a thin metallic layer, as shown in Fig. 2(a) and (b) (flow barriers on the longitudinal side are not represented for clarity). These features allow more contact area per unit length between the heat transfer medium and the pressure barrier (brazed plates). Nevertheless, this design/method for producing WMHE does offer some areas for improvement. Currently, the cost associated with brazing a thin metal sheet to the wire mesh is high and the operation is labor intensive. To replace this process, research has been performed where a thick and dense metallic coating is produced using thermal or kinetic spray processes. Once this coating has been applied, fins are machined on the outer surface to produce simple rectangular (straight cut) fin geometries (Fig. 2c). While this operation saves costs, it is time consuming and is currently restricted by machining tolerances.

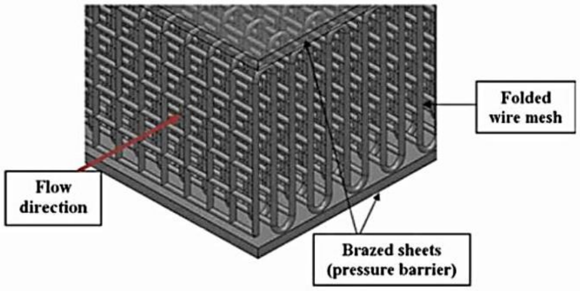

Fig. 1 Wire mesh heat exchanger using folded wire mesh geometry as heat transfer medium

Other interesting and promising types of heat exchangers were developed using a similar principle but with different types of internal heat transfer medium, such as metal foam heat exchangers encased in a metallic skin deposited using wire-arc or plasma spray, as investigated by Salimi Jazi et al. (Ref 10, 11). In this case, thermal spray processes are used to seal commercially available nickel foam bricks with Inconel 625 to create fully enclosed heat exchangers. No heat transfer enhancing features are used on the outer surface of the heat exchangers.

Thermal spray deposition processes operate on the principle of heating and accelerating a carrier gas to project particles onto a substrate in order to form a dense coating. Combustion and plasma spray processes such as high velocity oxy fuel (HVOF) and plasma spray use a high temperature gas stream to melt the projected particles, where adhesion is sustained by the particles solidifying on the substrate surface and onto each other. Kinetic spray processes such as cold spray, rely on momentum transferred from an inert gas, usually helium or nitrogen, to relatively cold particles (usually less than half the melting temperature) which are projected onto a substrate's surface. The gas is accelerated to supersonic speeds using a convergent-divergent (DeLaval) nozzle, where its kinetic energy is imparted to the particles from fluid drag effects (Ref 12, 13). Upon colliding with the substrate, this energy is used to plastically deform these particles and to induce adhesion.

In this paper, the viability of using cold spray to manufacture near-net shape fin arrays was investigated as a potential solution to the problems encountered by fin machining. Pyramidal fin arrays were produced using cold spray which required no post-processing. The aim of this study is to demonstrate the manufacturability of such fins and also to start comparing the heat transfer properties of pyramidal and rectangular fin arrays by studying specifically the 24 fins/in. case.

Two fin materials were selected for their widely different thermal and mechanical properties: aluminum and stainless steel. These materials have a high resistance to

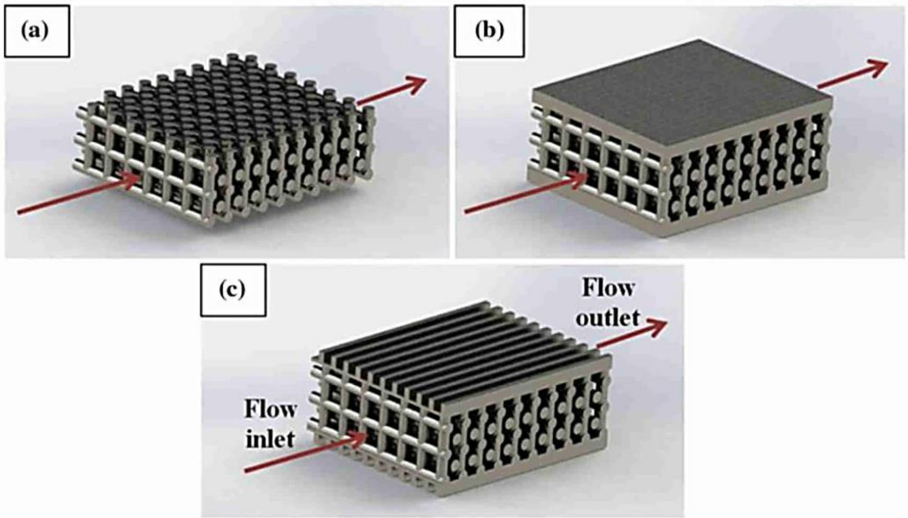

Fig. 2 Successive steps to manufacture wire mesh heat exchanger: (a) stacked wire mesh, (b) brazed thin metallic sheets, (c) machined external fins

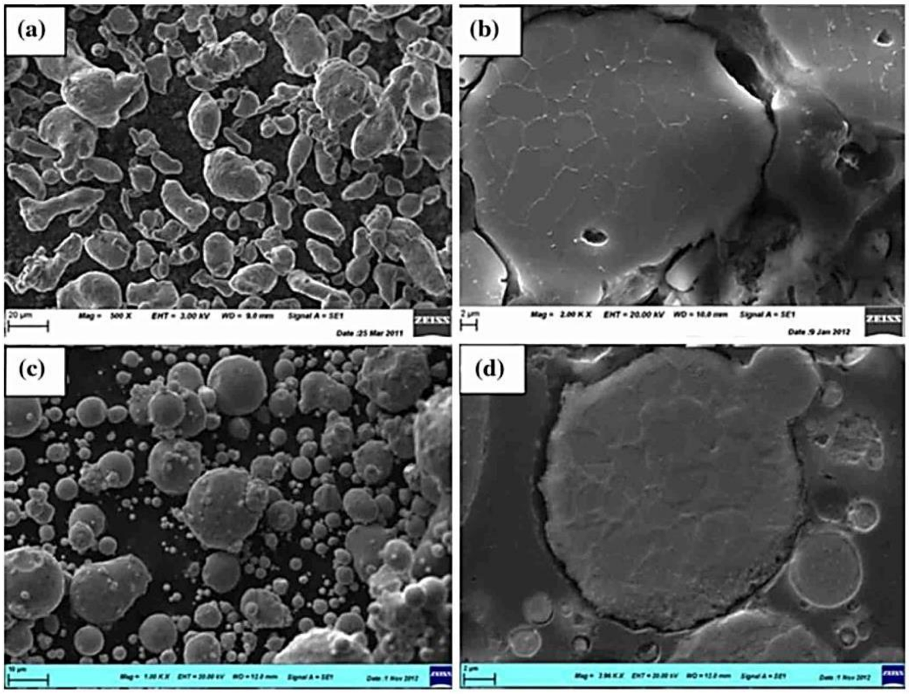

Fig. 3 SEM images of (a) As-received pure aluminum feedstock powder; (b) etched cross-section of pure aluminum particle; (c) As-received 304L stainless steel feedstock powder; (d) etched cross-section of 304L stainless steel particle

corrosion and are known to be easily deposited with cold spray. Stainless steel's operating temperature is higher than aluminum, but its thermal conductivity is lower. To this end, applications that have high process temperatures would require the former material, while lower process temperature applications could benefit from the increase in performance the latter material could offer.

2. Experimental Coating System Description

The cold spray system used for this work is a commercially available Plasma Giken PCS-1000 (Ref 14). The spray nozzle has a 3.0 mm throat diameter and a 6.5 mm exit diameter.

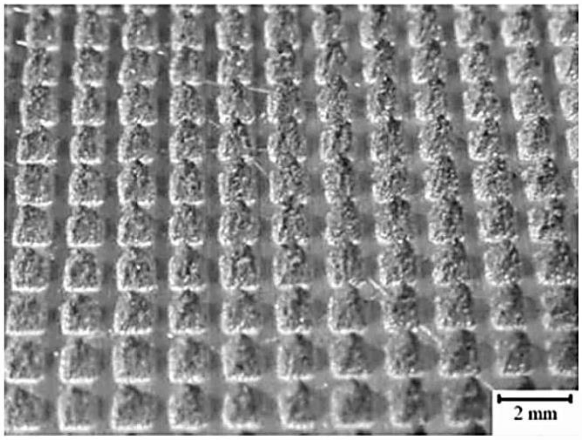

Fig. 4 Fin array overview of aluminum sample Al-2 produced using cold spray and masking technique

The first feedstock powder used was aluminum (99.8% Al), provided by Centerline (Windsor) Ltd. (Windsor, Ontario, Canada), and distributed commercially under the name SST-A5001. The powder size range is characterized by a D_{10} value of 13.29 μm, a D_{50} value of 25.35 μm, and a D_{90} value of 49.58 μm, as measured by a Microtrac S3500 laser diffraction analysis apparatus provided by Microtrac (Montgomeryville, Pennsylvania, USA). Figure 3(a) presents an image of the powder taken by a scanning electron microscopy (SEM) EVO-MA 10 provided by Zeiss (Oberkochen, Germany). It presents an elongated, non-spherical geometry. The grain structure is shown in Fig. 3(b), as etched with Keller's reagent. The grains have an equiaxial shape in the center of the particle, while the exterior is composed mostly of elongated grains.

The second material used was commercially available stainless steel grade 304L, provided by Sandvik Osprey Ltd (Sandviken, Sweden). The powder size range is characterized by a D_{10} value of 4.55 μm, a D_{50} value of 14.14 μm, and a D_{90} value of 31.30 μm, as assessed by cumulative volume based laser diffraction analysis. Figure 3(c) presents an SEM image of this powder. It presents a spherical geometry. The grain structure is shown in Fig. 3(d), as etched with Methanolic Aqua Regia reagent. The particles observed have an equiaxial grain geometry.

3. Experimental Procedure

3.1 Masking Technique

To create pyramidal fin arrays (Fig. 4), commercially available plain woven, steel wire mesh (McMaster-Carr, Aurora, OH, USA) was used to mask the substrate and generate the required fin geometry. This process is illustrated in Fig. 5, where SD_{MS} and SD_{GM} designate the standoff distances from the mesh to the substrate and from the mesh to the nozzle, respectively. This creates a pyramidal fin array that closely mimics the reversed geometry of the chosen wire mesh, with peaks aligning with the holes of the screened area and little to no deposition underneath the wires (Fig. 6). Other thermal spray processes were not considered for this production method as they would clog the mask.

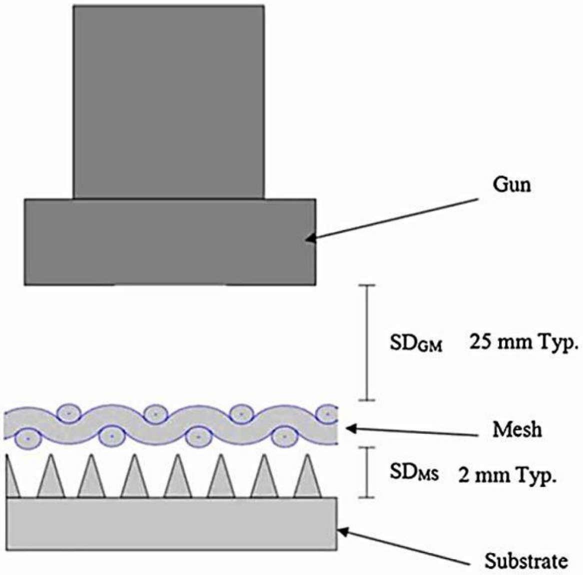

Fig. 5 Schematic of the masking technique used to create pyramidal fin arrays

Fins were cold sprayed on aluminum substrates (Al6061 T6) with standard dimensions of 5.1 cm by 5.1 cm. The cold spray trials detailed in this work were done on extruded aluminum substrates instead of thermal sprayed coatings on the WMHE to demonstrate viability. Further work will be performed to determine the parameters required to produce the same features on specific thermal spray sealed heat exchangers. The substrates were cleaned and degreased using acetone after being cut to size. No further coupon preparation, such as grit-blasting or heat treatments, was performed. The spray parameters used to obtain these samples using nitrogen as the carrier gas are given in Table 1 for both feedstock powders. The number of passes was varied according to the target height of the fin arrays. No post-treatment of the sprayed samples was performed.

Standard metallographic procedures were used to obtain cross-sections of the sprayed samples. Control specimens were sprayed without masking to obtain a standard for comparison and to establish a porosity level baseline. All the image analysis was performed using Clemex Vision Lite (Clemex Technologies Inc., Longueuil, QC, Canada) image analysis software. Porosity levels are reported with a mean value of 10 measurements for each data set. Spray angles are determined from the measured geometries of the sprayed samples.

Several trials were performed to determine the effect of the standoff distance between the wire mesh and the gun, as well as the distance between the mask and the substrate. It was determined that starting with a very small distance between the mesh and the substrate (less than

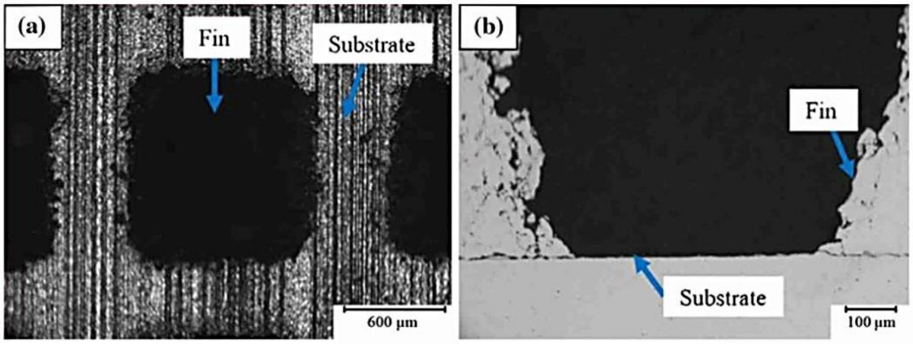

Fig. 6 (a) Top view of typical fin deposition (aluminum sample); (b) cross-section of typical fin deposition illustrating the clean area between the fins (aluminum sample)

Table 1 Spray parameters

Powder type	Nozzle inlet pressure, MPa	Nozzle inlet gas temperature, °C	SD_{GM}, mm	SD_{MS}, mm	Nozzle traverse speed, mm/s
Al SST-A5001	3	300	25.4	2.0	350
SS 304L	3	900	25.4	2.0	300

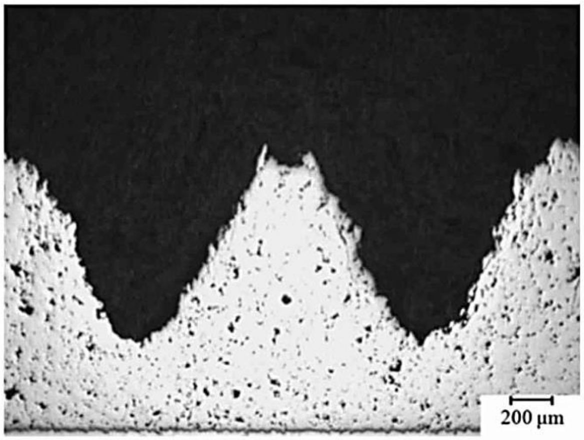

Fig. 7 Deposition between fins when mesh-substrate distance is larger than 3 mm for typical aluminum sample

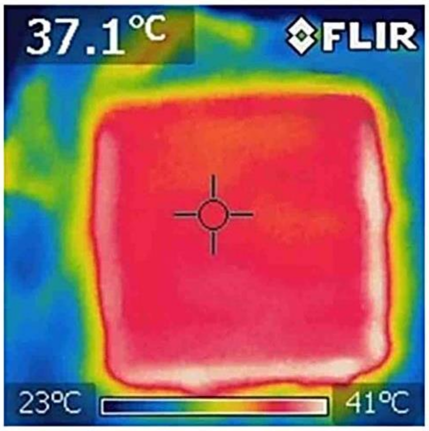

Fig. 9 Uniform heat flux on the fins (without flow) resulting in a uniform surface temperature

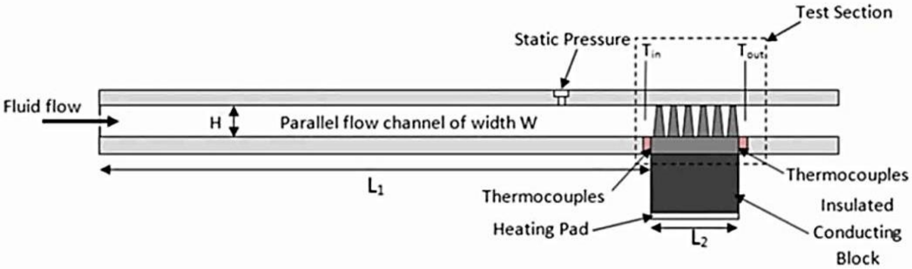

Fig. 8 Schematic of the heat transfer test fixture

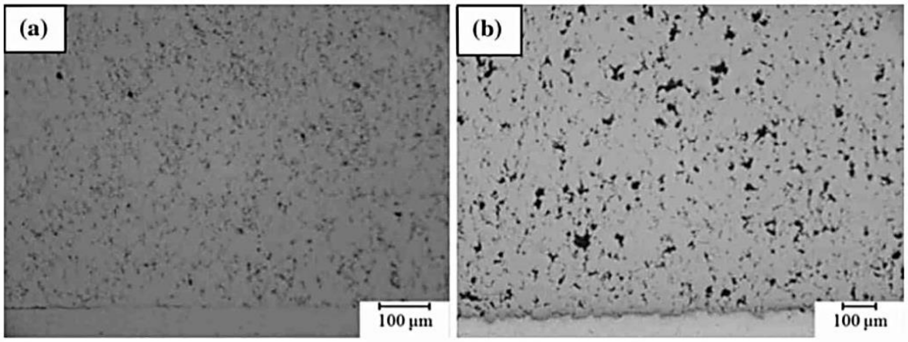

Fig. 10 Cross-section of coatings control samples used to characterize the porosity level (a) Al SST-A5001; (b) SS 304L

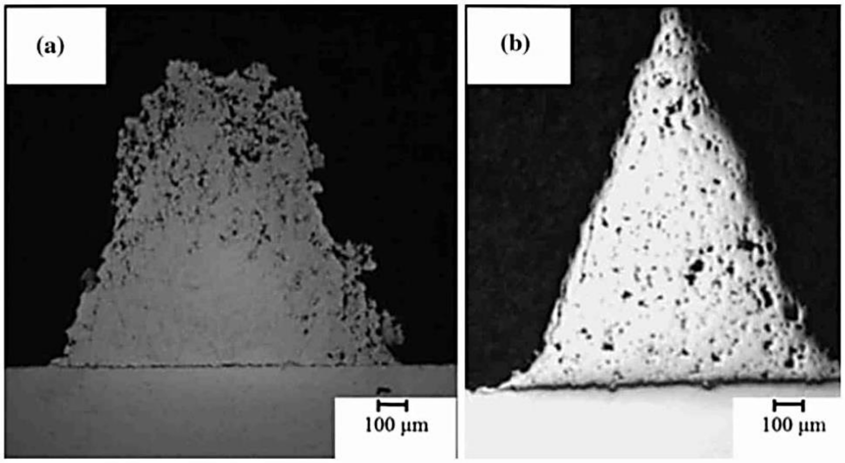

Fig. 11 Cross-section of a fin of samples showing different porosity distributions (a) Al-1; (b) SS-2

Table 2 Pyramidal fin geometry of tested samples

Sample number	Fin density, Fins/in.	Wire diameter, in.	Fin height, mm	Hydraulic diameter, mm	Total heat transfer area, mm^2	Spray angle, °
Al-1	12	0.035	1.8	1.57	4335	19.3
Al-2	16	0.028	2.2	1.49	5820	11.3
Al-3	16	0.018	1.4	1.13	4767	22.0
Al-4	24	0.014	1.4	0.92	6117	14.1
SS-1	12	0.035	2.0	1.67	4671	17.1
SS-2	16	0.028	1.5	1.27	4599	16.3
SS-3	30	0.016	1.0	0.76	5129	12.4

Table 3 Samples tested for comparison

Sample number	Fin density, Fins/in.	Fin width, in.	Fin spacing, in.	Height, mm	Hydraulic diameter, mm	Total heat transfer area, mm^2
US	N/A	N/A	N/A	2.0	3.85	2581
SC-B	24	0.015	0.025	1.7	0.92	9807
SC-C	24	0.015	0.025	1.4	0.87	8344

0.75 mm) created problems where the mask would become embedded in the coatings produced. Increasing the distance to more than 3.0 mm has a detrimental effect on spray angles and spray edge cleanliness. At this standoff distance, some deposition underneath the wires is noted and edges do not appear as sharp, as shown in Fig. 7. The optimal distance found is from 1.0 to 2.5 mm between the wire mesh mask and the substrate. A distance of 2.5 mm was used for the samples tested in this work. The optimal standoff distance between the mesh and the cold spray nozzle was found to be 25 mm.

3.2 Heat Transfer Test Apparatus

Performance of the various fin arrays produced was assessed using an in-house heat transfer and pressure drop test apparatus, adapted from the literature (Ref 5). A schematic diagram of the apparatus is shown in Fig. 8.

The main components of this apparatus are the test section, heating pad, air supply and data acquisition system. The air is supplied by a compressed air line, properly filtered and dehumidified to obtain room temperature, dry air, free from oil contamination. The air inlet flow rate is controlled by a flow meter and a needle valve. This air is forced into a rectangular channel with the test section located near the exit. This rectangular channel's top and bottom plates (76.2 mm wide by 457.2 mm long by 19.05 mm thick) are made of acrylic, and they are spaced apart using a rectangular rubber gasket, which is compressed to obtain the required hydraulic diameter. These gaskets also ensure that the joint is leak-proof. A length of 320 mm of unobstructed flow ensures that the fluid is fully developed hydrodynamically when it reaches the test section for the given hydraulic diameter and Reynolds number (Ref 15).

The test sample is subjected to a constant heat flux provided by a strip heater. A conducting block is used to ensure that heat is evenly distributed onto the substrate's surface, resulting in a constant surface temperature under free convection conditions, as shown in Fig. 9.

A stagnation pressure tap is located 25.4 mm upstream from the test section. Two thermocouples are located 6 mm before and after the test section at mid-height to record the fluid local average temperature. Four thermocouples are attached to the fin array's base, with two on the side facing the incoming flow, and two on the side facing the exiting flow. On each face, one thermocouple is located on the centerline, while the other thermocouple is located 6 mm from the wall. All the thermocouples used are T-type, butt-bonded, thin gage (28 gage) thermocouples.

Measurements were performed at steady-state conditions and repeated until statistical significance was achieved. Data samples were taken over a 30 s interval, at 2 Hz. Five sets of data samples were recorded for every flow condition. Measurements were taken at flow rates corresponding to Reynolds numbers varying from 200 to 2000, as this is the typical application range sought for these exchangers. Deviation of the measurements from the mean value was less than 5%.

4. Results

4.1 Fin Array Characterization

Low porosity levels are observed for the bulk control coatings produced (without masking), with measurements indicating less than 5% porosity levels, as shown in Fig. 10. Fins produced with the aluminum powder have a different porosity distribution than the fins produced with stainless steel powder. Figure 11(a) shows that the porosity in the aluminum fins varies from a fully dense core to a porous exterior layer. Stainless steel shows a relatively uniform porosity level throughout the coating, as seen in Fig. 11(b). Some of the voids are relatively large (20 μm) which is comparable to the voids observed in the outer layer of the aluminum fins. This difference in porosity distribution is attributed to the fact that aluminum and stainless steel have different bonding characteristics. The primary factor is that the aluminum core is compacted by the impacts of the subsequent particles on the newly formed coating, while the porous exterior layer does not benefit from this phenomenon. This phenomenon is much more pronounced for the aluminum feedstock because its surface oxide layer is easily broken, compared to stainless steel. Furthermore, the aluminum particles are larger and their non-spherical morphology tends to increase the fluid drag, which both contribute to increase the particle momentum and oxide breaking power. The second factor is that aluminum is sprayed at parameters on the lower edge of the deposition window to reduce nozzle clogging problems, while stainless steel is sprayed with a high enough gas temperature and pressure to overcome its higher critical velocity and allow a better initial adhesion without compaction (Ref 16, 17).

Several geometries of pyramidal fins were successfully deposited on aluminum substrates, from 12 to 30 fins/in. Table 2 presents the different pyramidal fin geometries of the samples produced while Table 3 shows the other samples tested for reference or comparison purposes. Sample labeled US is an unfinned surface while samples labeled SC are vertical rectangular (straight cut) fin samples, with the suffix B and C designating that the fins were machined from bulk Al 6061 T6 or from a pure aluminum cold sprayed coating, respectively.

Scalability does not seem to be an issue, as much larger samples (101.6 mm by 152.4 mm) were also successfully produced with no differences noted when compared to the smaller samples, as shown in Fig. 12.

Deposition of material is noted on the mesh, as shown in Fig. 13. The build-up has a pyramidal prism shape along the wire length, and once a critical height has been attained, deposition on the mesh slowly stops. This critical height is a function of the sprayed material, spray parameters and fin density. At this critical height, the impact angle is so small that the normal component of the particle velocity is not sufficient to create adhesion. The wire mesh sizes tested up to 24 wires/in. do not clog, even after several minutes of deposition. At 30 wires/in. with a wire diameter of 0.016″ (0.41 mm), clogging of some holes is noted with the aluminum feedstock. The stainless steel feedstock powder does not show this behavior. This is explained by looking at the particle size distribution for these two materials, noting that the average aluminum particle is 80% larger than the average stainless steel particle and that the aluminum adheres very easily when sprayed, making it much more likely to clog. The stainless steel, on the other hand, is much harder to deposit and has reduced tendency to block the mesh holes. Mesh densities higher than 30 wires/in. were not tested.

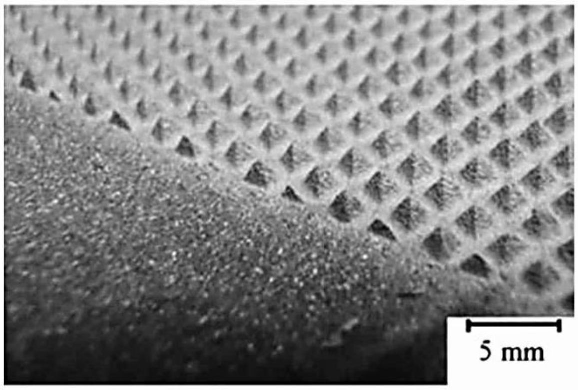

Fig. 12 Typical stainless steel pyramidal fin arrays

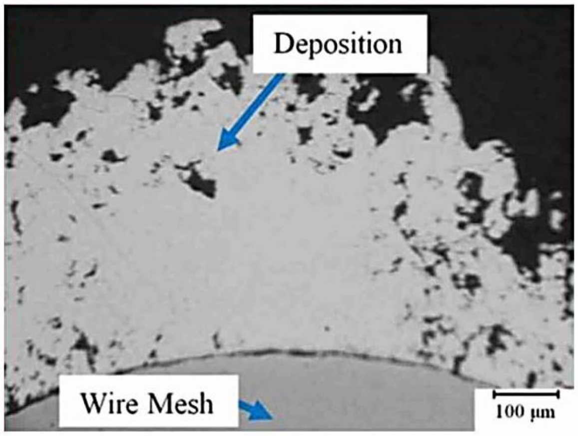

Fig. 13 Deposition on the masking mesh of aluminum sample Al-1

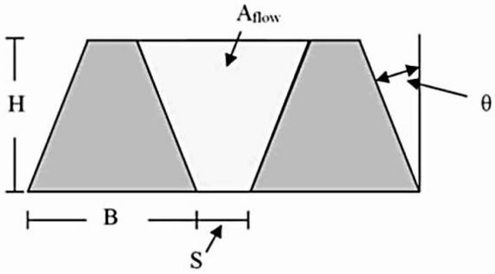

Fig. 14 Schematic of the fin array unit with geometric variables identification

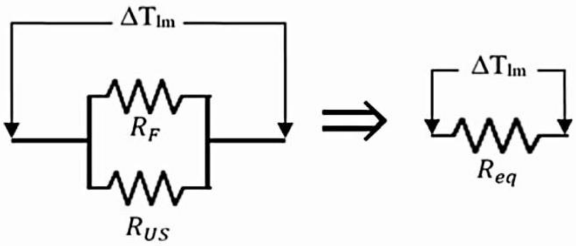

Fig. 15 Fin array thermal circuit diagram

4.2 Heat Transfer Performance

4.2.1 Data Analysis Method. To analyze the raw data obtained and compare it in suitable manner, non-dimensional parameters must be used. For this purpose, flow conditions are expressed using the Reynolds number. This study provides non-dimensional numbers with a characteristic length based on the hydraulic diameter for the comparison of different fin arrays. Performance is assessed using the thermal conductance of the fin array, which is equal to the amount of heat transferred per unit temperature difference between the fin array and the fluid, measured in Watts per degree Kelvin. Figure 14 illustrates the geometric variable used to perform the analysis.

The Reynolds number based on the hydraulic diameter is given by:

$$Re_{\mathrm{D}} = \frac{\rho V d_{\mathrm{h}}}{\mu} = \frac{\dot{m} \cdot d_{\mathrm{h}}}{W \cdot \mathrm{FD} \cdot A_{\mathrm{flow}} \cdot \mu} \quad \text{(Eq 1)}$$

where $\dot{m}$ is the mass flow rate, d_{h} is the hydraulic diameter of the fin array, W is the sample width, FD is the fin density, μ is the fluid's dynamic viscosity, and A_{flow} is the total face area the fluid can flow into. The variables d_{h} and A_{flow} are given by:

$$d_h = \frac{4 \cdot A_{\mathrm{flow}}}{P_{\mathrm{flow}}} = \frac{2 \cdot A_{\mathrm{flow}}}{\frac{H}{\cos(\theta)} + S + H \cdot \tan(\theta)} \quad \text{(Eq 2)}$$

$$A_{\mathrm{flow}} = (S + H \cdot \tan(\theta)) \cdot H \quad \text{(Eq 3)}$$

where P_{flow} is the flow channel's perimeter, θ is the fin angle, S is fin spacing from edge to edge, and H is the fin height.

Figure 15 shows a thermal circuit of the fin array, with the reduction of the thermal resistances of the fins and the unfinned surface designated respectively by R_{F} and R_{us} to an equivalent resistance R_{eq}.

The thermal conductance parameter UA can be calculated as:

$$\mathrm{UA} = \frac{1}{R_{\mathrm{eq}}} = h \cdot A_{\mathrm{tot}} \cdot \eta_{\mathrm{o}} \quad \text{(Eq 4)}$$

where h is the convective heat transfer coefficient, η_{o} is the overall surface efficiency, and A_{tot} is the total heat transfer area, given by:

$$A_{\mathrm{tot}} = A_{\mathrm{f}} + A_{\mathrm{u}} = \left(2N_{\mathrm{f}}B\sqrt{H^2 + \left(\frac{B}{2}\right)^2}\right) + \left(WL - N_{\mathrm{f}}B^2\right) \quad \text{(Eq 5)}$$

In the previous equation, N_{f} is the number of fins in the array, B is the fin's length at its base, L is the sample's length, A_{f} denotes the total fin heat transfer area, while A_{u} represents the unfinned base's exposed area. The overall efficiency is calculated using the following equation:

$$\eta_o = 1 - \frac{A_f}{A_{tot}}(1 - \eta_f) \qquad \text{(Eq 6)}$$

where η_f is the individual fin efficiency, defined as the heat transferred by the fin over the maximum possible heat that can be transferred, which is numerically equal to:

$$\eta_f = \frac{2}{mH}\frac{I_2(2mH)}{I_1(2mH)} \qquad \text{(Eq 7)}$$

with:

$$m = \sqrt{\frac{4h}{k_m D}} \qquad \text{(Eq 8)}$$

In the previous equations adapted from Incropera's work (Ref 15), I_1 and I_2 denote the first and second order Bessel functions, respectively, while k_m is the thermal conductivity of the fin's metal.

The individual fin efficiency equation for triangular pin fins are used for the sprayed pyramidal pin fins in this work since it is the shape with the most similar geometry. The only difference between the two is the shape of the base, since the equation is for a circular base while the manufactured fins have a square base. Therefore, D in the previous equation is replaced by the fin length at the base (B).

The fin array's convective heat transfer coefficient and Nusselt number are calculated with the following relations:

$$h = \frac{q}{\Delta T_{lm} A_{tot} \eta_o} \qquad \text{(Eq 9)}$$

$$Nu_D = \frac{h \cdot d_h}{k_f} \qquad \text{(Eq 10)}$$

In these equations, q is the heating rate, ΔT_{lm} is the log-mean temperature difference between the fluid and the fin array, and k_f is the fluid's thermal conductivity. The log-mean temperature difference is calculated with:

$$\Delta T_{lm} = \frac{\Delta T_1 - \Delta T_2}{\ln\left(\frac{\Delta T_1}{\Delta T_2}\right)} \qquad \text{(Eq 11)}$$

where ΔT_1 and ΔT_2 are the temperature difference between the fin surface and the flow at the inlet and outlet, respectively. The total heat input rate to the system is calculated using:

$$q = \dot{m} \cdot (T_{out} - T_{in}) \cdot \mathrm{Cp} \qquad \text{(Eq 12)}$$

where $(T_{out} - T_{in})$ is the fluid temperature difference between the entry and the exit of the test section, Cp is the fluid's thermal capacitance.

An uncertainty analysis was performed using the method described in Coleman and Steele (Ref 18). The uncertainties calculated with the root-square-method for the thermal conductance, the mean heat transfer coefficient, and Reynolds number were estimated to be less than 5% for all three measurement types.

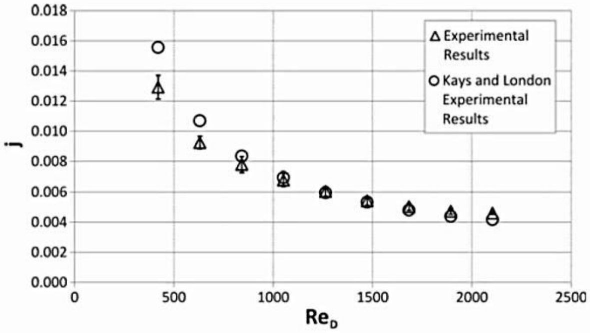

Fig. 16 Measurement accuracy comparison for an unfinned surface

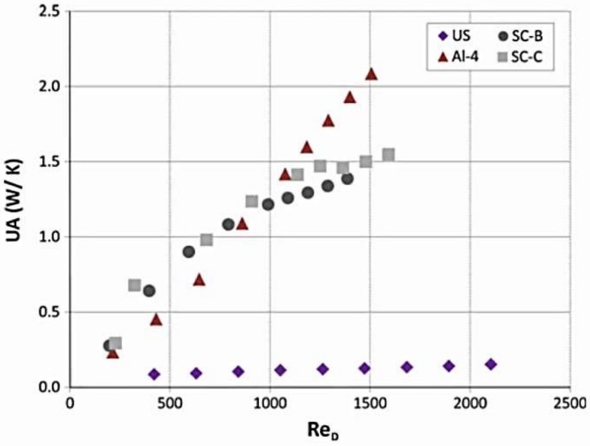

Fig. 17 Thermal conductance comparison between Al-4 (triangle), straight cut bulk (circle), and straight cut coating (square) while the unfinned surface is used as reference (diamond)

Tests were performed to determine the apparatus' accuracy. Experiments were conducted with an empty channel, heated on one side and insulated on the other, and then compared to existing curves for the same conditions produced by Kays and London (Ref 19). These curves use the Colburn factor as the performance indicator and their authors do not specify all the testing conditions required to transform this data back into raw data. The comparison must then be made using this parameter, which stems from an analogy between the transfer of heat and momentum, and which can be computed with:

$$j = \frac{Nu_D}{Re_D \cdot Pr^{1/3}} \qquad \text{(Eq 13)}$$

In the previous relation, Pr is the Prandtl number of the fluid. For these tests, the channel height was set to 2.0 mm, which yielded a hydraulic diameter of 3.85 mm. Tests were performed at flow rates of 0.0002 to 0.001 kg/s in 0.0001 kg/s increments, which correspond to Reynolds numbers of 421-2104. Figure 16 shows the results obtained using the test fixture, which show a high similarity with published results found in the literature, with the maximal deviation mostly at very low flow rates. The error can be

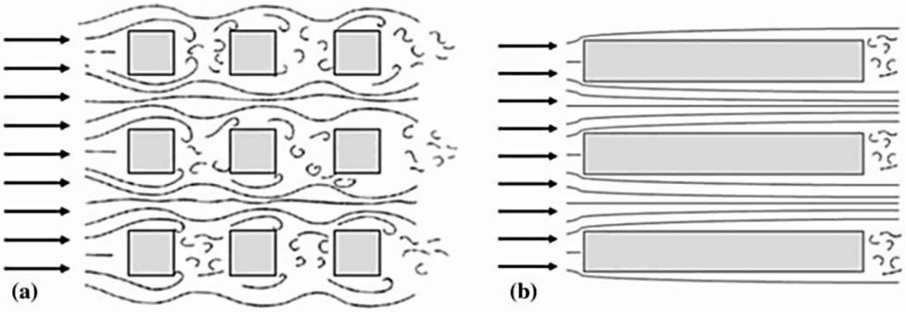

Fig. 18 Illustration of flow pattern for (a) pyramidal fin arrays; (b) straight cut fin arrays. Intensive mixing/turbulent zones are more frequent in pyramidal fin arrays

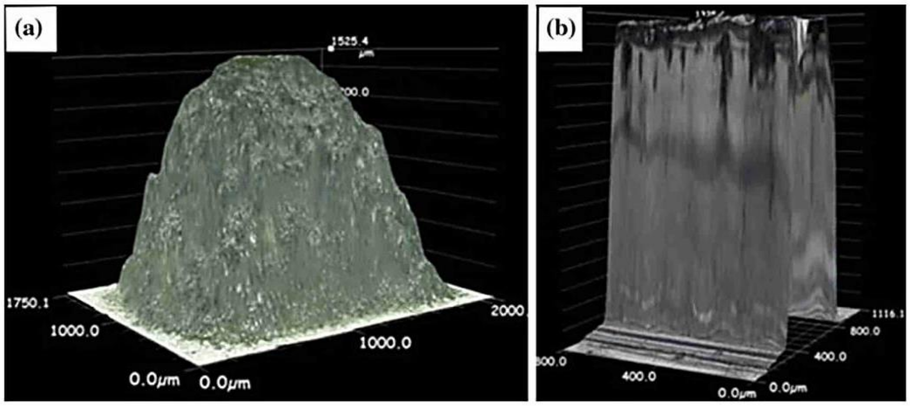

Fig. 19 Three dimensional images (from digital microscopy) of surface at ×300 magnification for (a) pyramidal fin arrays; (b) straight cut fin arrays

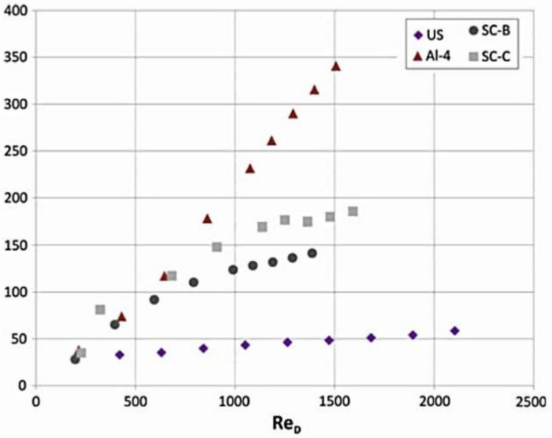

Fig. 20 Convective coefficient comparison between Al-4 (triangle), straight cut bulk (circle), and straight cut coating (square) while the unfinned surface is used as reference (diamond)

explained noting that the instrument uncertainty is highest at low flow rates due to the full scale measurement uncertainty, with the theoretical error at 15%. These tests act as a basis for the validation of the results obtained for the pyramidal fin arrays, where no published literature has been found to compare with.

4.2.2 Performance Comparison with Traditional Fin Arrays. The thermal conductance as a function of the Reynolds number for various fin array samples is shown in Fig. 17. The circle and square symbols represent data obtained from rectangular fin samples made from bulk aluminum and an aluminum coating, respectively. The triangle symbols represent a pyramidal fin sample made with the technique detailed previously, at the same fin density and hydraulic diameter than the straight cut samples. Finally, data obtained from an unfinned surface is represented by a diamond, and is shown for comparison purpose.

Very little performance difference can be seen between the rectangular fins cut from bulk Al 6061 and those cut from cold sprayed pure aluminum (Fig. 17). This is to be expected as the nominal compositions of these materials are very similar, the porosity level in the cold spray coating is less than 1% while the fin density, the width and the thickness of the samples are also identical. It is noted that the error bars on the graph were so small that they were barely visible and thus were not included. The increase in thermal conductance over the range of Reynolds number studied is due to the increase in the convective heat transfer coefficient. This is to be expected as flow detachment along the length of the fin creates turbulences which increase heat transfer. Increasing the Reynolds number also increases the detached flow length, creating more area with a higher heat transfer coefficient, leading to better thermal performance.

The performance of straight cut fins was compared with sprayed pyramidal fin array (Fig. 17). The pyramidal fin array with a fin density of 24 fin/in has a performance comparable to the straight cut fins with the same density when comparing thermal conductance up to 1200 Re_D. Beyond Re_D of 1200, pyramidal type fin thermal conductance values surpass those of straight cut fins with the same fin density by up to 30% at Re_D of 1500. This effect is believed to be due to a large increase in the convective heat transfer coefficient from fluid mixing attributable to two mechanisms. The first factor is the turbulent wake behind the fins. This turbulence is due to the flow detachment from the fin surface, which does not occur as prominently for continuous fins, as illustrated in Fig. 18. The second contributing effect is the fin roughness. Machined fins have a very low surface roughness due to the high quality surface finish inherent to the machining technique, while sprayed fins have a high degree of roughness (Fig. 19a, b). These three dimensional pictures were obtained using a depth of field microscope VHX-2000 provided by Keyence (Mississauga, ON, Canada), and show that the machined fins have a lower roughness than the instrument's resolution at 300× magnification (2 μm). The roughness levels found in pyramidal fins are believed to induce mixing of the fluid and further promote convective heat transfer. This is confirmed by Fig. 20, where the convective heat transfer coefficient of pyramidal fins is almost 100% greater than the convective coefficient of traditional fin arrays at Re_D of 1500. This increase in convective heat transfer coefficient is slightly offset by the increased heat transfer area offered by continuous straight cut fins. A 36% difference in total heat transfer area is measured between straight cut fins and pyramidal fins at the same fin density and height ($8344\ \text{mm}^2$ versus $6117\ \text{mm}^2$, respectively), as shown in Tables 2 and 3. Overall, the contribution of the increased convective heat transfer coefficient is sufficient to still provide an increased thermal conductance for pyramidal type fins.

5. Summary and Conclusion

Near-net shape pyramidal fin arrays of various sizes were deposited using commercially available wire mesh as a masking medium for the cold spray process. Fin characterization was performed using optical microscopy, while SEM micrographs were used to characterize the aluminum and stainless steel feedstock powders. The effect of standoff distances between the spray gun, mask and substrate was investigated, with an optimal range identified. Clogging of the wire mesh mask was found to occur at 30 wires/in. with a wire diameter of 0.016″ (0.41 mm) for the aluminum feedstock, while no problem was encountered with the stainless steel feedstock powder. Fin array performance was determined using a steady-stated forced air convection system subjected to a constant heat flux boundary condition on one side for a 24 fin/in. pyramidal sample and was compared to an equivalent 24 fin/in. rectangular fin sample. Further heat transfer experiments will be performed to determine the thermal performance of the other pyramidal fin array samples presented in this work and will be detailed in a later communication as the purpose of the current paper was to mostly demonstrate the process feasibility and potential. The new type of fins produced outperforms traditional straight cut fins at the same fin density and hydraulic diameter due to fluid mixing increasing the convective heat transfer coefficient. Significant opportunities exist to further improve this technique in every aspect, such as optimization of spray parameters and the study of the effect of other material types or anisotropy of the fin density, for example. A more in-depth characterization of the fluid mechanics properties of the pyramidal fin array will be performed in the near future.

Acknowledgments

The authors would like to thank Dr. Mohammed Yandouzi of the University of Ottawa Cold Spray Laboratory for his help obtaining the SEM micrographs shown in this publication. Acknowledgements are due to the MITACS Accelerate program for its financial support of this project.

References

1. A.B. Lovins, *Small is Profitable: The Hidden Economic Benefits of Making Electrical Resources the Right Size*, Rocky Mountain Institute, 2002
2. S.M. Kaplan and F. Sissine, *Smart Grid: Modernizing Electric Power Transmission and Distribution; Energy Independence, Storage and Security; Energy Independence and Security Act and Resiliency; Integra*, TheCapitol.Net Inc., 2009
3. A. Corbeil, "Study of Small Hydraulic Diameter Media for Improved Heat Exchanger," M.A.Sc. Thesis, University of Ottawa, 2009
4. D. Bohn, *Micro Gas Turbine and Fuel Cell: A Hybrid Energy Conversion System with High Potential*, NATO Research and Technology Organisation, 2005
5. J. Tian, T. Kim, T.J. Lu, H.P. Hodson, D.T. Queheillalt, D.J. Sypeck, and H.N.G. Wadley, The Effects of Topology Upon Fluid-Flow and Heat-Transfer Within Cellular Copper Structures, *Int. J. Heat Mass Transf.*, 2004, **47**(14-16), p 3171-3186
6. Z. Anxionnaz, M. Cabassud, C. Gourdon, and P. Tochon, Heat Exchanger/Reactors (HEX Reactors): Concepts, Technologies: State-of-the-Art, *Chem. Eng. Process.*, 2008, **47**(12), p 2029-2050
7. R.L. Shaner, Heat Exchanger Having Metal Wire Screens, and Method of Making Stack of Screens Therefor, US4840228, Year of Priority (Issued): 1985, 1989
8. J. Chisholm, Method of Making a Crimped Wire Mesh Heat Exchanger/Sink, US4843693, Year of Priority (Issued): 1988, 1989
9. J. Assad, A. Corbeil, P. Richer, and B. Jodoin, Novel Stacked Wire Mesh Compact Heat Exchangers Produced Using Cold Spray, *J. Therm. Spray Technol.*, 2011, **20**(6), p 1192-1200
10. H.R. Salimi Jazi, J. Mostaghimi, S. Chandra, L. Pershin, and T. Coyle, Spray-Formed, Metal-Foam Heat Exchangers for High

Temperature Applications, *J. Thermal Sci. Eng. Appl.*, 2009, **1**(3), p 1-7
11. F. Azarmi, J. Saaedi, T.W. Coyle, and J. Mostaghimi, Microstructure Characterization of Alloy 625 Deposited on Nickel Foam Using Air Plasma Spraying, *Adv. Eng. Mater.*, 2008, **10**(5), p 459-465
12. A.P. Alkhimov, A.N. Papyrin, V.F. Dosarev, N.I. Nesterovich, and M.M. Shuspanov, Gas-Dynamic Spraying Method for Applying a Coating, US5302414, Year of Priority (Issued): 1992, 1994
13. A.O. Tokarev, Structure of Aluminum Powder Coatings Prepared by Cold Gas-Dynamic Spraying, *Met. Sci. Heat Treat.*, 1996, **38**(3-4), p 136-139
14. Plasma Giken, http://www.plasma.co.jp/en/, Consulted November 2012
15. F.P. Incropera, D.P. DeWitt, T.L. Bergman, and A.S. Lavine, *Fundamentals of Heat and Mass Transfer*, 6th ed., Wiley, New York, 2006
16. T. Schmidt, F. Gärtner, H. Assadi, and H. Kreye, Development of a Generalised Parameter Window for Cold Spray Deposition, *Acta Mater.*, 2006, **54**, p 729-742
17. H. Assadi, T. Schmidt, H. Richter, J.-O. Kliemann, K. Binder, F. Gärtner, T. Klassen, and H. Kreye, On Parameter Selection in Cold Spraying, *J. Therm. Spray Technol.*, 2011, **20**(6), p 1161-1176
18. H.W. Coleman and W.G. Steele, *Experimentation and Uncertainty Analysis for Engineers*, Wiley, New York, 1999
19. W.M. Kays and A.L. London, *Compact Heat Exchangers*, 3rd ed., McGraw-Hill, New York, 1984

CHAPTER 6 FIN BASE ANGLE, HEIGHT AND FIN DENSITY EFFECTS ON THE THERMAL AND HYDRODYNAMIC PERFORMANCE

The following articles detail the effects of varying the fin base angle, height and fin density on the thermal and hydrodynamic performance of pin fin arrays produced by CGDS. The effect of the base angle was studied by spraying the fins taller than the desired height and subsequently grinding the array down to the desired size. This process was also found to increase process consistency and prevent the negative effects from potential flow bypass caused by fin tip clearance with the shroud. A new method for data comparison is adapted from the literature [16] and is used in subsequent performance evaluations. Empirical correlations are proposed, linking the Nusselt number to the Reynolds number for the height and fin density effects. A detailed study on the performance of tapered pin fin arrays to similar sized plain rectangular fin arrays is also reported, and a hypothesis regarding the mechanism behind the increased performance of tapered pin fins compared to continuous fins is emitted.

The following peer-reviewed articles were reproduced with the permission from the copyright owner, Elsevier Ltd.

.

International Journal of Heat and Mass Transfer 69 (2014) 34–43

Contents lists available at ScienceDirect

International Journal of Heat and Mass Transfer

journal homepage: www.elsevier.com/locate/ijhmt

Performance evaluation of near-net pyramidal shaped fin arrays manufactured by cold spray

Philippe Dupuis [a], Yannick Cormier [a,*], Aslan Farjam [a], Bertrand Jodoin [a], Antoine Corbeil [b]

[a] University of Ottawa, 161 Louis Pasteur Av., Ottawa, Ontario K1N 6N5, Canada
[b] Brayton Energy Canada, 710 rue Vernon, Unité #7, Gatineau, Québec J9J 3K5, Canada

ARTICLE INFO

Article history:
Received 29 July 2013
Received in revised form 27 September 2013
Accepted 27 September 2013

Keywords:
Pin fins
Heat transfer enhancement
Pressure loss
Heat exchanger
Forced convection
Cold Spray

ABSTRACT

Near-net pyramidal shaped fin arrays have been produced using the Cold Gas Dynamic Spraying (CGDS) process. Some fin arrays have been modified to trapezoid prism geometry by grinding the top of the pyramidal fins to study the effect of varying the base angle, at a constant fin height. All fin arrays have been tested for thermal and hydrodynamic performance. Little variation in thermal conductance between ground and as-sprayed fins is observed for the same fin heights, while a slightly more significant variation in pressure loss through the fin array is found. A comparison of these performances was performed with plain rectangular fins. The new fin geometry outperforms the traditional rectangular fins when comparing the thermal conductance per unit pumping power for a given heat exchanger volume over the range of Reynolds numbers studied.

1. Introduction

Significant efforts have been made in the last decades to decrease the world's dependency to fossil fuels. One of the fronts which has shown major improvement is gas turbine efficiency. To this end, components such as recuperators have been developed to recover heat that is usually trapped and wasted in the exhaust gases of combustion processes. Relatively new heat exchanger designs have shown promises, with the potential to increase the thermal efficiency of these components from 75–85% to 90–95% [1]. Emerging recuperator designs have a common structure comprised of an internal heat transfer media with a flow barrier which prevents the mixing of the hot and cold flows and another stage of heat transfer enhancing features encased in an external shell, as illustrated in Fig. 1. Several geometries have been proposed for the internal heat transfer media, such as metal foams, lattice frames, packed beds, and wire mesh.

Wire mesh heat exchangers (WMHE) were first investigated in the late 1980s, with the folded wire mesh geometry [3,4]. This geometry is obtained by folding wire screen on itself and brazing the resulting structure to flow barriers (plates), as shown in Fig. 2. This type of heat exchangers has the potential for a higher performance per unit volume and features low axial (along the flow direction) conduction losses compared to traditional heat exchangers. However, this configuration has its drawbacks. First, there is a maximum amount of times a wire mesh sheet can be folded on itself per linear inch, which depends on the mesh material and density [5]. Second, the small contact area per fold between the brazed sheet and the wire mesh sheet, as can be observed in Fig. 2 [5], creates a significant thermal resistance at this interface. The third disadvantage stems from the brazing process itself. This manufacturing technique is costly, mainly due to the use of a vacuum furnace, which is required to complete the joining process.

A new method for producing WMHE has recently been developed which mitigates these problems. Instead of folding the wire mesh onto itself, sheets are stacked and then cut perpendicular to the stacking direction, yielding thin wafers of wire mesh textiles. These wafers are then sealed using a dense metallic coating produced using thermal spray processes [5]. The applied coating thickness allows machining plain rectangular (straight cut) fins on its outer surface (Fig. 3). This design reduces the costs associated with producing WMHE by removing the costly brazing operation, but the external fin manufacturing is restricted by machining constraints. Furthermore, it is currently not economically viable to machine other types of fins, such as wavy offset or pin fin arrays.

---

* Corresponding author. Address: Mechanical Engineering, University of Ottawa, Colonel By Hall, 161 Louis Pasteur Av., Ottawa, ON K1N 6N5, Canada. Tel.: +1 (613) 5625800x2481; fax: +1 (613) 562 5177.

E-mail address: yannick.cormier@uottawa.ca (Y. Cormier).

0017-9310/$ - see front matter © 2013 Elsevier Ltd. All rights reserved.
http://dx.doi.org/10.1016/j.ijheatmasstransfer.2013.09.072

Nomenclature

ΔP_{outlet}	outlet differential pressure (Pa)
ΔP_{fin}	fin differential pressure (Pa)
ΔP_{inlet}	inlet differential pressure (Pa)
ΔP_{tot}	total differential pressure (Pa)
ΔT_1	inlet temperature difference (K)
ΔT_2	outlet temperature difference (K)
ΔT_{lm}	log mean temperature difference (K)
η	fan efficiency
η_f	individual fin efficiency
η_o	overall fin efficiency
θ	pyramid angle (°)
μ	dynamic viscosity (Pa s)
ρ	fluid density (kg/m^3)
A_f	fin heat transfer area (m^2)
A_{flow}	net flow area (m^2)
A_{tot}	total heat transfer area (m^2)
A_u	unfinned heat transfer area (m^2)
B	base fin length (m)
Cp	fluid specific heat capacity (kJ/(kg K))
D	base diameter (m)
D_{mean}	mean base fin length (m)
d_h	hydraulic diameter (m)
e_v	pumping power per unit volume (kW/m^3)
FD	fin density (fin/m)
H	fin height (m)
h	convective heat transfer coefficient (W/(m^2 K))
I_1	Bessel function of order one
I_2	Bessel function of order two
k_m	fin material thermal conductivity (W/(m K))
L	sample length (m)
$\dot{m}$	mass flow rate (kg/s)
m	fin heat transfer parameter (m^{-1})
N_f	number of fins
P_{flow}	flow perimeter (m)
q	heat flux (W/m^2)
Re_{Dh}	Reynolds number based on hydraulic diameter
R_{eq}	equivalent thermal resistance (K/W)
S	space between fin edges (m)
T	top fin length (m)
T_{in}	inlet fluid temperature (K)
T_{out}	outlet fluid temperature (K)
U_{max}	maximum fluid velocity (m/s)
UA	thermal conductance (W/K)
UA_v	thermal conductance per unit volume (kW/(m^3 K))
V	volume (m^3)
$\dot{V}_f$	volumetric flow rate (m^3/s)
W	channel width (m)

Metal foam heat exchangers enclosed in a metallic shell deposited using wire-arc or plasma spray have been investigated by Salimi Jazi et al. [6,7]. In this case, wire arc or plasma spray processes are used to seal commercially available nickel foam bricks with Inconel 625 to create fully encased heat exchangers. However, no heat transfer enhancing features, such as fins, are used on the outer surface of the heat exchangers.

Rectangular fin arrays provide an increase in heat transfer performance with respect to an unfinned surface due to the additional heat transfer area. Increases of the convective heat transfer coefficient due to this type of extended surface are usually neglected and the pressure loss through the array is low due to their geometry [8,9]. If the design specifications allow for a higher head loss, several other fin geometries can yield superior thermal performance for a given surface area. Wavy offset fins increase the amount of area available for heat transfer while also increasing the amount of fluid mixing. This creates a fin array with a lower thermal resistance at the expense of a slightly higher head loss [8,9]. These fins are typically produced using sheet metal strips bent over themselves to form a wavy shape, with each strip slightly offset from the previous to induce mixing. Using pin fins instead will further increase the convective heat transfer coefficient by creating turbulent wakes behind each fin, which subsequently promotes fluid mixing [10]. This yields fin arrays which have better thermal performance at the expense of a higher pressure drop. Sahiti et al. [11–13] have demonstrated that pin fins offer the most effective way of increasing the heat transfer rate within a given heat exchanger volume, when compared to other types of fins.

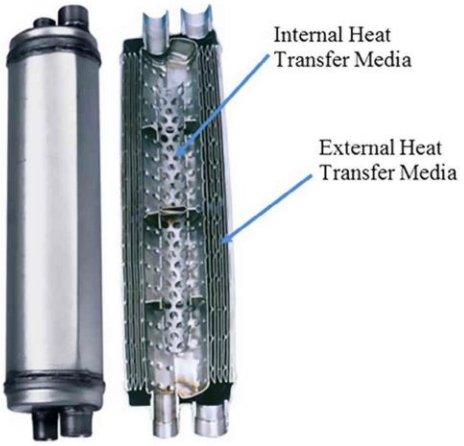

Fig. 1. Typical heat exchanger between two heat transfer media (adapted from [2]).

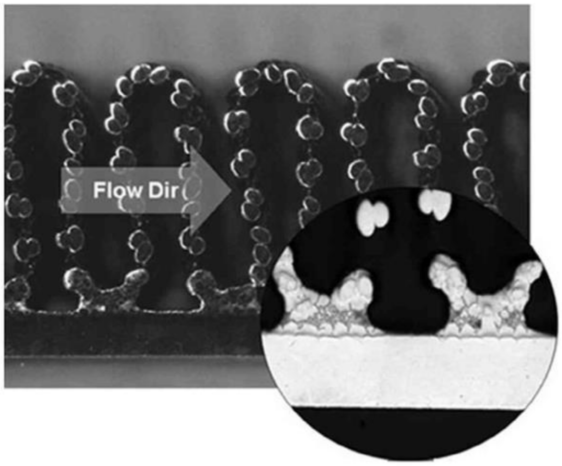

Fig. 2. Folded wire mesh with a zoomed section of the brazed plate contact surface.

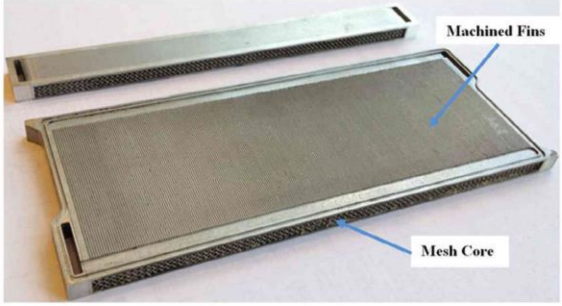

Fig. 3. Wire mesh heat exchanger with machined external fins on a mesh core.

Various types of pin fin array geometries were extensively studied. Staggered cylindrical pin fins were first investigated by Brigham and Van Fossen [14,15] and revealed that long pins fins (ratio of fin height to fin diameter is larger than 4) tend to transfer more heat than short pin fins. Work presented by Metzger et al. [16] detailed the effects of the array's orientation on the heat transfer and pressure loss through these arrays. Their results indicated that circular pins fins in an intermediate configuration between staggered and inline can reduce the pressure loss while increasing the amount of heat transferred. They also found that the surface convective heat transfer coefficient for pin fins was approximately 100% larger than that of the end wall. Since these landmark works, some attention has been given to pin fins with square cross-sections. You and Chang [17] studied the heat transfer and pressure loss properties of inline square pin fins confined in a rectangular channel using numerical modeling. Subsequently, Jeng and Tzeng [18] experimentally confirmed these numerical simulations of fluid flow through square based pin fins and determined that their performance can exceed that of circular pin fins.

The manufacturability of aluminum and stainless steel square base pyramidal pin fin arrays produced using Cold Gas Dynamic Spraying (CGDS or simply Cold Spray) was demonstrated by Cormier et al. [19]. Fin arrays were manufactured with fin densities varying between 12 and 30 fins per inch at fin heights of 1.0–2.2 mm. The thermal performance of the aluminum samples was determined and compared to a rectangular fin sample at 24 fins per inch, with the new type of fin having a higher thermal conductance than the traditional type of fin array. Much work is still left to be done to optimize the performance of this new type of fin geometry.

In this paper, the thermal and hydrodynamic performance of aluminum square base pyramidal and trapezoidal pin fin arrays produced with CGDS was investigated. The convective heat transfer coefficient and thermal conductance parameters were evaluated using a forced flow convective heat transfer apparatus at low Reynolds numbers (less than 3500). This fixture was also used to determine the pressure loss through the fin array, as well as the required pumping power. Investigations were limited to one configuration of uniformly distributed pin fins with a fin density of 12 fins per inch. The effect of varying the fin's base angle was characterized. Additionally, the performance of this new type of fin array was compared to traditional rectangular fin arrays with similar characteristic dimensions.

2. Experimental production technique description

2.1. CGDS process and masking technique

Thermal spray deposition processes, such as Plasma spraying and High Velocity Oxy Fuel (HVOF) spraying operate on the principle of using the thermal energy of a carrier gas to melt or partially melt solid powder particles and using the gas' kinetic energy to accelerate these particles onto a substrate in order to form a dense coating upon impact, deformation and solidification [20,21]. Kinetic spray processes such as Cold Gas Dynamic Spraying (CGDS), however, solely rely on the transfer of momentum from an inert gas, usually helium or nitrogen, to relatively cold particles (usually less than half the material's melting temperature) which are projected onto a substrate's surface [22]. A schematic of a CGDS apparatus is shown in Fig. 4. The high pressure driving gas is heated and is subsequently accelerated to supersonic speeds using a converging–diverging (DeLaval) nozzle, where its kinetic energy is imparted to the particles by drag effects [22,23]. Upon colliding with the substrate, the particle's kinetic energy is converted to plastically deform the particles and induce adhesion. This deformation is sustained by the adiabatic shear instabilities created during the impact, which causes the material to viscously flow outwards from the center of the particle [24]. Bonding to the substrate is attributed to localized high pressure waves breaking oxide layers and promoting intimate contact between the particle and the substrate [25].

Fig. 5 illustrates the technique used to create square based pyramidal fin arrays using commercially available plain woven, steel wire mesh (McMaster-Carr, Aurora, OH, USA) to mask the substrate. This configuration creates a pyramidal fin array (Fig. 6) which closely mimics the reversed geometry of the chosen wire mesh, with peaks aligning with the holes of the screened area

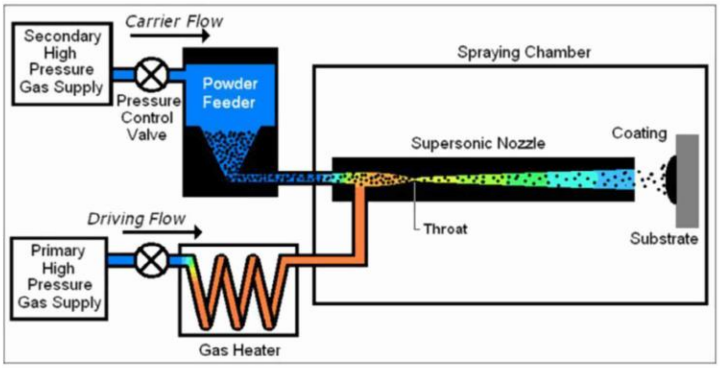

Fig. 4. Schematic of CGDS apparatus.

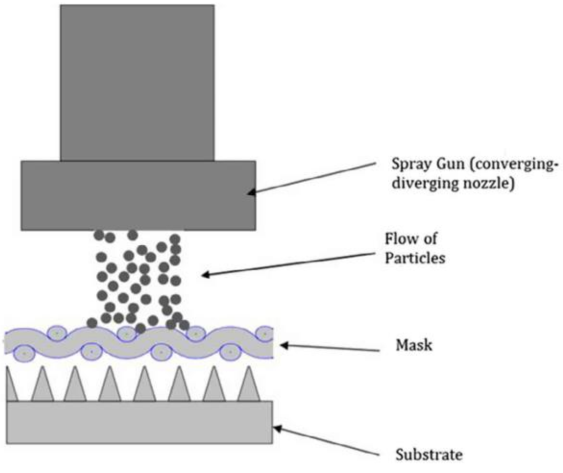

Fig. 5. Schematic of the spray process with masking technique.

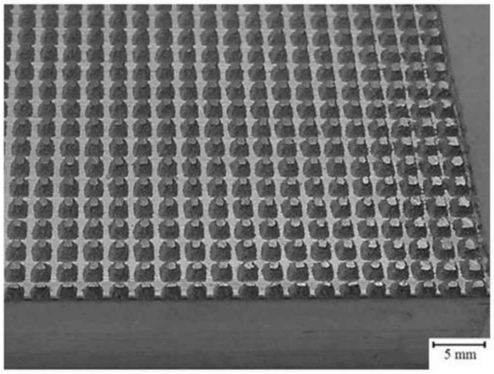

Fig. 6. Overview of typical fin array.

and little or no deposition underneath the wires [19]. The main factor that determines if adhesion occurs with the CGDS process is the particle's normal impact velocity with respect to the substrate. Thus, since the CGDS flow near the mask is affected by viscous effects (due to the presence of the mask walls and a shock wave present near the mask), particles present in the CGDS flow in the vicinity of the mask wires are slowed down. As such, the particles tend to build up a coating preferentially underneath the center of the mask holes, on the substrate. This creates a zone near the center of the holes where buildup is rapid when compared to the sides, leading to the creation of an angle between the top and the base, forming a pyramidal shape. When this angle becomes sharp enough, particles do not have a sufficient normal impact velocity and adhesion stops as particles simply bounce off. The working principles of the CGDS process make it an ideal candidate for the proposed masking technique used to produce pyramidal fins. Using other thermal spray techniques would cause issues where the mesh would either melt or be clogged by the molten particles in the high temperature gas stream. Manufacturing parameters were chosen to ensure that the dimensions of the pyramid base would follow those of the wire mesh mask as closely as possible.

The CGDS system used for this work is a commercially available Plasma Giken PCS-1000 [26]. The spray nozzle has a 3.0 mm throat diameter and a 6.5 mm exit diameter. The feedstock powder material used is commercially pure aluminum (99.8% Al) from Centerline (Windsor) Ltd. (Windsor, Ontario, Canada). It has an elongated shape with a mean particle size (D_{50}) of 25.35 microns. Other details about powder morphology and size distribution are given elsewhere [19].

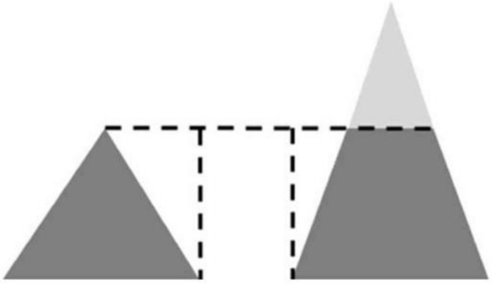

Fig. 7. Pyramidal vs trapezoidal geometries, showing the difference in base angle.

2.2. Test sample preparation

Fins were cold sprayed on aluminum substrates (Al6061 T6) with standard dimensions of 5.1 cm by 5.1 cm. The cold spray trials detailed in this work were done on extruded aluminum substrates instead of thermal sprayed coatings on the WMHE to isolate the effects of the fin parameters on the heat transfer and hydrodynamic performance of the test samples. The substrates were cleaned and degreased using acetone after being cut to size. No further surface preparation steps, such as grit-blasting or heat treatment, was performed. To determine the effect of changing the fin base angle for a constant height, samples were cold sprayed to a height larger than the target height and then ground down to a uniform height of 1.0 mm using a conventional sanding belt with 320 grit sandpaper and water as coolant. This process yielded fins with a trapezoidal prism shape, as illustrated in Fig. 7. No other type of post-treatment of the sprayed samples was performed.

3. Testing procedure

3.1. Performance test apparatus

Performance of the various fin arrays produced was assessed using an in-house heat transfer and pressure drop test apparatus, adapted from the literature [19,27]. A schematic of the apparatus and its various components is shown in Fig. 8.

The main components of this apparatus are the test section, the heating pad, the air supply and the data acquisition system. The air is supplied by a compressed air line, properly filtered and dehumidified to obtain room temperature, dry air, free from oil contamination. The air inlet flow rate is controlled by a needle valve and is measured with a flow meter. This air is smoothly expanded into a horizontal rectangular channel with a diffuser and a honeycomb flow straightener. This rectangular channel's top and bottom plates (76.2 mm wide by 457.2 mm long by 19.05 mm thick) are made of acrylic, and they are spaced apart using a rectangular rubber gasket, which is compressed to ensure there is no clearance between the fins and the shroud surface. These gaskets also ensure that the joint is leak-proof. A length of 457 mm of unobstructed flow ensures that the fluid is fully developed hydrodynamically before reaching the test section for the given hydraulic diameter and Reynolds number [8].

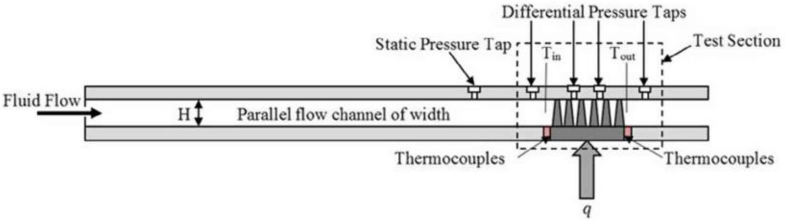

Fig. 8. Schematic of the heat transfer test fixture.

The test sample is subjected to a constant heat flux provided by a strip heater. A conducting block is used to ensure that heat is evenly distributed onto the substrate's surface, resulting in a constant surface temperature under free convection conditions.

A stagnation pressure measurement tap is located 25.4 mm upstream from the test section, while two sets differential pressure measurement taps are located 31.8 and 12.7 mm upstream (high pressure side) and downstream (low pressure side) from the middle of the test section. Two thermocouples are located 6 mm before and after the test section at mid-height to record the fluid local average temperature. Four thermocouples are attached to the fin array's base, with two on the side facing the incoming flow, and two on the side facing the exiting flow. On each face, one thermocouple is located on the centerline, while the other thermocouple is located 6 mm from the wall. All the thermocouples used are T-type, butt-bonded, thin gauge (28 gauge) thermocouples. Radiative heat transfer losses are neglected since they would account for less than 0.5% of the total heat input for similar test surfaces [28,29].

3.2. Heat transfer testing procedure

Measurements were performed at steady-state conditions and repeated until statistical significance was achieved. Data samples were taken over a 30 s interval, at 2 Hz. Five sets of data samples were recorded for every flow condition. Measurements were taken at flow rates corresponding to Reynolds numbers varying from 200 to 2000, as this is the typical application range sought for these exchangers. Deviation of the measurements from the mean value was less than 5%. The accuracy of the test fixture was validated with the experimental results of Kays' and London's work [9]. The error bars are not shown in the results section as they are smaller than the markers. A detailed description of the apparatus' accuracy and instrument uncertainties is given in Cormier et al. [19].

3.3. Pressure loss testing procedure

Measurements were performed at steady-state conditions and repeated until statistical significance was achieved. Five sets of data samples were recorded for every flow condition. Measurements were taken at flow rates corresponding to Reynolds numbers varying from 200 to 3500, to identify the trends and to obtain sufficient data for predictive modeling. Deviation of the measurements from the mean value was less than 5%. For hydrodynamic performance tests, one set of pressure taps is used to obtain the fin array friction losses, which include skin friction and form drag, while another set is used to determine the total pressure drop of the fin array, which includes entrance and exit effects as well as fin array friction losses. This allows the measurement of the fin array friction loss independently of the flow constriction and expansion pressure losses. Measurements were limited to Reynolds numbers of approximately 2500 for the total pressure loss due to instrumentation limits.

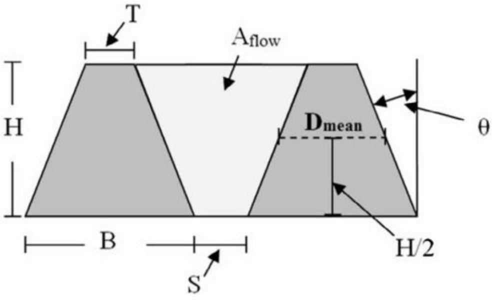

Fig. 9. Schematic of the fin array unit with geometric variables identification.

3.4. Data analysis method

To analyze the raw data obtained, flow conditions are expressed using the Reynolds number. Since the test samples have the same base dimensions, performance evaluations are done by comparing convective heat transfer coefficients and the thermal conductances. Fig. 9 illustrates the geometric variables used to perform the analysis.

The Reynolds number based on the hydraulic diameter is calculated with:

$$Re_{Dh} = \frac{\rho U_{max} d_h}{\mu} = \frac{\dot{m} \cdot d_h}{W \cdot FD \cdot A_{flow} \cdot \mu} \tag{1}$$

where $\dot{m}$ is the mass flow rate, d_h is the hydraulic diameter of the fin array flow passage, W is the fin array sample width, FD is the fin density, μ is the fluid's dynamic viscosity and A_{flow} is the face area the fluid can flow into between two fins. The variables d_h and A_{flow} are given by:

$$d_h = \frac{4 \cdot A_{flow}}{P_{flow}} = \frac{2 \cdot A_{flow}}{\frac{H}{\cos(\theta)} + S + H \cdot \tan(\theta)} \tag{2}$$

$$A_{flow} = (S + H \cdot \tan(\theta)) \cdot H \tag{3}$$

where θ is the fin angle, S is fin spacing from edge to edge at the base, H is the fin height and P_{flow} is the flow channel's perimeter.

The fin array's convective heat transfer coefficient is calculated from the raw data with:

$$h = \frac{q}{\Delta T_{lm} A_{tot} \eta_o} \tag{10}$$

In these equations, q is the heating rate, ΔT_{lm} is the log-mean temperature difference between the fluid and the fin array and A_{tot} is the total heat transfer area. The total heat input rate to the system is calculated using:

$$q = \dot{m} \cdot (T_{out} T_{in}) \cdot Cp \tag{12}$$

where $(T_{out} - T_{in})$ is the fluid temperature difference between the entry and the exit of the test section, Cp is the fluid's thermal capacitance. The log-mean temperature difference is calculated with:

$$\Delta T_{lm} = \frac{\Delta T_1 - \Delta T_2}{\ln\left(\frac{\Delta T_1}{\Delta T_2}\right)} \tag{11}$$

where ΔT_1 and ΔT_2 are the temperature difference between the fin surface and the flow at the inlet and outlet respectively. The total heat transfer area is given by:

$$A_{tot} = A_f + A_u = N_f\left(\frac{B^2}{\tan(\theta)\cos(\theta)} - \frac{T^2}{2\sin(\theta)}\right) + (WL - N_f B^2) \tag{5}$$

In the previous equation, N_f is the number of fins in the array, B is the fin's length at its base, L is the test sample's length, A_f designates the total fin heat transfer area, A_u denotes the unfinned base's exposed area while T is the fin's top length, given by:

$$T = B - 2H\tan(\theta) \tag{6}$$

The overall efficiency is calculated using the following equation:

$$\eta_o = 1 - \frac{A_f}{A_{tot}}(1 - \eta_f) \tag{7}$$

where η_f is the individual fin efficiency, defined as the heat transferred by the fin over the maximum possible heat that can be transferred, which is numerically equal to:

$$\eta_f = \frac{2}{mH}\frac{I_2(2mH)}{I_1(2mH)} \tag{8}$$

with:

$$m = \sqrt{\frac{4h}{k_m D}} \tag{9}$$

In the previous equations adapted from Incropera [8], I_1 and I_2 denote the first and second order Bessel functions, respectively, while k_m is the thermal conductivity of the fin's metal. The individual fin efficiency equation for triangular pin fins are used for the geometries in this work since it has the most similar geometry. The only difference between the two is the shape of the base, as the equation was developed for circular base cones while the manufactured fins present a square base. Therefore, the diameter of the fin (D) in the previous equation is replaced by the fin length at the base (B).

The thermal conductance is computed with:

$$UA = \frac{1}{R_{eq}} = h \cdot A_{tot} \cdot \eta_o \tag{4}$$

where η_o is the overall surface efficiency.

The total pressure loss measured over the fin array can be divided as:

$$\Delta P_{tot} = \Delta P_{inlet} + \Delta P_{fin} + \Delta P_{outlet} \tag{13}$$

where ΔP_{tot} is the total pressure loss through the fin array, ΔP_{inlet} is the pressure loss due to flow contraction at the inlet of the array, ΔP_{fin} is the pressure loss due to skin friction and flow separation through the fin array and ΔP_{outlet} is the pressure gained from the expansion of the flow at the outlet of the fin array.

To obtain the efficiency curves produced in Section 4.3, the required fan power input per unit volume was calculated using:

$$e_v = \frac{\dot{V}_f \cdot \Delta P_{fin}}{\eta \cdot V} \tag{14}$$

In the previous relation, adapted from Sahiti's work [12], e_v is the pumping power per unit volume, $\dot{V}_f$ is the volumetric flow rate of the fluid, η is the fan efficiency while V is the volume of the heat exchanger. A fan efficiency of 0.8 was arbitrarily chosen as a reasonable value to perform these calculations.

Table 1
1.0 mm Pyramidal fin dimensions (in microns) of tested samples for the spray angle study.

Sample	B		S		H	
	Average	SD[a]	Average	SD[a]	Average	SD[a]
1.0	1159	51	932	39	1006	69
M1.3	1394	81	821	55	901	41
M1.5	1586	67	490	67	1058	55
M1.8	1429	67	780	53	953	40
M2.0	1559	79	548	55	1075	43
M2.4	1626	70	583	79	954	45

[a] SD: standard deviation.

Table 2
Important geometric variables of pyramidal and trapezoidal samples.

Sample	Hydraulic diameter mm	Total heat transfer area mm^2	D_{mean} mm	H/D_{mean} ratio	Base angle °
1.0	1.12	3372	0.61	1.63	58.5
M1.3	1.02	3637	0.81	1.24	60.3
M1.5	0.96	3894	1.07	0.93	61.8
M1.8	0.95	3907	1.13	0.89	66.6
M2.0	0.94	4071	1.17	0.86	68.7
M2.4	0.93	4162	1.22	0.82	72.6

Table 3
Samples tested for comparison.

Sample number	Fin density Fins per in	Fin width mm	Fin spacing mm	Height mm	Hydraulic diameter mm	Total heat transfer area mm^2
US	N/A	N/A	N/A	2.0	3.85	2581
SC	12	1.23	0.89	1.0	0.94	3478

3.5. Test sample geometric data

Table 1 presents a list of the 1.0 mm height pin fin arrays produced and tested, with the average base (B), spacing (S) and height (H) dimensions and their associated standard deviations measured for 25 fins per sample. Fin array samples were measured using a depth of field microscope VHX-2000 which was acquired from Keyence (Mississauga, Ontario, Canada) which allows building three dimensional images of the given samples. The number next to the prefix "*M*" indicates the original height of the ground sample. For all pyramidal fin samples, the fin density was set at 12 fins per inch. Table 2 shows the important geometric variables for pyramidal and trapezoidal samples calculated using the data from Table 1. Table 3 shows a list of comparison/reference samples. The sample labeled SC (straight cut) has rectangular fins machined from bulk Al 6061 while the sample labeled US is an unfinned Al 6061 reference sample. Pictures of these two types of samples are shown in Fig. 10. Sample SC was used to compare with the pin fin samples, having comparable base length and fin spacing with a 90° base angle.

4. Results

4.1. Heat transfer performance

Fig. 11 shows the thermal conductance of the different fin arrays tested as a function of the Reynolds number. The results reveal

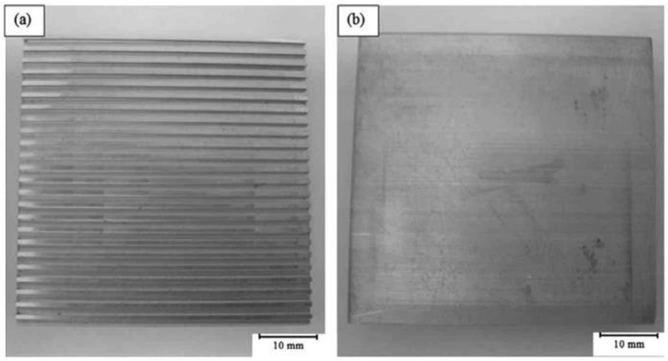

Fig. 10. Comparison samples (a) straight cut (SC) machined from bulk Al 6061 (b) unfinned surface (US) of bulk Al 6061.

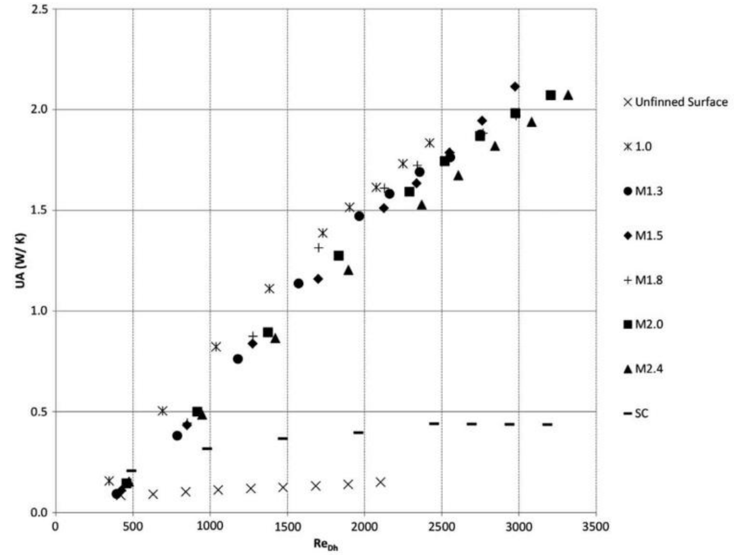

Fig. 11. Thermal conductance comparison between 1.0 (star), ground from 1.3 (circle), ground from 1.5 (diamond), ground from 1.8 (cross), ground from 2.0 (square), ground from 2.4 (triangle) and rectangular fin array (line) while the unfinned surface is used as reference (X).

little variations between the pyramidal/trapezoidal fin samples at all Reynolds number tested. It is observed that all the results could be grouped around a line of thermal conductance which increases linearly with Reynolds number up to approximately 1500–2000 Re_{Dh}. The trend seems to remains linear past that Reynolds number but with a reduced slope. These results suggest that there is little effect in changing the pyramid base angle at a given fin height on the thermal conductance of the fin array. However, a decrease of the convective heat transfer coefficient values can be observed in Fig. 12 as the base angle increases. Sample 1.0 has the highest convective coefficient value, which is reduced with each increase in initial fin height up to sample M2.4. This effect is moderated by an increase in the total heat transfer area available, explaining why the fin array thermal conductance can be considered independent of the fin base angle. The decrease of convective heat transfer coefficient observed is believed to be caused by a difference in the flow structure around the fins, with steeper base angles leading to a reduction of the amount of fluid mixing, and consequently of the convective heat transfer coefficient. The performance of a pyramidal type fin would approach that of a completely rectangular pin fin as the base angle is increased.

Examining the results from the rectangular fin array, one can observe that its thermal conductance is significantly lower than those of the pyramidal/trapezoidal fin arrays. This is expected due to the different flow structures between continuous geometries such as plain rectangular fins and pin fin geometries, which are discontinuous. These discontinuities are believed to cause turbulent wakes behind each column of fins, which increases fluid mixing and consequently increases the convective heat transfer coefficient. This is supported by Fig. 12, which shows a significant increase in the convective heat transfer coefficient between the two types of fins. This difference in convective coefficient reaches up to 300% increase at 2500 Re_{Dh} between the pyramidal sample 1.0 and the rectangular fin array, with increasing fin angle diminishing this difference to a 200% increase when comparing to the M2.4 sample at the same Reynolds number. A plateau of thermal performance is noted for the plain rectangular fin sample, which begins at 1000 Re_{Dh} and extends to 3000 Re_{Dh}. This plateau has a

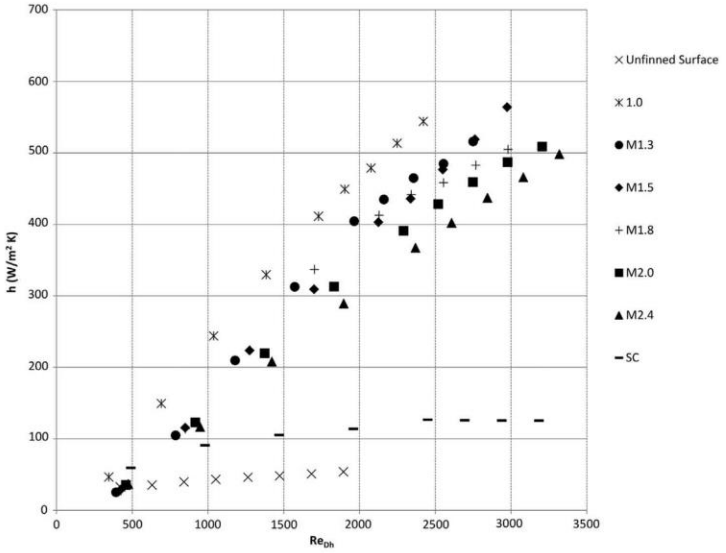

Fig. 12. Convective heat transfer coefficient comparison between 1.0 (star), ground from 1.3 (circle), ground from 1.5 (diamond), ground from 1.8 (cross), ground from 2.0 (square), ground from 2.4 (triangle) and rectangular fin array (line) while the unfinned surface is used as reference (X).

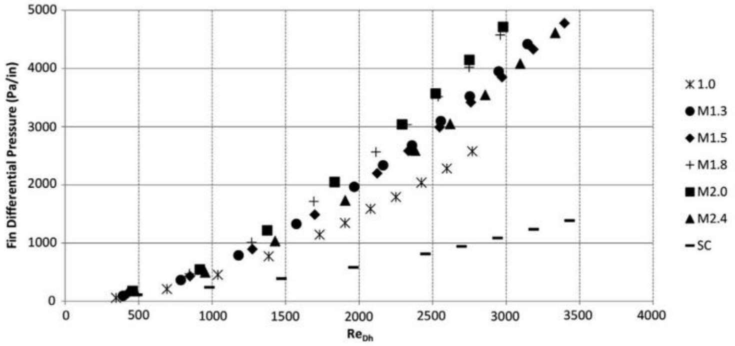

Fig. 13. Fin differential pressure comparison between 1.0 (star), ground from 1.3 (circle), ground from 1.5 (diamond), ground from 1.8 (cross), ground from 2.0 (square), ground from 2.4 (triangle) and rectangular fin array (line) while the unfinned surface is used as reference (X).

similar rate of increase of convective coefficient as an unfinned surface, which is to be expected as the major advantage of adding plain rectangular fins is not the increase in convective coefficient, which can usually be neglected, but the increase in total heat transfer area [8].

4.2. Hydrodynamic performance

The pressure loss through the arrays of the different fin geometries is shown in Fig. 13, while the total pressure loss including the entrance and exit effects is shown in Fig. 14. There is little difference between the hydrodynamic performances of the trapezoidal samples, which have a very similar pressure loss over the range of Reynolds number studied. The pyramidal sample, however, shows a slightly lower pressure loss than the trapezoidal samples. This is attributed to the slight clearance between the top of the fins and the shroud of the testing set-up, which stems from the variability in the manufacturing process of this type of fin array. The ground (trapezoid) fins have a very uniform height due to the material removal process, while the variability between the maximum and the minimum height of the pyramidal sample is more significant as shown in Table 1. This variability is believed to cause a clearance between the average fins and the shroud, which can reduce the pressure loss significantly. The results suggest that the convective heat transfer coefficient is not affected as much, however. The total pressure loss follows the same trends as the fin array pressure losses, which indicates that these observations are not due to entrance and exit effects.

The pressure loss of the rectangular fin sample is much lower than that of the pin fins tested, which is expected. The reduction in fluid mixing and turbulence zones allows a smooth flow along the length of the fins. Furthermore, pin fins have a large form drag pressure loss due to their discontinuity along the flow length, a feature which is not present for plain rectangular fins, which are continuous along the flow direction. The pressure losses due to the inlet and outlet effects are consistently measured to be approximately 30% of the total pressure loss through the pin fin arrays.

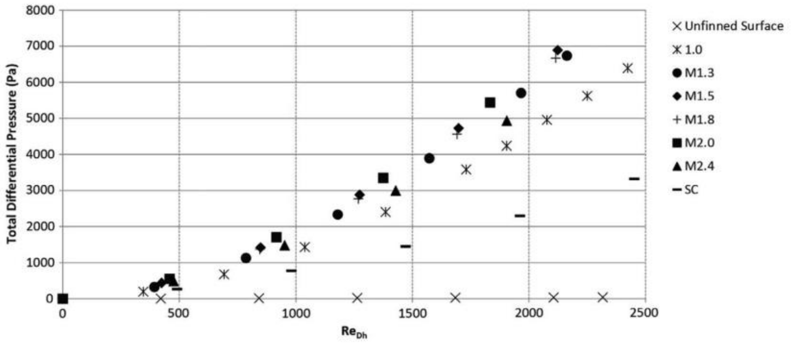

Fig. 14. Total differential pressure comparison between 1.0 (star), ground from 1.3 (circle), ground from 1.5 (diamond), ground from 1.8 (cross), ground from 2.0 (square), ground from 2.4 (triangle) and rectangular fin array (line) while the unfinned surface is used as reference (X).

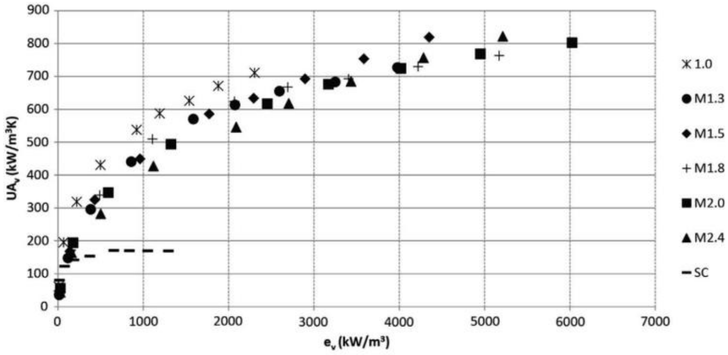

Fig. 15. Heat transfer surface efficiency comparison between 1.0 (star), ground from 1.3 (circle), ground from 1.5 (diamond), ground from 1.8 (cross), ground from 2.0 (square), ground from 2.4 (triangle) and rectangular fin array (line).

4.3. Heat transfer surface efficiency

To determine which fin array transfers heat more efficiently, an efficiency indicator must be selected. Based on an extensive literature review performed, the method proposed in Sahiti's work [12] was selected. This method is based on plotting the thermal and hydrodynamic data as a curve of thermal conductance per unit of fin array volume as a function of the required pumping power per unit volume for different flow conditions. This yields curves which can be directly compared one to another, with the most efficient fin array having a higher thermal conductance at a given pumping power.

Fig. 15 shows the efficiency indicator plotted for the different types of fin arrays tested. The performances of the pin fins are very similar over the range of test conditions, which indicates that little performance is lost when pyramidal fins are ground down to a trapezoid shape. An inflection point is noted for the pin fin samples, located near 500 kW/m^3. This inflection point denotes the zone where this type of fin array performs best, i.e. where the maximum amount of heat is transferred per unit pumping power. Further increasing the Reynolds number past this point leads to increasingly large pressure losses for little heat transfer gain. These facts lead to the conclusion that in this case manufacturing concerns should be accommodated, with the following production method: Fins should be produced several hundred microns higher than the target height and the top of the fins should be removed by grinding, which will allow the quality of the array to better be controlled. This process will ensure that all the fins over a sample are at the same height and that there is no bypass flow between the top of the fins and the shroud, which could have detrimental effects on fin array performance.

It can be observed that the performance of the plain rectangular fins is similar to that of pyramidal and trapezoidal fins at low Reynolds number, but rapidly peaks once their maximal thermal performance is reached. Indeed, at 1000 kW/m^3, a 300% increase in performance is attained when using pyramidal pins fins instead of plain rectangular fins for the same heat exchanger volume. This is due to the plateau of thermal performance that begins at about 1000 Re_{Dh} for rectangular fins, which was detailed in Section 4.1. The same type of inflection point is found in the performance curve of the rectangular fin array as in the pin fin arrays. This inflection, however, is located much earlier in the performance curve due to low pumping powers required by the rectangular fin array.

5. Summary and conclusion

This study investigates the thermal and hydrodynamic performance of pyramidal and trapezoidal fin arrays. The new geometries proposed are produced using Cold Gas Dynamic Spraying, with the former type being left as-sprayed while the latter type was sprayed and subsequently ground down to size. This operation removed the top part of the pyramid to yield fins with a trapezoid prism shape. This investigation concentrated on samples of 12 fins per inch at 1.0 mm height. The performances of these fins are compared using the thermal conductivity over the required pumping power per unit volume. The performances of these new types of fin arrays are also compared to traditional plain rectangular fin arrays. The conclusions of this work are summarized as:

1. There is a small difference in the thermal conductance when fins are ground down to the same height as an as-sprayed sample. This small difference is due to a decreasing convective heat transfer as the pyramid base angle increases, while the total available heat transfer surface area increases as the base angle increases. Since these two parameter offer a conflicting effect but change at a similar rhythm with the base angle parameter, there is little net change in the thermal conductance.
2. The hydrodynamic performance of the new types of fin is similar over the range of Reynolds numbers studied, with the pyramidal sample having the lowest pressure loss. This is believed to be caused by clearance induced by the manufacturing process used, and will be confirmed in a later publication which will focus on the flow structures found in these types of fin arrays.
3. The global performance of the trapezoidal and pyramidal fins was found to be very similar over the range of pumping power studied. This result confirms that removing the top of the fins by grinding is a viable way of controlling the quality of the end product without compromising the performance of the fin array. Using an industrial process for grinding could also tighten the tolerances and further ensure repeatability of production.
4. The new types of fins have a better performance value than traditional plain rectangular fins over the range of Reynolds number studied ($100 < Re_{Dh} < 3500$). This is due to the large increase in convective heat transfer coefficient due to the turbulence between the rows of fins, which increase fluid mixing. This gain is offset by the increased pressure loss through the discontinuous fin array. The increased thermal performance, however, still ensures that the total performance of the new type of fin array is superior to that of a comparable rectangular fin array.

Acknowledgements

Acknowledgements are due to the MITACS Accelerate program for its financial support of this project.

References

[1] D. Bohn, Micro gas turbine and fuel cell – a hybrid energy conversion system with high potential, NATO Research and Technology Organisation, 2005.
[2] Process Technology, TherMax^2 Heat Exchangers, http://process-technology.com, Consulted April 2013.
[3] R.L. Shaner, US Patent No. 4840228, 1989.
[4] J. Chisholm, US Patent No. 4843693, 1989.
[5] J. Assaad, A. Corbeil, P. Richer, B. Jodoin, Novel stacked wire mesh compact heat exchangers produced using cold spray, J. Therm. Spray Technol. 20 (6) (2011) 1192–1200.
[6] H.R. Salimi Jazi, J. Mostaghimi, S. Chandra, L. Pershin, T. Coyle, Spray-formed metal-foam heat exchangers for high temperature applications, J. Therm. Sci. Eng. Appl. 1 (3) (2009) 1–7.
[7] F. Azarmi, J. Saaedi, T.W. Coyle, J. Mostaghimi, Microstructure characterization of alloy 625 deposited on nickel foam using air plasma spraying, Adv. Eng. Mater. 10 (5) (2008) 459–465.
[8] F.P. Incropera, D.P. DeWitt, T.L. Bergman, A.S. Lavine, Fundamentals of Heat and Mass Transfer, sixth ed., Wiley, New York, 2006.
[9] W.M. Kays, A.L. London, Compact Heat Exchangers, third ed., McGraw-Hill, New York, 1984.
[10] A. Žukauskas, Heat transfer from tubes in crossflow, Adv. Heat Transfer 8 (1972) 93–160.
[11] N. Sahiti, F. Durst, A. Dewan, Heat transfer enhancement by pin elements, Int. J. Heat Mass Transfer 48 (2005) 4738–4747.
[12] N. Sahiti, F. Durst, A. Dewan, Strategy for selection of elements for heat transfer enhancement, Int. J. Heat Mass Transfer 49 (2006) 3392–3400.
[13] N. Sahiti, A. Lemouedda, D. Stojkovic, F. Durst, E. Franz, Performance comparison of pin fin in-duct flow arrays with various pin cross-sections, Appl. Therm. Eng. 26 (2006) 1176–1192.
[14] B.A. Brigham, G.J. Vanfossen, Length to diameter ratio and row number effects in short pin fin heat transfer, ASME J. Eng. Gas Turbines Power 104 (1984) 241–244.
[15] G.J. Vanfossen, Heat-transfer coefficients for staggered arrays of short pin fins, ASME J. Eng. Gas Turbines Power 102 (1982) 268–274.
[16] D.E. Metzger, C.S. Fan, S.W. Haley, Effects of pin shape and array orientation on heat transfer and pressure loss in pin fin arrays, ASME J. Eng. Gas Turbines Power 106 (1984) 252–257.
[17] H.I. You, C.H. Chang, Numerical prediction of heat transfer coefficient for a pin-fin channel flow, ASME J. Heat Transfer 119 (1997) 840–843.
[18] T.M. Jeng, S.C. Tzeng, Pressure drop and heat transfer of square pin-fin arrays in in-line and staggered arrangements, Int. J. Heat Mass Transfer 50 (2007) 2364–2375.
[19] Y. Cormier, P. Dupuis, B. Jodoin, A. Corbeil, Net shape fins for compact heat exchanger produced by cold spray, J. Therm. Spray Technol. J. Therm. Spray Technol. 22 (7) (2013) 1210–1221.
[20] J.R. Davis (Ed.), Handbook of Thermal Spray Technology, ASM International, 2004.
[21] H. Herman, S. Sampath, R. McCune, Thermal spray: current status and future trends, Mater. Res. Soc. Bull. 25 (7) (2000) 17–25.
[22] A.P. Alkhimov, A.N. Papyrin, V.F. Dosarev, N.I. Nesterovich, M.M. Shuspanov, US Patent No. 5302414, 1994.
[23] A.O. Tokarev, Structure of aluminum powder coatings prepared by cold gas-dynamic spraying, Metal Sc. Heat Treat. 38 (3–4) (1996) 136–139.
[24] M. Grujicic, C.L. Zhao, W.S. DeRosset, D. Helfritch, Adiabatic shear instability based mechanism for particles/substrate bonding in the cold-gas dynamic-spray process, Mater. Des. 25 (2004) 681–688.
[25] R.C. Dykhuizen, M.F. Smith, D.L. Gilmore, R.A. Neiser, X. Jiang, S. Sampath, Impact of high velocity cold spray particles, J. Therm. Spray Technol. 8 (4) (1999) 559–564.
[26] Plasma Giken, <http://www.plasma.co.jp/en/>, Consulted November 2012.
[27] J. Tian, T. Kim, T.J. Lu, H.P. Hodson, D.T. Queheillalt, D.J. Sypeck, H.N.G. Wadley, The effects of topology upon fluid-flow and heat-transfer within cellular copper structures, Int. J. Heat Mass Transfer 47 (14–16) (2004) 3171–3186.
[28] S. Naik, S.D. Probert, M.J. Shilston, Forced convective steady-state heat transfers from shrouded vertical fin arrays aligned parallel to an undisturbed air-stream, Appl. Energy 26 (1987) 137–158.
[29] J.J. Hwang, T.M. Liou, Heat transfer and friction in a low-aspect-ratio rectangular channel with staggered perforated ribs on two opposite walls, ASME J. Heat Transfer 117 (11) (1995) 843–850.

PERFORMANCE OF COLD SPRAYED NEAR-NET PYRAMIDAL SHAPED ARRAYS UNDER FORCED CONVECTION

Philippe Dupuis[1], Yannick Cormier[1,*,p], Antoine Corbeil[2] and Bertrand Jodoin[1]
[1] Mechanical Engineering Department
University of Ottawa, K1N 6N5, Ottawa, Ontario, Canada
[2]Brayton Energy Canada
710 rue Vernon, Unité #7, J9J 3K5, Gatineau, Québec, Canada,
[p] Presenting author
([*] Corresponding author: yannick.cormier@uottawa.ca)

ABSTRACT. This work studies the thermal and hydrodynamic performance of near-net square base pyramidal fins produced using the cold spray process. The manufacturing method for this new geometry of fin arrays is discussed. The fin array was tested in the inline configuration using a forced convection test apparatus. The efficiency of these surfaces is assessed by comparing the thermal conductances at the same required pumping powers. The effect of varying the array height and the fin density is evaluated and correlations are established. The performance of pyramidal pin fins is compared to that of several configurations of plain rectangular fins with similar dimensions. It is found that the pin fin arrays outperform the rectangular fins at the same fin density over the range of flow rates studied. This trend becomes more significant at increasing Reynolds number, especially in the sub-critical flow regime.

NOMENCLATURE

ΔP_{fin}	Fin differential pressure [Pa]	e_v	Pumping power per unit volume [kW/m^3]
ΔT_1	Inlet temperature difference [K]	FD	Fin density [fin/in]
ΔT_2	Outlet temperature difference [K]	Nu_{Dh}	Nusselt number based on hydraulic diameter
ΔT_{lm}	Log mean temperature difference [K]	P_{flow}	Flow perimeter [m]
η	Fan efficiency	P_{mean}	Mean pitch
η_o	Overall fin efficiency	Re_{Dh}	Reynolds number based on hydraulic diameter
A_{flow}	Net flow area [m^2]	R_{eq}	Equivalent thermal resistance [K/W]
A_{tot}	Total heat transfer area [m^2]	S	Spacing between two fins [m]
B	Base fin length [m]	T_b	Base temperature [K]
D_{mean}	Mean base fin length [m]	U_{max}	Maximum fluid velocity [m/s]
D_h	Hydraulic diameter [m]	UA	Thermal conductance [W/K]
e	Pumping power [kW]	UA_b	Thermal conductance per unit area [W/(m^2·K)]
e_b	Pumping power per unit area [W/m^2]	UA_v	Thermal conductance per unit volume [kW/(m^3·K)]

INTRODUCTION

The enhancement of heat transfer is a topic of utmost importance, which has received much attention over the past 30 years. Whether used for the cooling of electronic components or gas turbine blades, new fin types have been developed to enhance heat transfer surface performance. To this end, industrial applications have pushed towards miniaturization and thermal conductance enhancement while reducing the hydrodynamic cost of pumping fluid through a fin array. The first type of fin array that has been extensively studied is the plain rectangular fin (also called plate fin) array. Its precedence is explained by the ease of manufacturing this type of fin array. The maximal heat transfer attainable by such surfaces, however, is much inferior to that of pin fins, which were first investigated in the 1980s.

Pin fins with circular cross-sections were first studied by Sparrow *et al.* [1978, 1980] and Metzger *et al.* [1984] in the inline and staggered configurations, establishing that the main advantage of such pin fins is the increased local heat transfer coefficient. Drop shaped and oblong pin fin geometries have been investigated by Li *et al.* [1998] and Chen *et al.* [1997] who have determined that their heat transfer is increased, with both types also presenting a decrease in pressure loss when comparing to similar size circular cross-section pin fins. Numerical simulations and experimental testing of square shaped pin fins were performed to determine their efficiency by several authors [You and Chang 1997, Şara 2003, Jeng and Tzeng 2007].

Since these landmark publications, many researchers have compared different fin geometries and cross-sections to plate fins in order to determine which type of fin is the most efficient. One approach was to use simulation to determine the properties of both plate fin and pin fin heat exchangers [Sahiti *et al.* 2006, Zhou and Catton 2011]. Comparisons were made using different efficiency criterions which all lead to conclusion that pin fins have a better overall heat transfer surface efficiency when compared to plain rectangular fins. The flow structures were also extensively studied through numerical models to understand the mechanism beyond these gains, which is attributed to the increased turbulence and the periodic disruption of the boundary layer caused by the discontinuous features of pin fin arrays. Experimental validation of the comparisons between the different pin fin geometries previously detailed was also performed more recently by Yang *et al.* [2007], among others.

Previous studies of pin fin geometries have focused on fins whose geometry is constant along the height of the fin. Until very recently there existed little literature for variable cross-section fins such as pyramidal shaped fins. This is believed to be attributable to the lack of economically viable manufacturing methods for this type of fin. Traditional production methods (casting, machining, etching, etc.) cannot make fin arrays which do not have a constant dimension cross-section along their height on an industrial scale. The manufacturability of square base pyramidal shape pin fin arrays produced by additive manufacturing using cold spray was demonstrated by Cormier *et al.* [2013] in a study which presented information regarding the current limits of production. Currently, the fin density is limited to a maximum of 24 fins per inch for the specific aluminum powder used, while the maximal attainable fin height is determined to be inversely proportional to the fin density. For 12 fins per inch arrays, this limit is approximately 2.5 mm using the manufacturing equipment and method described. The thermal and hydrodynamic performance of such fin arrays was detailed by Dupuis *et al.* [2014]. In this work, it was shown that the thermal performance is insensitive to the base angle of the pyramid at a given fin height.

This study focuses on the thermal and hydrodynamic performance of inline short aluminum square base pyramidal pin fin arrays produced using cold spray. The efficiency of this new type of fin is also compared to that of plate fin arrays with similar geometries to determine the gain of using this type of discontinuous features instead of the traditional plain fins. The effect of varying the height and the fin density of pyramidal fins was also investigated and correlations were proposed linking the Nusselt number to the Reynolds number when varying the aforementioned geometric parameters.

EXPERIMENTAL PRODUCTION TECHNIQUE DESCRIPTION

CGDS Process and Masking Technique Kinetic spray processes such as Cold Gas Dynamic Spraying (CGDS) rely on the transfer of momentum from a high pressure and temperature inert gas (usually nitrogen) to relatively cold particles, which are deposited onto a substrate's surface. The high pressure driving gas is heated and subsequently accelerated to supersonic speeds using a converging-diverging (DeLaval) nozzle, where its kinetic energy is imparted to the particles by drag effects [Alkhimov *et al.* 1994, Tokarev 1996]. Upon colliding with the substrate, the particle's kinetic energy is used to plastically deform the particles and to induce adhesion. This impact between the particles and the substrate occurs at relatively low temperatures, which is typically less than half the material's melting temperature. The particle's mechanical deformation is sustained by the adiabatic shear instabilities created during the impact, which causes the material to viscously flow outwards from the center of the particle. Bonding to the substrate is attributed to localized high pressure waves breaking oxide layers and promoting intimate contact between the particle and the substrate.

Figure 1 illustrates the additive manufacturing technique used to create square based pyramidal fin arrays using commercially available plain woven, steel wire mesh (McMaster-Carr, Aurora, OH, USA) to mask the substrate from cold spray deposition. This configuration creates a pyramidal fin array with peaks aligning with the holes of the screened area and little or no deposition underneath the wires.

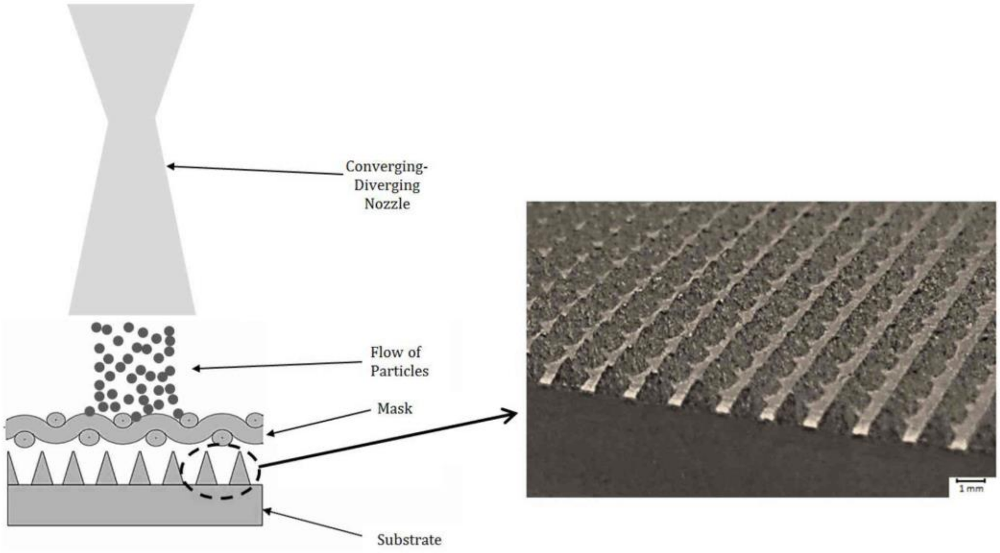

Figure 1. Schematic of the masking technique with resulting pyramidal fin array

The main factor that determines if adhesion occurs with the CGDS process is the particle's normal impact velocity with respect to the substrate. Thus, since the CGDS flow near the edges of the mask holes is affected by wall (viscous) effects, particles present in the CGDS flow in the vicinity of the mask wires are slowed down. As such, the particles tend to build up a coating preferentially on the substrate underneath the center of the mask holes. This creates a zone near the center of the holes where buildup is more pronounced than on the sides. This preferential buildup leads to the creation of an angle between the top and the base, thus forming a pyramid. When this angle becomes sharp enough, particles do not have a sufficient normal impact velocity and adhesion stops, with subsequent particles simply bouncing off the feature. The working principles of the CGDS process make it an ideal candidate for the proposed masking technique used to produce pyramidal fins. Using other thermal spray techniques such as Plasma Spraying and High Velocity Oxy Fuel (HVOF) would cause issues where the mesh would either melt or be clogged by the molten particles in the very high temperature gas stream. Production parameters were chosen to ensure that the dimensions of the pyramid's base would match those of the wire mesh mask as closely as possible.

Spray System and Powder Details The CGDS system used for this work is a commercially available Plasma Giken PCS-1000 with a spray nozzle that has a 3.0 mm throat diameter and a 6.5 mm exit diameter. The feedstock powder used was aluminum (99.8% Al, Centerline (Windsor) Ltd. (Windsor, Ontario, Canada)). The powder size is described with a D10 value of 13.29 microns, a D50 value of 25.35 microns and a D90 value of 49.58 microns. Figure 2 presents a Scanning Electron Microscopy (SEM) image of the powder where elongated, non-spherical particle geometry is noted.

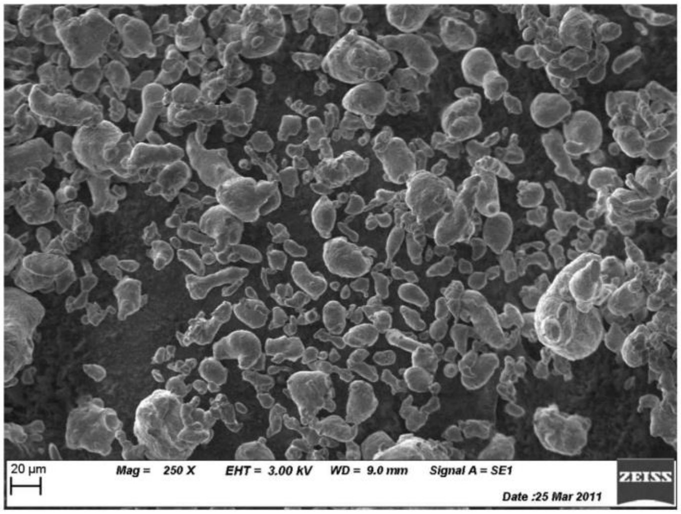

Figure 2. Scanning Electron Microscopy image of as-received pure aluminum powder

Test Sample Preparation Fins were produced on 5.1 cm by 5.1 cm aluminum substrates (Al6061 T6). These substrates were cleaned and degreased using acetone after being cut to size. No further surface preparation steps were performed. To ensure production consistency, samples were produced taller than the target height and then ground down to the target height using a conventional sanding belt with 320 grit sandpaper and water as coolant. This process yielded fins such as those presented in Fig. 3. No other type of post-treatment of the sprayed samples was performed.

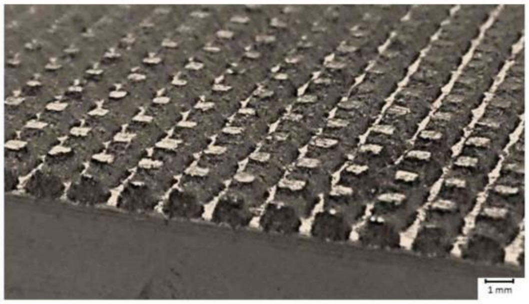

Figure 3. Ground fin array

TESTING PROCEDURE

Performance Test Apparatus Performance of the various fin arrays produced was assessed using an in-house heat transfer and pressure drop test apparatus. A schematic of the apparatus is shown in Fig. 4.

Figure 4. Schematic of test apparatus

The main components of this apparatus are the test section, the heating pad, the air supply and the data acquisition system. The air is supplied by a compressed air line equipped with a filter and dehumidifier to obtain dry room temperature air, free of oil contaminations. The air inlet flow rate is controlled by a needle valve and is measured with a flow meter. This air is smoothly expanded by a diffuser into a rectangular channel equipped with a honeycomb flow straightener. This rectangular channel is 51 mm wide by 457 mm long, with the top and bottom plates made of acrylic. These plates are spaced apart using a rectangular rubber gasket, which is compressed to ensure there is no clearance between the fins and the shroud surface. These gaskets also ensure that the joint is leak-proof. A length of unobstructed flow after the honeycomb flow straightener ensures that the fluid is fully developed hydrodynamically before reaching the test section for the given hydraulic diameter and Reynolds number [Incropera *et al.* 2006]. The test sample is subjected to a constant heat flux provided by a strip heater. A conduction block is used to ensure that heat is evenly distributed onto the substrate's surface.

A differential pressure measurement taps are located 12.7 mm on either sides of the test section. Two thermocouples are located 6 mm upstream and downstream of the test section at mid-height to record the fluid's local average temperature. Four thermocouples are attached to the fin array's base, with two on the side facing the incoming flow, and two more on the side facing the exiting flow. On each of these faces, one thermocouple is located in the middle of the width of the base, while the other thermocouple is located 6 mm from the wall. All the thermocouples used are T-type, butt-bonded, 32 gauge thermocouples. Radiative heat transfer losses are neglected since they account for less than 0.5% of the total heat input under similar testing conditions [Naik *et al.* 1987, Hwang *et al.* 1995].

Heat Transfer and Pressure Loss Testing Procedure All measurements were performed at steady-state and were repeated until statistical significance was achieved. Heat transfer data samples were taken at 2 Hz over a 30 second interval. For both types of tests, five sets of data samples were recorded for each flow rate tested. Measurements were taken at flow rates varying between 20 and 70 SLPM, which corresponds to Reynolds numbers varying from 200 to 4000 depending on sample geometry. Deviation of the measurements from the mean value was less than 5%, which led to error bars that were smaller than the markers. Since the error bars were not visible, they were not included in the corresponding figures. A detailed description of the apparatus' accuracy and of the instrument's uncertainties is given in Cormier *et al.* [2013].

Data Analysis Method To analyze the raw data obtained, flow conditions are expressed using the Reynolds number based on the flow hydraulic diameter, which is given by:

$$Re_{Dh} = \frac{\rho U_{max} D_h}{\mu} \tag{1}$$

Where ρ is the fluid's density, U_{max} is the maximal fluid velocity in the fin array, D_h is the hydraulic diameter of the fin array flow passage and μ is the fluid's dynamic viscosity. The variable D_h is given by:

$$D_h = \frac{4 \cdot A_{flow}}{P_{flow}} \tag{2}$$

where A_{flow} and P_{flow} are the flow channel's face area and perimeter, respectively.

The thermal conductance can be calculated using:

$$UA = \frac{1}{R_{eq}} = h \cdot A_{tot} \cdot \eta_o \tag{3}$$

where R_{eq} is the thermal circuit's equivalent resistance, h is the convective heat transfer coefficient, η_o is the overall surface efficiency and A_{tot} is the total heat transfer area of the exposed fin and base surface. The overall surface efficiency is calculated using the procedure detailed in Incropera's work [2006]. More details can be found elsewhere [Cormier *et al.* 2013, Dupuis *et al.* 2014].

The fin array's convective heat transfer coefficient and Nusselt number are calculated using the following relations:

$$h = \frac{\dot{q}}{\Delta T_{lm} A_{tot} \eta_o} \tag{4}$$

$$Nu_{Dh} = \frac{h \cdot D_h}{k_f} \tag{5}$$

In these equations, k_f is the thermal conductivity of the fluid, $\dot{q}$ is the heating rate and ΔT_{lm} is the log-mean temperature difference between the fluid and the fin array. The log-mean temperature difference is calculated with:

$$\Delta T_{lm} = \frac{\Delta T_1 - \Delta T_2}{\ln(\frac{\Delta T_1}{\Delta T_2})} \tag{6}$$

where ΔT_1 and ΔT_2 are the temperature difference between the fin surface and the flow at the inlet and outlet, respectively. The total heat input rate to the system is calculated using:

$$\dot{q} = \dot{M} \cdot (T_{out} - T_{in}) \cdot c_p \tag{7}$$

where $\dot{M}$ is the fluid mass flow rate, $(T_{out} - T_{in})$ is the fluid temperature difference between the entrance and the exit of the test section, c_p is the fluid's thermal capacitance.

To determine which fin array transfers heat more efficiently, an efficiency indicator must be selected. Based on the literature review performed, the method proposed in Sahiti's work [2005] was selected. This method is based on plotting the thermal and hydrodynamic data as a curve of thermal conductance as a function of the required pumping power for different flow conditions. This yields curves which can be directly compared one to another, with the most efficient fin array having a higher thermal conductance at a given pumping power. The pumping power for a given pressure loss was calculated according to Sahiti's definition [2006]:

$$\mathrm{e} = \frac{\dot{\mathrm{V}} \cdot \Delta P_{fin}}{\eta} \tag{8}$$

In the previous relation, e is the pumping power, $\dot{\mathrm{V}}$ is the volumetric flow rate of the fluid while η is the fan efficiency which was selected to be 0.8 [Sahiti 2006]. The pumping power is divided either by the fin array base (subscript b) to yield the pumping power per unit area or by the volume (subscript v) of the fin array to obtain the pumping power per unit volume.

For tube banks, the dimensionless pitch P_{mean} is defined as the ratio of fin spacing to fin size. This is described in Incropera's work [2006], and adapted for the pyramidal geometry in the following manner:

$$P_{mean} = \frac{D_{mean} + S}{D_{mean}} \tag{9}$$

where D_{mean} is the average fin base and S is the fin spacing, as shown in Fig. 5.

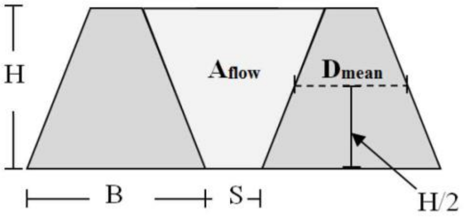

Figure 5. Important geometric parameters

EXPERIMENTAL RESULTS

Heat Transfer Efficiency of Pyramidal Pin Fins The first effect characterized was varying the height of the pyramidal fin samples. For this study, samples ranging from 1.0 to 2.0 mm heights were tested at a fin density of 12 fins per inch. The geometric data for these samples can be found in Table 1, with the prefix H designating that the sample was used for the height study and the numerical value besides it indicating the sample height in mm. These values were obtained using a VHX-2000 depth of field microscope (Keyence, Mississauga, Ontario, Canada).

Table 1
Important Geometric Variables for Height Study Samples

Sample	Hydraulic Diameter (mm)	D_{mean} (mm)	H/D_{mean} ratio	Total Heat Transfer Area (mm^2)
H1.0	1.02	0.81	1.24	3637
H1.2	1.19	1.56	0.77	3834
H1.4	1.30	1.83	0.76	4128
H1.6	1.24	1.53	1.05	5184
H1.8	1.35	1.84	0.98	5389
H2.0	1.45	2.20	0.91	5525

The fin array area based heat transfer efficiency is shown in Fig. 6(a), where it can be seen that increasing fin height yields a better performance but that the gains in performance tend to be minimal past a fin height of 1.6 mm. This conclusion is especially useful when designing heat sinks where the most important size parameter is the footprint area. However, Fig. 6(b) shows that when the fin array volume is taken into consideration, the pyramidal fins have a similar performance over the range of pumping powers tested, except for the H1.0 sample which has a slightly lower performance than its higher counterparts. The mechanism behind these trends is hypothesized to be due to the flow structure and the size of the recirculation zones behind the fins.

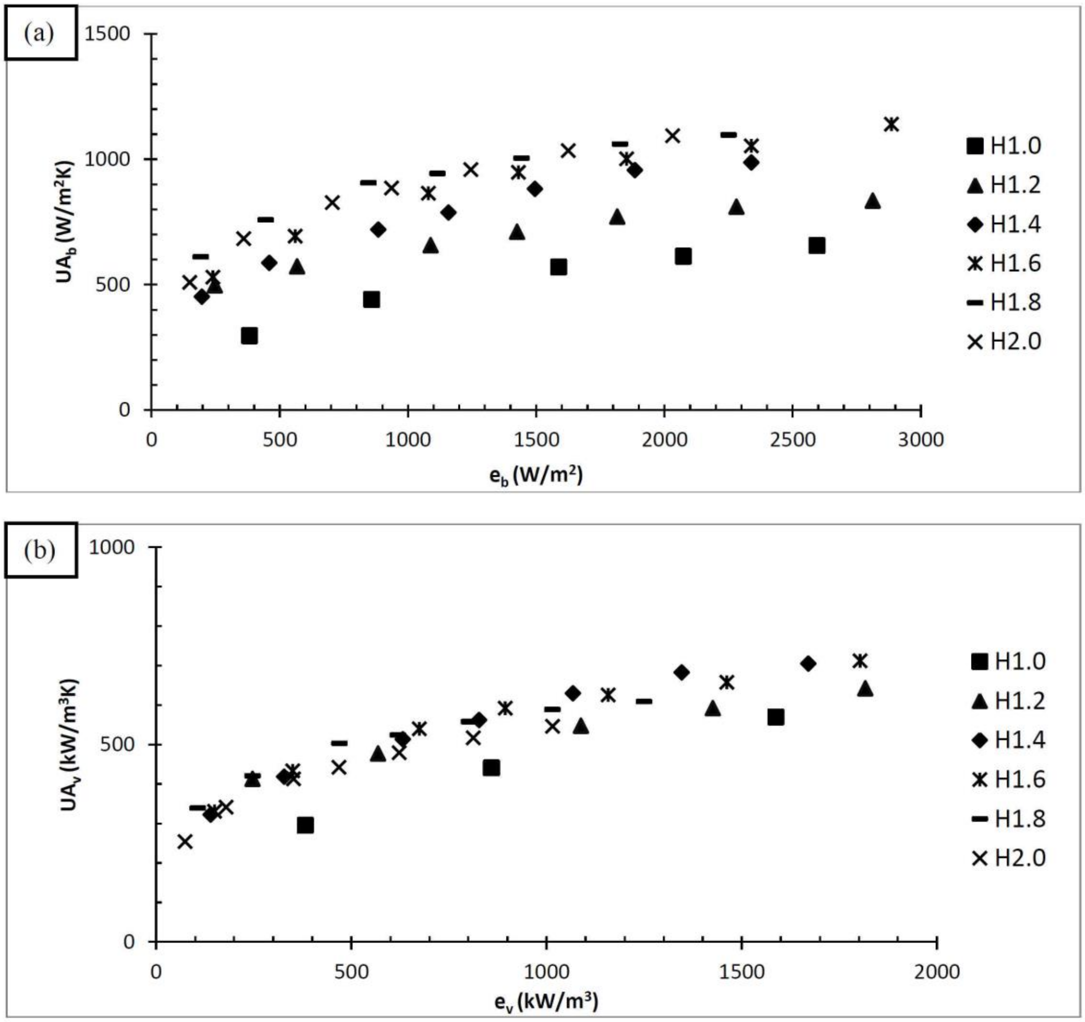

Figure 6. Heat transfer surface efficiency comparison for the height effect based on (a) footprint area; (b) volume

The second parameter that has been studied is the fin density. Samples were produced with 12, 16, 20 and 24 fins per inch at a height of 1.0 mm and are designated by the prefix FD followed by the fin density value. The geometric characteristics of these samples are given in Table 2 while Fig. 7 presents the volume based thermal efficiency of these samples. It can be noted that there is a large difference in heat transfer efficiency between the 12 fin per inch sample and the other samples. This difference is mostly due to the higher thermal conductance of the denser samples, offset by a small increase in the pressure loss. This increase in thermal conductance is explained by the increase in available heat transfer area since the FD16, FD20 and the FD24 samples have very similar heat transfer efficiency, with a maximal difference of 10% over the range of flow rates tested.

Table 2
Important Geometric Variables for Fin Density Study Samples

Sample	Hydraulic Diameter (mm)	D_{mean} (mm)	H/D_{mean} ratio	Total Heat Transfer Area (mm^2)
FD12	1.02	0.81	1.24	3637
FD16	0.90	0.72	1.38	4570
FD20	0.73	0.66	1.51	5524
FD24	0.66	0.55	1.81	6346

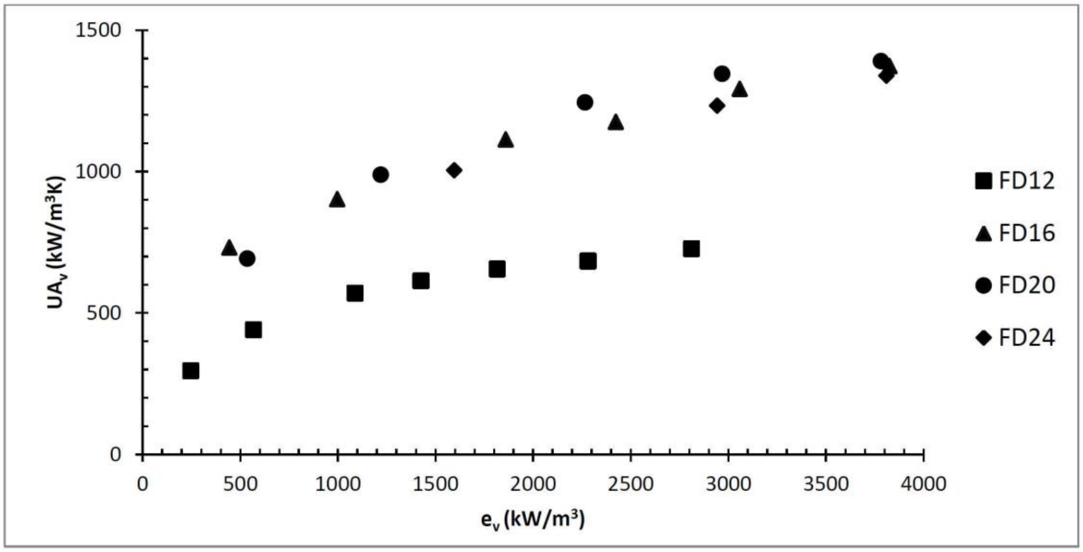

Figure 7. Volume based heat transfer surface efficiency comparison for the fin density effect

Performance Comparison with Rectangular Fins The thermal performance of pyramidal pin fins was compared to that of plain rectangular fins. The geometric data for the samples tested is presented in Table 3. In this table, the prefix SC designates a plain rectangular (straight cut) fin sample, while the prefix PY designates a pyramidal fin sample. For the first 3 samples, the numbers represent the height of the sample with 12 fins per inch, while for the next four, these numbers represent fin densities in fins per inch with a fin height of 1 mm.

Table 3
Important Geometric Variables for Straight Cut Comparison Samples

Sample	**Hydraulic Diameter** (mm)	**D_{mean}** (mm)	**H/D_{mean} ratio**	**P_{mean}**	**Total Heat Transfer Area** (mm^2)
SC1.3-1	1.33	0.76	1.71	2.8	4759
SC1.3-2	1.37	0.66	1.97	3.2	4864
PY1.3	1.33	0.61	2.12	3.2	4044
SC12	0.94	1.22	0.81	1.7	3478
SC24	0.78	0.39	2.63	2.7	6393
FD12	1.02	0.81	1.24	1.9	3637
FD24	0.66	0.55	1.81	1.9	6346

The first comparison is shown in Fig. 8(a), between the sample PY1.3 and the samples SC1.3-1 and SC1.3-2. It is to be noted that the rectangular fin samples respectively have the same hydraulic diameter (SC1.3-1) and the same mean pitch (SC1.3-2) as the pyramidal fin sample, with all three samples having a fin density of 12 fins per inch with a height of 1.3 mm. From this figure, it can be seen that that the PY1.3 sample is more efficient than the plain fin arrays over the range of pumping powers studied. Although the straight fins have a much lower pressure loss than the pyramidal fin array, their lower thermal conductance result in pyramidal pin fin samples having a better overall thermal efficiency. This fact is supported by Fig. 8(b), which shows the convective coefficients of these samples. Pin fins have a much higher convective coefficient at a given flow rate, especially at Reynolds numbers higher than 1000. This agrees with the theory advanced by Žukauskas [1972] for banks of tubes. According to his work, a laminar regime can be identified from very low Reynolds to approximately 1000 Re_{Dh}, where the flow is dominantly laminar with large scale recirculation regions behind the fins while the sub-critical regime would start near 500 Re_{Dh} and extend to 200 000 Re_{Dh}, with the flow structure being largely laminar but becoming increasingly turbulent, especially in the fin's wake. This theory explains why there is a larger performance gain in the sub-critical regime when using pin fins compared to rectangular fins.

The next comparison is between rectangular and pyramidal fin array samples at 1.0 mm height for both 12 and 24 fins per inch. From Fig. 9(a), it can be noted that the 12 fin per inch pin fin array outperforms both straight fin samples at pumping powers exceeding 1500 kW/m^3. It can be noted that when comparing the pyramidal and rectangular fin samples with similar fin densities, a gain of approximately 100% in thermal conductance can be observed at the same pumping powers over the domain of the curves. Once again, this performance is explained by the higher convective coefficients attainable by pin fin arrays. As it can be seen in Fig. 9(b), the slope of the convective coefficient as a function of Reynolds number for pin fins is much steeper that it is for the continuous fins studied. Furthermore, at approximately 1000 Re_{Dh}, the rectangular fin samples' slope gradually flattens out while the slope of the pin fin's slope remains almost constant for the range of Reynolds number tested.

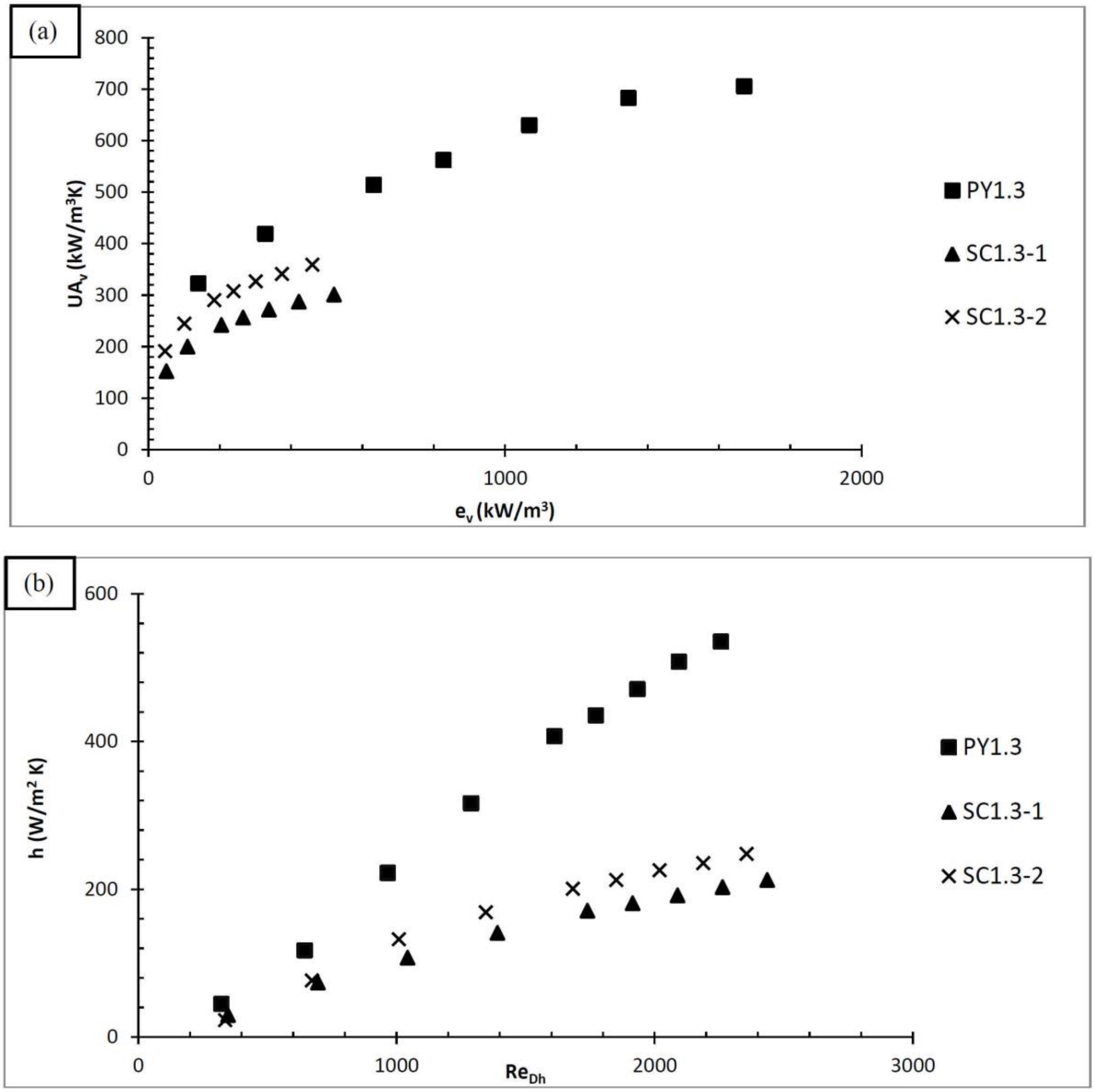

Figure 8. Straight cut comparison with a height of 1.3mm (a) volume based heat transfer surface efficiency ; (b) convective coefficient

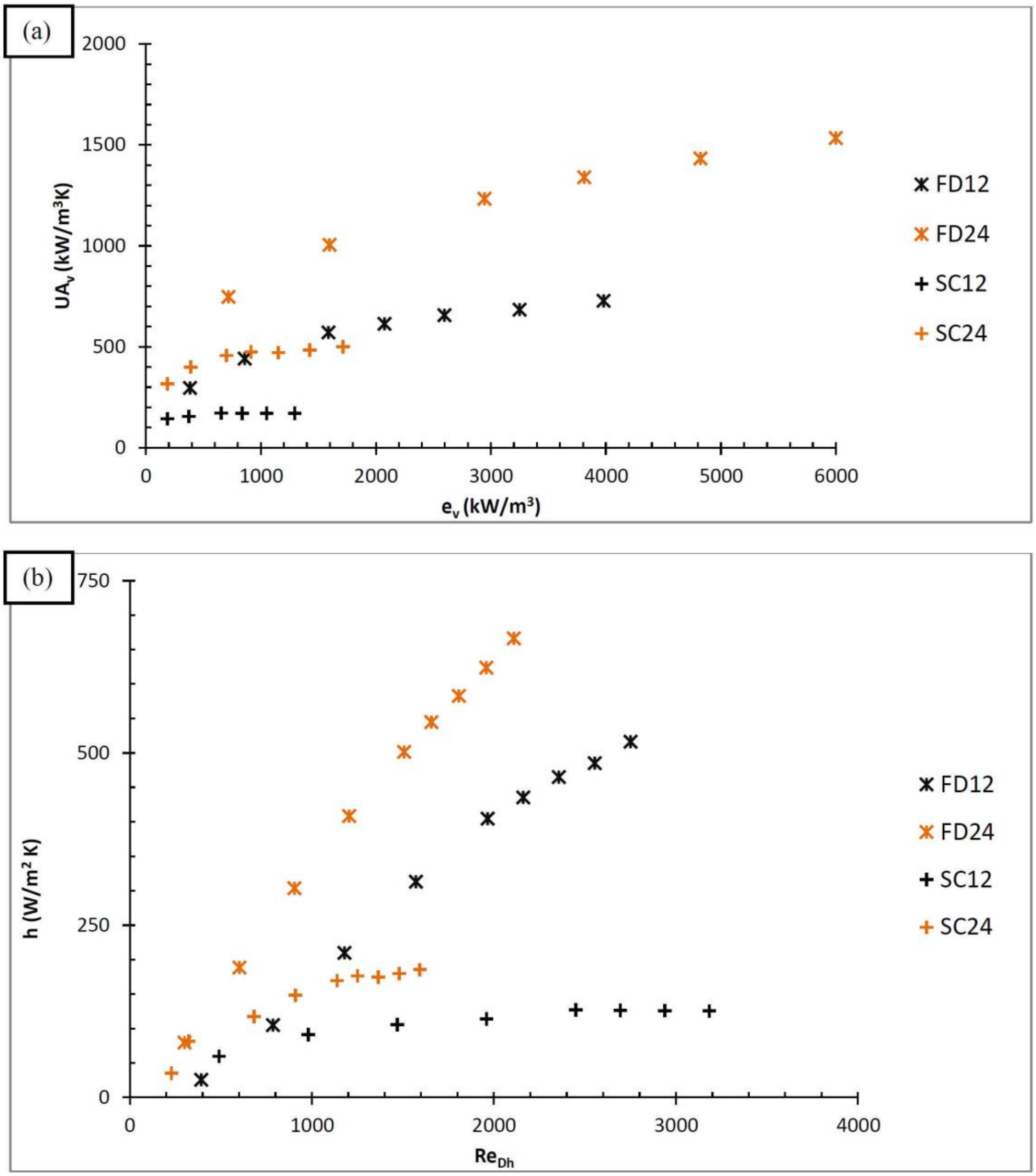

Figure 9. Straight cut comparison at different fin density (a) volume based heat transfer surface efficiency ; (b) convective coefficient

Heat Transfer Correlations for Fin Height and Fin Density To be able to predict the heat transfer performance of fin arrays at various fin heights and fin densities, correlations should ideally be developed using non-dimensional parameters. This would allow one to perform predictive modeling and to compare different fin array geometries without having to perform an excessive amount of experimental work. In this case, the Nusselt number acts as a dimensionless heat transfer performance scaling parameter. Due to the small number of samples tested, no cross-correlations were produced between the height effect and the fin density effect. Two linearly proportional relationships (regimes) between the Reynolds number and the Nusselt number have been identified. The performance of the H1.0 and the FD12 samples was observed to be different from that of the others in their respective groups and for this reason they have not been included in the correlations. It is hypothesized that this phenomenon is due to differences in the flow structures.

To determine the correlation linking the Nusselt number, fin height and the Reynolds number, the following procedure was used. The average Nusselt value line determined for the sub-critical regime was then reconverted to thermal conductance values with the geometric data to evaluate the error between the correlation and the actual experimental data. A linear regression was found which correlate the results appropriately with error averages of less than 15% for all samples, which validates the proposed approach. This would indicate that using the equation:

$$Nu_{Dh} = 0.0120\, Re_{Dh} + 2.8463 \quad \text{for } 750 < Re_{Dh} < 2000 \tag{10}$$

would appropriately model the thermal performance of 12 fin per inch pyramidal fin arrays with heights varying between 1.2 and 2.0 mm over the range of Reynolds number studied.

A different approach was used to create a correlation between the Nusselt number, Reynolds number and the fin density. The Nusselt number was found to be a quadratic function of the fin density. A correlation was built using first and second order terms for the fin density and a first order term for Reynolds number. Once again, the domain was restricted to the sub-critical regime, since this is the region of interest for pin fins. The correlation and experimental curves are found to have good agreement with the error averages of less than 5% using this approach. The following correlation is then proposed:

$$\begin{aligned} Nu_{Dh} = 2.61 \cdot 10^{-5}\, Re_{Dh}\, FD^2 + 0.0171\, FD^2 \\ - 0.00133\, Re_{Dh}\, FD - 1.05\, FD \\ +0.0238\, Re_{Dh} + 17.0 \end{aligned} \quad \text{for } 750 < Re_{Dh} < 2000 \tag{11}$$

to appropriately model the thermal performance of 1.0 mm height pyramidal fin arrays over the range of Reynolds number studied for fin densities between 16 and 24 fins per inch.

SUMMARY AND CONCLUSION

This work studies the thermal and hydrodynamic performance of various geometries of inline, square base pyramidal fin arrays. Fin densities varying between 12 and 24 fins per inch were tested at 1.0 mm height while other samples were tested at 12 fins per inch with heights varying between 1.0 and 2.4 mm. Heat transfer efficiency comparisons were made between pyramidal fin samples and several configurations of similar geometry plate fin arrays. For both 12 and 24 fins per inch samples, the pin fin arrays outperform their continuous counterpart, especially in the sub-critical regime (at Reynolds numbers exceeding 1000), due to the increased convective coefficient. The 12 fin per inch sample tested at 1.3 mm height also outperformed a 12 fin per inch rectangular fin sample with the same mean pitch and the another sample with the same hydraulic diameter over the range of Reynolds numbers tested. Correlations were built to describe and predict the performance of these samples with less than 15% error.

ACKNOWLEDGEMENTS

The authors would like to thank Dr. M. Yandouzi of the University of Ottawa Cold Spray Laboratory for help with the SEM micrographs and they would also like to acknowledge the financial support of the MITACS Accelerate program.

REFERENCES

Alkhimov, A.P., Papyrin, A.N., Dosarev, V.F., Nesterovich, N.I. and Shuspanov, M.M. [1994], US Patent No. 5302414.

Chen, Z., Li, Q., Meier D. and Warnecke, H.-J. [1997], Convective heat transfer and pressure loss in rectangular ducts with drop-shaped pin fins, *Heat Mass Transfer*, Vol. 33, pp. 219-224.

Cormier, Y., Dupuis, P., Jodoin, B. and Corbeil, A. [2013], Net Shape Fins for Compact Heat Exchanger Produced by Cold Spray, *J. Therm. Spray Technol.*, Vol. 22, No. 7, pp. 1210–1221.

Dupuis, P., Cormier, Y., Farjam, A, Jodoin, B. and Corbeil, A. [2014], Performance evaluation of near-net pyramidal shaped fin arrays manufactured by cold spray, *Int. J. Heat Mass Trans*, Vol. 69, pp. 34-43.

Hwang, J.J. and Liou, T.M. [1995], Heat transfer and friction in a low-aspect-ratio rectangular channel with staggered perforated ribs on two opposite walls, *ASME J. of Heat Transfer*, Vol. 117, No. 11, pp. 843-850.

Incropera, F. P., DeWitt, D. P., Bergman, T. L. and Lavine, A. S. [2006], *Fundamentals of Heat and Mass Transfer*, sixth ed., Wiley, New York.

Jeng, T.M. and Tzeng, S.C. [2007], Pressure drop and heat transfer of square pin-fin arrays in in-line and staggered arrangements, *Int. J. Heat Mass Transfer*, Vol. 50, pp. 2364-2375.

Li, Q., Chen, Z., Flechtner, U. and Warnecke, H.-J. [1998], Heat transfer and pressure drop characteristics in rectangular channels with elliptic pin fins, *Int. J. Heat Fluid Flow*, Vol. 19**,** pp. 245-250.

Metzger, D.E., Fan, C.S. and Haley, S.W. [1984], Effects of pin shape and array orientation on heat transfer and pressure loss in pin fin arrays, *ASME J. Eng. Gas Turbines Power*, Vol. 106**,** pp. 252-257.

Naik, S., Probert, S.D. and Shilston, M.J. [1987], Forced convective steady-state heat transfers from shrouded vertical fin arrays aligned parallel to an undisturbed air-stream, *Appl. Energy*, Vol, 26, pp. 137-158.

Sahiti, N., Durst, F. and Dewan A. [2005], Heat transfer enhancement by pin elements, *Int. J. Heat Mass Trans*, Vol. 48, pp. 4738-4747.

Sahiti, N., Durst, F. and Dewan, A. [2006], Strategy for selection of elements for heat transfer enhancement, *Int. J. Heat Mass Trans*, Vol. 49 pp. 3392-3400.

Sahiti, N., Lemouedda, A., Stojkovic, D., Durst, F. and Franz, E. [2006], Performance comparison of pin fin in-duct flow arrays with various pin cross-sections, *Appl. Therm. Eng.*, Vol. 26**,** pp. 1176-1192.

Şara, O.N. [2003], Performance analysis of rectangular ducts with staggered square pin fins, *Energy Convers. Manage.*, Vol. 44**,** pp. 1787-1803.

Sparrow, E.M. and Ramsey, J.W. [1978], Heat transfer and pressure drop for a staggered wall-attached array of cylinders with tip clearance, *Int. J. Heat Mass Transfer*, Vol. 21**,** pp. 1369-1377.

Sparrow, E.M., Ramsey, J.W. and Altemani, C.A.C. [1980], Experiments on in-line pin fin arrays and performance comparison with staggered arrays, *ASME J. of Heat Transfer*, Vol. 102**,** pp. 44-50.

Tokarev, A.O. [1996], Structure of aluminum powder coatings prepared by cold gas-dynamic spraying, *Met. Sci. Heat Treat.*, Vol. 38, No. 3-4, pp. 136-139.

Yang, K.S., Chu, W.H., Chen, I.Y., Wang, C.C. [2007], A comparative study of the airside performance of heat sinks having pin fin configurations, *Int. J. Heat Mass Transfer*, Vol. 50, pp. 4661-4667.

You, H.I. and Chang, C.H. [1997], Numerical prediction of heat transfer coefficient for a pin-fin channel flow, *ASME J. of Heat Transfer*, Vol. 119**,** pp. 840-843.

Zhou, F. and Catton, I. [2011], Numerical Evaluation of Flow and Heat Transfer in Plate-Pin Fin Heat Sinks with Various Pin Cross-Sections, *Numer. Heat Transfer, Part A*, Vol. 60, pp. 107-128.

Žukauskas, A. [1972], Heat Transfer from Tubes in Crossflow, *Adv. in Heat Transfer*, Vol. 8 pp. 93–160.

CHAPTER 7 FLOW STRUCTURE ANALYSIS FOR PYRAMIDAL PIN FINS

The focus of the following article was to establish a method to visualize the flow structures found in pyramidal pin fin arrays, with the goal of linking changes in flow structures to the thermal and hydrodynamic performance of such fin arrays. Furthermore, the turbulence intensity of the flow at different locations was evaluated to demonstrate that although the flow is in the sub-critical regime, the perturbations to the flow pattern caused by the fins are non-negligible, even though the large scale flow structures are well established after a few fin columns. Furthermore, after observing the flow structures, a slight misalignment of the axial and transverse flow channel was observed and studied in detail with the use of a CFD model to determine the effect on the thermal and hydrodynamic performance of this misalignment.

International Journal of Heat and Mass Transfer 93 (2016) 301–313

Contents lists available at ScienceDirect

International Journal of Heat and Mass Transfer

journal homepage: www.elsevier.com/locate/ijhmt

Flow structure identification and analysis in fin arrays produced by cold spray additive manufacturing

Philippe Dupuis [a,*], Yannick Cormier [a], Marianne Fenech [a], Antoine Corbeil [b], Bertrand Jodoin [a]

[a] University of Ottawa, 161 Louis Pasteur Av., Ottawa, Ontario K1N 6N5, Canada
[b] Brayton Energy Canada, 710 rue Vernon, Unité #7, Gatineau, Québec J9J 3K5, Canada

ARTICLE INFO

Article history:
Received 23 June 2015
Received in revised form 6 October 2015
Accepted 7 October 2015

Keywords:
Cold Gas Dynamic Spray
Flow structure
Forced convection
Micro-particle image velocimetry
Pin fins

ABSTRACT

The focus of this work is the identification and analysis of the flow structures found in pyramidal pin fin arrays produced using the Masked Cold Gas Dynamic Spraying (MCGDS) additive manufacturing process. The observed flow structures are described, with classic double recirculation patterns being identified. The turbulence intensity levels of the flow in the axial flow channels was measured and it was found that although the flow rates considered in this work correspond to low Reynolds numbers (500–3000), significant turbulence intensity levels are found. Furthermore, these levels increase as the flow progresses downstream, even though the large scale flow structures are well established after a few rows (as little as two in this case). A slight misalignment of the axial and transverse flow channels resulting from imperfections in the masks caused a bypass flow structure to arise in the wake of the pin fins, replacing the double recirculation pattern observed when there is no such misalignment. A CFD model was used to investigate the effect of these misalignments on heat transfer efficiency and predicted that there would be no significant effect in the configurations studied. Finally, this work shows the importance of not only considering the flow structures in the fin's wake, but also the effect of these structures on the turbulence levels of the axial flow channels, which could significantly affect the thermal and hydrodynamic performance.

1. Introduction

Increasing heat transfer in many industrial applications has been a major concern over the last 50 years. For example, in the aerospace and the automotive sectors, the use of compact heat exchangers has become widespread. Compact heat exchangers account for approximately 10% of the global heat exchanger market with a growth in sales ten times larger than that of other types of heat exchangers, as a result of the high industrial demand [1]. Indeed, the high surface area to volume ratio that characterizes compact heat exchangers allows this class of heat exchangers to obtain high heat transfer performance while minimizing the amount of space required for this component [2,3]. The drawback of using compact heat exchangers is that the high thermal performance is usually offset by high head losses [2,3]. The development of even more space efficient heat transfer surfaces could also bring significant benefits to the general commercial usage of compact heat exchangers.

To this end, pin fins have replaced traditional continuous fin arrays such as plate or wavy fins in state-of-the-art applications due to the higher volumetric heat transfer rates attainable [3,4]. The increased thermal performance that can be obtained by pin fins is usually partially offset by larger head loss through the fin array, but pin fin arrays typically offer a better overall performance than continuous fin arrays [5–8]. Sahiti et al. [6–8] have demonstrated that pin fins offer the best performance for a given pumping power and heat exchanger volume, when properly designed. This was justified by the fact that using pin fins instead of plate fins does not only increase the available heat transfer area, but also significantly increases the average convective heat transfer coefficient.

Pin fin array performance has been the subject of many studies over the past decades. Sparrow et al. [9,10] and Metzger et al. [11] have extensively studied the heat transfer characteristics of cylindrical pin fins in the inline and staggered configurations, concluding that the pin fin surface convective heat transfer coefficient was approximately 100% larger than that of the end walls. The conventional theory behind this type of heat transfer enhancement by pin fins is that the flow structures on the downstream side of a pin fin consists of a large recirculation zone enhancing the local heat transfer coefficient. This type of fluid motion was studied by

---

* Corresponding author at: Mechanical Engineering, University of Ottawa, Colonel By Hall, 161 Louis Pasteur Av., Ottawa, Ontario K1N 6N5, Canada. Tel.: +1 (613) 562 5800x2481; fax: +1 (613) 562 5177.

E-mail address: philippe.dupuis@uottawa.ca (P. Dupuis).

http://dx.doi.org/10.1016/j.ijheatmasstransfer.2015.10.019
0017-9310/© 2015 Elsevier Ltd. All rights reserved.

Nomenclature

ΔP	fin pressure difference (Pa)
ΔQ	heat flux difference (W)
η_p	relation for the increase in pressure loss
η_q	relation for the increase in heat transfer
μ	dynamic viscosity (Pa s)
ρ	fluid density (kg/m^3)
A_{flow}	net flow area (m^2)
C_p	fluid specific heat capacity (J/(kg K))
D_h	hydraulic diameter (m)
I	turbulence intensity
$\dot{m}$	mass flow rate (kg/s)
N_{flow}	flow perimeter (m)
P	pressure (Pa)
Q	heat flux (W)
R_{Dh}	Reynolds number based on hydraulic diameter
T	mass weighted average of the fluid temperature (K)
u'	root mean square (RMS) of the velocity fluctuations (m/s)
U	mean velocity (m/s)
U_{max}	maximum fluid velocity (m/s)
y^+	non-dimensional distance from wall to first mesh node
Subscripts	
in	inlet conditions
out	outlet conditions
straight	straight model geometry parameter
tilted	tilted model geometry parameter

Žukauskas for banks of tubes, who observed and split the flow structures into three flow regimes [5]. The first regime (laminar regime) would extend from very low Reynolds numbers up to 1000, where the flow is dominantly laminar with large scale recirculation regions behind the fins. The second regime (sub-critical regime) would start near Reynolds numbers of 500 and extend to 200,000, with the flow structure being largely laminar but becoming increasingly turbulent in the fin's wake. The third regime (fully turbulent regime, located at Reynolds numbers higher than 200,000) is where the flow is in a fully turbulent state, with the recirculations behind the fins dissipating into random fluid motion.

Novel methods of producing extended surfaces to increase heat transfer are currently being investigated, such as the creation of compact heat exchangers using metal foam cores [12,13], or by using additive manufacturing principles to simplify the manufacturing of fin arrays with complex geometries. For example, the Cold Gas Dynamic Spray (CGDS, or simply cold spray) process has been identified as a potential candidate for the production of near-net shape pin fin arrays [14–17]. The cold spray process was developed in the late 1980s at the Institute of Theoretical and Applied Mechanics of the Siberian Branch of the Russian Academy of Sciences [18,19]. This process is based on the addition of material to a substrate by the deposition of solid powder particles accelerated by a high pressure carrier gas flowing at supersonic speeds. Upon impact, the particles plastically deform as a result of adiabatic shear instabilities and adhere to the substrate and to the particles that were already deposited, creating dense coatings on the substrate's surface [20,21]. Using a mask to selectively shield the substrate from deposition, as depicted in Fig. 1, it is possible to create pin fin arrays of various shapes and dimensions. The operating principles of the spray process also encourage preferential build-up of material in the center of the mask openings, allowing the construction of features with tapered cross-sections along their height, such as pyramids or cones, when proper spray parameters are used [14]. The advantages of this new production method are its high productivity rates, combined with the low production costs of such fin arrays and the ease of implantation of this technology. This new fin array production technique yields near-net shape, short (height over base diameter ratio less than 4) pyramidal pin fin arrays that are lighter than constant cross-section fins due to the reduced amount of materials required.

The studies regarding the performance of pin fins described previously focused on pin fin arrays with constant cross-section along the fin height. The characterization of the thermal and hydrodynamic performance of tapered pin fin arrays was performed and reported by the authors in other works [14–16], and show great promise as an economically viable replacement for plate (continuous rectangular) fin arrays. The increase in thermal performance of pyramidal pin fins compared to constant cross-section rectangular fins reported in these works [14–16] was hypothesized to be attributable to the recirculation regions behind the pin fins, similarly to the structures and regimes identified by Žukauskas for regular (non-tapered) pin fins [5], however this has not yet been confirmed experimentally. Given that the increased performance is much larger at higher Reynolds numbers, it was proposed that this is potentially caused by an increased contribution to the total heat transfer due to recirculation structures that are believed to exist behind the pin fins. Another interesting finding is shown in Fig. 2, which presents data previously published by the authors [16], illustrating the typical Nusselt number vs Reynolds number curves for different pyramidal pin fin arrays, where it is possible to observe a change in the slope near Re_{Dh} 1000. This slope change occurs at Reynolds numbers in the transition zone from the laminar regime to the sub-critical regime (which are described in detail in Žukauskas' work [5]). This change in Nusselt number slope is then most likely a flow structure based phenomenon, which could potentially be studied in detail using flow visualization techniques.

Flow structure visualization in heat exchangers using particle image velocimetry (PIV) has been performed by several authors [22–25]. Wen et al. [22] focused on the determination of the effect of the flow structures found in the headers upstream of a plate fin heat exchanger and the consequences of maldistribution of fluid

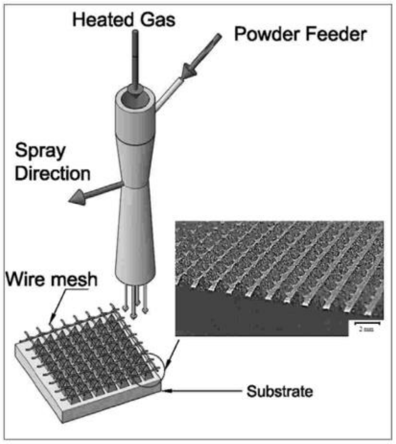

Fig. 1. Schematic of the masking spray process with its resulting pyramidal fin arrays.

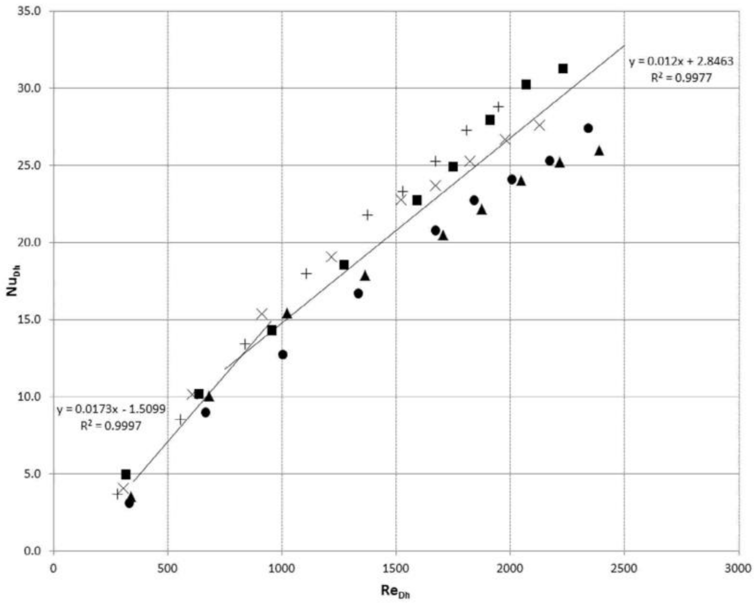

Fig. 2. Typical Nusselt vs Reynolds number plot for several fin array samples, with trendlines reflecting the average change in slope that occurs near Re 1000 (raw data obtained from [16]).

on these fin arrays. Jones et al. [23] used micro-particle image velocimetry (μPIV) measurements to examine the flow maldistribution in microchannel heat sinks, which allowed experimentally determining that maldistribution increases drastically as the Reynolds number is increased. Uzol et al. [24] studied both the performance and the flow structures arising from circular and elliptical pin fin arrays and found that the elliptical shaped fins transferred less heat, but did so at a much lower aerodynamic cost, yielding a better overall efficiency than their circular counterpart. This was explained to be due to the early flow separation from the circular pin fin's surface, which creates a large low velocity wake behind the fin, that has been identified and measured using PIV [25]. Furthermore, the higher levels of turbulent kinetic energy measured in the circular fin's wake helped explain the increased thermal performance of this type of geometry when compared to ellipses [25].

The focus of this work is to identify and study the fluid motion zones in pyramidal fin arrays using μPIV, in order to better understand the performance curves of such fin arrays. Particular attention is devoted in this study to try to identify if a change in the large scale flow structure or properties in the wake of the fins can be found which could explain the fundamental phenomenon that induces the change of slope of the heat transfer performance curve in the vicinity of $Re_{Dh} = 1000$ reported previously. Furthermore, the observations made using μPIV will help validate a computational fluid dynamics (CFD) model that serves the purpose of furthering the understanding of the flow patterns and their associated heat transfer properties. The investigations are focused on a 12 fin per inch sample with a fin height of 1.0 mm and a fin base length of 1.5 mm, in both axial and transverse flow directions.

2. Characteristics of the heat exchanger samples

2.1. Masked CGDS fin production technique

The technique used to create square based pyramidal fin arrays using cold spray is shown in Fig. 1. This additive manufacturing method consists of shielding parts of the substrate from the deposition of the particles accelerated by the cold spray nozzle by selectively masking the substrate, which allows the user to build features of various shapes and dimensions. The operating principles of the spray process also encourage preferential build-up of material in the center of the mask openings, allowing the construction of features with tapered cross-sections along their height, such as pyramids or cones, when proper spray parameters are used [14]. Commercially available, plain woven, steel wire meshes (McMaster-Carr, Aurora, OH, USA) were used as masks to produce square based pyramidal fin arrays, such as those presented in the detail of Fig. 1. These fin arrays closely mimic the reversed geometry of the chosen wire mesh, with peaks aligning with the holes of the screened area. Cold spray parameters were chosen to ensure that the deposited geometry is as close to the idealized geometry as possible.

A commercial SST series EP cold spray apparatus (Centerline (Windsor) Ltd, Windsor, ON, Canada) was used in conjunction with the process described previously to produce the fin arrays for this work. The carrier gas used in this work is commercially pure nitrogen, with a nozzle inlet pressure of 1.7 MPa and a nozzle inlet temperature of 350 °C. The feedstock powder material used is commercially pure aluminum (99.8% Al, Centerline (Windsor) Ltd, Windsor, ON, Canada) with an elongated shape and a mean particle diameter of 25 μm. Details regarding this feedstock powder are available elsewhere [12].

2.2. Test sample preparation and geometry evaluation

Fins were sprayed on Al6061 T6 aluminum substrates (Metal Supermarkets, Ottawa, ON, Canada) with dimensions of 7 mm by 51 mm (3 fin rows by 24 fin columns). The substrates were cleaned and degreased using acetone after being cut to size. No further surface preparation step was performed. The top of the pyramids were ground using a Tegra Pol circular polishing machine (Struers, Ballerup, Denmark) with 120 grit silicon oxide sandpaper to ensure fin height consistency and shroud sealing, as described in Dupuis et al. [15].

The detailed geometry measurements were obtained using a depth of field microscope (Keyence model VHX-2000, Mississauga, Ontario, Canada) which allows building three dimensional images of the given samples. Ten fin specimens were measured and average values with the associated standard deviations were reported for the relevant measurements.

3. Testing procedure

3.1. μPIV apparatus and equipment

A commercial μPIV Flowmaster3 apparatus (LaVision, Goettingen, Germany) was used to capture the flow structures using a cross-correlation algorithm. The pin fin array sample was mounted in an aluminum sample holder equipped with a transparent polycarbonate viewing window, built at the University of Ottawa. A 1/25 hp centrifugal pump (The Pump House, Ottawa, ON, Canada) was used to pump the fluorescent polyester particle doped water through the system. A high-accuracy flow meter (McMaster-Carr, Aurora, OH, USA) equipped with a valve was used to adjust the flow rates between 2 and 8 ml/s, which corresponds to Reynolds numbers varying between 500 and 2000. Schematics of the apparatus are shown in Figs. 3 and 4.

The camera used to record the visual information is a double pulsed CCD camera equipped with a microscope to condition the incoming light. It has a 5 Hz frame rate with a minimal time interval of 0.5 μs between two successive exposures. The camera offers a resolution of 1376 × 1040 pixels with an exposure plate of 8.9 × 6.7 mm and was used in conjunction with a long working distance microscope objective lens with 5× magnification. This yielded a pixel width of 1.31 μm and a depth of field of 28 μm.

The laser source used for sample illumination is a double pulsed Nd:YAG laser used in conjunction with a dichroic filter, which only allows green light ($\lambda = 532$ nm) towards the sample and the red light ($\lambda = 650$ nm) that is emitted by the fluorescent tracer particles back to the camera. The laser pulses are collinear and produce a full volume illumination in the test section, which causes the depth of focus to be solely a function of the microscope optics. The laser pulse delay between successive exposures was adjusted to maintain particle displacements of five to ten pixels for the bulk of the fluid in each measurement zone, as the local fluid velocity distribution varied significantly at a given Reynolds number.

The tracer particles used are Fluoro-Max red particles (Fisher, Waltham, MA, USA) with a particle diameter of 0.8 μm. These polystyrene particles have a density of 1.05 g/cm^3 and a refractive index of 1.59 for 589 nm wavelength light at 298 K. This particle size, used in conjunction with the aforementioned lens, yielded a depth of correlation of 27 μm [26,27].

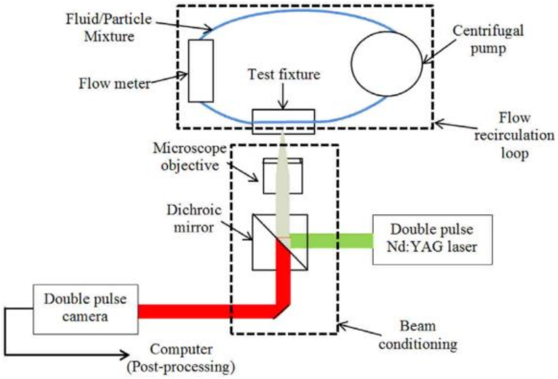

Fig. 3. μPIV setup.

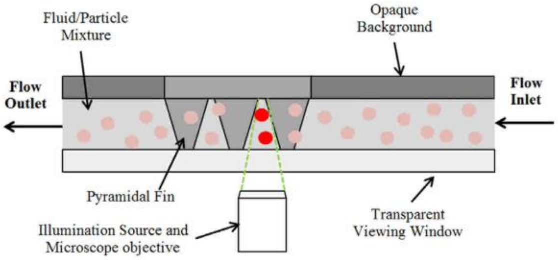

Fig. 4. Schematic of the μPIV test fixture.

The PIV images were taken at a 100 μm intervals one from another, depth-wise (Fig. 5(a)). These data were used to reconstruct a stepped profile of the fluid flow at three areas on the fin array deemed to be critical: between two columns of fins (Fig. 5(b) region i), at the junction of a longitudinal and a transverse flow channel (at the corner of four fins, Fig. 5(b) region ii) and in a longitudinal flow channel (Fig. 5(b) region iii). Due to the high background intensity near the viewing window and the base of the fins, data was collected 200 microns offset from each of these surfaces. Sets of 100 pairs of images were taken for each measurement height to determine reliable averages and root mean square (RMS) values of the velocity and its fluctuations, respectively.

3.2. Image post-processing

The raw image pairs in a set were first averaged to obtain a picture of the background. The averaged picture was then subtracted from the raw images, yielding images that contained only the position of particles, with the background intensity removed. These images were then post-processed using Flowmaster's standard PIV cross-correlation algorithm, using a two-step process in which the interrogation window size is reduced from 64 × 64 pixels to 32 × 32 pixels, both with 0% overlap. Spurious vectors were then removed using the software's built-in vector filter function. The image sets were then processed to create maps of average velocity, velocity fluctuation RMS and turbulence intensity.

3.3. Data reduction

The Reynolds number was calculated according to the following relation:

$$R_{Dh} = \frac{\rho U_{max} D_h}{\mu} \tag{1}$$

where ρ is the fluid's density, U_{max} is the maximal fluid velocity in the fin array, D_h is the hydraulic diameter of the fin array flow passage and μ is the fluid's dynamic viscosity. For the works related to pyramidal fins [14–17], the characteristic length was chosen to be the hydraulic diameter, as the fin array geometry promotes structures typical of internal flows. Indeed, due to the small size of the passages, the boundary layer growth and coalescence in this type of fin array is more akin to that of internal flows than to external flows. The variable D_h is given by:

$$D_h = \frac{4 \cdot A_{flow}}{N_{flow}} \tag{2}$$

where A_{flow} and N_{flow} are the flow channel's face area and perimeter, respectively.

The turbulence intensity (I) of the flow was computed as:

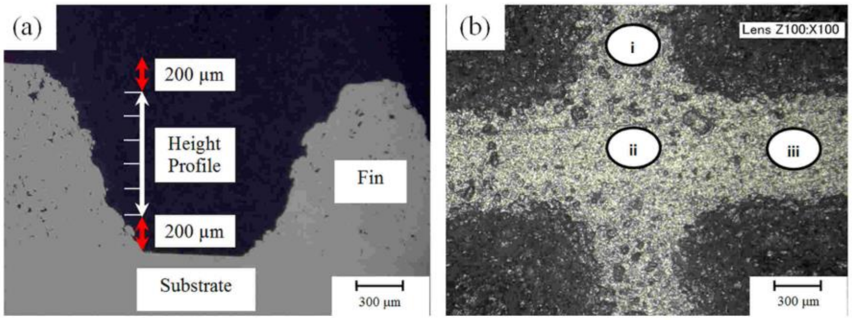

Fig. 5. Data collection zones for the experimental work; (a) along the height of the fin illustrating that the data was collected 200 μm from the top and bottom surface, (b) in the fin array channels.

$$I = \frac{u'}{U} \tag{3}$$

where u' denotes the RMS of the velocity fluctuations in time and U represents the mean velocity.

4. CFD model details

A computational model was developed to complement the experimental studies and to evaluate how the flow structures observed experimentally for geometrically imperfect fins (rough and rounded fins produced by cold spray) differ from pin fin arrays with idealized geometries. The model was also used to evaluate the potential effects of these imperfections on the fin array performance. This model was constructed using commercial CFD software: Gambit was used to create the domain geometry and mesh, while Fluent was used to solve the mass, momentum and energy equations in a coupled semi-implicit scheme (SIMPLE) for steady-state, incompressible fluid flow. The Reynolds Averaged Navier–Stokes (RANS) equations approach was used to model the turbulent behavior of the flow, using the realizable k–ε turbulence equations for three different mass flow rates (0.00136, 0.00272 and 0.00550 kg/s), which correspond to Reynolds numbers of 500, 1000 and 2000. Although the Reynolds numbers involved potentially lie in the sub-critical regime, the use of a turbulence model (instead of a purely laminar model) is warranted due to the complexity of the expected flow structures and the non-negligible presence of turbulence, as demonstrated in the literature [28,29]. Furthermore, as it will be shown in Section 5.3, the turbulence intensity levels obtained with the simulation cannot be neglected, especially near the surface of the heat transfer enhancing features. Fluent's standard wall functions were selected, as the mesh is sufficiently fine ($y^+ = 0.31$) to appropriately resolve the near-wall features of the flow. Radiative heat transfer was neglected due to the fact that it accounted for much less than 0.1% of the total heat transfer during the grid independency test (described in the following paragraph). The influence of gravity was neglected due to the fact that forced convection largely dominates free convection, in this case.

The three dimensional solution domain is separated in a solid zone (pin fins) and a fluid zone (flow), with the fluid zone meshed with unstructured tetrahedral mesh and the solid zone meshed with hexahedral element dominated mesh. The solid zone mesh point density was set at 20 points per edge, while the fluid zone was set to 50 mesh points per edge. A schematic of the computational domain is shown in Fig. 6(a) and the boundary conditions applied to the different surfaces are summarized in Table 1. To model the heat transfer, a constant wall surface temperature of 360 K and a fluid inlet temperature of 300 K were selected to reflect typical temperature differences observed experimentally by the authors [14–17]. For the purpose of simplicity, the fin surface walls were treated as smooth conductive surfaces in the solid zone, while the bounding walls were considered to be smooth, adiabatic surfaces. The model has the same width as the experimental samples, but has a reduced length, to save computation time. This reduction in domain length can be achieved as it was observed experimentally that the large scale recirculation structures do not vary significantly as the number of rows increases. The dimensions used for the pyramids and passage width reflect the average measured dimensions of the specimens used for the μPIV study which are presented in Section 5.1. Fig. 6(b) shows a second computational domain that was used for modeling, with the main difference being that the middle row of the fin array has transverse flow passages at an 85° angle with the axial flow passages (instead of being purely perpendicular), following observations which are detailed in Section 5. A grid independency test was performed and it was determined that 597 275 cells yielded satisfactory results while not being too expensive on computational time. Calculations were conducted until the absolute residuals were evaluated to be less than 10^{-6}, at which point the solution was considered to have reached convergence. Temperature and pressure were also monitored at the outlet to ensure that their value had reached a steady value that did not change with further iterations.

The heat transfer performance of the fin arrays under the different simulation conditions was assessed by setting the bottom surface (base of the fin array and base of the fluid passages) to a fixed temperature of 360 K, and evaluating the total heat output by the system (Q) using the following equation

$$Q = \dot{m} \cdot C_p \cdot (T_{out} - T_{in})_{average} \tag{4}$$

In this equation, $\dot{m}$ represents the mass flow rate, C_p is the thermal capacitance of the fluid while T_{in} and T_{out} are the mass-weighted average temperatures of the fluid at the inlet and outlet, respectively. This criterion accurately reflects the thermal conductance (UA), which is calculated in its most basic form using the following relation.

$$UA = \frac{Q}{\Delta T_{LM}} \tag{5}$$

In the previous equation, ΔT_{LM} represents the log-mean temperature difference between the fluid and the solid surface which can be calculated with:

$$\Delta T_{lm} = \frac{\Delta T_1 - \Delta T_2}{\ln\left(\frac{\Delta T_1}{\Delta T_2}\right)} \tag{6}$$

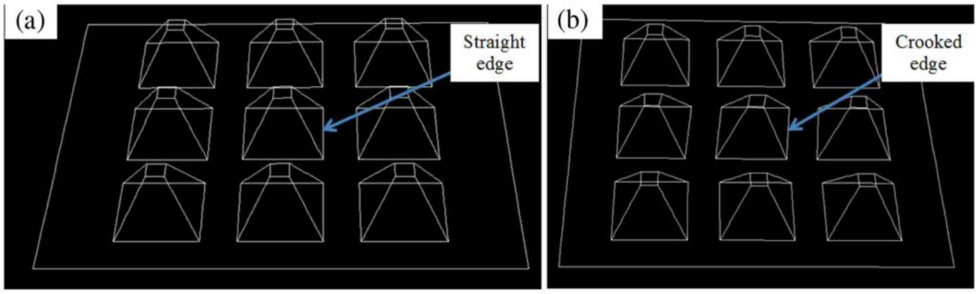

Fig. 6. Computational domain (a) for the regular (straight pyramidal fin) domain (b) for the modified (tilted pyramidal fin) domain.

Table 1
Surface boundary conditions for fluent model.

Surfaces	Boundary condition	Comment/values
Inlet	Mass flow inlet	Flow normal to surface, turbulence intensity specified at 5% with hydraulic diameter of 1.019 mm, flow rate dependant on target Reynolds number, fluid temperature of 300 K
Outlet	Outflow	No outlet specifications
Top, sides	Wall	Adiabatic, no-slip
Flow channel bottom, pyramid bottom	Wall	Constant surface temperature (T = 360 K), no slip
Pyramid surfaces	Wall	Conductive, no-slip

Table 2
Pyramidal fin array measured geometric data.

Fin height (μm)	Base (μm)	Base angle °	Hydraulic diameter (μm)	Flow area (mm^2)
978 ± 65	1477 ± 31	58.4 ± 1.0	1016 ± 86	1.22 ± 0.08

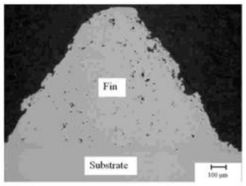

Fig. 8. Typical cross-section of pyramidal fins.

where ΔT_1 and ΔT_2 are the temperature difference between the fin surface and the flow at the inlet and outlet respectively. In this case, by imposing the temperature of the fluid at the inlet and the base temperature at both the inlet and the outlet, one solely needs to evaluate the heat output to accurately predict the gain in thermal conductance.

5. Results

5.1. Test sample geometric data

Fig. 7 shows the nomenclature used with regards to the locations of the μPIV data collection zones on the fin array sample, as well as identifying the terms "fin row" to the axial alignment of fins and "fin column" to the alignment transverse to the flow direction. Table 2 presents the average geometric data of the pin fin arrays used in this work, which served for the elaboration of the CFD model domain.

The pin fins produced using masked CGDS do not have an idealized geometry due to the nature of the deposition process. Slight variations in the particle speed or in the mask geometry and weave can yield macroscopic differences in the actual shape and roughness of the resulting pin fins in the array. Fig. 8 shows a typical cross-section profile of a pyramid produced using this process. One of the important differences between the actual geometry and the modeled geometry, aside from the general shape, is the presence of roughness on the fin surface. This factor can affect the turbulence intensity levels measured, compared to smooth pyramids with idealized geometry.

5.2. μPIV results

The particle image velocimetry experiments yielded information on the large scale flow structures encountered in pyramidal pin fin arrays. The average velocity in the axial flow channels measured for the different Reynolds numbers is 0.37, 0.75 and 1.55 m/s, respectively. Relatively large stable flow zones were identified in the axial flow channels A and B, especially at the data collection zones 7 and 10, as shown in Fig. 9. The data is presented alternatively from zones 7 and 10 to demonstrate the similarity between the flow patterns encountered in these two zones. As expected, the maximal fluid velocity is found near the center of the flow channels and boundary layer effects can easily be observed.

The locations at the corner of four fins (zones 5, 6, 8 and 9 from Fig. 7) exhibit fluid entering and exiting the transverse flow

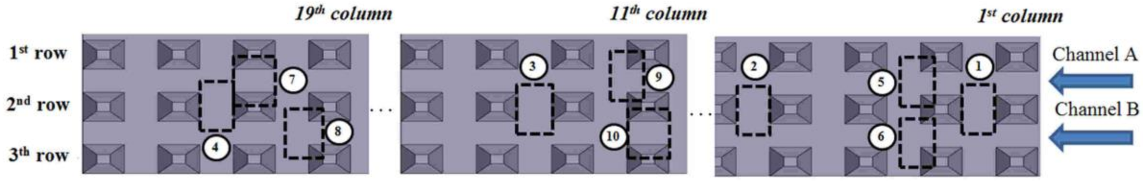

Fig. 7. Nomenclature of the μPIV measurement locations (zones) along the fin array. Flow direction is from right to left.

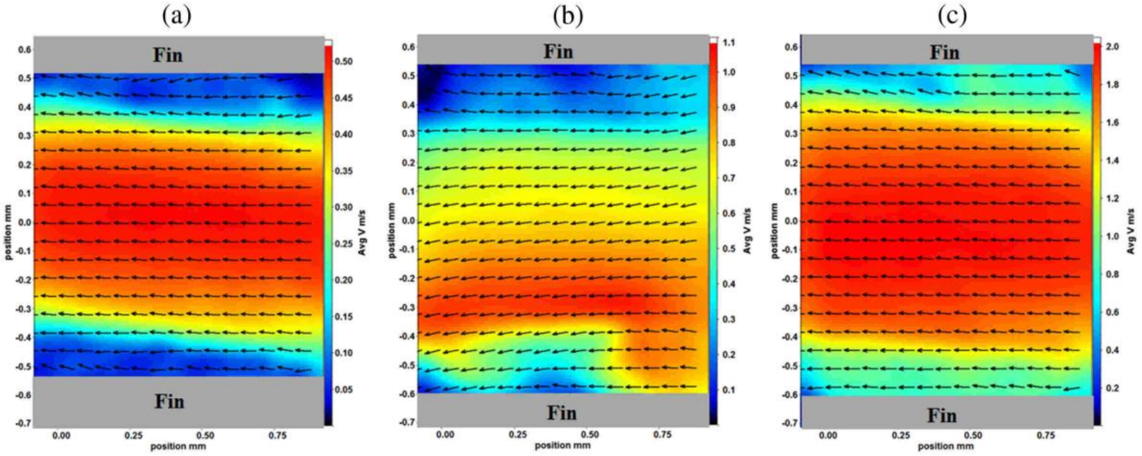

Fig. 9. Flow between two fin rows, observed at the mid-height plane of (a) zone 10 at *Re* 500, (b) zone 7 at *Re* 1000, (c) zone 10 at *Re* 2000, obtained by µPIV.

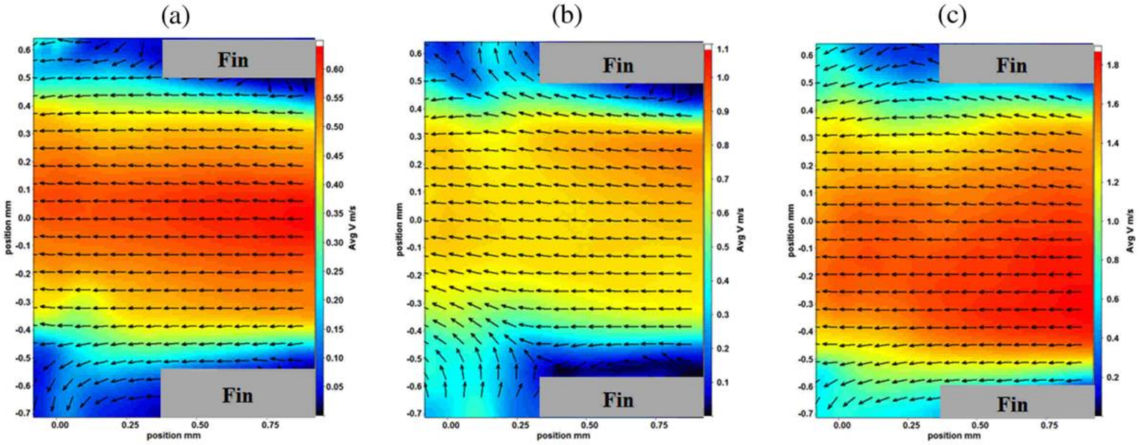

Fig. 10. Intersection between axial and transverse flow channels, showing flow moving between the axial channel and the transverse flow channel, observed at the mid-height plane of (a) zone 5 at *Re* 500, (b) zone 9 at *Re* 1000, (c) zone 8 at *Re* 2000, obtained by µPIV.

channels. This is illustrated in Fig. 10, where the influence of the transverse flow on the fluid motion in the axial channel can be observed. This is most evident at the junction between these flow channels, where the fluid motion either to or from the transverse flow channel widens or constricts the higher velocity portion of the fluid structure and the position of maximum velocity, respectively. This type of effect, combined with the increased instability it causes, can potentially increase the local heat transfer coefficient and the amount of fluid mixing, which could consequently increase the amount of heat transfer that occurs in the axial flow channels. Once again, the data presented in Fig. 10 is alternatively taken from zones 5, 8 and 9 to present the similarities in the flow structures observed between the four zones aforementioned. This also seems to indicate that the global flow structure reaches a fully developed state quite rapidly, after the first or second column.

The average velocity as a function of height in the axial flow channels are plotted for the three Reynolds numbers tested in Fig. 11. In this case, the curves presented are the average of the all the velocity values obtained from zones 5 through 10. The three curves produced exhibit the expected velocity profiles for fins with cross-sections tapered along their height and bounded by a solid wall at the bottom and top. They present a parabolic profile, with the highest average velocity values slightly skewed towards the top of the fins where the free stream zone is largest. These shapes are consistent along the flow channel length, as supported by Fig. 12, which shows the normalized average velocity as a function of height for data collection zones 5 through 10 at a Reynolds number of 2000. The curves for the other Reynolds numbers are not shown for the sake of simplicity, but exhibit a very similar behavior. It is important to note that the low velocity values noted for zones 7 and 8 near the bottom of the channel are attributed to noise caused by the background intensity leftover after the application of the data filter. This residual noise caused dark zones in certain images, which skewed the results to lower the average velocity measurements. The use of this data is warranted, despite the measurement artifacts, to illustrate the similarities between the profiles obtained at the different data collection zones.

The turbulence intensity in the axial flow channels was measured at locations 5 through 10 for the three different Reynolds numbers tested, and are presented in Table 3. The first observation

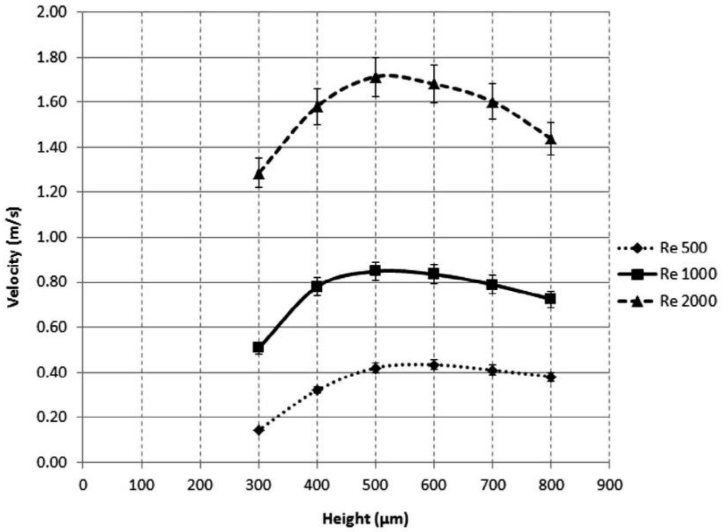

Fig. 11. Average channel velocity of zones 5 through 10, along the height of the fin array, for the three Reynolds number tested, obtained from μPIV analysis.

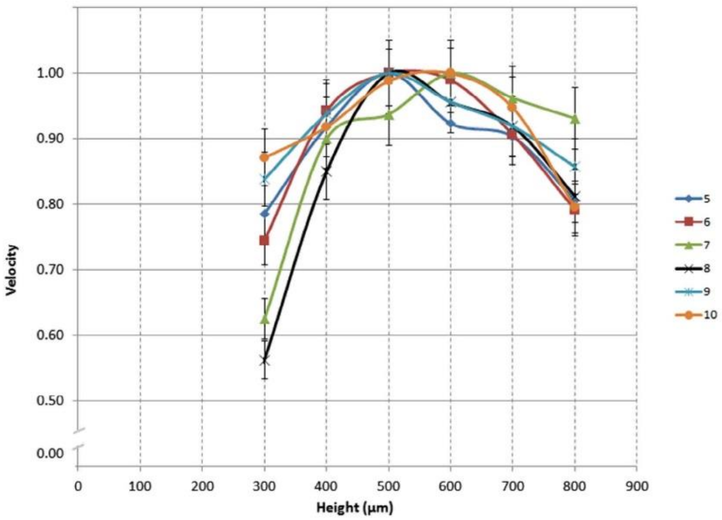

Fig. 12. Normalized average velocity in the flow channels as a function of the height of the fin array for the different collection zones at *Re* 2000, obtained from μPIV analysis.

Table 3
Average turbulence intensity (%) in the axial flow passages, measured by μPIV.

Data collection point	*Re* 500	*Re* 1000	*Re* 2000
5	18.6	22.1	14.9
6	19.5	20.8	12.8
7	24.5	29.7	26.9
8	29.6	31.0	27.3
9	22.3	24.2	21.0
10	17.8	18.8	17.4

that can be made is that the turbulence intensity values between zone 5 and 6 are similar, which is expected as there should be no significant differences in the turbulence intensity between channels A and B. It is possible to note that the average turbulence intensity for zones 8 and 9 (junction zones) are higher than those for their axial zone counterparts (locations 7 and 10), which is attributed to the influence of the flow structures in the fin wake affecting in a measurable manner the fluctuation of the flow at the channel junctions. Furthermore, the average turbulence intensity increases for locations downstream of the first measurements zones (9 compared to 5 and 8 compared to 6), which indicates that the disturbances in fluid motion stack increasingly as the fluid flows downstream, increasing faster than the dissipation rate. These increases in the turbulence intensity as the fluid moves downstream are expected to contribute to increasing the local convective coefficient of the fin array, thus promoting heat transfer. Another interesting conclusion is that the data presented in Table 3 may explain why there is a change in the Nusselt number slope for pyramidal fin arrays such as the one under scrutiny in this work. One can refer back to Fig. 1 which illustrates a change in the slope

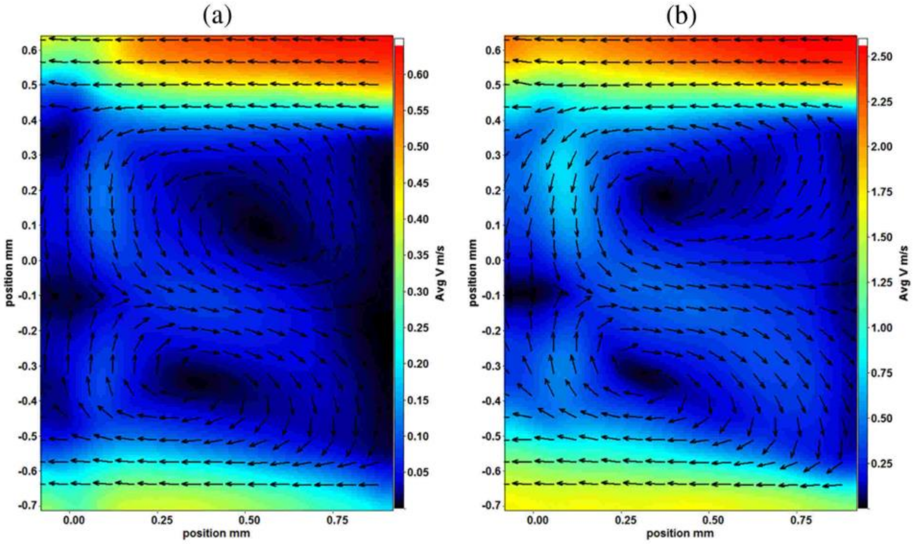

Fig. 13. Double recirculation flow structures observed experimentally between fin columns at the mid-height plane at (a) *Re* 500 and (b) *Re* 2000 (taken at zone 2).

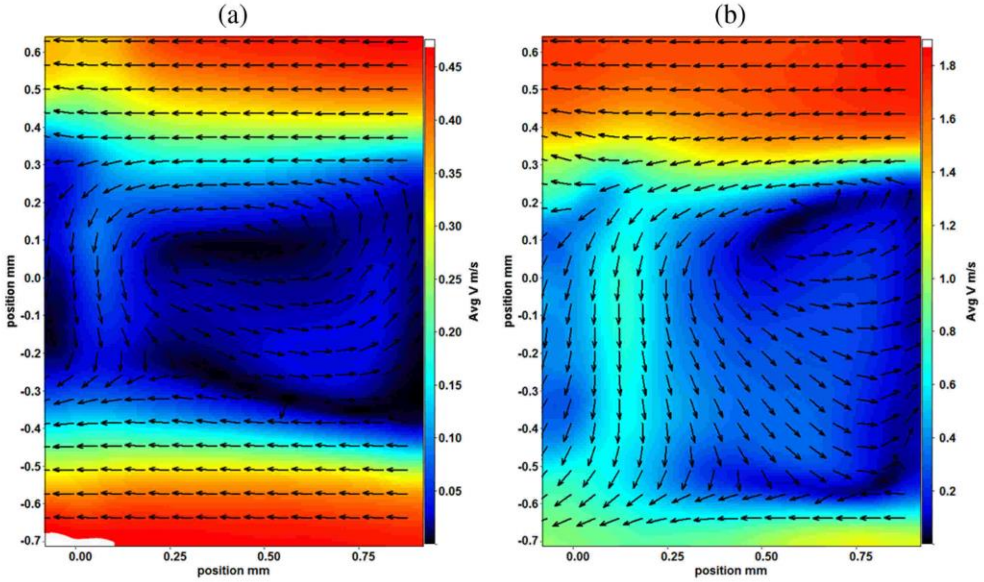

Fig. 14. Bypass flow structures observed experimentally between fin columns at the mid-height plane at (a) *Re* 500 and (b) *Re* 2000 (taken at zone 3).

Table 4
Fin flow passage tilt data measured by optical microscopy.

Tilt direction	Number of passages affected	Average tilt angle (°)
Orientation A	6	5.3 ± 2.7
Orientation B	10	5.6 ± 2.1
No tilt	7	N/A

near *Re* 1000, that can be observed in typical Nusselt number vs Reynolds number curves for different pyramidal pin fin arrays. The initial increase in turbulence intensity measurements obtained by µPIV from *Re* 500 to *Re* 1000 and its subsequent decrease between *Re* 1000 and *Re* 2000 (Table 3) could explain why the slope of the Nusselt number (or convective coefficient) is steeper between the first two values than between the second and third values of Reynolds number. Of course, these observations are insufficient to establish a definitive relationship between the cause and the effect, but may serve as a starting point for future research into this type of slope transition and the factors affecting this transition.

The region between two columns of fins is of particular interest (zones 1 through 4), due to the widespread belief that it is the main heat transfer enhancing feature of pin fins when compared to continuous fins. It is also reported in the literature [24,25,30–33]

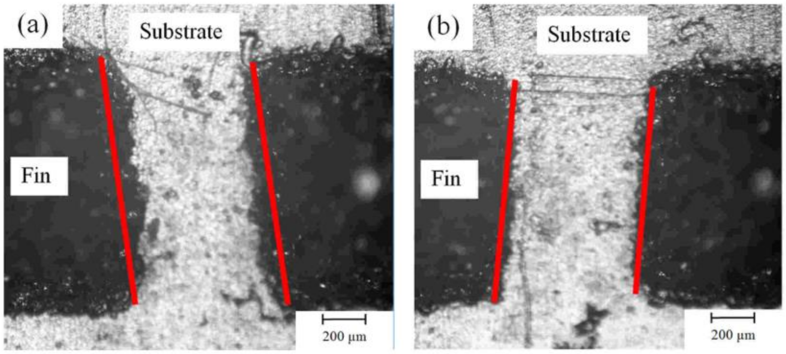

Fig. 15. Top view of tilted flow passage geometry for (a) orientation A and (b) orientation B, with guidelines indicating the assumed position of the wire mesh mask's tilted wire (flow would be from right to left along the sample length).

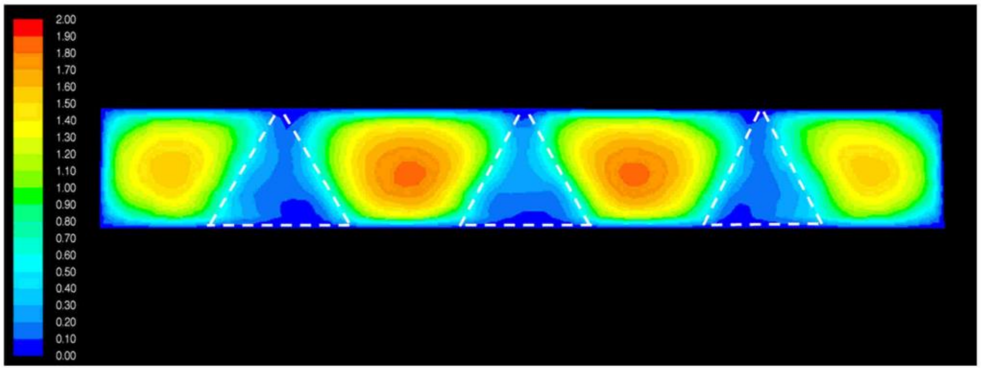

Fig. 16. Velocity distribution taken at the exit plane, with the projection of the position of the last column of pyramidal fins shown in white dashed lines for *Re* 2000, obtained from the simulation.

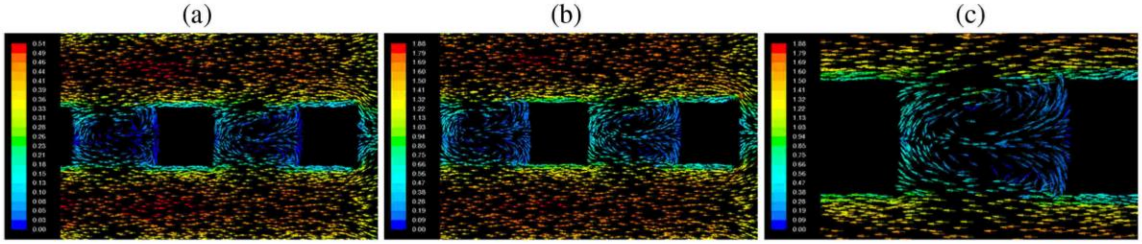

Fig. 17. Double recirculation flow structures encountered in the straight computational model at (a) *Re* 500, (b) *Re* 2000 and (c) detail view at *Re* 2000.

that the flow structures at low Reynolds number between columns of conventional pin fins (pin fins with the same cross-section along their height) is that of double recirculations with laminar flow bounding those recirculations in the axial flow channels. This type of flow structure is also observed in pyramidal fin arrays, as can be seen in Fig. 13(a) and (b), where a double recirculation structure in the fin's wake, bounded by stable flow in the axial flow channel, can be observed. These findings are consistent with the theory outlined by Žukauskas for banks of tubes, which was discussed in Section 1. A notable feature of the double recirculation structure observed for the pyramidal pin fins is that a portion of the fluid is fed out of plane (either towards the base or the top of the fin), which can be deduced by noticing the local acceleration or deceleration (in-plane) of the fluid in a given area (acceleration near the point where the recirculating flows combine, and deceleration as it approaches the fin's downstream surface). Since the flow is incompressible, for the continuity equation to be satisfied, it must then follow that the in-plane acceleration must be compensated by an out-of-plane fluid motion. This type of motion is also observed in the simulation, and is further discussed in Section 5.3. Although the double recirculation flow structure can be encountered in any column of the fin array, it is only observed infrequently. The typical

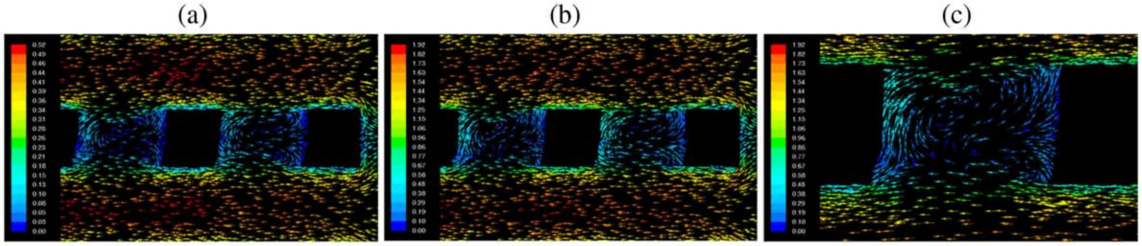

Fig. 18. Single bypass flow structures encountered in the tilted geometry computational model at (a) *Re* 500, (b) *Re* 2000 and (c) detail view at *Re* 2000.

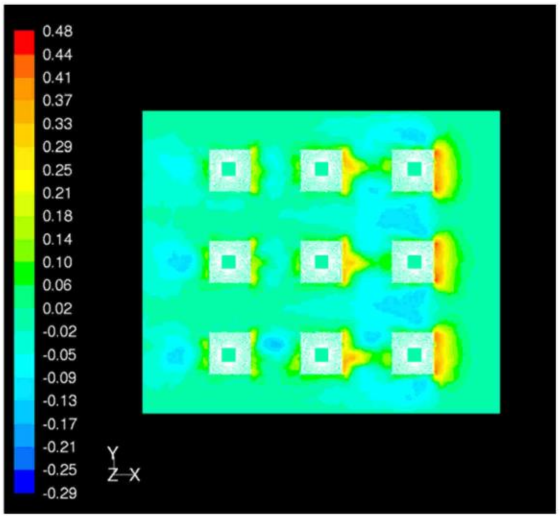

Fig. 19. Out of plane fluid motion (*Z* axis component of fluid velocity) for the straight pyramidal fin array model at mid-height and *Re* 2000, with fluid flowing from right to left.

flow structure observed is presented in Fig. 14, where a significant amount of fluid is fed from one flow channel to the other between fin columns, with the presence of a single recirculation. A portion of fluid moves out of plane, which can once again be inferred from the deceleration of the fluid near the fin's downstream wall. This type of flow structure should not arise from fin arrays with idealized geometry, regardless of whether the fin is tapered along the height or not. Fins with idealized geometries are, by definition, produced to be completely symmetrical from one row to another. It would then be illogical for fluid to bypass from one flow channel to the other, as both would have the same pressure losses along their length. The fins which yielded this type of flow structure, however, were tilted either to one side or to the other. Table 4 presents the observations made regarding the tilt direction, with the number of passages affected and the average tilt angle reported (the tilt directions are shown in Fig. 15). It is interesting to note that consecutive fins are always tilted in the same direction, indicating that the imperfections in the tilt angle of the pin fin array is not due to the spray process itself but rather to the weave of the wire mesh mask used to produce this type of fin array. The small bends that must be made to weave a wire around another may explain the observed tilts. With a strict control of the mask production technique, it is then believed that these imperfections could be controlled. The bypass observed must then be due to irregularities in the geometry of the fin array, such as those presented in Fig. 15. It is unclear whether this phenomenon assists or hinders the heat transfer performance of pyramidal pin fins solely using the data provided by μPIV. Consequently, this factor has been investigated using numerical simulation, as presented in the following section.

5.3. CFD model results

The CFD model provides valuable heat transfer performance data prediction on the flow structures observed with the μPIV apparatus for both straight and tilted fins, regardless of their lack of roughness or shape imperfections. The fluid velocity profile along the height of the axial flow channels observed experimentally was also observed in the simulation, where the location of maximum velocity is found at midheight with the velocity profile skewed to higher velocities near the top of the channel, as shown in Fig. 16.

The flow structures between columns of fins previously described in Section 5.2 are also encountered with the CFD model. The flow in the axial flow channels is laminar, with small amounts of fluid entering and exiting the transverse flow channels. When the fins are arranged with perfectly perpendicular flow channels, the double recirculation pattern is observed (Fig. 17(a) and (b)) between two columns of fins. Conversely, when there is a small angle between the flow channel's perpendiculars (5° offset), bypass flow can be observed (Fig. 18(a) and (b), with a detail view shown in (c)). These observations were made in the three cases tested, at Reynolds numbers of 500, 1000 and 2000. Additionally, the significant portion of out of plane motion discussed in Section 5.2 can be observed in the model (an example of this can be found in Fig. 19). On the leading edge of the fins, the fluid follows the pyramid's taper towards the top of the flow channel, with a smaller amount being fed towards the top from the trailing edge. To satisfy the continuity equation, some fluid motion towards the bottom of the flow channel must occur, which is concentrated on the sides of the pyramid in contact with the axial flow channel or in the middle of the recirculation region between fin columns.

The model predicts that there will be no significant enhancement or detriment to the heat transfer performance in having slightly tilted flow passages such as those modeled (with an angle

Table 5
Heat transfer simulation results.

Reynolds number	Fin orientation	$(Q_{out} - Q_{in})$ W	η_Q (%)	$(P_{in} - P_{out})$ Pa	η_P (%)
500	Straight	56.3	−1.07	193	0.52
	Tilted	55.7		194	
2000	Straight	78.2	5.88	1689	6.51
	Tilted	82.8		1799	

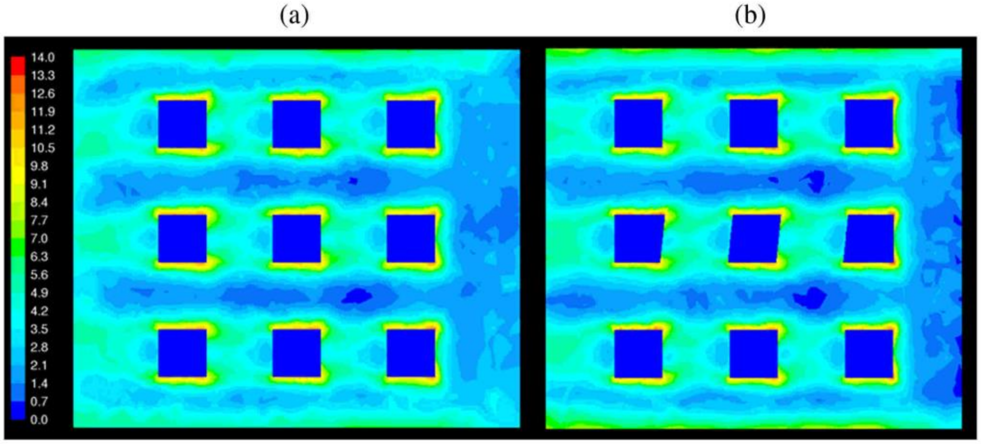

Fig. 20. Turbulence intensity contour plot at Reynolds number of 500, taken at mid-height for (a) straight geometry, (b) tilted geometry, obtained from the simulation.

between flow channels of 85° instead of 90°). This performance can be evaluated by calculating the relative increase in heat transfer η_Q and the relative increase in pressure loss η_P:

$$\eta_Q = \frac{\Delta Q_{tilted} - \Delta Q_{straight}}{\Delta Q_{straight}} \tag{7}$$

and

$$\eta_P = \frac{\Delta P_{tilted} - \Delta P_{straight}}{\Delta P_{straight}} \tag{8}$$

The results of these calculations are presented in Table 5. Although the increase in heat transfer may reach up to 6% between the tilted fins and straight fins model, it is offset by a similar value of pressure loss increase, effectively yielding no overall performance gain, although the flow structures can differ substantially between the two model geometries.

For both model geometries, the turbulence intensity calculated with the CFD model are lower than those measured with the PIV apparatus, as illustrated in Fig. 20. This discrepancy is most likely attributable to the differences between the smooth, idealized geometry of the model and the rougher geometry of the physical sample. As expected, due to the low Reynolds numbers involved, the axial flow channels have a low level of turbulence. For both configurations, where fluid enters and leaves the transverse flow channel, there is a notable increase in the local turbulence intensity, when compared to that of the free stream (approximately 6% vs 1%), indicating that the fluid motion in the transverse flow channel has a non-negligible effect on the flow structures in the axial flow channels. The magnitude of these variations is similar for both the tilted and straight geometries, indicating that the turbulence levels are not significantly affected by the flow structures themselves, but rather by the amount of fluid flowing in and out of the region between fin columns. In the simulation, the turbulence intensity continually increases with the Reynolds number, which is different than what was observed with the μPIV. This discrepancy illustrates that the model cannot yet distinguish all the flow features obtained experimentally, which is most likely attributable the differences between the modeled fin's geometry (which is perfectly smooth, with sharp edges and constant slope) and the actual geometry of the pin fins produced using masked CGDS.

The model predicts a roughly even distribution between the heat transferred by the surfaces in contact with the axial flow channel and by those in contact with the transverse flow channel (45% vs 55% of the total heat transfer, respectively), which is believed to be due to the increased turbulence intensity and the presence of large scale recirculations between columns of fins. This indicates that the flow structures in the wake of the pin fins play an important role in the total performance of this type of heat exchanger, as it is a turbulence generator that not only increase the heat transfer in the wake of the fin, but also contributes to increase the turbulence intensity (and as a byproduct the local convective heat transfer coefficient) in the axial flow channel. Furthermore, as discussed earlier, the flow characteristics in the transverse channel significantly affect those in the axial flow channels, both in the experimental (Fig. 10) and the numerical (Figs. 18 and 19) investigations. These conclusions demonstrate the importance of optimizing the flow structures in the wake of the fins to maximize heat transfer, minimize pressure losses and further increase the performance of pyramidal pin fin arrays and help to understand why this type of fin outperforms similar sized plate fin arrays at the same fin density [17].

6. Summary and conclusion

The conclusions reached in this work could be summarized as follows:

1. The velocity profiles obtained by μPIV match the expected velocity profiles for the flow between pin fins with tapered cross-sections along their height. The turbulence intensity in the axial channels was found to increase significantly as the fluid moves downstream due to the significant turbulence production of the flow structures in the fin's wake and of the mixing that occurs at the junctions of the axial and transverse flow channels.
2. Trends were found where the turbulence intensity increased up to *Re* 1000 and then subsequently decreased, which could explain the change in slope of the Nusselt number and convective coefficients of similar pin fin arrays, which was discussed in detail in prior work [16]. This trend cannot be definitely confirmed with the small amount of data points obtained in this regard in the current work, but demonstrates the possible advantages of studying the flow structures encountered in pin fin arrays in parallel to the heat transfer and hydrodynamic performance tests.

3. The types of flow structure observed in the wake region of the pin fins were: classic double recirculation structures, which were reported in various other works dealing with pin fins and banks of tubes, and flow bypass structures, where a significant amount of fluid is fed from one flow channel to another. In both these types of fluid motion, there is a portion of the flow which is redirected out of plane, either towards the top or the base of the fins, revealing a complex 3-dimensional flow structure.
4. The bypass flow structure previously described is believed to be caused by imperfections in the alignment of the transverse and axial flow channels, with the direction of the bypass being dictated by the direction of the misalignment. This imperfection in alignment is attributed to the weave of the wire mesh mask used to produce the pyramidal pin fins studied in this work. Furthermore, the recirculation flow structures can be encountered after the first or second row, and are maintained whenever there is no misalignment between the flow channels, which also indicates that the flow structures become periodic quite rapidly, even after a single column of fins, although the turbulence intensities measured increase as the fluid flows downstream.
5. A CFD model was developed to evaluate the heat transfer performance of both the well aligned and misaligned flow channel configurations (straight and tilted fins). The important flow structures observed in using μPIV were also encountered in the CFD model. The model predicts that the heat transfer performance for both configurations is similar. The model, however, lacks the capacity to predict the turbulence intensities with accuracy due to its idealized geometry and the lack of surface roughness of the modeled pyramids.
6. The performance gain that is measured when using pin fin arrays instead of using plate fin arrays can be attributed to the large amount of heat transfer that occurs in the wake of the fins, which accounts for approximately 50% of the total heat transferred. Furthermore, the flow structures obtained in the transverse flow channel (wake of the fins) affect the flow stability, structure and turbulence levels in the axial flow channels. These factors contribute to the increase of the convective heat transfer coefficient, which consequently increases the thermal conductance.

Acknowledgements

Acknowledgements are due to the Mitacs Accelerate Program for its financial support of this project. The authors would also like to thank Rym Mehri for providing training on the use of the μPIV apparatus and Aslan Farjam for his insights regarding the CFD model.

References

[1] D. Reay, C. Ramshaw, A. Harvey, Process Intensification, Butterworth-Heinemann, Oxford, 2013.
[2] R.L. Webb, Enhancement of single-phase heat transfer, in: S. Kakac, K. Ramesh, W. Aung (Eds.), Handbook of Single-Phase Convective Heat Exchanger Design, Wiley, New York, 1987.
[3] W.M. Kays, A.L. London, Compact Heat Exchangers, McGraw-Hill, New York, 1984.
[4] F.P. Incropera, D.P. DeWitt, T.L. Bergman, A.S. Lavine, Fundamentals of Heat and Mass Transfer, Wiley, New York, 2006.
[5] A. Žukauskas, Heat transfer from tubes in crossflow, Adv. Heat Transfer 8 (1972) 93–160.
[6] N. Sahiti, F. Durst, A. Dewan, Heat transfer enhancement by pin elements, Int. J. Heat Mass Transfer 48 (2005) 4738–4747.
[7] N. Sahiti, F. Durst, A. Dewan, Strategy for selection of elements for heat transfer enhancement, Int. J. Heat Mass Transfer 49 (2006) 3392–3400.
[8] N. Sahiti, A. Lemouedda, D. Stojkovic, F. Durst, E. Franz, Performance comparison of pin fin in-duct flow arrays with various pin cross-sections, Appl. Therm. Eng. 26 (2006) 1176–1192.
[9] E.M. Sparrow, J.W. Ramsey, Heat transfer and pressure drop for a staggered wall-attached array of cylinders with tip clearance, Int. J. Heat Mass Transfer 21 (1978) 1369–1377.
[10] E.M. Sparrow, J.W. Ramsey, C.A.C. Altemani, Experiments on in-line pin fin arrays and performance comparison with staggered arrays, ASME J. Heat Transfer 102 (1980) 44–50.
[11] D.E. Metzger, C.S. Fan, S.W. Haley, Effects of pin shape and array orientation on heat transfer and pressure loss in pin fin arrays, ASME J. Eng. Gas Turbines Power 106 (1984) 252–257.
[12] H.R. Salimi Jazi, J. Mostaghimi, S. Chandra, L. Pershin, T. Coyle, Spray-formed, metal-foam heat exchangers for high temperature applications, J. Therm. Sci. Eng. Appl. 1 (3) (2009) 1–7.
[13] F. Azarmi, J. Saaedi, T.W. Coyle, J. Mostaghimi, Microstructure characterization of alloy 625 deposited on nickel foam using air plasma spraying, Adv. Eng. Mater. 10 (5) (2008) 459–465.
[14] Y. Cormier, P. Dupuis, B. Jodoin, A. Corbeil, Net shape fins for compact heat exchanger produced by cold spray, J. Therm. Spray Technol. 22 (7) (2013) 1210–1221.
[15] P. Dupuis, Y. Cormier, B. Jodoin, A. Corbeil, Performance evaluation of near-net pyramidal shaped fin arrays manufactured by cold spray, Int. J. Heat Mass Transfer 69 (2014) 34–43.
[16] Y. Cormier, P. Dupuis, A. Farjam, B. Jodoin, A. Corbeil, Additive manufacturing of pyramidal pin fins: height and fin density effects under forced convection, Int. J. Heat Mass Transfer 75 (2014) 235–244.
[17] P. Dupuis, Y. Cormier, A. Corbeil, B. Jodoin, Performance of cold sprayed near-net pyramidal shaped arrays under forced convection, in: Proceedings of CONV-14: International Symposium on Convective Heat and Mass Transfer, Turkey, June 8–13, 2014.
[18] A.P. Alkhimov, A.N. Papyrin, V.F. Dosarev, N.I. Nesterovich, M.M. Shuspanov, US Patent No. 5302414, 1994.
[19] E. Irissou, J.-G. Legoux, A.N. Ryabinin, B. Jodoi, C. Moreau, Review on cold spray process and technology: Part I-intellectual property, J. Therm. Spray Technol. 17 (4) (2008) 495–516.
[20] J.R. Davis, Handbook of Thermal Spray Technology, ASM International, Materials Park, 2004.
[21] H. Herman, S. Sampath, R. McCune, Thermal spray: current status and future trends, Mater. Res. Soc. Bull. 25 (7) (2000) 17–25.
[22] J. Wen, Y. Li, A. Zhou, K. Zhang, An experimental and numerical investigation of flow patterns in the entrance of plate-fin heat exchanger, Int. J. Heat Mass Transfer 49 (2006) 1667–1678.
[23] B. Jones, P.-S. Lee, S.V. Garimella, Infrared micro-particle image velocimetry measurements and predictions of flow distribution in a microchannel heat sink, Int. J. Heat Mass Transfer 51 (2008) 1877–1887.
[24] O. Uzol, C. Camci, Elliptical pin fins as an alternative to circular pin fins for gas turbine blade cooling applications; Part 1: endwall heat transfer and total pressure load characteristics, in: Proceedings of 46th ASME International Gas Turbine, Aeroengine Congress and Exposition and Users Symposium, New Orleans, Louisiana, USA, 2001.
[25] O. Uzol, C. Camci, Elliptical pin fins as an alternative to circular pin fins for gas turbine blade cooling applications; Part 2: wake flow field measurements and visualization using particle image velocimetry, in: Proceedings of 46th ASME International Gas Turbine, Aeroengine Congress and Exposition and Users Symposium, New Orleans, Louisiana, USA, 2001.
[26] C.D. Meinhart, S.T. Wereley, M.H.B. Gray, Volume illumination for two-dimensional particle image velocimetry, Measure. Sci. Technol. 11 (2000) 809–814.
[27] J.G. Santiago, S.T. Wereley, C.D. Meinhart, D.J. Beebe, R.J. Adrian, A particle image velocimetry for microfluidics, Exp. Fluids 25 (1998) 316–319.
[28] Y. Rao, Y. Xu, C. Wan, An experimental and numerical study of flow and heat transfer in channels with pin fin-dimple and pin fin arrays, Exp. Therm. Heat Fluid Sci. 38 (2010) 237–247.
[29] P.-X. Jiang, R.-N. Xu, Heat transfer and pressure drop characteristics of mini-fin structures, Int. J. Heat Fluid Flow 28 (2007) 1167–1177.
[30] K. Minakami, S. Mochizuki, A. Murata, Y. Yagi, H. Iwasaki, Visualization of flow mixing mechanisms in pin-fin arrays, in: Proceedings of 6th International Symposium on Flow Visualization, Yokohama, Japan, 1992.
[31] K.Y. Kim, M.A. Moon, Optimization of a stepped circular pin-fin array to enhance heat transfer performance, Heat Mass Transfer 46 (2009) 63–74.
[32] J.-H. Ko, M.E. Ewing, Y.G. Guezennec, Development of a low Reynolds number enhanced heat transfer surface using flow visualization techniques, Int. J. Heat Fluid Flow 23 (2009) 444–454.
[33] A. Armellini, L. Casarsa, P. Giannattasio, Low Reynolds number flow in rectangular cooling channels provided with low aspect ratio fins, Int. J. Heat Fluid Flow 31 (2010) 689–701.

CHAPTER 8 PERFORMANCE AND FLOW STRUCTURE CHARACTERIZATION OF DIFFERENT PIN FIN GEOMETRIES PRODUCED BY COLD SPRAY

The article presented in this chapter details the thermal and hydrodynamic performance of round base, diamond base and square base tapered pin fins. The manufacturability of fin arrays with the use of several commercially available masks with two different fin densities was established. The findings of the performance tests are supported by the µPIV analysis. This analysis also yielded valuable information regarding the turbulence kinetic energy and the turbulence intensity, and hypotheses regarding the role of these turbulence quantities on the performance of the fin array are proposed, in terms of the influence of the Reynolds number, the configuration of the array and the influence of the shape of the cross-section of the fin.

International Journal of Heat and Mass Transfer 98 (2016) 650–661

Contents lists available at ScienceDirect

International Journal of Heat and Mass Transfer

journal homepage: www.elsevier.com/locate/ijhmt

Heat transfer and flow structure characterization for pin fins produced by cold spray additive manufacturing

Philippe Dupuis *, Yannick Cormier, Marianne Fenech, Bertrand Jodoin

University of Ottawa, Mechanical Engineering, Canada

ARTICLE INFO

Article history:
Received 10 December 2015
Received in revised form 14 March 2016
Accepted 18 March 2016
Available online 1 April 2016

ABSTRACT

The focus of this work is the characterization of the thermal and hydraulic performance of pin fin arrays produced using the cold spray additive manufacturing process. The heat transfer and the pressure losses of 1 mm high round base, square base and diamond base tapered pin fin arrays were assessed in both the inline and staggered configurations for fin densities of 8 fpi and 12 fpi. These performances were correlated to the turbulence intensity and the turbulent kinetic energy values at various locations in the flow, measured by micro-particle image velocimetry. It was inferred that the form drag is the main contributor to the pressure loss and was found to correlate with the flow turbulent kinetic energy in the fin wake. In contrast, the convective heat transfer coefficient correlated better with the turbulence intensity, leading to the conclusion that heat transfer is not dictated solely by the turbulent kinetic energy, but by the relative strength of the velocity fluctuations with respect to the average flow velocity at the same location. Furthermore, the flow structures for the different fin array samples were visualized and are discussed. Finally, it was found that although the samples had very varied thermal and hydrodynamic performances as a function of Reynolds number, the different samples at a given fin density had similar thermal conductances at a given pumping power.

1. Introduction

The prevalent use of electronics in today's society has translated to great interest in the broad subject of thermal management for this type of component. The problems associated with the heat production of electronics has become even more complex in the last few decades, as miniaturization of the power consuming components has left designers with an increased thermal load to manage with very limited heat transfer area [1]. If left unchecked, this increased power load results in heightened operating temperatures, which in turn yields higher rates of component failure and reduced life of the electronic package. These problems have pushed the general market towards the development of more efficient heat exchangers.

Several types of heat transfer surfaces have been proposed to transfer the maximum amount of heat possible at a given head loss in a restricted amount of space using forced convection, such as micro-channels, metal foam heat exchanger media and pin fin arrays, to name a few. Fin arrays have been extensively used due to the relative simplicity of manufacturing, combined with their versatility. In high heat removal applications, pin fins have replaced continuous fin geometries such as plain rectangular or wavy fins due to the higher heat transfer rates attainable [2,3]. It has been demonstrated that although pumping fluid through pin fin arrays instead of plate fin arrays typically involves a higher hydrodynamic cost, pin fins offer a higher heat transfer rate for a given heat exchanger volume [4–7]. Sahiti et al. [5–7] have demonstrated that pin fins offer the best performance for a given pumping power and heat exchanger volume, when properly designed. This increase in heat transfer performance can be attributed to the fact that unlike their continuous counterparts, pin fins not only increase the total heat transfer area, but also the average convective coefficient of the fin array [8–10].

Various pin fin geometries and fin array parameters have been investigated to determine the optimal configuration for pin fin heat exchangers and build correlations helping in the selection and design of these components. Circular pin fins in a staggered configuration were the subject of some of the earliest investigations by Brigham and Van Fossen [11,12], who determined that longer pin fins ($H/d > 4$, where H is the fin height and d is the pin fin diameter) tended to transfer more heat than shorter fins. Further studies conducted by Sparrow et al. [8,9] and Metzger et al. [10] on circular pin fins determined that the pin fin's surface convective heat transfer coefficients measured were 100% larger than those measured for the bounding walls. The performance of square and diamond base pin fins was investigated by several authors, such as You

---

* Corresponding author.

http://dx.doi.org/10.1016/j.ijheatmasstransfer.2016.03.069

Nomenclature

ΔP_{fin}	fin differential pressure [Pa]
ΔT_1	inlet temperature difference [K]
ΔT_2	outlet temperature difference [K]
ΔT_{lm}	log mean temperature difference [K]
η	fan efficiency
η_f	individual fin efficiency
η_o	overall fin efficiency
λ	wavelength [m]
μ	dynamic viscosity [Pa·s]
ρ	fluid density [kg/m^3]
A_f	fin heat transfer area [m^2]
A_{flow}	net flow area [m^2]
A_{tot}	total heat transfer area [m^2]
B	fin Base Length [m]
C_p	fluid specific heat capacity [kJ/(kg·K)]
D_h	hydraulic diameter [m]
e_v	pumping power per unit volume [kW/m^3]
h	convective heat transfer coefficient [W/(m^2·K)]
H	fin height [m]
I	turbulence intensity
k	turbulence kinetic energy [m^2/s^2]
$\dot{m}$	mass flow rate [kg/s]
P_{flow}	flow perimeter [m]
q	heat input rate [W]
Re_{Dh}	Reynolds number based on hydraulic diameter
R_{eq}	equivalent thermal resistance [K/W]
S	average Flow Channel Width [m]
T_{in}	inlet fluid temperature [K]
T_{out}	outlet fluid temperature [K]
u'	root mean square (RMS)of the velocity fluctuations [m/s]
$\overline{u'_1}$	axial velocity fluctuations [m/s]
u'_2	transverse velocity fluctuations [m/s]
U	mean velocity [m/s]
U_{max}	maximum fluid velocity [m/s]
UA	thermal conductance [W/K]
UA_v	thermal conductance per unit volume [kW/(m^3·K)]
V	volume [m^3]
$\dot{V}_f$	volumetric flow rate [m^3/s]

and Chang [13], who produced numerical simulation based correlations, Jeng and Tzeng [14] who have experimentally confirmed certain correlations found in the literature and Şara [15], who has produced correlations for several fin array geometry parameters such as shroud clearance and fin spacing. It was found that, in general, circular base pin fins have superior heat transfer efficiency than their square base counterparts [15]. It is worth noting, however, that some configurations of square base pin fins can have a better performance than cylindrical pin fins under the same flow conditions and geometric constraints [15].

Flow structure visualization using Particle Image Velocimetry (PIV) has been performed by several authors with the goal of characterizing heat transfer [16–19]. In particular, Uzol et al. studied both the performance and the flow structures arising from circular and elliptical pin fin arrays and found that the elliptical shaped fins transferred less heat at a much lower aerodynamic cost, which yields a better overall efficiency than their circular cross-section pin fins [18]. This was attributed to the early flow separation from the circular pin fin's surface, which creates a large low velocity wake behind the fin, which could be identified and measured using PIV [19]. Furthermore, the higher levels of turbulent kinetic energy measured in the circular fin's wake helped explain the increased thermal performance of this type of geometry when compared to ellipses [19].

These studies focused on pin fin arrays with constant cross-section along the fin height. New types of tapered pin fins have recently been developed using the masked Cold Gas Dynamic Spraying (CGDS or simply cold spray) technique as an additive manufacturing process [20]. The cold spray process was developed in the late 1980s at the Institute of Theoretical and Applied Mechanics of the Siberian Branch of the Russian Academy of Sciences [21,22]. This process is based on the addition of material to a substrate by the deposition of solid powder particles accelerated by a high pressure carrier gas flowing at supersonic speeds. Upon impact, the particles plastically deform as a result of adiabatic shear instabilities and adhere to the substrate and to the particles that were already deposited, creating dense coatings on the substrate's surface [22–24]. Using a mask to selectively shield the substrate from deposition, as depicted in Fig. 1, it is possible to create pin fin arrays of various shapes and dimensions. The operating principles of the spray process encourage preferential build-up of material in the center of the mask openings, allowing the construction of features with tapered cross-sections along their height, such as pyramids or cones, when proper spray parameters are used [20]. The advantages of this new production method are its high productivity rates, combined with the low production costs and the ease of large scale implementation of this technology. This new fin array production technique yields near-net shape, short (height over base diameter ratio less than 4) pin fin arrays that are lighter than constant cross-section fins due to the reduced amount of materials required.

Characterization of the thermal and hydrodynamic performance of this type of tapered pin fin array was performed and reported for different inline pyramidal pin fin heights, fin densities

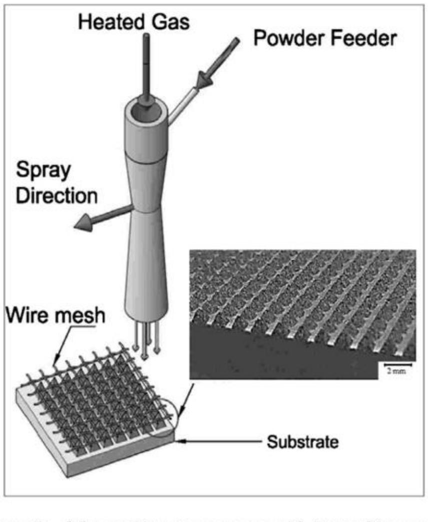

Fig. 1. Schematic of the masking spray process with its resulting pyramidal fin arrays.

and base angles [20,25–27]. The increase in thermal performance of inline pyramidal pin fins, when compared to constant cross-section continuous rectangular fins, was hypothesized to be attributable to the recirculation regions behind the pin fins increasing the average convective coefficient of the array. A micro-PIV (μPIV) investigation of the flow structures that occur in a fluid flowing in an array of inline pyramidal fins with a density of 12 fpi concluded that in the range of Reynolds number of interest ($500 \leqslant Re_{Dh} \leqslant 3000$), the flow structures did not vary significantly from those typical of fluid flow around constant cross-section fins [28]. The classic double recirculation pattern was observed in the wake of the fin, with steady flow channels found between rows of fins. The turbulence intensity levels were measured at diverse locations in the axial flow channels of this fin array, where significant turbulence intensities were found (from 15% to 30%) [28]. Furthermore, it was noted that the steady state average turbulence intensity in the axial flow channels increased as the fluid flows downstream, indicating that the flow structure generates more turbulence that it can dissipate as the fluid moves from the entrance to the exit. A variable flux of fluid was found to move to and from the recirculatory structure in the fin's wake, which seems to be the mechanism by which the turbulence in the axial flow channel is generated [28]. Many questions remain, however, as to the extent of the impact of these flow structures and of the turbulence quantitie on the thermal and hydrodynamic performance of the fin array.

The focus of this work is to characterize the heat transfer properties of several geometries of tapered fin arrays produced using masked CGDS. Fin arrays with square, diamond and round profiles were produced in the inline or staggered arrangements at 8 and 12 fins per inch (fpi) fin densities, depending on the commercial availability of the masks used for manufacturing. The heat transfer and hydrodynamic performance of the different fin array samples is characterized and discussed. A μPIV analysis of the flow structure around the fins with quantitative measurements of the flow turbulence properties in both the fin wake and in the flow channels is performed to help further understand the trends found in the results obtained from the thermal and hydrodynamic performance study.

2. Characteristics of the heat exchanger samples

2.1. Masked CGDS fin production technique

The technique used to create pin fin arrays using cold spray is shown in Fig. 1. This additive manufacturing method consists of shielding parts of the substrate from deposition by selectively masking the substrate, which build features of various shapes and dimensions which closely mimic the inverse of the mask opening geometry. The operating principles of the spray process also encourage preferential build-up of material in the center of the mask openings, allowing the construction of features with tapered cross-sections along their height, such as pyramids or cones [20]. Cold spray parameters were chosen to ensure that the deposited geometry is as close to the idealized geometry as possible. Commercially available materials were used as masks, including plain woven steel wire mesh and circular hole punched metal sheets (both procured from McMaster-Carr, Aurora, OH, USA), to produce square based, diamond based and round based fin arrays with tapered cross-sections along their length, as shown in Fig. 2.

A commercial SST series EP cold spray apparatus (Centerline (Windsor) Ltd, Windsor, ON, Canada) was used in conjunction with the process described previously to produce the fin arrays. The carrier gas used in this work is commercially pure nitrogen, with a nozzle inlet pressure of 1.7 MPa and a nozzle inlet temperature of 350 °C. The feedstock powder material used is commercially pure aluminum (99.8% Al, Centerline (Windsor) Ltd) with an elongated shape and a mean particle diameter of 25 microns. Details regarding this feedstock powder are available elsewhere [20].

2.2. Test sample preparation and geometry evaluation

Fins were sprayed on Al6061 T6 aluminum substrates (Metal Supermarkets, Ottawa, ON, Canada) with dimensions of 7 mm by 51 mm for the μPIV tests, while substrates with dimensions of 51 mm by 51 mm were used for the heat transfer and hydrodynamic performance evaluation. The substrates were cleaned and degreased using acetone after being cut to size. No further surface preparation steps, such as heat treatment, was performed.

The fins were produced slightly higher than 1.0 mm, with the top of the pyramids subsequently ground using a Tegra Pol circular polishing machine (Struers, Ballerup, Denmark) with 120 grit silicon oxide sandpaper to ensure fin height consistency and shroud sealing, as described in Dupuis et al. [25]. Detailed geometry measurements were obtained using a depth of field microscope (Keyence model VHX-2000, Mississauga, Ontario, Canada) which allows building three dimensional images of the given samples. Ten fin specimens were measured and average values with the associated standard deviations are reported for the important geometric quantities. The relevant geometric quantities are presented in Table 1 and are illustrated in Fig. 3.

Prior to the flow characteristics evaluation using μPIV, the fin array samples' surface were coated with a thin layer of black ink to reduce the background noise intensity and greatly diminish the intensity of the particles' reflected light from the metallic surface.

3. Testing procedure

3.1. Performance test apparatus and procedure

Performance of the various fin arrays produced was assessed using an in–house heat transfer and pressure drop test apparatus,

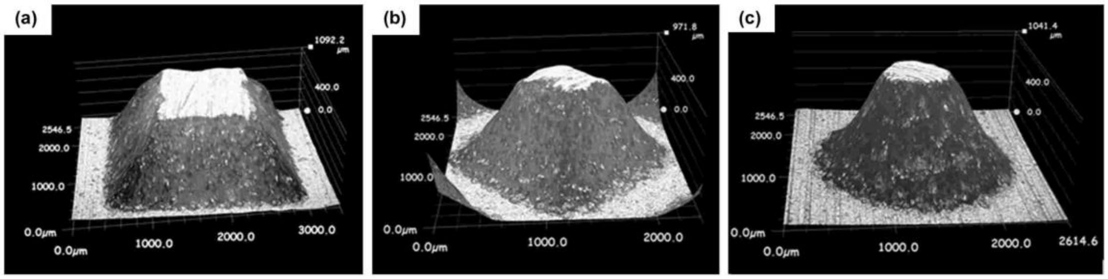

Fig. 2. Pin fin geometry types; (a) square base, (b) diamond base, (c) round base.

Table 1
Fin array sample characteristics.

Sample #	Base shape	Configuration 2117	Density fin/in	Base dimension (B) µm	Flow Channel Width (S) µm	Height (H) µm	Hydraulic diameter (D_h) µm	Fin frontal area mm^2	Heat transfer area mm^2
1	Square	Inline	8	2232 ± 106	943 ± 106	1023 ± 34	1140 ± 128	1.80	3335 ± 190
2	Round	Staggered	8	1797 ± 37	1378 ± 37	1014 ± 25	1269 ± 51	1.27	3092 ± 91
3	Diamond	Staggered	8	2220 ± 129	955 ± 129	1011 ± 32	1117 ± 158	2.64	3356 ± 272
4	Square	Inline	12	1401 ± 30	716 ± 30	1048 ± 12	1083 ± 40	0.88	3775 ± 66
5	Round	Inline	12	1644 ± 62	473 ± 62	1044 ± 45	913 ± 95	1.31	3881 ± 373
6	Round	Staggered	12	1615 ± 30	502 ± 30	1006 ± 41	930 ± 58	1.18	3733 ± 167
7	Diamond	Staggered	12	1600 ± 101	517 ± 101	1034 ± 45	967 ± 147	1.61	4038 ± 280

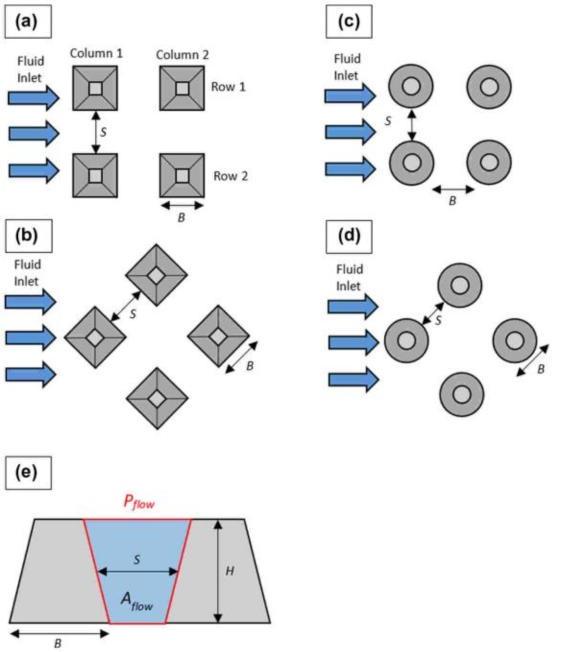

Fig. 3. Pin fin array geometry diagram, with relevant associated dimension variables. Top views of: (a) inline square base, (b) staggered diamond base, (c) inline round base, (d) staggered round base and (e) section view applicable for all samples.

adapted from the literature [29]. A schematic of the apparatus and of the sensor placement locations is shown in Fig. 4.

The main components of this apparatus are the air supply, the test section, the heating pad and the data acquisition system. The air is supplied by a compressed air line equipped with a filter and dehumidifier. The air inlet flow rate is controlled by a needle valve and is measured with a flow meter. This air is smoothly expanded into a horizontal rectangular channel with a diffuser and a honeycomb flow straightener, with the shroud touching the top of the fins in the test section for every trial. An unobstructed 457 mm long section ensures that the flow is fully developed before reaching the test section. The test sample is subjected to a constant heat flux provided by a strip heater.

A stagnation pressure measurement hole is located 25.4 mm upstream from the test section, while a set of differential pressure measurement holes are located 12.7 mm upstream (high pressure side) and downstream (low pressure side) from the middle of the test section. Two thermocouples are located 6.0 mm ahead and afterward the test section at mid-height to record the fluid local average temperature. Four thermocouples are attached to the fin array's base, with two on the side facing the incoming flow, and two on the side facing the exiting flow. On each face, a thermocouple is located on the centerline, while the other thermocouple is located 6.0 mm away from the wall. All the thermocouples used are T-type, butt-bonded, thin gauge (28 gauge) thermocouples. Radiative heat transfer losses are neglected.

All measurements were performed at steady-state and were repeated until statistical significance was achieved. Heat transfer data samples were taken at 2 Hz over a 30 s interval. For both types of tests, five sets of data samples were recorded for each flow rate tested. Measurements were taken at flow rates of 20 to 70 SLPM, which corresponds to Reynolds numbers varying from 200 to 3500 depending on sample geometry. Deviation of the measurements from the mean value was less than 5%, which led to error bars that were smaller than the markers. Since the error bars were not visible, they were not included in the graphs of Section 4. A detailed description of the apparatus' accuracy and of the instrument's uncertainties is given in Cormier et al. [20]. For hydrodynamic performance tests, a set of pressure taps is used to obtain the fin array friction losses, which include skin friction and form drag.

3.2. µPIV apparatus and procedure

A commercial µPIV Flowmaster3 apparatus (LaVision, Goettingen, Germany) was used to capture the flow structures of the

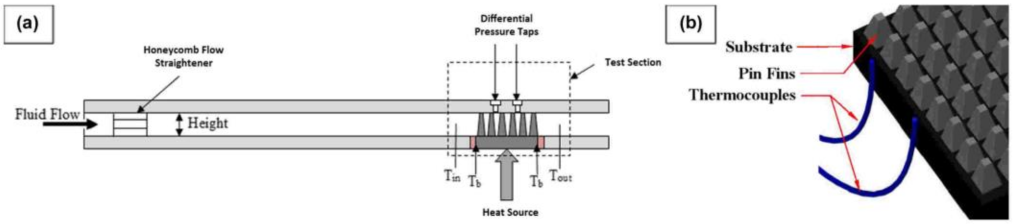

Fig. 4. Schematic of heat transfer fixture used to evaluate the fin arrays heat transfer performance;: (a) fixture with differential pressure transducer and flow thermocouple locations, (b) base thermocouple locations.

12 fpi samples using a cross-correlation algorithm. The 8 fpi samples could not be subjected to a μPIV analysis due to the larger flow rate required and the high head loss encountered through these samples, which could not be achieved by the pumping apparatus used for this work. The pin fin array sample was mounted in an aluminum sample holder equipped with a transparent polycarbonate viewing window, built at the University of Ottawa. A 1/25 hp centrifugal pump (The Pump House, Ottawa, ON, Canada) was used to pump the fluorescent polyester particle doped water through the system. A high-accuracy flow meter (McMaster-Carr, Aurora, OH, USA) equipped with a valve was used to adjust the flow rates between 2 and 8 ml/s, which corresponds to Reynolds numbers varying between 500 and 2000. Schematics of the apparatus are shown in Figs. 5 and 6.

The camera used to record the visual information is a double pulsed charged couple device (CCD) camera equipped with a microscope lens to condition the incoming light. It has a 5 Hz frame rate with a minimal time interval of 0.5 μs between two successive exposures. The camera offers a resolution of 1376 × 1040 pixels with an exposure plate of 8.9 × 6.7 mm and was used in conjunction with a long working distance objective lens with 5x magnification. This yielded a pixel width of 1.31 μm and a depth of field of 28 μm.

The laser source used for sample illumination is a double pulsed Nd:YAG laser used in conjunction with a dichroic filter, which only allows green light ($\lambda = 532$ nm) towards the sample and the red light ($\lambda = 650$ nm) that is emitted by the fluorescent tracer particles back to the camera. The laser pulses are collinear and produce a full volume illumination in the test section, which causes the depth of focus to be solely a function of the microscope optics. The laser pulse delay between successive exposures was adjusted to maintain particle displacements of five to ten pixels for the bulk of the fluid in the measurement zone.

The tracer particles used are Fluoro-Max red particles (Fisher, Waltham, MA, USA) with a particle diameter of 0.8 μm. These polystyrene particles have a density of 1.05 g/cm^3 and a refractive index of 1.59 for 589 nm wavelength light at 298 K. This particle size, used in conjunction with the lens described previously, yielded a depth of correlation of 27 μm [30,31].

The μPIV images were taken at mid-height of the pin fin, at Reynolds numbers of 500, 1000 and 1500. Sets of 100 pairs of images were taken to determine reliable averages and Root-Mean-Square (RMS) values of the velocity and its fluctuations, respectively.

The raw image pairs in a set were first averaged to establish the background intensity, which was then subtracted from the raw images, creating images that contained only the signal of particles, without the reflection of the particle's emitted light from the metallic fin surface. These images were then post-processed using Flowmaster's standard PIV cross-correlation algorithm, using a two-step process in which the interrogation window size is reduced from 64 × 64 pixels to 32 × 32 pixels, both with 0% overlap. Spurious vectors were then removed using the software's built-in vector filter function (remove and iteratively replace filter) with the removal of vectors with values that differed by more than three standard deviations from the mean of its neighbors. The image sets were then processed to create color maps of average velocity, turbulence intensity and turbulence kinetic energy. Individual images of the flow field for a given fin array sample were composed into a single image for a clearer presentation of the results.

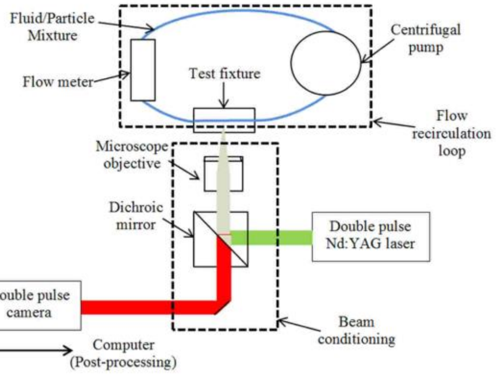

Fig. 5. μPIV Setup.

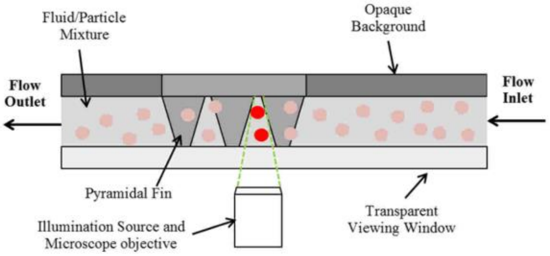

Fig. 6. Schematic of the μPIV test fixture.

3.3. Data reduction

The Reynolds number was calculated according to the following relation:

$$Re_{Dh} = \frac{\rho \cdot U_{max} \cdot D_h}{\mu} \tag{1}$$

where ρ is the fluid's density, U_{max} is the maximal fluid velocity in the fin array, D_h is the hydraulic diameter of the fin array flow channel and μ is the fluid's dynamic viscosity. For the works related to pyramidal fins [20,25–27], the characteristic length was chosen to be the hydraulic diameter, as the fin array geometry promotes structures typical of internal flows. Indeed, due to the small size of the channels, the boundary layer growth and coalescence in this type of fin array is more akin to that of internal flows than to external flows. The variable D_h is given by:

$$D_h = \frac{4 \cdot A_{flow}}{P_{flow}} \tag{2}$$

where A_{flow} and P_{flow} are the flow channel's face area and perimeter, respectively.

The equivalent thermal conductance for the heat exchanger specimen can be calculated using:

$$UA = \frac{1}{R_{eq}} = \frac{q}{\Delta T_{lm}} \tag{3}$$

where R_{eq} is the thermal circuit's equivalent resistance, q is the total heat input rate to the system and ΔT_{lm} is the log-mean temperature difference between the fluid and the fin array.

The total heat input rate to the system is calculated using:

$$q = \dot{m} \cdot (T_{out} - T_{in}) \cdot C_p \tag{4}$$

where $\dot{m}$ is the fluid mass flow rate, $(T_{out} - T_{in})$ is the fluid temperature difference between the entrance and the exit of the test section, C_p is the fluid's thermal capacitance.

The log-mean temperature difference is calculated with:

$$\Delta T_{lm} = \frac{\Delta T_1 - \Delta T_2}{\ln\left(\frac{\Delta T_1}{\Delta T_2}\right)} \tag{5}$$

where ΔT_1 and ΔT_2 are the temperature difference between the fin surface and the flow at the inlet and outlet, respectively.

To determine which fin array transfers heat more efficiently, the thermal conductances of the various heat exchanger samples must be compared at the same pumping power required for air, which was calculated according to Sahiti's definition [6]:

$$e_v = \frac{\dot{V}_f \cdot \Delta P_{fin}}{V \cdot \eta} \tag{6}$$

In the previous relation, e_v is the pumping power per unit volume, $\dot{V}_f$ is the volumetric flow rate of the fluid, V is the volume occupied by the heat exchanger sample while η is the fan efficiency. A fan efficiency of 0.8 was chosen as a reasonable value to perform these calculations [6].

The fin array's convective heat transfer coefficient is calculated using the following relation:

$$h = \frac{q}{\Delta T_{lm} \cdot A_{tot} \cdot \eta_o} \tag{7}$$

with A_{tot} representing the total heat transfer area of the fin array and η_o represents the overall surface efficiency which can be calculated as:

$$\eta_o = 1 - \frac{A_f}{A_{tot}}(1 - \eta_f) \tag{8}$$

where A_f is the exposed fin area and η_f is the individual fin efficiency, defined as the heat transferred by the fin over the maximum possible heat that can be transferred, which is computed with the procedure detailed in Incropera's work [3]. More details can be found in the authors' previous work [20,25], but for the samples described previously, the overall surface efficiency is computed to be over 0.99 due to the very large cross-sectional area to height ratio of the fin arrays produced, which drives the individual fin efficiency to near unity values.

The turbulence intensity (I) of the flow was computed as:

$$I = \frac{\overline{u}'}{U} \tag{9}$$

where $\overline{u}'$ denotes the Root-Mean-Square value of the velocity fluctuations in time and U represents the mean velocity.

The turbulence kinetic energy (TKE) of the fluid is evaluated using:

$$k = \frac{1}{2}\left(\overline{u_1'}^2 + \overline{u_2'}^2\right) \tag{10}$$

where k is turbulence kinetic energy, $\overline{u_1'}$ is the value of the axial velocity fluctuations and $\overline{u_2'}$ is the value of the transverse velocity fluctuations.

Finally, the theoretical form drag (F_d) caused by an individual feature can be calculated with the following relation:

$$F_d = \frac{1}{2} C_d \cdot \rho \cdot U^2 \cdot A_{front} \tag{11}$$

where C_d is the drag coefficient and A_{front} is the fin's projected frontal area. It is important to note that although an extensive amount of data can be obtained regarding the drag coefficient of cones, square and diamond base pyramids exists in re-entry type situations (with the flow either coming from the base or from the top of the features), very little literature can be found regarding the drag coefficients of such shapes in a cross-flow (flow towards the sides of the features). As such, estimation of the drag force is tricky at best, and must be based on the assumption that more aerodynamic profiles lead to lower drag coefficients.

4. Results and dicsussion

4.1. Hydrodynamic performance results and discussion

The pressure losses through the different fin array samples described in Table 1 are presented in Fig. 7. At first glance, the results obtained are unexpected considering that the square fins have the lowest amount of pressure loss, with the round fin arrays having higher losses and the diamond fins having the highest hydrodynamic losses. One would expect that more aerodynamic profiles would yield lower pressure losses. Looking at Eq. (11), it is possible to see the multiple factors which affect the theoretical drag force caused by an individual fin. It would then be logical to assume that for fin arrays with the same configuration (either staggered or inline), the more streamlined the shape is, the lower would be the associated drag force, due to the decreased drag coefficient. Consequently, the conical sample should have the lowest drag coefficient, followed by the diamond base pyramid and finally the square base pyramid. It is possible to make sense of the results by comparing the data sets in smaller groups and observing the marked differences in hydraulic diameter and in fin frontal area of the various samples.

The first factor to consider, however, is the configuration of the fin array. It is widely recognized in the literature that staggered fin array configurations lead to higher hydrodynamic losses than having the same fin geometries in the inline configuration, due to the increased amount of flow disruption created by the features, which require the fluid to deviate from its course at each fin column [2–5,9–11]. The measurements obtained from this study are consistent with this explanation, as the staggered samples, at a given fin density, have higher pressure losses than their inline counterparts.

The second observation that can be made concerns samples 1, 2 and 3, which are all 8 fpi samples. For this data set the samples are ranked from lowest to highest pressure losses, in the following order: square (pyramid) inline (sample #1), round (conical) staggered (#2) and diamond (pyramid) staggered (#3). In this case, although the form drag caused by an individual conical shape fin with a lower average fluid velocity (a consequence of its larger hydraulic diameter) and a smaller frontal area is lower than its square base pyramid counterpart, the array configuration (staggered vs inline, respectively) causes sample 2 to have higher hydrodynamic losses than sample 1. When the fin arrays are in the same configuration, such as for samples 2 and 3, then the theoretical measure of drag force becomes relevant, where the fin array with the lower average velocity, lower frontal area and lower (assumed) drag coefficient for its features has a much lower pressure loss.

The next data set consists of samples 4 through 7, the 12 fpi samples. For this set, the samples are ranked from lowest to highest pressure losses in the following order: square inline (pyramidal) (#4), round (conical) inline (#5), round (conical) staggered (#6) and finally diamond (pyramidal) staggered (#7). This order can be understood by noting first that, once again, the inline samples have a lower pressure loss than the staggered samples. The next observation that can be made is that the hydraulic diameter of the round base sample (#5) is much smaller than its square base (#4) counterpart, as seen in Table 1. This consequently increases the average fluid velocity, which in turn increases the pressure loss (since drag force is proportional to velocity squared). In this case, the reduction in hydraulic diameter causes a 20% increase in the average flow velocity (44% increase for the average velocity

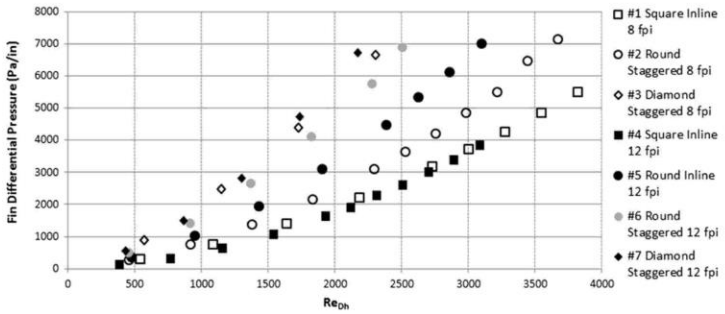

Fig. 7. Pressure loss results as a function of the Reynolds number for the different samples.

squared factor) at the same Reynolds number. This, compounded with the fact that the fin frontal area is approximately 50% larger for #5 compared to #4, could explain the causes behind the increased pressure loss of sample #5 with respect to sample #4, although the conical shape is much more streamlined than a square base pyramid for cross-flows. Concerning the staggered round (#6) and diamond (#7) fin arrays, the hydraulic diameter is very similar (less than 4% difference), yielding similar average flow velocities, with the difference being explained by the lower frontal area and by the lower drag coefficient of the more streamlined shape of the round base sample.

The three preceding observations are summarized in Table 2. The last observation that can be made is that the pressure losses of the 8 fin per inch samples compared to their 12 fpi counterparts do not always have the same trends: the inline square base fins have identical pressure losses, the staggered diamond sample at 8 fpi has a slightly lower pressure loss than its 12 fpi counterpart, which becomes more and more noticeable as the Reynolds number increases while the staggered round base 8 fpi sample has widely different losses compared to the 12 fpi sample with the same shape and configuration. This can be explained by looking at Table 3, where the velocity ratios between the 12 fpi samples and their 8 fpi counterparts are presented. The velocity ratios are calculated by dividing the squared average flow velocity obtained for the 12 fpi fin array sample by the squared average velocity of its 8 fpi counterpart at the same Reynolds number, to understand the effect of increased fluid velocities on pressure loss (since pressure loss is proportional to velocity squared). For the square samples, a 10% increase of the average velocity ratio yields a negligible pressure loss difference for these two samples. In a similar manner, the 84% increase between the round samples' velocity ratio causes a significant difference in pressure loss, with the relatively smaller increase of 36% of the velocity ratio between the diamond samples causing a smaller difference in pressure loss at the same Reynolds number.

The observations regarding the pressure loss order of the 12 fpi samples are supported by the μPIV measurements of the average TKE in the least turbulent part of the flow located in the wake of the tenth column, center row of the fins samples, which is presented in Table 4. The data contained in this table reveals that measurement of the average TKE could be used as a predictor for the pressure loss order of the samples in this study. Indeed, the data is presented in order of increasing pressure loss, with the TKE increasing accordingly. This correlation between pressure loss and TKE can be understood as being a consequence of the low pressure, turbulent wake, increasing the form drag experienced by the individual fins. The more turbulent the wake is, the lower is the associated pressure in this region, which causes stronger form drag.

These data seem to suggest that the governing factor behind the hydrodynamic performance of the different fin arrays tested in this work is the flow structure in the wake of the fins and its turbulence level. This implies that at low Reynolds numbers, such as those tested in this work, the form drag largely dominates the skin friction drag for the types of bluff bodied fin arrays under consideration. Indeed, the increased pressure losses of the staggered arrays

Table 2
Pressure loss comparison summary.

Sample comparison	Samples	Drag Equation Parameter			Conclusion
		C_d	U^2	A_{front}	
Configuration	Inline Staggered	– –	– –	– –	As seen in the literature [2–5,9–11], the inline configuration produces less pressure loss than the staggered configuration.
8 fpi samples	Square inline (#1)	High	Intermediate	Intermediate	#1 has lower losses than #2 and #3 due to its inline configuration.
	Round staggered (#2)	Low	Low	Low	#2 outperforms #3 because of its lower (assumed) drag coefficient, lower flow velocity and lower fin frontal area.
	Diamond staggered (#3)	Intermediate	High	High	
12 fpi samples	Square inline (#4)	High	Low	Low	#4 and #5 outperform #6 and #7 due to their inline configuration.
	Round Inline (#5)	Low	High	Intermediate	#4 has a lower pressure loss than #5 due to its significantly lower flow velocity and fin frontal area.
	Round Staggered (#6)	Low	High	Intermediate	
	Diamond Staggered (#7)	Intermediate	High	High	#6 outperforms #7 due its lower drag coefficient and its lower frontal area.

Table 3
Fin array flow characteristics.

Sample #	Base shape	Configuration	Density fin/in	Hydraulic diameter (D_h) μm	Fin frontal area mm^2	Velocity ratio (12/8)*
1	Square	Inline	8	1140	1.80	1.10
4	Square	Inline	12	1083	0.88	
2	Round	Staggered	8	1269	1.27	1.84
6	Round	Staggered	12	930	1.18	
3	Diamond	Staggered	8	1117	2.64	1.36
7	Diamond	Staggered	12	967	1.61	

* Velocity ratios are calculated by dividing the square of the average flow velocity obtained for the 12 fpi fin array sample at an arbitrary Reynolds number by the square of the average velocity of its 8 fpi counterpart at the same Reynolds number (used for the prediction of the hydrodynamic losses).

Table 4
Average turbulent kinetic energy (TKE) [m^2/s^2] in the wake of the fins for the 12 fpi samples, measured by μPIV analysis. The measurements were taken in the center row, behind the tenth column of fins.

Sample	Re_{Dh} = 500	Re_{Dh} = 1000	Re_{Dh} = 1500
Square Inline	0.00006	0.00147	0.00609
Round Inline	0.00090	0.00438	0.02010
Round Staggered	0.00270	0.00608	0.02800
Diamond Staggered	0.00325	0.01690	0.03390

compared to their inline array counterpart is attributed to the high levels of turbulence in the wake of the fins caused by the non-periodic nature of these arrays from one fin column to the next, causing significant flow disruptions. Conversely, the periodic nature of the inline arrangement allows preferred flow channels to develop with more stable fin wake structures. This can also be observed in Fig. 8, which presents the turbulence kinetic energy maps of the wakes of the four 12 fpi fin array samples characterized in this work, showing that the inline samples have less turbulent flow structures in the fin wake than the staggered samples, which is inferred from the lower TKE values measured.

4.2. Heat transfer test results

The heat transfer test results for thermal conductances and convective coefficients are presented in Figs. 9 and 10, respectively. At this point, it is useful to point out that by rearranging Eq. (3), it is possible to obtain the definition of the thermal conductance for convective flows with the following equation:

$$UA_{conv} = \frac{1}{R_{conv}} = h \cdot A_{tot} \cdot \eta_o \tag{12}$$

For the fin arrays discussed in this work, as mentioned previously, the overall surface efficiency η_o was calculated to be near unity for all the samples tested, with the total heat transfer area of the different samples presented in Table 1. Looking at Eq. (12), it then becomes obvious that the only parameter which defines the thermal conductance that can vary with the flow conditions is the convective heat transfer coefficient. Since the total heat transfer areas are similar (as seen in Table 1), in this case the convective coefficient becomes a performance indicator.

When comparing the convective coefficients of samples 1 to 3 (8 fpi samples) in Fig. 10, it is possible to observe that samples 2 and 3 perform similarly, especially at lower Reynolds numbers, and vastly outperform sample 1. This data distribution is explained through the fin array configuration, where the staggered fin array samples (samples #2 and 3) have similar convective coefficient values at a given Reynolds number, which are much higher than for the inline fin array sample (#1). The same trends can be observed when comparing samples 4 through 7, where the inline fin arrays (#4 and #5) have similar convective coefficients and the staggered arrays (#6 and #7) present larger convective coefficients. Once again, it is well known that the staggered configuration for fin arrays leads to higher convective coefficients than having the same fin geometries in the inline configuration, due to the increased amount of flow disruption created by the features [2–5,9–11]. The effect of turbulence on the convective coefficient was first described through the mass-momentum-heat transfer analogies developed by Reynolds and adapted by Chilton and Colburn [2,3]. These analogies stipulate that increases in wall shear stresses, such as those caused by turbulence, are accompanied by larger momentum and heat dissipation rates, which translate to higher pressure losses and convective coefficients, respectively. Although these analogies were developed for fully turbulent flows where skin friction is dominant and that their applicability for form drag dominated flows is questionable [2,3], this type of analogy may justify the explanation that turbulence generating features increase the average convective heat transfer coefficients through the disruptions of boundary layer development and through the increase of fluid mixing within this boundary layer.

For both the 8 and 12 fpi data sets, a correlation between the convective coefficient and the hydraulic diameter cannot be established, which indicates that the difference between the flow structures of staggered and inline samples contributes more importantly to the performance than the hydraulic diameter or, consequently, the average fluid velocity in the fin array.

The next observation that can be made from these results is that increasing the fin density from 8 to 12 fpi also increases the convective coefficient for the three fin shapes tested (samples 1 vs 4, 2 vs 6 and 3 vs 7). This implies that the increase in performance between the 12 fpi samples and their 8 fpi counterparts is not due solely to the increased heat transfer area, but is caused by differences in the flow properties, affecting the convection coefficient.

The third conclusion that can be reached by observing these graphs is that the heat transfer for pin fin arrays, such as those discussed in this work, is not only affected by the flow structures or turbulence levels in the wake of the fins. Indeed, if the heat transfer were solely a wake driven phenomenon, there would be a strong similarity between the sample order in the pressure drop curves and in the convective coefficient curves, where increasing one would consequently increase the other. The data presented earlier in Tables 2–4 does not correlate well with the heat transfer data for fin cross-section (round vs square vs diamond base), or for the Reynolds number dependency, which indicates that there is another parameter other than the turbulence of the flow in the fin's wake affecting the array average convective coefficient.

The conventional theory for banks of tubes and non-tapered, ideally shaped pin fins in general is that at low Reynolds numbers (such as those involved in this work) there is little or no turbulence of importance in the flow channels, with the velocity fluctuations being mainly concentrated in the wake of the fins [2–5]. These velocity fluctuations in the wake of fins have been discussed in the literature as being the main driver of the heat transfer enhancement by pin fins, as the turbulence included in the wake

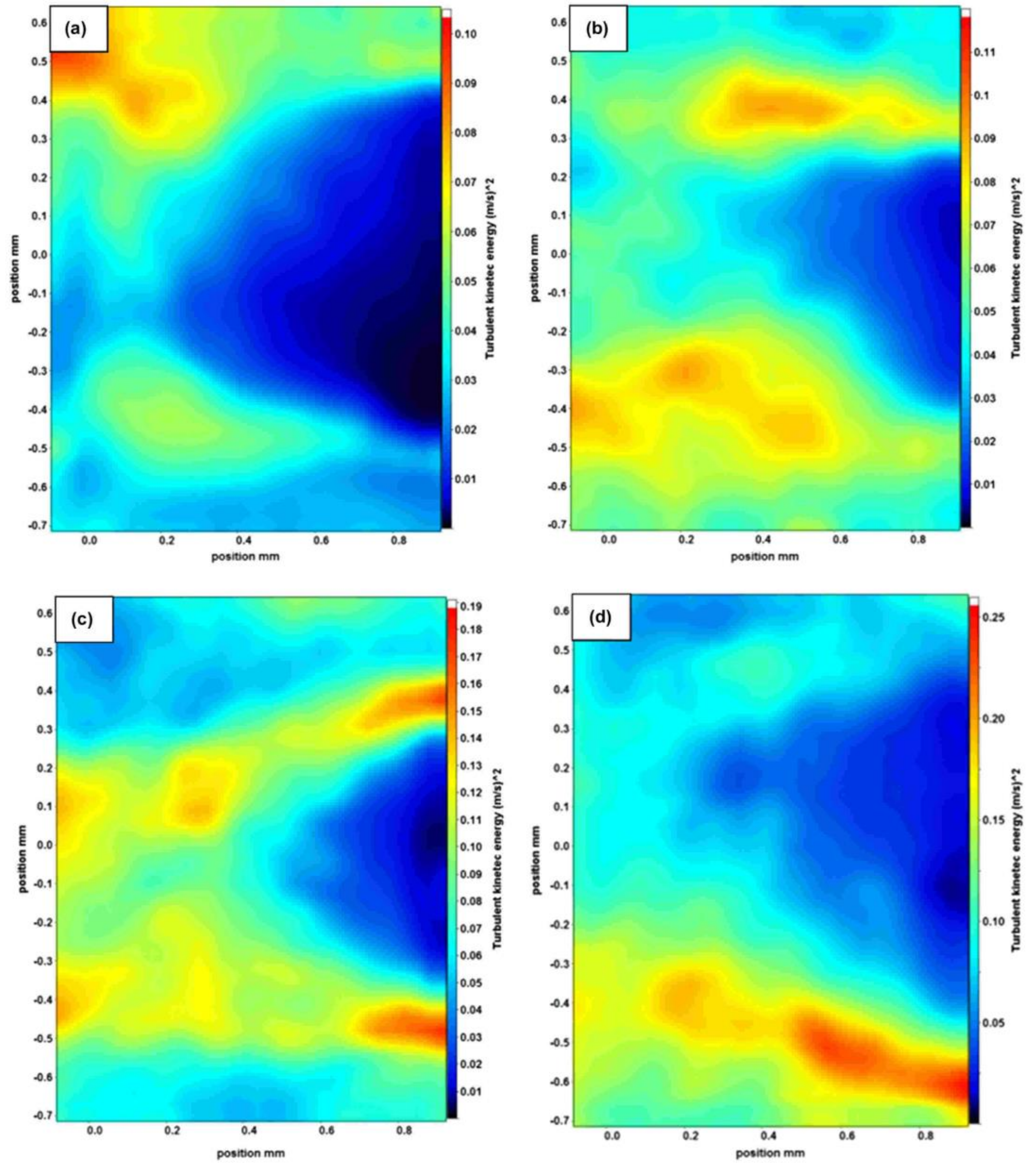

Fig. 8. Turbulent kinetic energy map for the 12 fpi samples at Re_{Dh} = 1500; (a) square inline, (b) round inline, (c) round staggered, (d) diamond staggered.

of the fins creates higher surface convective heat transfer coefficients, especially on the front and back surfaces of the pin fins [2–5,8–11]. In the case of tapered fins produced by CGDS, there is a significant turbulence intensity not only in the wake of the fins, but in the flow channels as well, as can be seen in Table 5. It is believed that this turbulence in the flow channels promotes heat transfer by contributing to the increase of the average convective coefficient of the fin array on the sides of the fins that are in contact with the flow channels, alongside the increase of the convective coefficient on the front and back surfaces of the pin fin that occurs due to the increased turbulence levels in the wake of the fins. Furthermore, the observed increase and subsequent decrease of the turbulence intensity in the flow channels from Re_{Dh} = 500 to 1000 and then from 1000 to 1500 could potentially explain the change in slope of the convective coefficient curves for the different pin fin samples around Re_{Dh} = 1000, which was also reported in earlier works [25–27]. There is not enough evidence at this point to create a definitive quantitative relationship between the turbulence intensities measured by μPIV in the fin wake and flow channel to the convective heat transfer coefficient, but these observation may serve as a starting point for future research into this type of slope transition.

Finally, the specific performance of the different fin arrays is presented in Fig. 11. In this chart, the thermal conductance per unit volume is plotted against the pumping power per unit volume required for the given flow rate. Observing this graph, it is possible

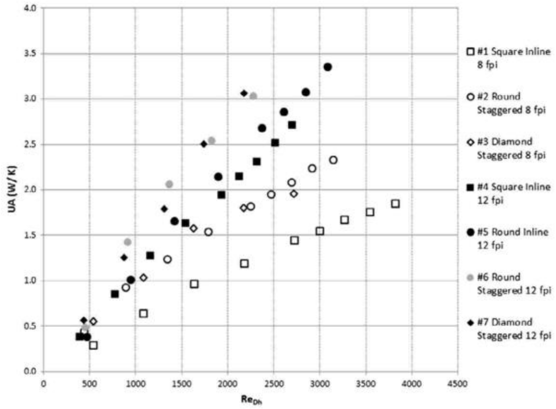

Fig. 9. Thermal conductance as a function of the Reynolds number for the different samples.

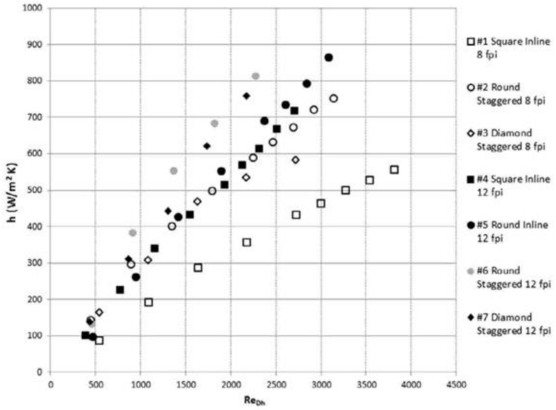

Fig. 10. Convective coefficient as a function of the Reynolds number of the different samples.

to see that the efficiencies are similar for the samples at the same fin density, with the higher density group performing better than the lower fin density samples. It seems that at a given fin density, the increased heat transfer performance is moderated by an increase in the hydrodynamic losses, which in turn translates to a larger required pumping power, yielding similar fin array thermal efficiencies for the different samples at the same fin density. The only notable exception to these trends is the 8 fpi circular section fin array sample, which tends to outperform the other two 8 fpi samples, especially at high flow rates. This could be attributed to its large hydraulic diameter, which would not significantly affect its heat transfer performance but significantly decrease the pressure losses.

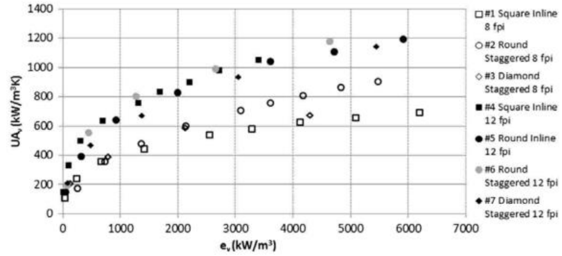

Fig. 11. Thermal conductance per unit heat exchanger volume as a function of the required pumping power per unit volume for the various samples included in this study.

4.3. Flow structure discussion

The velocity profiles of the fluid flowing around the different 12 fpi fin samples at Reynolds numbers of 500 and 1500 were reconstructed from different images and composed into one image for each fin array type at a given Reynolds number, and is presented in Fig. 12. It is important to note that although agreement between the various frames composed together is good, it is not seamless. In any case, this figure serves to illustrate the point that at the Reynolds numbers investigated, there is no significant change in the large scale recirculation structures for any of the fin geometries as the Reynolds number increases. For both inline configurations, a skewed double recirculation pattern can be observed, where the recirculation centers are offset from one another in the flow direction (one of the recirculations is located downstream with respect to the other). The offset between the positions of the upper and lower recirculations in these images is attributed to the imperfect geometry of the fins, which can be slightly tilted and thus affect the flow structure downstream. Furthermore, small defects in the flow channel alignment caused by imperfections in the mask used to produce the fin array samples can also significantly affect the flow structures, as was reported in previous work performed by the authors [28]. For the staggered samples, the flow detachement at the tips of the diamond fins and near the 6 and 12 o'clock position of the circular section fin can be observed, which causes a broad fin wake for the diamond sample but a smaller, tear drop shaped wake for the round fin array. This significant difference in turbulent wake size also helps explain the increased pressure loss, detailed in Section 4.1, of the pyramidal sample compared to that of the conical sample.

From all of these observations, it is surmised that the increase in heat transfer that occurs between the different fin geometries for the 12 fpi samples tested in this work is not due to a large scale flow structure change. Indeed, the flow structures observed did not change significantly with the fin section geometry (square vs round vs diamond) or with Reynolds number, as long as the samples are in the same configuration (inline or staggered). The two different configurations create distinct flow structures, where the inline fin arrays have a double recirculation pattern between fin columns, with relatively unperturbed flow channels between fin

Table 5
Average turbulence intensity (TI) values measured by μPIV analysis for the 12 fpi samples. The measurements were taken in the center row, at the tenth column of fins.

Sample	TI in fin wake (%)			TI in flow channel (%)		
	Re_{Dh} = 500	Re_{Dh} = 1000	Re_{Dh} = 1500	Re_{Dh} = 500	Re_{Dh} = 1000	Re_{Dh} = 1500
Square Inline	34.6	76.8	111.3	14.2	16.3	14.7
Round Inline	67.8	125.5	147.0	17.4	20.0	18.0
Round Staggered	93.5	89.0	75.0	19.2	20.8	17.2
Diamond Staggered	70.9	94.0	107.5	25.1	26.6	21.8

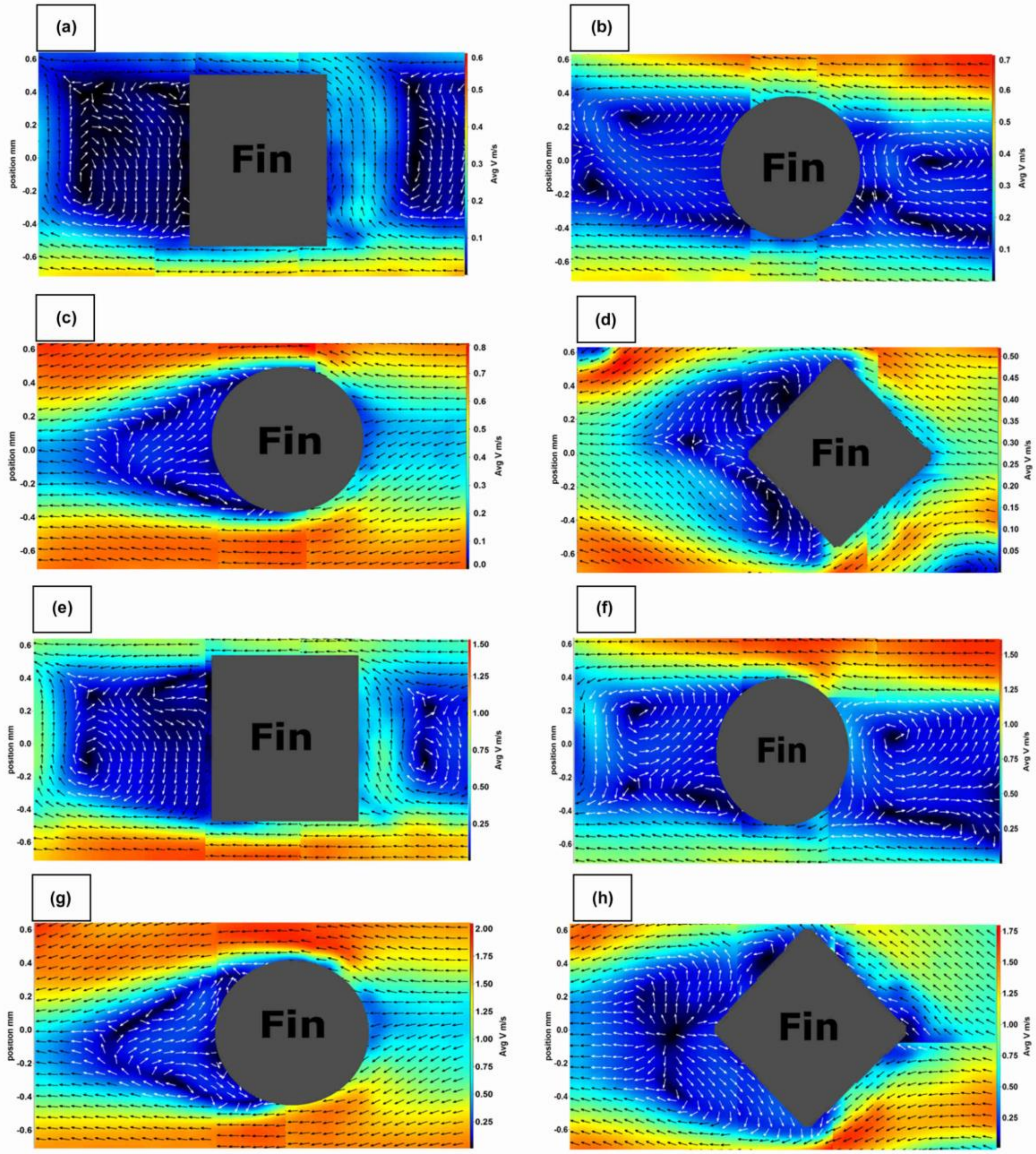

Fig. 12. Velocity profiles (each composed from four images) for the flow around the different 12 fpi samples; (a) square inline at $Re_{Dh} = 500$, (b) round inline $Re_{Dh} = 500$, (c) round staggered $Re_{Dh} = 500$, (d) diamond staggered $Re_{Dh} = 500$, (e) square inline at $Re_{Dh} = 1500$, (f) round inline $Re_{Dh} = 1500$, (g) round staggered $Re_{Dh} = 1500$, (h) diamond staggered $Re_{Dh} = 1500$ (approximate fin location and size illustrated on the drawing, with some arrows recolored white to increase their visibility).

rows, while the staggered arrays have a much more profiled wake which also includes recirculations, and flow channels that constrict and expand to circumvent the fins and their low velocity wakes.

5. Summary and conclusion

In this work, the pressure losses and the convective coefficients of square base, round base and diamond base tapered pin fins produced by cold spray additive manufacturing were measured and plotted as a function of the Reynolds number. The turbulence intensity and the turbulent kinetic energy were measured by µPIV and were correlated to the performance of the different 12 fpi fin array samples.

The principal factor affecting both the hydrodynamic performance and the thermal performance of the fin arrays tested in this work is the fin array configuration, where staggered configurations produce higher convective coefficients and higher pressure losses.

Furthermore, it was observed that increasing the hydraulic diameter caused a decreased pressure loss, which can be understood through the reduction of the form drag on individual pin fins due to the reduction of the average flow velocity, while the thermal performance curves did not exhibit a pronounced sensitivity to variations in the hydraulic diameter. As the samples in the staggered configuration produced much higher convective coefficients and pressure losses compared to the samples in the inline configuration, the different fin arrays turned out to have similar thermal conductances at a given fin density and pumping power. Increasing the fin density did not significantly affect the pressure losses of tapered pin fin arrays but largely increased their thermal conductance, which amounted to the 12 fpi fin arrays having a higher specific performance than their 8 fpi counterparts.

The observations made in this work indicate that although the flow field is considered to be in a sub-critical regime, the turbulence properties of the flow are important to consider, as high turbulence levels were measured in both the fin wake and flow channels. An interesting trend was found where the turbulence intensity values increased from $Re_{Dh} = 500$ to $Re_{Dh} = 1000$ and subsequently decreased from $Re_{Dh} = 1000$ to $Re_{Dh} = 2000$, which could potentially explain the change in the convective coefficient slope observed experimentally near $Re_{Dh} = 1000$. Furthermore, these large turbulence levels, which increase the average convective coefficient of the fin array, explain why the tapered pin fin samples greatly outperform similar sized plain rectangular fin arrays (tested in previous work [25–27]), which have been extensively reported by other authors to have low convective heat transfer coefficients and small amounts of flow disruptions [2–5,8–10]. The turbulent kinetic energy values measured in the flow structure in the fin's wake qualitatively correlate with the pressure loss, which indicates that the pressure loss due to form drag is much larger than the pressure loss due to skin friction. Conversely, the turbulent kinetic energy values do not correlate well with the convective coefficient values, which indicates that the heat transfer enhancement from pin fins does not depend solely on the flow structure in the fin's wake. Quantitative relationships have yet to be established between the turbulence quantities and the measured performances, but the information contained in this work will serve to guide future work in the development and characterization of tapered pin fin arrays.

Acknowledgements

Acknowledgements are due to the MITACS Accelerate program for its financial support of this project. The authors would also like to thank Rym Mehri for providing training on the use of the µPIV apparatus.

References

[1] Cornell Aeronautics Laboratory, Heat Transfer in Miniaturized Electronic Equipment, Bureau of ships, Navy Department, US Army, 1955.

[2] W.M. Kays, A.L. London, Compact Heat Exchangers, McGraw-Hill, New York, 1984.

[3] F.P. Incropera, D.P. DeWitt, T.L. Bergman, A.S. Lavine, Fundamentals of Heat and Mass Transfer, Wiley, New York, 2006.

[4] A. Žukauskas, Heat transfer from tubes in crossflow, Adv. Heat Transfer 8 (1972) 93–160.

[5] N. Sahiti, F. Durst, A. Dewan, Heat transfer enhancement by pin elements, Int. J. Heat Mass Transfer 48 (2005) 4738–4747.

[6] N. Sahiti, F. Durst, A. Dewan, Strategy for selection of elements for heat transfer enhancement, Int. J. Heat Mass Transfer 49 (2006) 3392–3400.

[7] N. Sahiti, A. Lemouedda, D. Stojkovic, F. Durst, E. Franz, Performance comparison of pin fin in-duct flow arrays with various pin cross-sections, Appl. Therm. Eng. 26 (2006) 1176–1192.

[8] E.M. Sparrow, J.W. Ramsey, Heat transfer and pressure drop for a staggered wall-attached array of cylinders with tip clearance, Int. J. Heat Mass Transfer 21 (1978) 1369–1377.

[9] E.M. Sparrow, J.W. Ramsey, C.A.C. Altemani, Experiments on in-line pin fin arrays and performance comparison with staggered arrays, ASME J. Heat Transfer 102 (1980) 44–50.

[10] D.E. Metzger, C.S. Fan, S.W. Haley, Effects of pin shape and array orientation on heat transfer and pressure loss in pin fin arrays, ASME J. Eng. Gas Turbines Power 106 (1984) 252–257.

[11] B.A. Brigham, G.J. Vanfossen, Length to diameter ratio and row number effects in short pin fin heat transfer, ASME J. Eng. Gas Turbines Power 104 (1984) 241–244.

[12] G.J. Vanfossen, Heat-transfer coefficients for staggered arrays of short pin fins, ASME J. Eng. Gas Turbines Power 102 (1982) 268–274.

[13] H.I. You, C.H. Chang, Numerical prediction of heat transfer coefficient for a pin-fin channel flow, ASME J. Heat Transfer 119 (1997) 840–843.

[14] T.M. Jeng, S.C. Tzeng, Pressure drop and heat transfer of square pin-fin arrays in in-line and staggered arrangements, Int. J. Heat Mass Transfer 50 (2007) 2364–2375.

[15] O.N. Şara, Performance analysis of rectangular ducts with staggered square pin fins, Energy Convers. Manage 44 (2003) 1787–1803.

[16] J. Wen, Y. Li, A. Zhou, K. Zhang, An experimental and numerical investigation of flow patterns in the entrance of plate-fin heat exchanger, Int. J. Heat Mass Transfer 49 (2006) 1667–1678.

[17] B. Jones, P.-S. Lee, S.V. Garimella, Infrared micro-particle image velocimetry measurements and predictions of flow distribution in a microchannel heat sink, Int. J. Heat Mass Transfer 51 (2008) 1877–1887.

[18] O. Uzol, C. Camci, Elliptical pin fins as an alternative to circular pin fins for gas turbine blade cooling applications; Part 1: Endwall heat transfer and total pressure load characteristics, in: Proceedings of 46th ASME International Gas Turbine, Aeroengine Congress and Exposition and Users Symposium, New Orleans, Louisiana, USA, 2001.

[19] O. Uzol, C. Camci, Elliptical pin fins as an alternative to circular pin fins for gas turbine blade cooling applications; Part 2: wake flow field measurements and visualization using particle image velocimetry, in: Proceedings of 46th ASME International Gas Turbine, Aeroengine Congress and Exposition and Users Symposium, New Orleans, Louisiana, USA, 2001.

[20] Y. Cormier, P. Dupuis, B. Jodoin, A. Corbeil, Net shape fins for compact heat exchanger produced by cold spray, J. Therm. Spray Technol. 22 (7) (2013) 1210–1221.

[21] A.P. Alkhimov, A.N. Papyrin, V.F. Dosarev, N.I. Nesterovich, M.M. Shuspanov, US Patent No. 5302414, 1994.

[22] E. Irissou, J.-G. Legoux, A.N. Ryabinin, B. Jodoi, C. Moreau, Review on cold spray process and technology: Part I-intellectual property, J. Therm. Spray Technol. 17 (4) (2008) 495–516.

[23] J.R. Davis, Handbook of Thermal Spray Technology, ASM International, Materials Park, 2004.

[24] H. Herman, S. Sampath, R. McCune, Thermal spray: current status and future trends, Mater. Res. Soc. Bulletin 25 (7) (2000) 17–25.

[25] P. Dupuis, Y. Cormier, B. Jodoin, A. Corbeil, Performance evaluation of near-net pyramidal shaped fin arrays manufactured by cold spray, Int. J. Heat Mass Transfer 69 (2014) 34–43.

[26] Y. Cormier, P. Dupuis, A. Farjam, B. Jodoin, A. Corbeil, Additive manufacturing of pyramidal pin fins: height and fin density effects under forced convection, Int. J. Heat Mass Transfer 75 (2014) 235–244.

[27] P. Dupuis, Y. Cormier, A. Corbeil, B. Jodoin, Performance of cold sprayed near-net pyramidal shaped arrays under forced convection, in: Proceedings of CONV-14: International Symposium on Convective Heat and Mass Transfer, Turkey, June 8–13, 2014.

[28] P. Dupuis, Y. Cormier, A. Corbeil, M. Fenech, B. Jodoin, Flow structure identification and analysis in fin arrays produced by cold spray additive manufacturing, Int. J. Heat Mass Transfer 93 (2016) 301–313.

[29] J. Tian, T. Kim, T.J. Lu, H.P. Hodson, D.T. Queheillalt, D.J. Sypeck, H.N.G. Wadley, The effects of topology upon fluid-flow and heat-transfer within cellular copper structures, Int. J. Heat Mass Transfer 47 (14–16) (2004) 3171–3186.

[30] C.D. Meinhart, S.T. Wereley, M.H.B. Gray, Volume illumination for two-dimensional particle image velocimetry, Meas. Sci. Technol. 11 (2000) 809–814.

[31] J.G. Santiago, S.T. Wereley, C.D. Meinhart, D.J. Beebe, R.J. Adrian, A particle image velocimetry for microfluidics, Exp. Fluids 25 (1998) 316–319.

CHAPTER 9 CONCLUSION AND FUTURE WORK

9.1 General Conclusions

This thesis has presented the work performed by the author regarding the thermal and hydrodynamic performance of pin fin arrays produced by cold spray. This new method of additive manufacturing for the production of pin fins has proven to have the potential for commercial viability, due to the ease of manufacturing and due to the high volumetric thermal efficiency. In the context of this research, the flow structures arising from fluid motion around the extended heat transfer surfaces were also characterized and the relevant turbulence quantities were measured. The results obtained from these endeavours are presented in the form of peer-reviewed articles, which address the specific research objectives set out for this project. These research objectives were successfully reached within the timeframe allowed. Much work still remains to be performed before the analysis of the performance metrics of pin fin arrays produced using cold spray is complete.

9.2 Significant Contributions of this Research

This work contributed in many respects to the scientific literature available regarding the performance of pin fins and the possibility of using cold spray as an additive manufacturing technique, especially for the production of near-net shape fin arrays.

The first significant contribution of this work is **the proof of concept regarding the production of pin fin arrays using cold spray technology as an additive manufacturing technique**. Indeed, the rapid production of fin array samples, combined with the low cost and the potential for automation of the cold spray process make this type of fin production a very interesting alternative to the complex and usually labour or time intensive operations required to obtain complex geometries for pin fin arrays. The potential for creating fins with a tapered geometry also presents new and exciting opportunities for fin array manufacturing that have yet to be explored, in addition to those currently used commercially by the project's industrial partner.

Another contribution of this work is the extensive studies regarding the influence of the various geometric parameters on the thermal and hydrodynamic performance of the pin fin arrays. Indeed, the influence of the fin height and of the fin density were characterized and reported, with the results agreeing well with what was published previously in the literature. It was found that **increasing the fin density increases the thermal performance of the fin arrays as well as the pressure loss, with the net effect of these two parameters showing that denser fin arrays have a better overall performance than less dense fin arrays, with a plateau at fin densities greater than 16 fpi. Increasing the fin height was also found to increase both the thermal conductance and the hydrodynamic losses, yielding an increased heat transfer surface efficiency as the fins are taller, with diminishing returns as the height increases when comparing on the basis of footprint area.** The height did not significantly increase the thermal conductance per unit pumping power when compared on a unit volume basis. The effect of varying the base angle of the fin's taper was also characterized, with the results indicating that a very similar thermal conductance per unit pumping power can be expected when the taper angle is increased.

The flow structures of the fluid flowing around square base pyramids, diamond base pyramids and cones were characterized by µPIV, with more focus being accorded to the square base pyramids. For both the inline and staggered fin configurations, the flow structures observed resembled those previously described in the literature for banks of tubes in cross-flow. **For the staggered configuration, expanding and contracting flow channels were found, with tear-shaped recirculation zones located in the fin's wake. For the inline configuration, relatively unperturbed flow channels are evident, with large, slow moving recirculation zones found in**

the fin’s wake. These differences in the flow structures causes a significant difference in the performance of staggered and inline fin arrays, with the former configuration increasing both the heat transfer and the pressure loss. Globally, these increases lead to similar performance at a given pumping power. **Evidence of flow channel misalignment was found for the inline configuration of square base pyramidal fins**, which was investigated both by µPIV and by numerical simulation. This misalignment caused a transition in the fin wake flow structure from the classic double recirculation pattern to a single recirculation with bypass flow structure. This slight misalignment is most likely caused by production inconsistencies of the wire mesh masks used for the production of the pin fins. From the numerical simulation, it is expected that this slight misalignment and **the associated flow structures do not significantly influence the thermal and hydrodynamic performance of the pin fin array, which does not compromise the commercial viability of using pin fin arrays with slightly skewed passages**.

Lastly, the performance metrics were tentatively correlated to the flow instability quantities measurable by µPIV: the turbulence intensity and the turbulent kinetic energy. It seems that for the pin fin arrays studied in this work, the turbulent kinetic energy values measured for the fluid in the fin’s wake can be directly correlated to the pressure loss of the fin arrays, indicating that **the principal driver for the hydrodynamic performance of such pin fin arrays is the pressure loss resulting from form drag, with skin friction playing a minor role**. The turbulence intensity in the flow channel and the turbulent kinetic energy of the fluid in the fin’s wake are both important factors contributing to increase the thermal performance of the fin array, indicating **that the turbulence levels in the axial flow channels needs to be taken into account for the performance of fin arrays such as those presented in this work, even at Reynolds numbers usually considered to be in the sub-critical regime**. Finally, **the change in the slope of the**

thermal conductance curve as a function of the Reynolds number identified between Re_{Dh}=500 and Re_{Dh}=1000 was explained as being due to the initially increasing contribution of turbulence intensity before this value, and its subsequent decrease after this point is reached. This turbulence contribution is measured with the turbulence intensity found in the axial flow channel, which correlates well with the change in slope for all samples described in this work. These correlations are still tentative, however, as further work should be performed to identify the precise transition point and the mechanism for this transition.

9.3 Recommended Future Work

The work contained in this thesis consists of the preliminary studies required to demonstrate the viability of using pin fin arrays produced using cold spray and understand some of the effects of the various fin geometrical parameters. Much work remains to be done regarding the characterization of the thermal and hydrodynamic performance of such pin fin arrays. Furthermore, the exploratory experiments regarding the flow structures and the links between the turbulence quantities and the performance of the fin arrays needs to be explored in more details.

The first study that should be performed is to test the manufacturing limits of the masked cold spray technique. Soft limits were explored in this work, with respect to the constraints from the industrial partner and for the two cold spray apparatuses that were available for testing at the time, but a more in-depth study linking nozzle size, particle size distribution and mask opening size should be performed to better understand the multiple factors influencing production quality. For example, the particle size and feed rate strongly influence the maximal fin density that can be obtained without clogging the mask. A study which describes the maximal particle size for a given mask opening at a specific powder feeding rate could be performed to broaden the range of application and identify the maximal fin density attainable under the given conditions through correlations, instead of by trial and error. Other limits such as the maximal taper angle, maximal height and the minimal base dimension for various fin densities could also be investigated to reduce the amount of material that requires to be deposited to obtain a given fin performance. Performing studies to identify the optimal fin to passage width ratio to optimize performance for a given fin density is also mandated, which could also help reducing the amount of material deposited. The last manufacturing study proposed is to determine the most efficient spray pattern possible to limit deposition on the wire mesh mask and to reduce overspray, which would once again reduce the amount of material required to build a given fin array and help further reduce the costs associated with this technique.

Other experimental work concerning the performance of the fin array could also be performed with the purpose of creating correlations usable for the analytical investigation of fin array performance. Broadening the correlations proposed for the Nusselt number and the friction factor as functions of the Reynolds number for more fin densities and for a larger range of Reynolds number should also be performed.

The physical properties of different materials cold sprayed into fin arrays should also be determined to ensure that the product survives the application stresses and temperatures, especially in a full configuration including the bond coat and wire mesh core. Indeed, preliminary studies regarding the mechanical strength of the fin arrays have been performed by the University of Ottawa Cold Spray Lab, but insufficient data has been collected yet to assert with certainty that the fin arrays could be used in commercial heat exchangers with infinite life. In particular, thermal cycling tests and oxidations tests should be performed at temperatures resembling those found in industrial applications of heat exchangers to ensure that delamination does not occur between the various layers, and that the thermal conductivities of the materials do not degrade significantly in corrosive environments.

Some modelling work has been performed for the purpose of the evaluation of the performance of the fin arrays, but much can also be performed to predict the effects of parameters that cannot easily be controlled experimentally, such as the fin surface's roughness. Indeed, preliminary calculations regarding the fin roughness height for flow conditions such as those tested in this work show that the roughness elements are significant enough to affect the viscous generation of unsteadiness in the flow. A more in depth study of the flow structure around a single fin could also be performed numerically, ranging from macroscopic structures down to Kolmogorov scale structures, which cannot currently be resolved near the walls using experimental methods such as µPIV.

Finally, the hypotheses linking the turbulence metrics and the thermal and hydrodynamic performance should be investigated in much detail to determine both the extent of the validity of the correlation between these quantities and the range of application of such correlations. Specifically, the transition point between the high slope and low slope regimes for the thermal conductance as a function of the Reynolds number curve should be precisely identified. Furthermore, a quantitative correlation between the turbulence intensity value increase and the slope increase should be computed and a verification of this correlation should be made for different samples with the same geometry, to ensure a strong link between these values can be established. The mechanism behind this increase and subsequent decrease in the turbulence intensity should be investigated, as it could lead to the identification of a significant thermal performance driving phenomenon. Similarly, the mechanism behind the transfer of instabilities from the turbulence generating wake region of the fin to the relatively stable flow in the axial flow channel should also be investigated further, in order to maximize this contribution. This would allow the growth of the thermal performance with only small corresponding increases in the hydrodynamic losses due to the form drag, which should yield a better overall performance for the fin array.

CHAPTER 10 REFERENCES

[1] A. B. Lovins, *Small is Profitable: The Hidden Economic Benefits of Making Electrical Resources the Right Size*, Rocky Mountain Institute, 2002

[2] S. M. Kaplan and F. Sissine, *Smart Grid: Modernizing Electric Power Transmission and Distribution; Energy Independence, Storage and Security; Energy Independence and Security Act ... and Resiliency; Integra*, TheCapitol.Net Inc., 2009

[3] A. Corbeil, *Study of Small Hydraulic Diameter Media for Improved Heat Exchanger*, M.A.Sc. Thesis, University of Ottawa, 2009

[4] D. Bohn, *Micro Gas Turbine and Fuel Cell - A Hybrid Energy Conversion System with High Potential*, NATO Research and Technology Organisation, 2005

[5] R.L. Shaner, Heat Exchanger Having Metal Wire Screens, and Method of Making Stack of Screens Therefor, US Patent No. 4840228, 1989

[6] J. Chisholm, Method of Making a Crimped Wire Mesh Heat Exchanger/Sink, US Patent No. 4843693, 1989

[7] Brayton Energy, http://www.braytonenergy.net/heat-exchangers/, consulted April 2014

[8] J. Assad, A. Corbeil, P. Richer and B. Jodoin, Novel Stacked Wire Mesh Compact Heat Exchangers Produced Using Cold Spray, *Journal of Thermal Spray Technology*, 2011, **20**(6), pp. 1192–1200

[9] W. M. Kays and A. L. London, *Compact Heat Exchangers*, third ed., McGraw-Hill, New York, 1984

[10] F. P. Incropera, D. P. DeWitt, T. L. Bergman and A. S. Lavine, *Fundamentals of Heat and Mass Transfer*, 6th ed., Wiley, 2006

[11] Z. Anxionnaz, M. Cabassud, C. Gourdon and P. Tochon, Heat Exchanger/Reactors (HEX reactors): Concepts, Technologies: State-of-the-Art, *Chemical Engineering and Processing*, 2008, **47**(12), pp. 2029–2050

[12] J. Tian, T. Kim, T.J. Lu, H.P. Hodson, D.T. Queheillalt, D.J. Sypeck and H.N.G. Wadley, The Effects of Topology Upon Fluid-Flow and Heat-Transfer Within Cellular Copper Structures, *International Journal of Heat and Mass Transfer*, 2004, **47**(14–16), pp. 3171–3186

[13] H. R. Salimi Jazi, J. Mostaghimi, S. Chandra, L. Pershin and T. Coyle, Spray-Formed, Metal-Foam Heat Exchangers for High Temperature Applications, *Journal of Thermal Science and Engineering Appications*, 2009, **1**(3), pp. 1-7

[14] F. Azarmi, J. Saaedi, , T. W. Coyle and J. Mostaghimi, Microstructure Characterization of Alloy 625 Deposited on Nickel Foam Using Air Plasma Spraying, *Advanced Engineering Materials*, 2008, **10**(5), pp. 459–465

[15] A. Žukauskas, Heat Transfer from Tubes in Crossflow, *Advances in Heat Transfer*, 1972, **8**, pp. 93–160

[16] N. Sahiti, F. Durst and A. Dewan, Strategy for selection of elements for heat transfer enhancement, *International Journal of Heat and Mass Transfer*, 2006, **49**(1), pp. 3392-3400

[17] F. Zhou and I. Catton, Numerical Evaluation of Flow and Heat Transfer in Plate-Pin Fin Heat Sinks with Various Pin Cross-Sections, *Numerical Heat Transfer, Part A: Applications*, 2011, **60**(1), pp. 107-128

[18] K.S. Yang, W.H. Chu, I.Y. Chen and C.C. Wang, A comparative study of the airside performance of heat sinks having pin fin configurations, *International Journal Heat and Mass Transfer*, 2007, **50**, pp. 4661-4667

[19] N. Sahiti, F. Durst and A. Dewan, Heat transfer enhancement by pin elements, *International Journal of Heat and Mass Transfer*, 2005, **48**, pp. 4738-4747

[20] N. Sahiti, A. Lemouedda, D. Stojkovic, F. Durst and E. Franz, Performance comparison of pin fin in-duct flow arrays with various pin cross-sections, *Applied Thermal Engineering*, 2006, **26,** pp. 1176-1192

[21] B.A. Brigham and G.J. Van Fossen, Length to diameter ratio and row number effects in short pin fin heat transfer, *ASME Journal of Engineering for Gas Turbines and Power*, 1984, **104**, pp. 241-244

[22] G.J. Van Fossen, Heat-transfer coefficients for staggered arrays of short pin fins, *ASME Journal of Engineering for Gas Turbines and Power*, 1982, **102**, pp. 268-274

[23] E.M. Sparrow and J.W. Ramsey, Heat transfer and pressure drop for a staggered wall-attached array of cylinders with tip clearance, *International Journal of Heat and Mass Transfer*, 1978, **21**, pp. 1369-1377

[24] E.M. Sparrow, J.W. Ramsey and C.A.C. Altemani, Experiments on in-line pin fin arrays and performance comparison with staggered arrays, *ASME Journal of Heat Transfer*, 1980, **102**, pp. 44-50

[25] D.E. Metzger, C.S. Fan and S.W. Haley, Effects of pin shape and array orientation on heat transfer and pressure loss in pin fin arrays, *ASME Journal of Engineering for Gas Turbines and Power*, 1984, **106**, pp. 252-257

[26] Q. Li, Z. Chen, U. Flechtner and H.-J. Warnecke, Heat transfer and pressure drop characteristics in rectangular channels with elliptic pin fins, *International Journal of Heat and Fluid Flow*, 1998, **19**, pp. 245-250

[27] Z. Chen, Q. Li, D. Meier and H.-J. Warnecke, Convective heat transfer and pressure loss in rectangular ducts with drop-shaped pin fins, *Heat and Mass Transfer*, 1997, **33**, pp. 219-224

[28] V.B. Grannis and E.M. Sparrow, Numerical simulation of fluid flow through an array of diamond-shaped pin fins, *Numerical Heat Transfer*,1991, **19** (Part A), pp. 381-403

[29] H.I. You and C.H. Chang, Numerical prediction of heat transfer coefficient for a pin-fin channel flow, *ASME Journal of Heat Transfer*, 1997, **119**, pp. 840-843

[30] O.N. Şara, Performance analysis of rectangular ducts with staggered square pin fins, *Energy Conversion and Management*, 2003, **44**, pp. 1787-1803

[31] T.M. Jeng and S.C. Tzeng, Pressure drop and heat transfer of square pin-fin arrays in in-line and staggered arrangements, *International Journal of Heat and Mass Transfer*, 2007, **50,** pp. 2364-2375

[32] A.P. Colburn, Heat transfer by natural and forced convection, *Engineering Bulletin of Purdue University Resources Services*, 1942, **26** (84), pp. 47–50

[33] A.L. London and C.K. Ferguson, Test results of high-performance heat exchanger surfaces used in aircraft intercoolers and their significance for gas-turbine regenerator design, *ASME Transactions*, 1949, **71**, pp. 17–26

[34] S.W. Chang, T.L. Yang, C.C. Huang and K.F. Chiang, Endwall heat transfer and pressure drop in rectangular channels with attached and detached circular pin-fin array, *International Journal of Heat and Mass Transfer*, 2008, **51**, pp. 5247-5259

[35] Y. Zhang, J. Liu, D. Chong and J. Yan, Experimental investigation on the heat transfer and flow performances of fin array with shield in bypass, *International Journal of Heat and Mass Transfer*, 2013, **56**, pp. 674-682

[36] J. G. Soland, W. M. Mack and W. M. Rohsenow, Performance ranking of plate-fin heat exchanger surfaces, *ASME Transactions*, 1978, **100**, pp. 514-519

[37] J.R. Davis, *Handbook of Thermal Spray Technology*, ASM International, 2004

[38] A.P. Alkhimov, A.N. Papyrin, V.F. Dosarev, N.I. Nesterovich and M.M. Shuspanov, Gas-Dynamic Spraying Method for Applying a Coating, US Patent No. 5302414, 1994

[39] A.O. Tokarev, Structure of Aluminum Powder Coatings Prepared by Cold Gas-Dynamic Spraying, *Metal Science and Heat Treatment*, 1996, **38**(3-4), pp. 136-139

[40] M. Grujicic, C.L. Zhao, W.S. DeRosset and D. Helfritch, Adiabatic shear instability based mechanism for particles/substrate bonding in the cold-gas dynamic-spray process, *Materials and Design*, 2004, **25**, pp. 681–688

[41] R.C. Dykhuizen, M.F. Smith, D.L. Gilmore, R.A. Neiser, X. Jiang and S. Sampath, Impact of High Velocity Cold Spray Particles, *Journal of Thermal Spray Technology*, 1999, **8**(4), pp. 559–564

[42] S.H. Huang, P. Liu, A. Mokasdar, L. Hou "Additive manufacturing and its societal impact: a literature review", *Int. J. Adv. Manuf. Technol.*, **67,** pp. 1191-1203, 2013.

[43] L. Laperrière and D. Reinhart, *CIRP Encyclopedia of Production Engineering*, Springer Berlin Heidelberg, 2014

[44] L.E. Weiss and F. B. Prinz, Method for Fabrication of Three Dimensional Articles, US Patent No. 5301415, 1994

[45] R. Merz, F.B. Prinz, K. Ramaswami, M. Terk and L.E. Weiss, Shape Deposition Manufacturing, *In: Proceedings of the Solid Freeform Fabrication Symposium*, 1994

[46] D.Y. Kim, J.J. Park, J.G. Lee, D. Kim, S.J. Tark, S. Ahn, J.H. Yun, J. Gwak, K.H. Yoon, S. Chandra and S.S. Yoon, Cold Spray Deposition of Copper Electrodes on Silicon and Glass Substrates, *Journal of Thermal Spray Technology*, 2013, **22**(7), pp. 1092–1102

[47] J. Westerweel, Fundamentals of digital particle image velocimetry, *Measurement Science and Technology*, 1997, **8**, pp. 1379-1392

[48] National Research Council Canada, http://archive.nrc-cnrc.gc.ca/eng/ projects/ibd/ laser-speckle-techniques.html, consulted April 2014

[49] C.D. Meinhart, S.T. Wereley and M.H.B Gray, Volume illumination for two-dimensional particle image velocimetry, *Measurement Science and Technology*, 2000, **11**, pp. 809–814

[50] J.G. Santiago, S.T. Wereley, C.D. Meinhart, D.J. Beebe and R.J. Adrian, A particle image velocimetry for microfluidics, *Experiments in Fluids*, 1998, **25**, pp. 316–319

[51] J. Wen, Y. Li, A. Zhou and K. Zhang, An experimental and numerical investigation of flow patterns in the entrance of plate-fin heat exchanger, *International Journal of Heat and Mass Transfer*, 2006, **49**, pp. 1667-1678

[52] B. Jones, P.-S. Lee and S.V. Garimella, Infrared micro-particle image velocimetry measurements and predictions of flow distribution in a microchannel heat sink, *International Journal of Heat and Mass Transfer*, 2008, **51**, pp. 1877-1887

[53] O. Uzol and C. Camci, Elliptical Pin Fins as an Alternative to Circular Pin Fins for Gas Turbine Blade Cooling Applications; Part 1: Endwall Heat Transfer and Total Pressure Load Characteristics, *In: Proceedings of 46th ASME International Gas Turbine, Aeroengine Congress and Exposition and Users Symposium*, New Orleans, Louisiana, USA, 2001

[54] O. Uzol and C. Camci, Elliptical Pin Fins as an Alternative to Circular Pin Fins for Gas Turbine Blade Cooling Applications; Part 2:Wake Flow Field Measurements and Visualization Using Particle Image Velocimetry, *In: Proceedings of 46th ASME International Gas Turbine, Aeroengine Congress and Exposition and Users Symposium*, New Orleans, Louisiana, USA, 2001

[55] M.M. AbuOmar and R.J. Martinuzzi, Vortical structures around a surface-mounted pyramid in a thin layer, *Journal of Wind Engineering and Industrial Aerodynamics*, 2008, **96**, pp. 769-778

[56] M.J. Morrison, R.J. Martinuzzi, E. Savory and G.A. Kopp, Vortex shedding from slender surface mounted pyramids, In: Canadian Society of Mechanical Engineering Forum, Kananaskis, Canada, 2006

[57] R.J. Martinuzzi, Dual vortex structure shedding from low aspect ratio, surface-mounted pyramids, *Journal of Turbulence*, 2008, **9**(28), pp. 1-16

[58] S. Naik, S.D. Probert and M.J. Shilston, Forced convective steady-state heat transfers from shrouded vertical fin arrays aligned parallel to an undisturbed air-stream, *Applied Energy*, 1987, **26**, pp. 137-158

[59] J.J. Hwang and T.M. Liou, Heat transfer and friction in a low-aspect-ratio rectangular channel with staggered perforated ribs on two opposite walls, *ASME Journal of Heat Transfer*, 1995, **117**(11), pp. 843-850

[60] Y. Rao, Y. Xu and C. Wan, An experimental and numerical study of flow and heat transfer in channels with pin fin-dimple and pin fin arrays, *Experimental Thermal and Fluid Science*, 2010, **38**, pp. 237-247

[61] P.-X. Jiang and R.-N. Xu, Heat transfer and pressure drop characteristics of mini-fin structures, *International Journal of Heat and Fluid Flow*, 2007, **28**, pp. 1167-1177